



Norwegian University of
Science and Technology

Power Pylons in Aluminium

Behaviour of Axial Statically Loaded Hollow
Cylinders in Aluminium

Andreas Vestermo Nesje
Pål Arild Nilsen

Civil and Environmental Engineering

Submission date: June 2016

Supervisor: Magnus Langseth, KT

Co-supervisor: Marius E. H. Andersen, KT

Norwegian University of Science and Technology
Department of Structural Engineering



MASTER THESIS 2016

SUBJECT AREA: Buckling of cylinders in aluminium	DATE: 10 June 2016	NO. OF PAGES: 233 (22+164+47)
---	-----------------------	----------------------------------

TITLE:

Power Pylons in Aluminium

Høyspentmaster i Aluminium

BY:

Andreas Vestermo Nesje

Pål Arild Nilsen



SUMMARY:

The buckling behaviour of T6-tempered aluminium alloys 6060 and 6082 were analysed for two cylindrical cross-sections with r/t relationship 10 and 35. These were studied up to the point of maximum load with various lengths, and the effect of inelastic behaviour was discussed. Theoretical approaches including Eurocode 9 were compared to conducted compression tests from laboratory and FEA. Three types of laboratory setups were conducted: Dog bone specimen tension test, short stub column compression tests with lengths two and four times the diameter and compression tests of 2 metres long cylinders. In addition, an intended laboratory setup with low-friction spherical BCs was discarded based on preliminary FEM analyses of the setup, as results displayed an unachievable strict limit for friction. Material behaviour on a basis of tension tests was thoroughly adapted to fit Voce hardening law. Digital image correlation was applied to extract strain data, and the material calibration process involved broad data-treatment due to several challenges in material behaviour and numerical results. Using the results in compression tests rendered 2-4 percent underestimation of capacity for 6060T6 and 6-7 percent for 6082T6. Challenges and improvements to the FEA model are suggested. Imperfection is thoroughly assessed for longer members. Results from laboratory, FEM analyses, analytical solutions and recommendations from Eurocode 9 were compared. The Eurocode predicted correct failure mode, but estimations were conservative with an underestimation of up to 16 percent. The analytical solutions had higher capacity accuracy and the FEM analyses even more so, but both these failed at predicting correct failure mode for some profiles. The FEA model predicted correct failure mode on all except the slenderest, longest profile, and less than 7 percent deviation in capacity compared to the compression tests.

RESPONSIBLE TEACHER:	Professor Magnus Langseth
SUPERVISOR(S):	Professor Magnus Langseth and consultant Marius Endre Andersen
CARRIED OUT AT:	The Department of Structural Engineering, NTNU.

MASTEROPPGAVE 2016

for

Andreas Nesje og Pål Arild Nilsen

Høyspentmaster i aluminium

Power pylons in aluminum

Statnett ønsker å vurdere bruk av aluminium som konstruksjonsmateriale i høyspentmaster. Enkle beregninger basert på EC9 indikerer en totalvekt på ca 5500kg for en aluminiummast sammenlignet med 9100kg for en tilsvarende mast i stål. Foreløpige vurderinger indikerer at denne vektbesparelsen ikke gir tilstrekkelig kostnadsbesparelse til at dette er et interessant prosjekt for Statnett. Dette synliggjør behovet for mere nøyaktige verktøy hvor en optimal kombinasjon av material og geometri kan etableres. Avanserte FEM beregninger tilpasset aluminium som konstruksjonsmateriale kan være et alternativ for å få en tilfredsstillende vektbesparelse.

Denne oppgaven er en del av dette prosjektet. Målet med oppgaven er å etablere validerte numeriske analysemodeller for søyler i aluminium hvor interaksjon mellom lokal og global knekking inntreffer. I dette ligger også en vurdering av hvordan varmepåvirket sone ved opplegg og i felt vil påvirke kapasiteten og hvordan dette skal modelleres. De numeriske analysene skal valideres mot utførte forsøk og vurderes opp mot beregninger etter EC9.

Følgende foreløpige plan er definert for denne oppgaven:

- Det skal gjennomføres et litteraturstudium knyttet til oppførsel og modellering av søyler i aluminium utsatt for aksiallast. Spesielt skal det legges vekt på søyler med sirkulært tverrsnitt. Klassiske metoder for lokal og global knekking inklusive interaksjon skal presenteres og evalueres opp mot kandidatenes egne forsøk og simuleringer.
- Kandidatene skal delta i planlegging og gjennomføring av forsøk i laboratoriet. Dette gjelder både materialforsøk og komponentforsøk.
- Det skal etableres numerisk modeller for global og lokal knekking samt validering basert på de tester som er utført.
- Det skal gjennomføres parameterstudier samt at retningslinjer for modellering skal angis. I tillegg skal nøyaktigheten til EC9 evalueres og diskuteres med bakgrunn i kandidatenes egne forsøk og simuleringer.
- Rapportering.

Veiledere: Magnus Langseth og Marius Andersen

Kandidatene kan fravike den foreslåtte plan, men kun etter avtale med veilederne. Hovedoppgaven skal skrives på engelsk og utformes som en forskningsrapport og i henhold til gjeldende regler for en hovedoppgave. Oppgaven skal leveres til Institutt for konstruksjonsteknikk, NTNU innen 10. juni 2016.

NTNU, 14. januar 2016

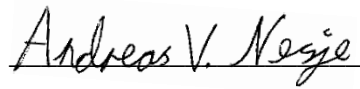
Magnus Langseth
Professor

Preface

This thesis is written for department of structural engineering at NTNU in the time period 15th of January to 10th of June 2016. The department of structural engineering is a collaborator in the project “Design of power pylons in aluminium customized for automatic production” led by Hydal Aluminium Profiler. The project has been granted 10 million Norwegian Kroner over a time period of three years by Forskningsrådet, and is still in its early stages.

The focus of this thesis is directed to aluminium on a general level rather than its direct appliance to power pylons in specific. The purpose is to study the mechanical properties of aluminium, with focus on the treatment of instability.

Trondheim, 10 June 2016



Andreas V. Nesje



Pål Arild Nilsen

Acknowledgements

We would like to thank professor Magnus Langseth for thorough help through the work with this thesis, for clarifying complex mechanical and analytical problems, for long discussions and helpful feedback.

We will give a special thanks to Marius E. Andersen for brilliant insight in the computational part of the thesis, both regarding modelling, scripting and understanding the underlying problems encountered. Both have been indispensable in the work with this thesis.

We would also like to thank our co-student Sigurd Guddal, who wrote his thesis on the same project, and our co-student Andreas Myräng for insightful feedback. Through the execution of laboratory sessions, the help from Senior Engineer Trond Auestad was appreciated.

Great thanks to Researcher Egil Fagerholt, who contributed in understanding his software, eCorr. Professor Per Kristian Larsen was also very helpful, we thank him for his insight and contribution.

We have received good help from employees at SIMLab and SINTEF and would like to thank them for their contribution and support.

Abstract

This thesis studies the behaviour of axial statically loaded circular hollow cylinders in aluminium and is written as a part of the project “Design of power pylons in aluminium customized for automatic production”.

Theoretical approaches regarding mechanics of instability and plasticity, including guidelines from Eurocode 9, were expounded. The buckling behaviour was studied up to the point of maximum load for cylinders with various lengths, and the effect of inelastic behaviour was discussed. These approaches were compared to conducted compression tests from laboratory and finite element analyses (FEA).

T6-tempered aluminium alloys 6060 and 6082 were analysed for two cross-sections with r/t relationship 10 and 35.

The choices behind FEA modelling in the finite element method (FEM) software Abaqus was elaborated and discussed. Intended laboratory setup with low-friction spherical BCs was discarded based on preliminary FEM analyses of the setup, as results displayed an unachievable strict limit for friction. Three types of laboratory setups were conducted: Dog bone specimen tension test, short stub column compression tests with lengths two and four times the diameter and compression tests of two metres long cylinders. Measurements of geometry were discharged for all sessions and the influence of deviations are assessed.

Material behaviour on a basis of tension tests was thoroughly adapted to fit Voce hardening law. Digital image correlation was applied to extract strain data, and the material calibration process involved broad data-treatment due to several challenges in material behaviour and numerical results. Using the results in compression tests rendered 2-4 percent underestimation of capacity for 6060T6 and 6-7 percent for 6082T6.

Calibration of FEA model with a broad parameter study focusing on mesh and imperfections led to a partially robust model regarding compression of cylinders with clamped boundary conditions. The slenderest cross-section presented a challenge, as introducing a necessary global imperfection to the FEA caused it to predict a global buckling mode on cylinders that in laboratory were observed to buckle locally.

Results from laboratory, FEM analyses, analytical solutions and recommendations from Eurocode 9 were compared. The Eurocode predicted correct failure mode, but estimations were conservative with an underestimation of up to 16 percent. The analytical solutions had higher capacity accuracy and the FEM analyses even more so, but both these failed at predicting correct failure mode for some profiles. The FEA model predicted correct failure mode on all except the slenderest, longest profile, and less than 7 percent deviation in capacity compared to the compression tests.

Sammendrag

Denne avhandlingen omhandler aksielt statisk belastede hule sirkulære sylindere i aluminium, og er skrevet som en del av prosjektet «Design av aluminiummast tilpasset automatisert produksjon».

Teoretiske tilnærminger angående instabilitet og plastisitet, inkludert retningslinjer fra Eurokode 9, ble utdypet. Knekningsoppførselen ble studert frem til maksimal last for sylindere med ulike lengder, og effekten av inelastisk oppførsel ble diskutert. Disse tilnærmingene ble sammenlignet med utførte trykkforsøk fra laboratorium og finite element analyser (FEA).

Aluminiumslegeringene 6060 og 6082 med varmhærding T6 ble analysert for to tverrsnitt med r/t-forhold på 10 og 35.

Valg bak FEA modelleringen i elementmetode-programmet Abaqus ble utdypet og diskutert. Et planlagt laboratoriumsforøk med en lavfriksjons halvkule som opplagerbetingelse ble forkastet basert på innledende FEM-forsøk av oppsettet, da resultatene krevde uoppnåelige friksjonsverdier. Tre nye laboratoriumsforøk ble utført: Dog bone strekktest, kort sylinder i trykk med lengde på to og fire ganger diameteren og trykktester for to meter lange sylindere. For hver laboratoriumsøkt ble geometri målt, og påvirkningen av avvik ble behandlet.

Materialoppførsel basert på strekktestene ble grundig tilpasset Voce herdingslov. Digital bildekorrelasjon ble brukt for å uthente tøyingsdata, og materialkalibreringsprosessen involverte en bred databehandling på grunn av flere utfordringer tilknyttet materialoppførselen og numeriske resultater. Resultatene ble brukt i trykkmodellering, og viste 2-4 prosent underestimering av kapasitet for 6060T6 og 6-7 prosent for 6082T6.

Kalibrering av FEA modellen med et omfattende parameterstudie med fokus på elementnett og imperfeksjoner, førte til en delvis robust modell for sammentrykking av sylindere med fast innspente grensebetingelser. Det tynneste tverrsnittet bød på utfordringer, da en innføring av en nødvendig global imperfeksjon førte til at FEA modellen foreslo en global knekningsform for sylindere som i laboratorium knakk lokalt.

Resultater fra laboratorium, elementmetodeanalyser, analytiske løsninger og anbefalinger fra Eurokode 9 ble sammenlignet. Eurokoden forutså riktig knekningsform for alle profiler, men anslagene var konservative med en underestimering på opptil 16 prosent. Analytiske løsninger hadde høyere nøyaktighet med tanke på kapasitet, og elementmetodeanalysene var bedre enn disse, men begge anslo feil knekkform på enkelte profiler. FEA modellen resulterte i riktig knekningsmode på alle unntatt det lengste, slankeste profilet, og hadde mindre enn 7 prosent avvik på alle trykkprøver.

Table of content

List of Figures	xiii
List of Tables.....	xix
Abbreviations and terms.....	xxi
1 Introduction	1
2 Software	5
3 Theoretical Approach.....	7
3.1 Analytical background.....	7
3.2 Mechanics and statics	8
3.2.1 Coordinate system	8
3.2.2 Elasticity.....	9
3.2.3 Plasticity.....	10
3.2.4 Material behaviour	11
3.3 Stability.....	14
3.3.1 Global stability	14
3.3.2 Local stability	18
3.4 Geometry and material	22
3.4.1 Imperfections.....	25
3.5 Eurocode.....	27
3.5.1 Eurocode 9 Part 1-1: General structural rules	27
3.5.2 Eurocode 9 Part 1-5: Shell structures	31
3.5.3 Characteristic load according to Eurocode 9.....	33
3.6 Comparison buckling resistance from theoretical approaches	38
4 Finite Element Method – Modelling in Abaqus.....	41
4.1 Geometry and boundary conditions.....	41
4.1.1 Introducing imperfections to the FEA model.....	42
4.2 Material data	44
4.3 Solution algorithm and scaling	45

4.3.1	Implicit solution algorithm.....	45
4.3.2	Explicit solution algorithm.....	46
4.3.3	Scaling of the analysis.....	47
4.4	Element type and mesh.....	48
4.4.1	Shell elements	50
4.4.2	Volume elements.....	50
4.4.3	Mesh.....	51
4.5	Validation of analyses	51
4.6	Output data	52
5	Laboratory Design with Spherical Hinge.....	55
5.1	FEA model.....	56
5.1.1	Troubleshooting and improvement of the model	56
5.1.2	Sensitivity analyses	58
5.1.3	Conclusions	61
6	Tension Material Test.....	63
6.1	Phase one: Laboratory setup and DIC	63
6.2	Theoretic calculations of stresses and strains	66
6.3	Phase two: Data analysis and extraction.....	69
6.4	Phase three: Generation and FEM verification of stress-strain relationship	80
6.5	Verification through force-displacement correlation	86
7	Hollow Cylindrical Columns in Compression	93
7.1	Compression test for L2D and L4D	93
7.1.1	Laboratory setup and geometry.....	93
7.1.2	Compression test results.....	97
7.2	Compression test for L2000	105
7.2.1	Compression test results.....	107
7.3	The FEA model for compression tests	111
7.3.1	Basis for the FEA model	112

7.3.2	Sensitivity analyses	112
7.4	Comparison of FEA model and executed compression tests	123
7.4.1	FEM Analyses of L2D and L4D	123
7.4.2	FEA model extrapolation	128
7.4.3	FEM analyses of L2000	137
7.5	Comparison of Eurocode 9 and laboratory	141
7.5.1	Local slenderness	142
7.6	Comparison of theoretic approaches and compression tests	143
7.7	Comparison of all approaches	148
7.7.1	Results for L2D, L4D and L2000.....	148
7.7.2	Results for all lengths	150
8	Conclusions	155
9	Future Work	157
	Bibliography.....	161
Appendix A	NACA reports.....	A
Appendix B	Laboratory: Premeasurement of geometry	E
Appendix C	Eurocode 9 part 1-1	I
Appendix D	Eurocode 9 part 1-5	M
Appendix E	Executed laboratory test and measurements for L2D and L4D.....	Q
Appendix F	Mesh sensitivity L2D.....	AA
Appendix G	Laboratory L2000mm.....	KK
Appendix H	Results from FEA	SS

List of Figures

Figure 1 Example of (a) global and (b) local buckling patterns of cylinders..... 8

Figure 2 Cylindrical coordinate system 8

Figure 3 Globally buckling simply supported column,..... 15

Figure 4 Notation for profiles..... 22

Figure 5 Schematic representation of systematic and random error 23

Figure 6 Examples of the three types of imperfections..... 26

Figure 7 Characteristic load according to Eurocode 9 for material A6060D100 and EC6060T6 with clamped BCs. 34

Figure 8 Characteristic load according to Eurocode 9 for material A6060D127 and EC6060T6 with clamped BCs. 35

Figure 9 Characteristic load according to Eurocode 9 for material A6082D100 and EC6082T6 with clamped BCs. 36

Figure 10 Characteristic capacity according to Eurocode 9 with clamped BCs. 37

Figure 11 Local imperfections imposed by changing node coordinates 43

Figure 12 Main path and bifurcated (buckling) path cross at a bifurcation point..... 45

Figure 13 Laboratory setup with SKF GX 80 F components and a customized endplate. 56

Figure 14 Spherical surfaces discretized y straight elements..... 57

Figure 15 Failure mode with different frictional coefficients. Displayed deformation scaled with factor 3, rigid bowl-endplate component is not shown. 60

Figure 16 (a) Relation between capacity and frictional coefficient (b) Mechanical model including rotational stiffness from friction..... 60

Figure 17 The dog bone specimens were slightly curved. 64

Figure 18 The specimens were cut out of the cylinders 64

Figure 19 Geometry of the UT 110 dog bone tension specimen 64

Figure 20 Camera setup to allow usage of DIC technology 64

Figure 21 Typical speckled paint applied to the dog bone..... 64

Figure 22 Rectangle and arc 64

Figure 23 Mesh applied before analysis, on undeformed specimen	65
Figure 24 Deformed mesh at final stage of the test.....	65
Figure 25 From the deformation, an interpolated strain field was created	65
Figure 26 The four stages of tension tests.....	66
Figure 27 Strain averaging over 10 elements.....	71
Figure 28 Typical strain bands at 1-2 % strain.....	71
Figure 29 Very rough mesh.....	71
Figure 30 Very fine mesh.....	71
Figure 31 Dependency of element size.	73
Figure 32 Smoothing of the average ϵ_z for a column of elements in the neck.....	73
Figure 33 Smoothed columns of elements with different mesh and placement.....	74
Figure 34 Compressive strains at tensile loading	75
Figure 35 Tangent modulus as yield criterion - A6060D127.....	76
Figure 36 Translation of the stress-strain curve - A6082T6D100 specimen 1	77
Figure 37 True strain in different directions for 20x20 pixel mesh.	78
Figure 38 Rotation of principal strains, smoothed with span 33.....	79
Figure 39 Difference between principal and perceived (camera) longitudinal strain	79
Figure 40 Model with curve A6060D127	81
Figure 41 Mesh for A6060D100.	81
Figure 42 Initial parameters for Voce hardening - A6060D127.	82
Figure 43 Effect of altering the value of C_2 – A6060D127	83
Figure 44 Voce hardening rule for the three material types.....	84
Figure 45 Sensitivity of mesh size and MS.....	85
Figure 46 Mechanical model including machine compliance.....	87
Figure 47 Chosen Voce hardening and laboratory results - A6060D100	88
Figure 48 Force-displacement comparison - A6060D100	88
Figure 49 Chosen Voce hardening and laboratory results - A6060D127	89
Figure 50 Force-displacement comparison - A6060D127	89

Figure 51 Chosen Voce hardening and laboratory results - A6082D100	90
Figure 52 Force-displacement comparison - A6082D100	90
Figure 53 Setup in the laboratory before testing, with laser and mounted steel plate to the right	95
Figure 54 Setup in laboratory during testing with visible speckled paint	95
Figure 55 Force – displacement curves from compression tests of profile A6060D100L2D and A6060D100L4D	98
Figure 56 Stress – strain curves from compression tests of profile A6060D100L2D and A6060D100L4D	98
Figure 57 Deformation in transverse direction (towards camera) at maximum load. Pictures generated in eCorr, (a) A6060D100L2D (b) A6060D100L4D (c) scale [mm]	99
Figure 58 Force – displacement curves from compression tests of profile A6060D127L2D and A6060D127L4D	100
Figure 59 Stress – strain curves from compression tests of profile A6060D127L2D and A6060D127L4D	100
Figure 60 Deformation in transverse direction (towards camera) at maximum load. Pictures generated in eCorr, (a) A6060D127L2D with scale [mm] (b) A6060D127L4D	101
Figure 61 Force – displacement curves from compression tests of profile A6082D100L2D and A6082D100L4D	102
Figure 62 Stress – strain curves from compression tests of profile A6082D100L2D and A6082D100L4D	102
Figure 63 Deformation in transverse direction (towards camera) at maximum load. Pictures generated in eCorr, (a) A6082D100L2D (b) A6082D100L4D	103
Figure 64 Laboratory setup for L2000mm	106
Figure 65 Force – displacement curves from compression tests of profile A6060D100L2000	108
Figure 66 Stress – strain curves from compression tests of profile A6060D100L2000	108
Figure 67 Force – displacement curves from compression tests of profile A6060D127L2000	109
Figure 68 Stress – strain curves from compression tests of profile A6060D127L2000	109

Figure 69 Force – displacement curves from compression tests of profile A6082D100L2000	110
Figure 70 Stress – strain curves from compression tests of profile A6082D100L2000	110
Figure 71 Assembly in Abaqus model used for compression test	112
Figure 72 Sensitivity of mesh for A6060D100L2D	114
Figure 73 Sensitivity of mesh for A6060D100L2D (zoomed)	114
Figure 74 Sensitivity of mesh for A6060D127L2D	115
Figure 75 Sensitivity of mesh for A6060D127L2D (zoomed)	115
Figure 76 Study of the effect of ill-conditioning for different ratios of element length to element thickness A6060D127L2D, C20R elements	116
Figure 77 Mesh sensitivity - A6060D127L20D	118
Figure 78 Sensitivity tests of friction - A6060D100L2D	119
Figure 79 Sensitivity tests of friction - A6060D100L2D (zoomed)	119
Figure 80 Influence of imperfection for the profile A6060D100L2D	121
Figure 81 Influence of imperfection for the profile A6060D127L2D	121
Figure 82 Failure mode from vase-shaped imperfection	122
Figure 83 Cross-section with translated inner circle	123
Figure 84 Stress – strain graphs from compression tests and FEA analyses for A6060D100L2D and A6060D100L4D	124
Figure 85 Stress – strain graphs from compression tests and FEA analyses for A6060D127L2D and A6060D127L4D	124
Figure 86 Stress – strain graphs from compression tests and FEA analyses for A6082D100L2D and A6082D100L4D	125
Figure 87 FEM contour plot of logarithmic strain at maximum load for A6060D100L2D ..	126
Figure 88 Radial displacement from DIC - A6082D100L2D	127
Figure 89 Radial displacement from DIC and FEA - A6082D100L2D	128
Figure 90 Maximum load from tests and FEA for A6060D100 for lengths 1D to 30D	129
Figure 91 Maximum load from tests and FEA for A6060D100 for lengths 1D to 5D	129

Figure 92 Buckling-shape at maximum load for A6060D100 with imperfection $a = L/1000$	130
Figure 93 Maximum load from tests and FEA for A6060D127 for lengths 0.5D to 30D.....	131
Figure 94 Maximum load from tests and FEA for A6060D127 for lengths 0.5D to 12D.....	131
Figure 95 Buckling-shape at maximum load for A6060D127 with imperfection $a = L/1000$	132
Figure 96 Maximum load from tests and FEA for A6082D100 for lengths 1D to 30D	133
Figure 97 Maximum load from tests and FEA for A6082D100 for lengths 1D to 5D	133
Figure 98 Buckling-shape at maximum load for A6082D100 with imperfection $a = L/1000$	134
Figure 99 Comparison of stresses. Tension test results have been down sampled (fewer frames) for easier graph comparison	135
Figure 100 Force – displacement from compression tests and FEA, A6060D100L2000.....	137
Figure 101 Force – displacement from compression tests and FEA, A6082D100L2000.....	138
Figure 102 Force - displacement from compression tests and FEA, A6060D127L2000	139
Figure 103 Global imperfection amplitude study for A6060D127L2000.....	140
Figure 104 Reduction of global imperfection in FEA model for A6060D127L2000.....	140
Figure 105 Buckling reduction factor according to Eurocode 9 and estimated from compression tests L2D and L4D	143
Figure 106 Inelastic instability criteria and laboratory results - A6060D100.....	145
Figure 107 Inelastic instability criteria and laboratory results – A6060D127	146
Figure 108 Inelastic instability criteria and laboratory results - A6082D100.....	147
Figure 109 Comparison of results for A6060D100.....	150
Figure 110 Comparison of results for A6060D127	151
Figure 111 Comparison of results for A6082D100.....	151
Figure 112 Normalized capacity as a function of global slenderness from compression tests, FEA and Eurocode 9.	153
Figure 113 New hinged laboratory setup to analyse globally buckling cylinders	158

List of Tables

Table 1 Chosen and calculated mean thickness and diameter with corresponding covariance. 24

Table 2 Material and geometry properties for the cylinders studied..... 25

Table 3 Characteristic value of 0.2 % proof strength from Eurocode 9..... 28

Table 4 Cross-sectional classes according to Eurocode 9 Part 1-1 29

Table 5 Classification of cross-section according to Eurocode 9 29

Table 6 Limit values for different failure modes 39

Table 7 Elastic and physical properties of aluminium and steel 44

Table 8 Measured geometry of the dog bone specimens 68

Table 9 Voce parameters for the materials..... 85

Table 10 Characteristic stress f_0 85

Table 11 Spring stiffnesses to account for machine compliance 87

Table 12 Material and length of column specimen 94

Table 13 Measured thickness for laboratory tests on L2D and L4D 96

Table 14 Results from compression tests for L2D and L4D profiles..... 97

Table 15 Axial capacity [kN] from mesh sensitivity analyses at L2000 118

Table 16 Basis for introducing vase-shaped imperfections 120

Table 17 Capacity of short column compression tests [kN] FEA model with different imperfections and compression test results 125

Table 18 Axial capacity and buckling mode according to Eurocode 9 part 1-1, part 1-5 and compression tests..... 142

Table 19 Estimated and observed capacity and failure mode 148

Table 20 Measured and predicted buckling stress (engineering longitudinal stress)..... 149

Abbreviations and terms

A	Area [mm^2]
BC	Boundary condition
Dof	Degree of freedom
E	Young's Modulus [MPa]
ETT	Number of elements through the thickness of the cylinder
FEA	Finite element analysis
FEM	Finite element method
G	Global buckling mode
I	Second moment of area [mm^4]
L	Length of cylinder [mm], Local buckling mode
LBA	Linear Bifurcation Analysis or Eigenmode analysis
M	Bending moment [Nmm]
MS	Mass scaling [s]
N	Normal (axial) force [N]
RP	Reference point (in FEA)
V	Velocity [mm / s]
X	No buckling mode affects capacity
a	Imperfection amplitude [mm]
e	Engineering strain [-]
f_0	0.2 % proof strength [MPa]
r	Radius [mm]
s	Engineering stress [MPa]
t	Thickness [mm]
w	Width of tension test gauge
β	Local slenderness parameter [-]
ε	Logarithmic strain [-]
$\bar{\lambda}$	Global slenderness parameter [-]
μ	Friction coefficient [-]
ν	Poisson's ratio [-]
ρ	Density [kg / m^3]
σ	True stress [MPa]
ω	Natural oscillation frequency [rad / s]

Subindices and superindices

o	Outer
i	Inner
m	Middle
0	Initial
V	Volume/volumetric
R	Resistance
y	Yield/yielding
Pl	Plastic
El	Elastic
i,j,k,m	Direction indices

1 Introduction

This thesis investigates the inelastic material and mechanical behaviour of hollow aluminium cylinders in axial compression. Theoretic approaches, guidelines from Eurocode 9 and FEM analyses are expounded and compared to results from performed compression tests.

The thesis is written as a part of a research project named “Design of power pylons in aluminium customized for automatic production” at the department of structural engineering, NTNU. Project Manager Tore Tryland [1] presents the project vision as: *“It is expected that high tension towers in aluminium based on welded modules in aluminium can replace steel profiles in countries with lower cost levels.”*

When creating power pylons, smaller members are put together to form modules which are transported by helicopter to the construction site. Module size is restricted by the helicopters’ load carrying capacity, and a large number of modules gives rise to both economical and work-safety issues. According to a presentation by Tore Tryland [1], the existing power pylons in steel requires 12 helicopter lifts. With effective utilization of aluminium modules, it is anticipated that the number of helicopter rides can be reduced to 5. This prospect stems from the low density of aluminium [2], which is roughly one third as dense as steel [3], while still exhibiting a high yield stress. The disadvantages of aluminium compared to steel includes high price and low stiffness [4]. By establishing numerical FEA models, it is desirable to exploit the strength and capability of the material to a larger extent than permitted by the existing guidelines.

The primary focus of this thesis is a literature study of inelastic instability problems, followed by modelling of material as well as mechanical stability behaviour through FEM analyses. The study is restricted to axially loaded hollow cylinders, with calculations limited to alloys 6060T6 and 6082T6 combined with two types of cross-section with r/t relationship 10 and 35. The aim of these buckling analyses is to study the behaviour of the columns up to the point of maximum load, when buckling occurs. The thesis is limited to extruded aluminium profiles without welds under quasi-static loading conditions at room temperature. The calculations are purely based on accuracy and does not include safety factors necessary for design.

The chapters in this thesis are:

Chapter 2, Software: Shortly summarizes all software used in the thesis.

Chapter 3, Theoretical Approach: Introduces the mechanical formulas used for data treatment and evaluation. Solution to instability problems from different sources are treated. Capacity according to Eurocode 9 with material parameters from tension tests are discussed with a possible fallacy. This chapter concludes with graphical representations of axial capacity of cylinders on different lengths up to 6 metres according to Eurocode 9.

Chapter 4, Finite Element Method – Modelling in Abaqus: Parameters and choices behind the FEM analyses are discussed. Several ways of introducing imperfections to models, a crucial aspect of modelling instability, are explained. The choice of elements and solution algorithms are discussed.

Chapter 5, Laboratory Design with Spherical Hinge: A laboratory setup with spherical low-friction boundary conditions is analysed through FEA

Chapter 6, Tension Material Test: Based on dog bone tension tests executed in laboratory, the material properties are fitted to Voce hardening rule. DIC technology was enabled through the laboratory setup. Several aspects and solutions to challenges from the material treatment phase are discussed.

Chapter 7, Hollow Cylindrical Columns in Compression: Compression tests on hollow columns of three different lengths are performed. A FEA model is established and a thorough parameter study is discharged. The model is extrapolated to other lengths and deviations towards laboratory results as well as sensitivity towards imperfections are evaluated. Deficiencies of the material model are discussed. The accuracy of Eurocode 9 and theories derived in chapter 3 is assessed.

Chapter 8, Conclusions: A short summary of the results of the thesis is presented, including the challenges faced.

Chapter 9, Future Work: Based on the conclusions, several solutions and improvements are suggested. These are partially based on the already planned and ordered tasks, such as a new laboratory setup.

2 Software

During the course of this thesis, several software were used for different purposes. These are listed and briefly explained below.

Abaqus

Abaqus is a FEM software written by Dassault Systems and released by Simulia [5]. It was chosen as the FEM software for this thesis both because it is renowned as a robust multi-purpose FEA software, and because the authors had previous experience using the program. The majority of analyses in Abaqus were scripted in Python, using the software Notepad ++. The modelling in Abaqus is explained in detail throughout the thesis, in particular in chapter 4.

Matlab

Mathworks' program Matlab is chosen as the main data treatment program. All graphs and plots in this thesis were generated in Matlab. Several other tasks were carried out in this versatile software, from calculations of results from analyses and laboratory to imposing imperfections to some of the FEM models.

eCorr

eCorr is a Digital Image Correlation (DIC) software developed at NTNU by Egil Fagerholt. This software was used to extract strains from pictures captured at the testing in laboratory. If two or more cameras are used in the laboratory, a calibration process can be discharged to enable three-dimensional DIC.

Word

The thesis is written in Microsoft Office Word with the add-ons EndNote X7 and MathType.

Excel

Microsoft Office Excel is used for certain data treatment operations and creation of tables.

Autocad

Autodesk's software Autocad is used to sketch simple figures.

3 Theoretical Approach

3.1 Analytical background

Axially compressed hollow cylinders of various lengths and failure modes are studied. The goal of this chapter is to explore theoretical background as well as different rules and guidelines given in literature. The study focus on axial capacity and instability modes. Three main literature sources are analysed regarding rules and guidelines as well as analytical and empirical derivations. Firstly, reports by NACA (the National Advisory Committee for Aeronautics), dated back to 1950-1960 are analysed in the treatment of local instability [6-8]. Secondly, global buckling formulas are extended to the plastic domain by Jones [9]. Thirdly, the Eurocodes that governs structures of aluminium and aluminium shells structures are discussed, which are part 1999-1-1 [2] and part 1999-1-5 [10].

Three important aspects complicated the analysis of circular hollow cylinders in axial compression in this thesis:

1. The instabilities may be local or global (figure 1), as different failure modes can be observed at different lengths, and these buckling modes can affect each other.
2. The instabilities are inelastic. The stability problem that relates to slenderness and stiffness is therefore related to the capacity problem where yield stress and hardening are essential.
3. The uniaxial compressive loading produces a tri-axial stress field. This complexify the calculations on material behaviour.

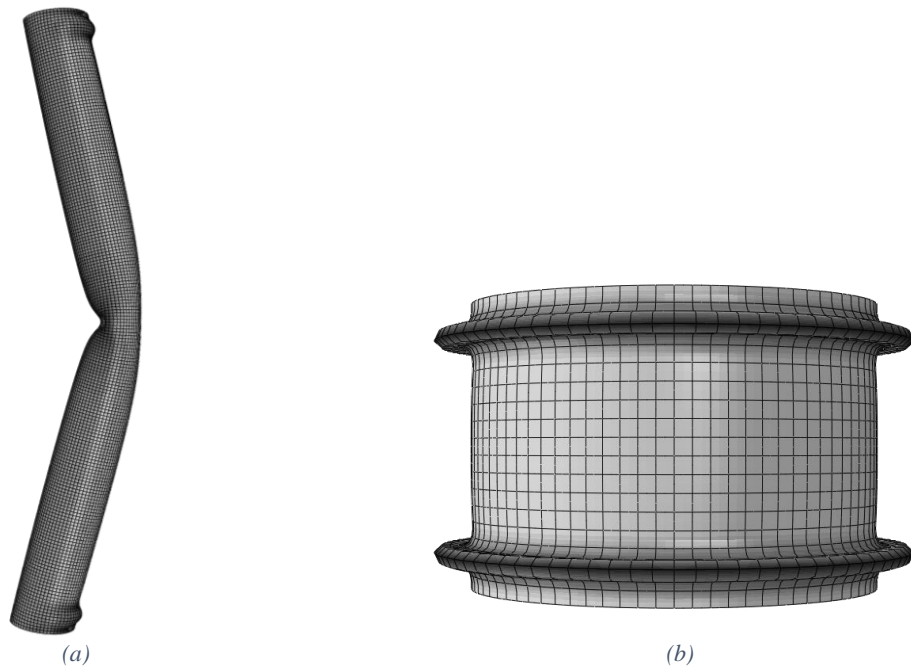


Figure 1 Example of (a) global and (b) local buckling patterns of cylinders

3.2 Mechanics and statics

3.2.1 Coordinate system

The cylindrical coordinate system given in figure 2 is used herein, unless specified otherwise. The x -direction coincides with the radial direction, the y -direction with the circumferential and the z -direction is the longitudinal direction. The y -coordinate is given in radians. All externally applied forces act in the z -direction. The deformation in the respective directions are labelled u , v and w . The sub-indices i and j are used as arbitrary coordinate or deformation indices.

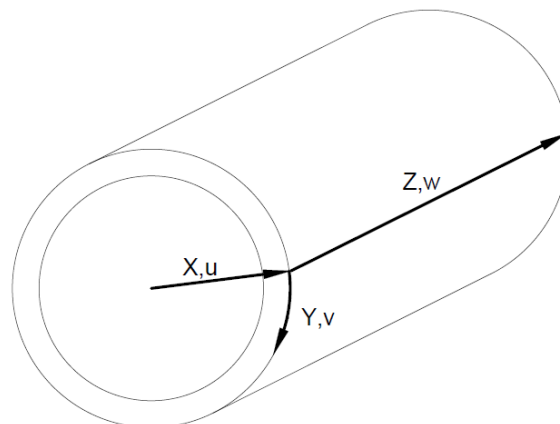


Figure 2 Cylindrical coordinate system

3.2.2 Elasticity

Aluminium on a molecular level consists of many small grains with random orientation. Due to very small grains, the metal still exhibits close to isotropic behaviour. Metals are often assumed to be plastically incompressible, meaning that no deformation can change the volume permanently. The material is also homogenous, and the strength of the material is assumed identical in tension and compression. [11]

An axial force N applied to a material gives rise to internal stresses

$$\sigma = \frac{N}{A} \quad (3.1)$$

These stresses, labelled true stress, relates to the area deformed by the force. Engineering stress relates to the initial, undeformed area

$$s = \frac{N}{A_0} \quad (3.2)$$

The deformation leads to internal strains in the material, and two measures of strains are used in this thesis; the logarithmic strain relating to the current length

$$\varepsilon = \int \frac{dL}{L} = \ln\left(\frac{L}{L_0}\right) \quad (3.3)$$

and the engineering strain, relating to the initial length

$$e = \int \frac{dL}{L_0} = \frac{L - L_0}{L_0} = \exp(\varepsilon) - 1 \quad (3.4)$$

Small strains cause $e \approx \varepsilon$ and $s \approx \sigma$. The strain measures e and ε deviates with increasing strains. For larger strains, the volumetric strains are assumed to be zero, keeping the volume constant:

$$AL = A_0L_0 \rightarrow A_0 = \frac{L}{L_0} A \quad (3.5)$$

The relationship between the true- and engineering stress can be written as

$$s = \frac{N}{A_0} = \frac{N}{\frac{L}{L_0} A} = \sigma \exp(-\varepsilon) = \frac{\sigma}{1+e} \quad (3.6)$$

True stress and logarithmic strain are energy conjugates, which means that the strain energy per unit volume can be expressed as

$$U_0 = \int \sigma d\varepsilon \quad (3.7)$$

Engineering stress and engineering strain are also energy conjugates. The strain energy is the basis for the non-linear finite element method equations. The thesis favours true stress and logarithmic strain, not only because it is most accurate at high strains, but also as it is the units used in two key software: Abaqus and eCorr. Note that Eurocode relates its formulas to the engineering stress and strain.

For both alloys there exists a unique relationship between σ and ε . Before yielding, the stress-strain relationship for uniaxial stress state is given by Hookes' law through E, Young's Modulus:

$$\sigma = E\varepsilon \quad (3.8)$$

The elastic strain energy from formula (3.7) can then be written as

$$U_0 = \frac{1}{2} E\varepsilon^2 = \frac{1}{2} \sigma\varepsilon \quad (3.9)$$

3.2.3 Plasticity

After reaching yield stress, the strains are partially plastic, leading to a non-linear relationship between stresses and strains, hence equation (3.8) is no longer valid. The strains are split into an elastic and a plastic part:

$$\varepsilon = \varepsilon^{El} + \varepsilon^{Pl} \quad (3.10)$$

Only the elastic part leads to stresses in the material

$$\sigma = E\varepsilon^{El} \quad (3.11)$$

The tangent modulus is introduced as the incremental stiffness modulus, which is the slope of the stress-strain curve

$$E_T = \frac{d\sigma}{d\varepsilon} \quad (3.12)$$

The secant modulus is defined as the "mean" stiffness modulus, relating the total stresses to the total strain

$$E_S = \frac{\sigma}{\varepsilon} = \frac{\sigma}{\varepsilon^{El} + \varepsilon^{Pl}} \quad (3.13)$$

Note that in the elastic region, $\varepsilon^{Pl} = 0$ and $E_T = E_S = E$.

The plastic moduli can be found by considering only the plastic strains, viz.

$$E_T^{Pl} = \frac{d\sigma}{d\varepsilon^{Pl}} \quad (3.14)$$

$$E_s^{Pl} = \frac{\sigma}{\varepsilon^{Pl}} \quad (3.15)$$

Applying a force on the material in one direction causes strains in all three directions. These strains are related through the Poisson ratio ν . If the force is applied in the z-direction:

$$\varepsilon_x = \varepsilon_y = -\nu\varepsilon_z \quad (3.16)$$

The Poisson ratio for elastic strains is assumed equal to 0.3, while for the plastic strains, plastic volumetric strain is assumed zero

$$\varepsilon_v^{Pl} = \varepsilon_x^{Pl} + \varepsilon_y^{Pl} + \varepsilon_z^{Pl} = 0 \quad (3.17)$$

Inserting plastic strains from (3.16) into equation (3.17) gives $\nu^{Pl} = 0.5$. At a plastic loading increment, the strain increment is split into plastic and elastic strain increments:

$$d\varepsilon = \frac{d\sigma}{E_T} = d\varepsilon^{El} + d\varepsilon^{Pl} = \frac{d\sigma}{E} + \frac{d\sigma}{E_T^{Pl}} \quad (3.18)$$

The relationship between the tangent moduli is found by dividing equation (3.18) by $d\sigma$

$$\frac{1}{E_T} = \frac{1}{E} + \frac{1}{E_T^{Pl}} \quad (3.19)$$

The same relationship is found with secant moduli if the Poisson ratio is assumed to be equal 0.5 for all strains

$$\frac{1}{E_s} = \frac{1}{E} + \frac{1}{E_s^{Pl}} \quad (3.20)$$

3.2.4 Material behaviour

Tri-axial stress – strain states complexify the mechanics of plasticity, and plays a key role in many of the considered analyses. For example, a short cylinder compressed between two plates develops compressive strains in the axial (or longitudinal) direction. The circumferential (or hoop) strain is in tension, and there will also be a tension stain in the radial or thickness direction. Close to the plates, frictional forces causes a complex stress state which may alter the buckling mode, as the stress state causes yielding at an earlier stage, lowering the stiffness in that area. The stress capacity in any one direction is dependent upon the stress in the other two, hence tri-

axiality must be included in the definition of the yield stress. The stress matrix is defined by Hopperstad [12] as

$$\boldsymbol{\sigma} = \begin{bmatrix} \sigma_x & \sigma_{xy} & \sigma_{zx} \\ \sigma_{xy} & \sigma_y & \sigma_{yz} \\ \sigma_{zx} & \sigma_{yz} & \sigma_z \end{bmatrix} \quad (3.21)$$

The off-diagonal terms in the stress matrix represent the shear stresses, while the diagonal contain the normal stresses in the three directions. The hydrostatic and deviatoric stress matrices are defined [12] as

$$\boldsymbol{\sigma}_H = \mathbf{I}_3 \bar{\sigma} = \begin{bmatrix} 1 & 0 & 0 \\ 0 & 1 & 0 \\ 0 & 0 & 1 \end{bmatrix} \frac{1}{3} (\sigma_x + \sigma_y + \sigma_z) \quad (3.22)$$

$$\boldsymbol{\sigma}' = \boldsymbol{\sigma} - \boldsymbol{\sigma}_H$$

Different yield criteria are indirectly based on the stress matrices presented, by using three distinct invariants, defined [12] as

$$I_1 = \sigma_{ii} = 3\bar{\sigma}$$

$$J_2 = \frac{1}{2} \sigma_{ij} \sigma_{ij} - \frac{1}{6} \sigma_{kk} \sigma_{mm} = \frac{1}{2} \sigma'_{ij} \sigma'_{ij} \quad (3.23)$$

$$J_3 = \det(\boldsymbol{\sigma}')$$

Note the use of Einstein's summation convention, which implies that repeated indices are summed over all variables, i.e.

$$\sigma_{kk} = \sigma_{11} + \sigma_{22} + \sigma_{33} \quad (3.24)$$

The yield criteria can be defined as the stress state when an equivalent stress σ_{eq} reaches a threshold (yield stress) σ_0

$$\sigma_{eq} = \sigma_0 \quad (3.25)$$

Several different yield criteria are defined solely by the definition of the equivalent stress σ_{eq} . In section 3.1 the material was assumed isotropic and plastically incompressible as well as having identical properties in compression and tension. Any pressure applied in all three directions should therefore not influence yielding, and only the deviatoric stress should govern the chosen yield criterion. A further assumption is that the isotropy gives equal capacity in each of the three directions. With these assumptions, the Von Mises is a natural choice of yield

criterion. The Von Mises yield criterion is often called the J_2 flow criterion [12], defining the equivalent stress as

$$\sigma_{eq} = \sqrt{3J_2} \quad (3.26)$$

The hardening due to plastic strain is a function of the accumulated plastic strain [12], given as

$$p = \int \left| \frac{d\varepsilon^{pl}}{dt} \right| dt \quad (3.27)$$

The material in this thesis is assumed to follow the Voce hardening rule as defined by Hopperstad [12]. This hardening relates the equivalent stress σ_{eq} to the accumulated plastic strain p , or in the uniaxial case, relates the stress σ to the plastic strain ε^{pl} , as

$$\sigma(\varepsilon^{pl}) = \sigma_{eq}(p) = \sigma_0 + \sum_{i=1}^n Q_i (1 - \exp(-C_i \varepsilon^{pl})) \quad (3.28)$$

with the derivative

$$\frac{\delta\sigma}{\delta\varepsilon^{pl}} = E_T^{pl} = \sum_{i=1}^n Q_i C_i \exp(-C_i \varepsilon^{pl}) \quad (3.29)$$

The advantage of applying hardening is discussed in chapter 6.

3.2.4.1 Strength differential effect

Unpublished work at NTNU by PhD candidate Holmen et al documents higher compressive than tensile strength for aluminium alloys. This pressure dependency is previously documented for pure titanium by Nixon et al [13], who labelled it the strength differential effect. The yield criterion is therefore dependent upon hydrostatic stress σ_H , not only the deviatoric stress σ' . The reason for this increased strength is believed to be related to the plastic strains. Plastic deformation moves dislocations along grain boundaries as shear deformation. The tip of the dislocation is a void that deforms and stores strain energy. When a sufficient amount strain energy is stored, the imperfection slip past another atom on the grain boundary, and plastic deformation takes place. The strength differential effect is believed to stem from higher required strain energy to move dislocation lines in materials loaded in compression. According to the Holmen et al, the effect in aluminium alloys are greatest for T4 tempered alloys, up to 10 percent difference, and around 4-7 percent for T6 tempers. Although no official reports have been released per June 2016, the results clearly indicate that it is possible that the alloys used in this thesis exhibit greater yield and ultimate strength in compression than tension.

In order to implement the strength differential effect, a change of yield criterion can be discharged. Nixon et al [13] suggested an orthotropic yield criterion which depended on J_3 . It is beyond the scope of this thesis to explore alternative yield criterions as several formulas imply the Mises yield criterion, and there is not enough data to confirm or deny this strength differential effect.

3.3 Stability

Any structural member subjected to axial compression is prone to stabilisation problems, which can be local or global. Local stability problems assess the stability of thin-walled members and is only partially dependant on length, while global instability may lower the capacity of long, slender structural components. The formulas derived are in both cases a result of solving the differential equations for instability. These equations are formed when deformation is imposed on a system with applied loads and transverse deformations. If the applied loads (in compression) exceeds a certain limit, any transverse deformation will cause system collapse.

Most stability problems, including those studied herein, cause collapse at low plastic strain. A common assumption is therefore that the area and length of the members are approximately constant during the pre-buckling phase (until maximum axial force is obtained), viz.

$$A \approx A_0, L \approx L_0 \quad (3.30)$$

3.3.1 Global stability

Global buckling, illustrated in figure 1 (a), can greatly reduce the capacity of long, slender structural members. If these members are subjected to an axial load N and deformed transversely du as shown in figure 3, the cross-section is loaded with a moment $M = Ndu$.

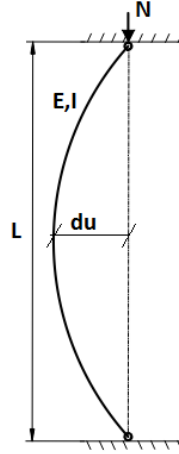


Figure 3 Globally buckling simply supported column,

This is the driving moment of the buckle, leading to greater deformations. Sufficiently large column stiffness given in terms of E , I and L will bring the column back to equilibrium. The load N which causes system collapse is therefore a function of the stiffness of the columns, and is named the Euler load.

$$N_E = \frac{\pi^2 EI}{L_E^2} \quad (3.31)$$

The load N_E serves as an upper bound for the axial capacity. In this equation, I is the second moment of area, which for circular cross-sections are given on the form

$$I = \frac{\pi(r_o^4 - r_i^4)}{4} \quad (3.32)$$

L_E is the buckling length of the member. This length is equal to the distance between the points of zero moment after applying a deformation du . For simply supported columns this is equal to the length of the column, while for fully clamped columns the buckling length of the column is half its length, increasing the Euler load by a factor of 4, as seen in formula (3.31). The radius of gyration, i , and the global slenderness factor λ_k is introduced as

$$i^2 = \frac{I}{A}, \lambda_k = \frac{L_E}{i} \quad (3.33)$$

The Euler load can be re-written to find the critical stress leading to global instability and buckle

$$\sigma_{E,crit} = \frac{N_E}{A} = \frac{\pi^2 EI}{L_E^2 A} = \frac{\pi^2 E i^2}{L_E^2} = \frac{\pi^2 E}{L_E^2 / i^2} = \frac{\pi^2 E}{\lambda_k^2} \quad (3.34)$$

A column buckles at this stress level, given that the stress is lower than the yield stress defined in equation (3.25). Yield stress lower than the buckling stress causes strain hardening as described in section 3.2.4, and the instability is inelastic. While loaded in the plastic regime, any deformation is resisted by a much lower stiffness than the elastic modulus E . The buckling stress after yielding is therefore lower than in the elastic regime. Several different theoretical approaches and assumptions aims at solving this problem, such as the Reduced-Modulus Theory, the Tangent-Modulus Theory, the Transcendental Plastic Buckling approach as well as iterative schemes, all presented by Jones [9]. A simplification deemed to fit well to laboratory results for different metals and alloys, according to Jones [9], is the tangent-modulus theory, where Young's modulus in equation (3.34) is exchanged with the tangent modulus defined in (3.12)

$$\sigma_{E,crit}^{Pl} = \frac{\pi^2 E_T}{\lambda_k^2} \quad (3.35)$$

As described earlier, the stress – strain relationship will be calibrated to the Voce hardening rule in chapter 6. The tangent modulus is found using equations (3.29) and (3.19), as a function of the plastic strain. Finding the strain value that gives $\sigma = \sigma_{cr}$ is therefore an iterative process. Presented formulas in the previous paragraphs impose several simplifications regarding the geometry and material. One such simplification is that the column or structural member is assumed initially straight. This simplification leads to a model that assumes no transversal deflection below the critical stress and infinitely high deflection at any stress above the critical stress. In reality, imperfections from production and heat treatment, transport and montage or in some cases self-weight will give rise to a transverse deformation at low stress. If the initial deformation a_0 is assumed to have the shape of the main buckling mode (for a simply supported column: the shape of a half sine wave), Larsen [3] shows that the mid-span sideways deformation of the column when loaded with a force N can be written as

$$a = \frac{a_0}{1 - \frac{N}{N_E}} \quad (3.36)$$

Where a is the transverse mid-span deformation of the cross-section. The resulting moment from this eccentricity can be written as

$$M = Na = \frac{Na_0}{1 - \frac{N}{N_E}} \quad (3.37)$$

As $N \rightarrow N_E$, the moment becomes infinitely large. The buckling problem is now presented as a capacity problem of the mid-span cross-section, loaded with axial force and bending moment. Design cases with both bending moment and axial force is often expressed on the form

$$\left(\frac{N}{N_R}\right)^\alpha + \left(\frac{M}{M_R}\right)^\beta \leq 1.0 \quad (3.38)$$

The subindex R represents the resistance and α and β are factors that account for the interaction of the forces, typically larger than 1. This equation in combination with (3.37) can be re-written as

$$\left(\frac{N}{N_R}\right)^\alpha + \left(\frac{N}{M_R} \frac{a_0}{1 - \frac{N}{N_E}}\right)^\beta \leq 1.0 \quad (3.39)$$

Eurocode 9 part 1-1 [2] assumes $\beta = 1.0$ and allows $\alpha > 1.0$, depending on the local slenderness of the section. In the case of $\alpha = \beta = 1.0$

$$N \left[\frac{1}{N_R} + \frac{1}{M_R} \frac{a_0}{1 - \frac{N}{N_E}} \right] \leq 1.0 \quad (3.40)$$

Note that because $a_0 \neq 0$ for all real columns, formula (3.40) states that N never reaches N_R . However for short columns, N_E can be large enough for the reduction of axial capacity to be negligible.

To account for inelasticity in global buckling of members with imperfections, N_E given in (3.31) can be augmented as shown previously, exchanging E with E_T .

When analysing an axially loaded member through a non-linear FEA software, the stiffness of a member is dependent upon the axial force. Loading in tension increases bending stiffness, while loading in compression reduces it. The tangent modulus can according to Cook [14] be written as

$$[\mathbf{K}_t] = [\mathbf{K}_m] + [\mathbf{K}_g] \quad (3.41)$$

Here, \mathbf{K}_t is the tangent stiffness matrix of the member, relating externally applied forces and moments to the displacements. \mathbf{K}_g adjusts the tangent stiffness according to the axial force, typically through a linear relationship. The buckling problem can be analysed by solving for

the axial force that cause the stiffness of the system to become singular. Analysing a system with several degrees of freedom (dofs) this way gives a numerical solution to more complex buckling problems that is hard to solve analytically. The solution of this buckling problem for the j 'th eigenmode (buckling shape) $\boldsymbol{\varphi}$ and buckling load λ is given [14] as

$$\left([\mathbf{K}_m] + \lambda_j [\mathbf{K}_g]\right) \{\boldsymbol{\varphi}\}_j = \{0\} \quad (3.42)$$

This approach is applied for eigenmode analyses described in section 4.1.1 and applied in section 7.3.2.4.

3.3.2 Local stability

Slender cross-sections can buckle locally, as seen in figure 1 (b). Local buckling patterns for cylinders varies depending on the r/t and L/r ratios. Local buckling of cylinders is defined by the deformation in the radial or circumferential directions or in both, and the centre of the cross-section is not moved transversely. While the global buckling relates to the global slenderness defined in (3.33), local buckling is related to the local slenderness parameter, which for hollow cylinders is defined in Eurocode 9 [2] as

$$\beta = 3 \sqrt{\frac{2r_m}{t}} \quad (3.43)$$

Structural members with slenderness factor higher than a certain limit buckles locally before reaching yield stress. This limit depends upon the geometry of the member, the hardening of the material and whether or not the cross-section is welded. Slenderness lower than this limit causes some plastic hardening, however the slenderness close to this limit still reduces the capacity of the member. For thick members, local slenderness will not reduce the capacity.

The complexity of solving the differential equations of a local slenderness problem exceeds that of the global case. The global stability problems require solving the connection between stiffness and applied force, a second-degree differential equation. For local buckling the differential equation is of eighth order [8]. Both the local and the global solution present an upper bound to the capacity.

3.3.2.1 Theoretic derivations according to NACA

In the following paragraphs, solutions to the local buckling problem are presented. The validity of the solutions improves as inelasticity is included, and the focus is shifted from analytical to empirical solutions.

The National Advisory Committee for Aeronautics (NACA) released several reports in the period 1940 – 1960 regarding thin-walled aluminium shells and their behaviour. At the time, the computer technology was limited, causing the reports to rely on theoretic derivations to a greater extent than more recent studies.

Three reports are studied in this thesis governing local buckling of cylinders. The first report is technical note 3783, part III – Buckling of curved plates and shells [8]. In this report, the theory of thin and intermediate thick shells is derived, analysed and compared with empirical results. The basis of the theory is Donnell's equation, an eight order differential equation of the displacement in the radial direction (x -direction, as described in section 3.2.1), along with two fourth order differential equations, one with respect to y and the other to z . The equations are only fully valid in the elastic region, but can be modified to describe inelastic effects.

With the results from Donnell's equation [8], the critical stress that gives local instability in an elastic material can be written as

$$\sigma_{cr} = k_c \frac{\pi^2 E}{12(1-\nu^2)} \left(\frac{t}{L} \right)^2 \quad (3.44)$$

The scaling factor k_c is taken as a function of the geometry and the number of buckles

$$k_c = \frac{(m^2 + \theta^2)^2}{m^2} + \frac{12Z_L^2 m^2}{\pi^4 (m^2 + \theta^2)^2}, \quad \theta = \frac{nL}{\pi r} \quad (3.45)$$

In this equation, m is the number of buckles in the longitudinal direction and n is the number of buckles in the circumferential direction, both variables taking integer values. The combination of m and n that gives the lowest k_c represents the buckling stress.

The length parameter Z_L plays an important role in classifying the cylinders as well as finding the factor k_c

$$Z_L = \frac{L^2}{rt} \sqrt{1-\nu^2} \quad (3.46)$$

Three different ranges based on length are defined by the value of $\frac{Z_L}{\sqrt{1-\nu^2}}$ [8].

The short-cylinder range

$$\frac{L^2}{rt} < 1 \rightarrow L = \sqrt{rt} \quad (3.47)$$

The transition-length range

$$1 < \frac{L^2}{rt} < 100 \rightarrow \sqrt{rt} < L < \sqrt{100rt} \quad (3.48)$$

The long-cylinder range

$$\frac{L^2}{rt} > 100 \rightarrow L > \sqrt{100rt} \quad (3.49)$$

Cylinders classified as short get a buckling factor that is constant with respect to Z_L due to $m=1$ and $\theta = 0$ in equation (3.45). Long cylinders obtain the correct buckling factor k_c by minimizing formula (3.45) with respect to $\frac{(m^2 + \theta^2)^2}{m^2}$, resulting in a linear relationship with Z_L

$$k_{c,long} = \frac{4\sqrt{3}}{\pi^2} Z_L \quad (3.50)$$

The critical stress from equation (3.44) for long cylinders can then be written as

$$\sigma_{cr} = \frac{4\sqrt{3}}{\pi^2} \left(\frac{L^2}{rt} \sqrt{1-\nu^2} \right) \frac{\pi^2 E}{12(1-\nu^2)} \left(\frac{t}{L} \right)^2 = \frac{4\sqrt{3}}{12} \frac{\sqrt{1-\nu^2}}{1-\nu^2} E \frac{t}{r} \quad (3.51)$$

$$\sigma_{cr} = \frac{E}{\sqrt{3(1-\nu^2)}} \frac{t}{r} \approx 0.608E \frac{t}{r} \quad (3.52)$$

This local buckling stress is not directly a function of the length of the cylinders, in contrast to the cylinders in the short and transition ranges. For cylinders in the long-cylinder range the boundary conditions is found to have negligible influence on the buckling stress for local buckling. This makes up the majority of the cylinders considered in this thesis. Note that the influence of BC will dominate for longer cylinders that display a global buckling pattern (described in section 3.3.1).

The validity of formula (3.52) is assessed in NACA report 1343, and it is stated that the formula overestimates capacity by 15-40 percent [6]. Note that this claim holds for very thin-walled cylinders, with r/t relationship between 500-3000. The figures describing these claims are shown in Appendix A, where figure a1 suggests that formula (3.52) does not overestimate the critical stress for low values of r/t . Furthermore, figure a1 displays that setting $Z_L > 10$ gives the theoretical answer in formula (3.52).

Note that formula (3.52) is only valid for the elastic buckling, as all solutions based on equation (3.44) scales with Young's modulus. If the estimated elastic buckling stress is higher than the yield stress, the plastic strains causes a decrease of the resistance towards local instability.

Formula (3.52) is a result from a series of differential equations simplified by assuming elasticity. Substituting E with E_T in formula (3.52), as was done with the global buckling in formula (3.34) is therefore not permitted.

The plastic behaviour of the material is crucial in determination of the capacity in inelastic buckling. The slope of the stress – strain curve largely defines the buckling resistance through the plastic tangent (3.14) and secant (3.15) moduli.

In NACA technical note 3726 [7], G. Gerard suggested a plasticity-reduction factor defined as

$$\eta = \sqrt{\frac{E_T^{Pl}}{E_S^{Pl}} \frac{E_S^{Pl}}{E}} \sqrt{\frac{1-\nu^2}{1-(\nu^{pl})^2}} \quad (3.53)$$

This reduction factor is applied directly to formula (3.52), and the new critical inelastic stress becomes

$$\sigma_{cr,Pl} = \frac{\sqrt{E_T^{Pl} E_S^{Pl}}}{\sqrt{3(1-(\nu^{pl})^2)}} \frac{t}{r} = \frac{2}{3} \sqrt{E_T^{Pl} E_S^{Pl}} \frac{t}{r} \quad (3.54)$$

One assumption behind this result is axisymmetric buckling shape, which will be shown in chapter 7 to be the valid for the governing failure modes on cylinders that buckle locally. The axisymmetric assumption means setting n , and therefore θ , equal to 0 in equation (3.45). The buckling length was further calculated in NACA technical note 3726 [7] and from this the number of buckles in the longitudinal direction was found:

$$\left(\frac{L}{m}\right)^2 = \pi^2 \left(\frac{1}{4} + \frac{3 E_T^{Pl}}{4 E_S^{Pl}}\right) \frac{rt}{3} \sqrt{\frac{E_S^{Pl}}{E_T^{Pl}}} \quad (3.55)$$

$$m = \frac{1}{\pi} \left(\frac{1}{4} + \frac{3 E_T^{Pl}}{4 E_S^{Pl}}\right)^{-1/2} \left(\frac{3L^2}{rt}\right)^{1/2} \left(\frac{E_T^{Pl}}{E_S^{Pl}}\right)^{1/4} \quad (3.56)$$

The buckling mode that occurs on the lowest stress gives m buckles. In the case where formula (3.56) yields decimal values, a slight increase in stress is required to enforce the buckling pattern with an integer number of buckles, as m has to take integer values.

Gerard's derivation further assumed that all strains are plastic. At low plastic strains the capacity is somewhat overestimated due to large plastic secant modulus calculated with formula (3.15). The theory simplifies by assuming ν always to be equal to the plastic value, however it can be regarded as adequate for modelling inelastic buckling at high plastic strains. Gerard's

derivation also assumes uniaxial stress state in the pre-buckling phase, which is equivalent to assuming no friction between the cylinder and its BCs.

3.4 Geometry and material

Numerous extruded 5 metres long cylinders with two types of cross-sections are used for all laboratory tests. One of the two cross-sections were cast in two different alloys. Consequently, three combinations of alloy and cross-section are analysed. The alloys were 6060T6 and 6082T6, the cross-sectional diameters were roughly 100 and 127 mm. When referencing to the combinations of cross-section and alloy, their names signify these properties: A6060D100, A6060D127 and A6060D100 (figure 4).

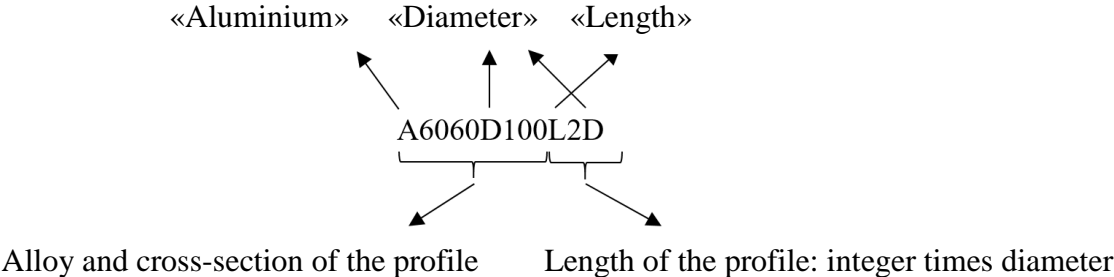


Figure 4 Notation for profiles

The geometry was studied in order to get reliable geometrical measurements. The thickness and diameter was measured for one cylinder of each of the three types (table b1 and table b2). The measurement of the cylinder thickness was discharged using an ultrasonic thickness gauge from DeFelsko named PosiTector.

Each cylinder was measured every 500 mm longitudinally and at four different locations around the circumference. At each of these points, data was sampled four times to reduce the effect of “noise”, the term used to describe random numerical deviations. The random error (figure 5, [15]) was therefore reduced. In total, each cylinder was measured $n = 10 * 4 * 4 = 160$ times. The ultrasonic gauge measures differences of 0.01 mm, leading to three significant digits for the thicknesses studied. The scatter in results might in part stem from inaccuracy from the instrument, as it is based on the speed of sound through the material. This wave speed is dependent upon the density and stiffness of the material, which may cause a systematic error (figure 5). The ultrasonic gauge sensor is flat, making it difficult to correctly measure the thickness of an object with curvature, leading to further systematic error. A slight angle between the sensor and the surface may lead to overestimation of the thickness. Through the measuring

process, the measuring technique was most likely improved, which may have reduced this error and somewhat reduced the random error of the measurements as well.

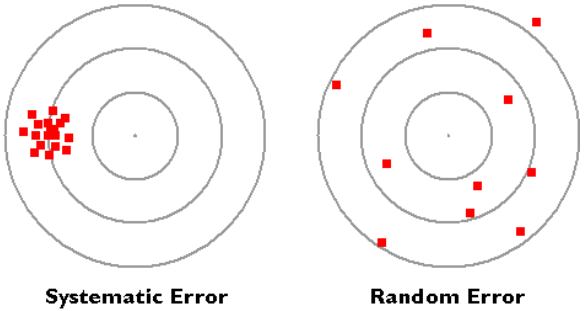


Figure 5 Schematic representation of systematic and random error

The mean (3.57), standard deviation (3.58) and coefficient of variance (3.59) was calculated

$$\bar{t} = \frac{\sum_{i=1}^n t_i}{n} \tag{3.57}$$

$$s_t = \sqrt{\frac{1}{n-1} \sum_{i=1}^n (t_i - \bar{t})^2} \tag{3.58}$$

$$CoV_t = \frac{s}{\bar{t}} * 100\% \tag{3.59}$$

Similar measurements were made for the outer diameter, using an electronic caliper, albeit only endpoint measurements were discharged. The coefficient of variance was low for both t and D (table 1), and the results were deemed satisfactory. The mean thickness and diameter were slightly rounded off (table 1), which increased the thickness less than 0.2 percent. The diameter was also increased, and the difference in area is calculated to be less than 1 percent (table 1)

Table 1 Chosen and calculated mean thickness and diameter with corresponding covariance.

	A6060D100	A6060D127	A6082D100
\bar{t} [mm]	4.696	1.773	4.696
s_t [mm]	0.054	0.055	0.048
CoV_t [%]	1.15	3.10	1.03
t_{chosen}	4.70	1.77	4.70
\bar{D} [mm]	99.87	126.78	99.49
s_D [mm]	0.163	0.159	0.654
CoV_D [%]	0.163	0.126	0.658
D_{chosen}	100	127	100
$\frac{\Delta A}{A_{measured}}$ [%]	0.218	0.009	0.620

T6 tempered alloys includes heat treatment and then artificial ageing, leading to high strength and good corrosion resistance, according to Borrego et al [16]. The 6xxx-series alloys obtain these properties in part from their major alloy elements Mg and Si, and other elements such as Mn, Fe and Cr. The amount of Mn and Cr can affect the crack growth of the material, and 6082 typically contain 5-100 times larger amounts of these elements [16]. This causes the 6082 alloy to exhibit a more brittle fracture pattern than 6060T6. Brittle fracture mechanisms are expected to have a larger scatter in fracture stress and strain compared to ductile fracture. Later in this thesis, the covariance is calculated from executed compression tests in laboratory in order to give a measurement of this scatter.

The profiles are extruded, and due to the closed cross-section, some seam welds were formed. These are assumed to not alter the properties of the material. After extrusion, the cylinders were cooled. Due to a lower thickness the D127 cross-section cooled faster than its thicker counterpart, which is anticipated to cause a slight relative decrease in stress capacity.

Eurocode 9 part 1-1 gives conservative values for the material strength. The characteristic stress or proof stress labelled f_0 is defined as the stress that is obtained by loading the material to 0.2

percent plastic strain [2]. A large amount of the safety margins built in to the Eurocode is introduced in this stress, as these values are often lower than what is found from material tests. Conducted material tests (described in chapter 6) resulted in a modelled proof stress of 192 *MPa* and 315 *MPa* for 6060T6 and 6082T6, respectively.

The geometric and mechanical properties of all three types of profile properties are shown in table 2. The table also includes the radius of gyration and local slenderness factors, given in (3.33) and (3.43) respectively, as well as the buckling class according to Eurocode 9 [2].

Table 2 Material and geometry properties for the cylinders studied

Reference name	A6060D100	A6060D127	A6082D100
Aluminium alloy	EN-AW 6060T6	EN-AW 6060T6	EN-AW 6082T6
f_0 [<i>MPa</i>]	192	192	315
Buckling class [2]	A	A	A
Outer diameter [<i>mm</i>]	100	127	100
Thickness, t [<i>mm</i>]	4.70	1.77	4.70
Middle radius, r_m [<i>mm</i>]	47.65	62.62	47.65
r/t	10.14	35.38	10.14
β (3.43)	13.51	25.23	13.51
A [mm^2]	1407.2	696.4	1407.2
I [mm^4]	$1.601 * 10^6$	$1.365 * 10^6$	$1.601 * 10^6$
i [<i>mm</i>]	33.735	44.280	33.735

3.4.1 Imperfections

Imperfections are small unintended deformations, defects or irregularities that are present in structural members to some degree. The imperfections are deviations from the mathematically perfect circular and straight cylinder. Three imperfection categories are assessed:

1. Longitudinal, bend-like imperfections mainly affect the global stability, as discussed in section 3.3.1. These imperfections are assumed to be shaped as a half sinus wave, governing the main buckling mode (figure 6 c)
2. The radius and thickness of the section can vary with respect to the z coordinate. This gives a vase-like shape, governing the deformation shape prebuckling (figure 6 b)
3. The radius and thickness of the section can vary with respect to the y coordinate (loop direction). This causes an out-of-roundness and may correspond to the first *eigenmode* (section 3.3.1) of cylinders of certain lengths (figure 6 a)

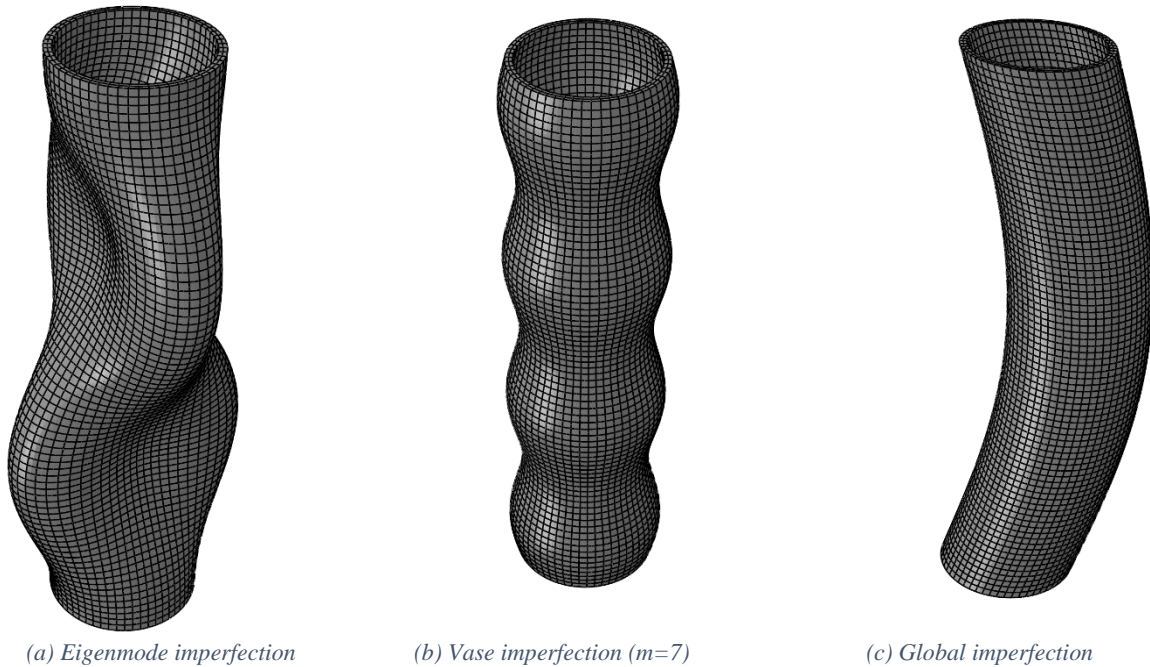


Figure 6 Examples of the three types of imperfections

The inelastic failure mode for short, locally unstable cylinders is shown to be independent of length, as seen in formula (3.54), while the longer, globally buckling cylinders are dependent upon length through the tangent-modulus formula (3.35). As a consequence of this, the local imperfections (figure 6 a, b) governing local buckling are mainly given as a multiple of the thickness and the global imperfections (figure 6 c) governing global failure modes as a multiple of the length.

The longitudinal imperfections in extruded profiles are anticipated to be small. A conservative measurement for the imperfections assumed to be present in a cylinder was given by Mazzolani

as $a = \frac{L}{1000}$ albeit a more accurate estimate from a broad data base estimates this imperfection to be $a = \frac{L}{2000}$ [17].

The measurements from the previous section displayed a low covariance, which suggests that $a = \frac{L}{2000}$ will be the best estimate.

3.5 Eurocode

The Eurocodes are a series of ten European standards for constructing structures, released in the time period 2000-2010. In light of project “design of power pylons in aluminium”, there exists no specific Eurocode. Eurocode 3 part 3-1 [18] is specifically designed for power pylons in steel. Due to a high degree of generalization in this Eurocode, applying this code leads to models that are too conservative and uneconomical to be competitive. In Eurocode 1990 [19], which governs structures in general, section 1.4 (5) allows alternative ways of design. The code specifies that “*relevant principles of design and that the bearing constructions safety, usability and resistance must be at least equivalent to expected quality of the design from the Eurocode*” [19]. This is now the leading way of practise regarding power pylons in steel. As a consequence of the lack of Eurocodes for power pylons in aluminium, and lack of fit for the existing code for steel, it is assumed that design of power pylons by todays Eurocodes in aluminium are neither economical nor competitive. In the later phases of this project, generation and verification of alternative rules and formulas might be necessary in order to create a competitive power pylon in aluminium.

Eurocode 9 contains the rules and guidelines for constructing aluminium structures. It consists of five parts, of which two are relevant for the objective of this thesis: part 1-1 for general aluminium structures [2] and part 1-5 for shell structures[10].

In this theses only design of individual components are considered. Hollow circular cylinders in compression with the idealization of clamped boundary condition are designed according to Eurocode 9.

3.5.1 Eurocode 9 Part 1-1: General structural rules

Eurocode 9 part 1-1 provide rules and formulas for structural components and connections with various loads. Members in exposed to pure compression are described by Part 1-1 in chapter 6.3.1: *Buckling resistance of members in compression* [2]. A calculation algorithm for circular

hollow cross-sections according to this code is presented in 0. It assesses basic material and capacity problems, as well as global and local stability problems.

In order to ensure sufficient safety of aluminium structures, several safety margins are introduced. Firstly, the codes do not directly allow hardening of the material, hence a lower, characteristic proof stress marks the limit of the allowable stresses. This was introduced in section 3.4 as the engineering stress obtained at 0.2 percent plastic engineering strain. The characteristic yield stress is then further reduced by a partial safety factor $\gamma_{M1} = 1.10$ (C.12). This factor is neglected in all calculations because a conservative design recommendation is not of interest in this thesis. Characteristic proof strength as given by Eurocode 9 [2] are presented in table 3.

Table 3 Characteristic value of 0.2 % proof strength from Eurocode 9

		Thickness [mm]	EC6060T6	EC6082T6
f_0 [MPa]	$t \leq 5$			250
f_0 [MPa]	$t \leq 15$		140	

Material parameters in table 2 displays a 26 percent increase in f_0 for 6082T6 and 37 percent larger for 6060T6.

Different tempers affect the amount of residual stresses found in the profiles, and this affects the resistance towards local and global buckling. In Eurocode 9, alloys are categorized into one of two buckling classes, and the T6 tempered alloys are of buckling class A, which are the least influenced by residual stresses.

Slenderness may reduce the capacity of a member due to local buckling, as discussed in section 3.3.2. The Eurocode classifies cross-sections into four classes according to their local slenderness. Classification criteria and class property are presented in table 4 [2, 11].

Table 4 Cross-sectional classes according to Eurocode 9 Part 1-1

	Cross-sectional behaviour	Requirement	Method of calculation
Class 1	Can create plastic hinge with sufficient rotation	$\beta/\varepsilon \leq \beta_1$	Load effect: plastic or elastic Capacity: plastic or elastic
Class 2	Can achieve full plasticization, but is limited by rotational capacity.	$\beta_1 \leq \beta/\varepsilon \leq \beta_2$	Load effect: elastic Capacity: plastic or elastic
Class 3	Cannot be plasticized, but can achieve proof strength in the outermost fibre without local buckling	$\beta_2 \leq \beta/\varepsilon \leq \beta_3$	Load effect: elastic Capacity: elastic
Class 4	Local buckling will take place before proof strength occurs in the cross-section	$\beta/\varepsilon \geq \beta_3$	Load effect: elastic Capacity: elastic, but must account for local buckling in compressed components.

The slenderness factor β is given in formula (3.43) and the limit values β_1 , β_2 and β_3 are shown in table c2. The factor ε (table c2) takes into account that materials with different strength may buckle differently. High-strength alloys in class 4 members may to a lesser degree obtain characteristic stress. Classification according to Eurocode for geometry in table 2 and materials defined in table 2 and table 3 is displayed in table 5.

Table 5 Classification of cross-section according to Eurocode 9

	A6060	A6082	EC6060T6	EC6082T6
D100	Class 2	Class 2	Class 1	Class 2
D127	Class 4	-	Class 3	-

The thick-walled cross-sections analysed in this thesis buckle inelastic according to Eurocode 9 (table 4 and table 5). They obtain some plastic hardening while loaded in axial compression, but buckle before reaching their maximum true stress because of stability problems.

Note that the elevated value of f_0 due to material testing caused A6060D127 to be a class 4 cross-section, its thickness has to be reduced with a factor ρ_c (C.4). The fact that the Eurocode uses conservative values for f_0 may cause it to predict the wrong failure mode, as the classification with a conservative f_0 can lead to a non-conservative cross-sectional class. This effect is now studied.

In the following derivation, β/ε is denoted ϕ . The cross-section is further assumed to be thin-walled, so that the reduction in area can be assumed equal to the reduction in thickness, with ρ_c given in formula (C.5) and (C.6). Assuming $\rho_c < 1.0$ (class 4), axial capacity of the member without considering global stability or shell buckling can be written as

$$N_R = f_0 A_{eff} \approx f_0 A \rho_c \quad (3.60)$$

Any change of characteristic proof stress, e.g. as a results of performing material tests, causes a change in the axial capacity:

$$\begin{aligned} \frac{\delta N_R}{\delta f_0} &= \frac{\delta}{\delta f_0} (f_0 A \rho_c) = A \left(\rho_c + f_0 \frac{\delta \rho_c}{\delta f_0} \right) \\ \frac{\delta \rho_c}{\delta f_0} &= \frac{\delta \rho_c}{\delta \phi} \frac{\delta \phi}{\delta \varepsilon} \frac{\delta \varepsilon}{\delta f_0} = \left(-\frac{C_1}{\phi^2} + 2 \frac{C_2}{\phi^3} \right) \left(-\frac{\phi}{\varepsilon} \right) \left(-\frac{1}{2} \frac{\varepsilon}{f_0} \right) \end{aligned}$$

Any increment in f_0 will lead to increased axial capacity as long as $\frac{\delta N_R}{\delta f_0} > 0$:

$$\begin{aligned} A \left(\frac{C_1}{\phi} - \frac{C_2}{\phi^2} - f_0 \left(\frac{C_1}{\phi} - 2 \frac{C_2}{\phi^2} \right) \left(\frac{1}{2 f_0} \right) \right) &> 0 \\ \frac{C_1}{\phi} - \frac{C_2}{\phi^2} - \frac{1}{2} \frac{C_1}{\phi} + \frac{C_2}{\phi^2} &> 0 \\ \frac{1}{2} \frac{C_1}{\phi} &> 0 \end{aligned}$$

C_1 and ϕ are both positive, thus $\frac{\delta N_R}{\delta f_0} > 0$. Although an increased value of f_0 can initiate or

propagate the reduction of effective area, this reduction effect is smaller than the increase in characteristic stress. Increased proof strength always leads to increased capacity for members

in cross-sectional class 3 and 4, according to Eurocode 9 part 1-1. The transition from class 3 to class 4 is smooth for Eurocode 9 part 1-1. The elevated f_0 that transformed A6060D127 into a class 4 cross-section caused a thickness reduction factor of $\rho_c = 0.997$.

If the cross-sectional class is increased from 1 or 2 to 2 or 3 because of an increment in f_0 , the transition is less smooth. This change of cross-sectional class may disable calculations with plastic hinges or plasticization, possibly resulting in a great reduction in capacity (table 4). In the case of axially loaded cylinders, the reduction of capacity from cross-sectional class 1 to 3 is small. Eurocode gives low values for f_0 , but this is not always a conservative approach. Establishing an upper bound of the material strength may improve the code.

3.5.2 Eurocode 9 Part 1-5: Shell structures

Eurocode 9 part 1-5 [10] gives guidelines in calculations regarding shell buckling similar to the theory presented in section 3.3.2. The calculations according to this code is shown in Appendix D, while some of its features are presented and discussed in this chapter.

The code defines a buckling resistance, which serves as an upper bound for the capacity of the stress, hence the lowest capacity of part 1-5 and 1-1 is chosen. In the simple case of axially loaded circular un-welded cylinders, the code assumes a multiplicative relationship between global and local reduction of capacity. The axisymmetric failure mode, labelled meridional buckling, is in good accordance to the formulas derived by NACA (section 3.3.2.1). Through the formulas given in Eurocode, the buckling resistance is calculated (D.2) based on the parameters reducing capacity due to local and global buckling, α_x and χ_x .

From formula (D.1) it is specified that cylinders need not be checked against meridional shell buckling if they satisfy $\frac{r}{t} \leq 0.03 \frac{E}{f_0}$ which in terms of β and ε can be written as

$$\begin{aligned} \frac{r}{t} \frac{f_0}{0.03 * 70000} &= \frac{rf_0}{t} \frac{3^2 2}{250} \frac{5}{756} \leq 1 \\ \left(3 \sqrt{\frac{2r}{t}} \right) \frac{1}{\sqrt{\frac{250}{f_0}}} &\leq \sqrt{\frac{756}{5}} \\ \frac{\beta}{\varepsilon} &\leq 12.30 \end{aligned} \quad (3.61)$$

In this derivation, the value for β is given for hollow cylinders and tubes from formula (3.43). The value 12.30 means that class 2 cross-sections (that allows plasticization of the cross-

section) might be subjected to meridional buckling. With the materials and cross-sections defined in table 2, A6060D127 and A6082D100 needs to be calculated with reduction due to meridional buckling, while A6060D100 does not – neither for the material data given in part 1-1 nor for the data from the material tests.

Annex A in part 1-5 is used to find a critical (elastic) meridional buckling stress defined in formula (D.9). Note the close resemblance to formula (3.52). The parameter C_x is defined according to the value of $\frac{Z_L}{\sqrt{1-\nu^2}}$. For cylinders with $\frac{Z_L}{\sqrt{1-\nu^2}} \geq \left(0.5 \frac{r}{t}\right)^2$, C_x takes on values between 0.6 and 1 (table d2). When $C_x < 1.0$, the code yields lower values than the report by NACA claimed (section 3.3.2.1, formula (3.52)).

Point 6.2.3.2(3) in Eurocode 9 part 1-5 [10] mentions two approaches for calculating the critical buckling stress $\sigma_{x,cr}$ and therefore the slenderness $\bar{\lambda}_x$ through formula (D.8). The calculations can be based on annex A in the code, as discussed in the previous paragraph, or they can be carried out by (a series of) linear elastic bifurcation analyses (LBA). These analyses give the eigenvalue of the first buckling modes under several assumptions, such as negligible imperfections, conservative loading, no yielding or dynamic effects, and thus give a linear-elastic estimate of the capacity.

On short cylinders, the eigenvalue corresponds to the critical stress from the analytical solution, calculated in annex A. The critical stress is close to $\sigma_{x,cr}$, resulting in similar slenderness $\bar{\lambda}_x$ and thus similar α_x and χ_x . For long specimens with an elastic global failure mode, the slenderness $\bar{\lambda}_x$ acquired from the LBA stress are closely corresponding to the $\bar{\lambda}$ given in Eurocode 9 part 1-1. The global reduction factor χ_x therefore takes the same values in the two codes, with the application of this alternative approach for $\sigma_{x,cr}$. The only difference between the two codes is that part 1-5 includes a further reduction through α_x . This factor gives a reduction for local buckling on clearly globally buckling columns. The validity of this alternative approach is therefore flawed on longer specimens.

Formula (D.9) leads to higher stresses than those allowable by Euler buckling, given a long enough specimen. Its range of validity is not given directly from the code, but the lower capacity of part 1-1 and part 1-5 is used, hence its faulty values are never applied.

In section 3.5.1 it was shown that using actual values of f_0 could cause a change of the cross-sectional class. For A6060D127, the cross-sectional class was changed from 3 to 4, which introduced a negligible reduction of the thickness. In part 1-5, however, the parameter Q (table d5), which affects the local reduction factor α_x (D.11), is increased from 40 to 60, lowering the

capacity of the cylinder. For a length of two times the diameter, this change of capacity is 2.6 percent.

When treating cylinders through Eurocode 9 part 1-5, increasing the characteristic yield stress may induce meridional buckling. Similarly as changing cross-sectional class from 3 to 4 in part 1-1, increasing f_0 past the limit of meridional buckling (criterion (D.1)) will always cause an increased axial capacity: $\frac{\delta N_R}{\delta f_0} > 0$.

3.5.3 Characteristic load according to Eurocode 9

The characteristic load for the three combinations of cross-section and alloy in table 2 is calculated for all lengths up to 6000 *mm*. Calculations on the same cross-section are also done with material strength defined in table 3 labelled EC6060T6 and EC6082T6.

Three approaches have been discussed in order to calculate the stress leading to buckle or failure of a cylinder subjected to meridional shell buckling. These three approaches are compared in a series of graphs in the case of clamped boundary conditions (figure 7-figure 9). These approaches are the Eurocode part 1-1, Eurocode part 1-5 (analytical solution) and part 1-5 (alternative method with LBA). For A6060D100, only Eurocode part 1-1 limits the capacity, rendering a smooth graph (figure 7). A6060D127 and A6082D100 have reduced capacity due to meridional buckling on certain lengths (figure 8, figure 9), which displays three distinct ranges where the relationship between capacity and length is different. These ranges are presented in figure 10, where the characteristic capacity based on material tests are displayed. For very short lengths $L \ll r$, the capacity is higher, as the cylinder then is in the short-cylinder range defined in (3.47). This range is not studied any further.

In the first range in figure 10, the capacity is reduced as C_x takes on lower values for longer specimens. In this range the columns buckle locally. On intermediate lengths, the local buckling strength is independent upon length, giving a constant capacity. The buckling pattern is still local, as this failure mode gives a lower capacity than the globally instable mode. The third range of failure mode is the globally buckling failure mode (figure 10). Here, the capacity from part 1-1 decreases below that of 1-5, and will continue to decrease as length increases. The Eurocode does not predict any smooth transition between the second and third range, although some interaction possibly takes place.

When comparing the Eurocode material to the material based on tension tests, the difference in strength in the first two ranges is approximately equal to the change in f_0 , despite changes in cross-sectional class.

In subsequent analyses and calculations, the alternative method based on LBA is discarded due to its invalidity on globally buckling columns, and the lowest capacity from Eurocode part 1-1 and part 1-5 is used. The material data from Eurocode 9 is also discarded in favour of the results from the material tests. The characteristic capacity according to Eurocode 9 is presented in figure 10.

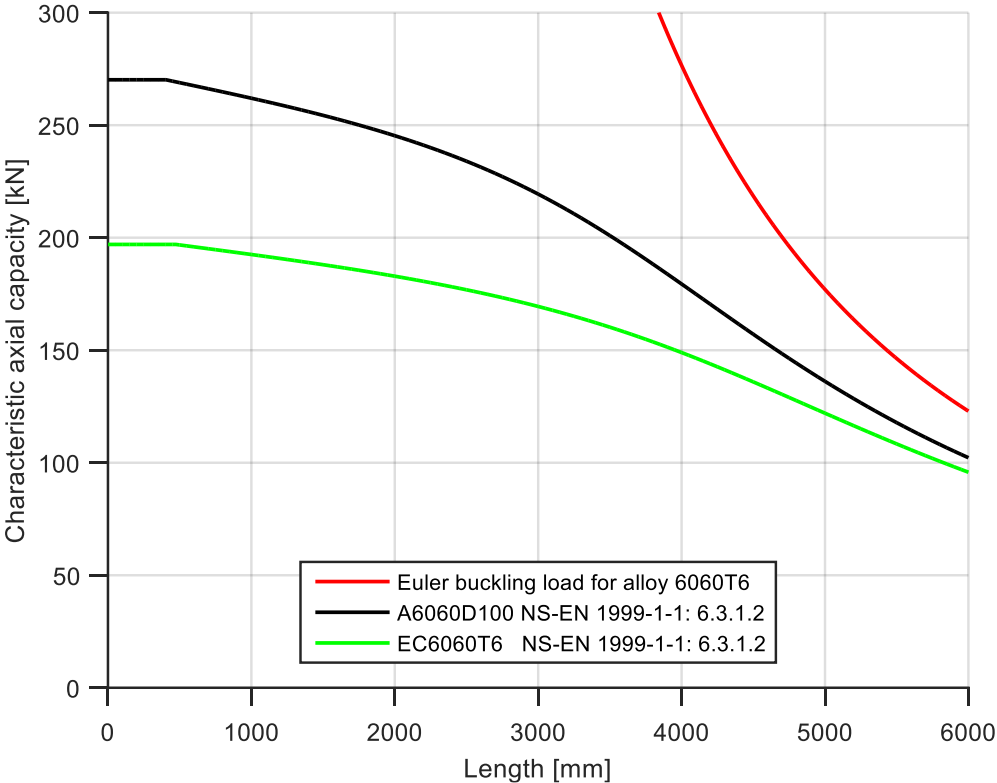


Figure 7 Characteristic load according to Eurocode 9 for material A6060D100 and EC6060T6 with clamped BCs.

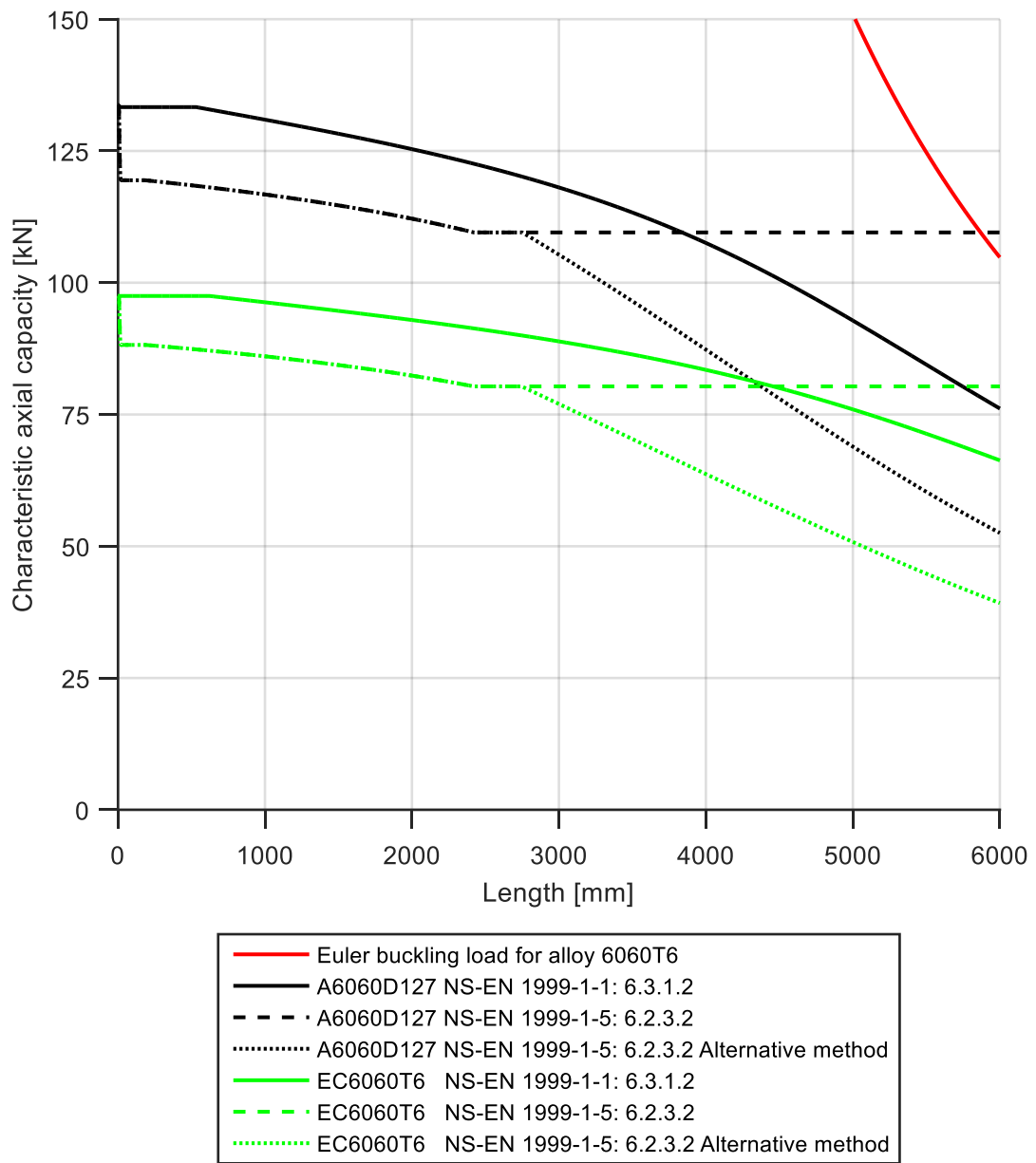


Figure 8 Characteristic load according to Eurocode 9 for material A6060D127 and EC6060T6 with clamped BCs.

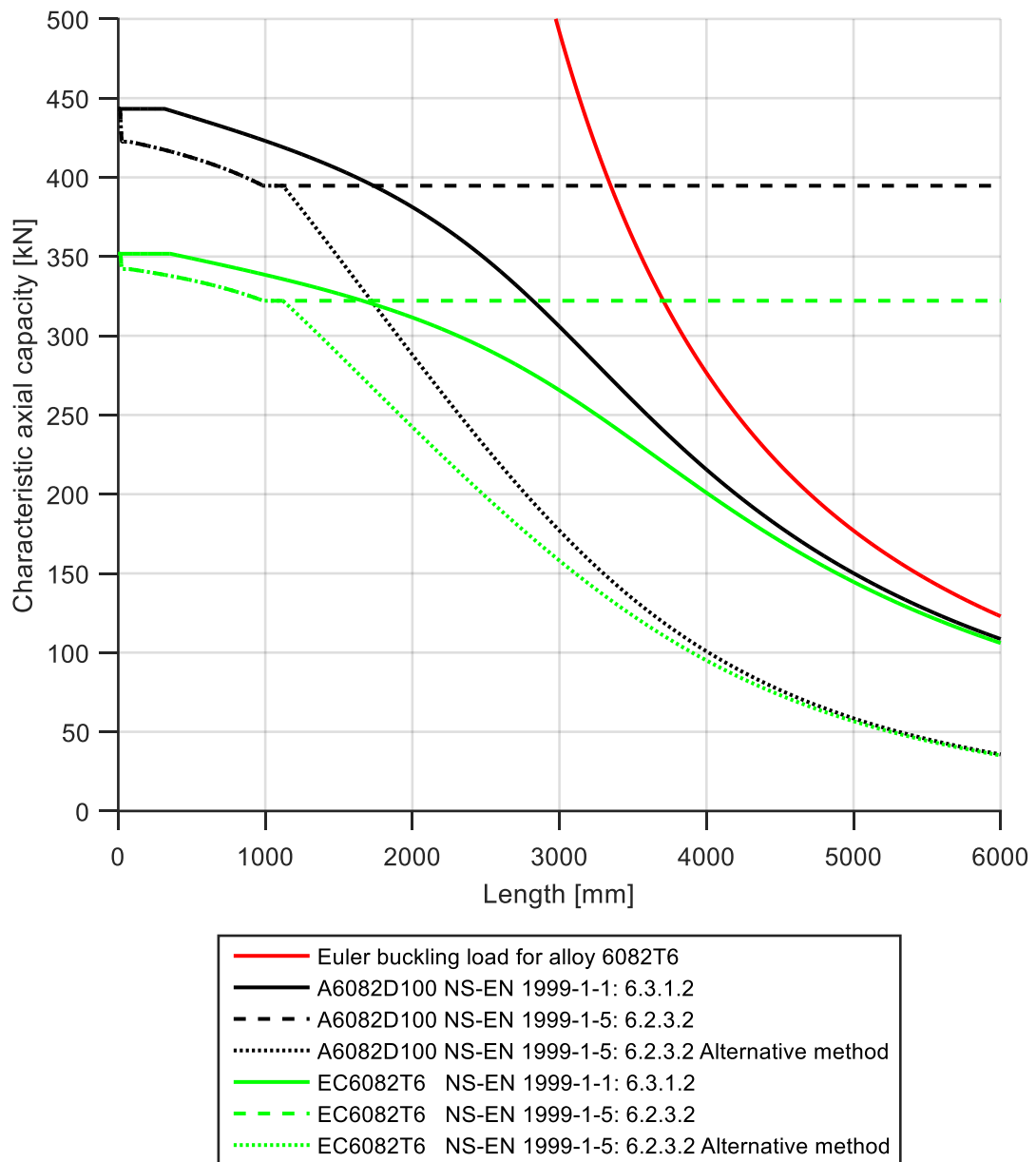


Figure 9 Characteristic load according to Eurocode 9 for material A6082D100 and EC6082T6 with clamped BCs.

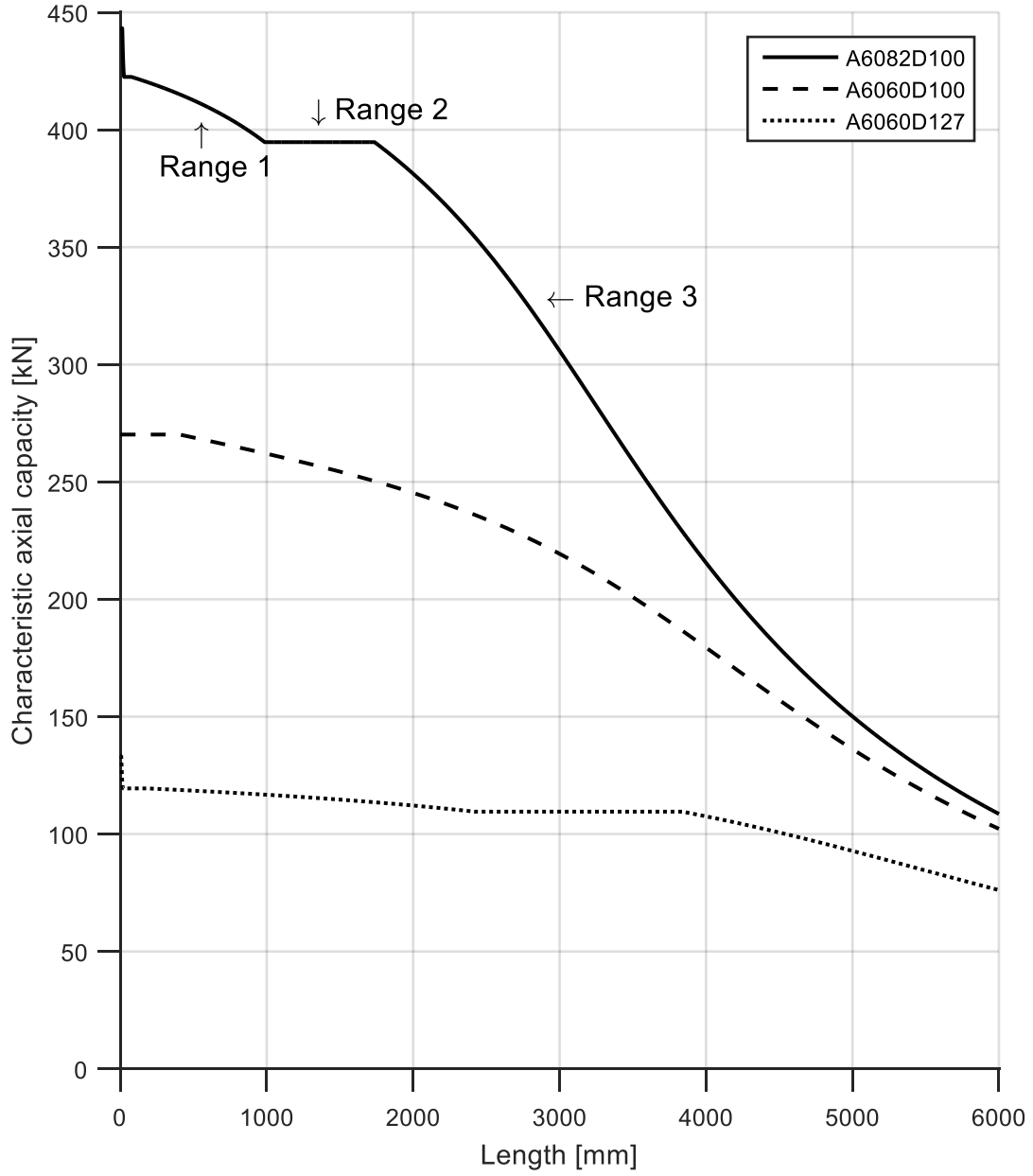


Figure 10 Characteristic capacity according to Eurocode 9 with clamped BCs.

3.6 Comparison buckling resistance from theoretical approaches

In this chapter, different measurements of capacity of cylinders have been assessed. The formulas are given for elastic and inelastic buckling taking into account both local and global inelasticity.

This section is meant to clarify the predicted failure modes at different lengths. The theoretical background from NACA and Jones gives one set of limits for the different buckling modes, and after these are derived, the sets of lengths from Eurocode 9 are explained.

Short and transition range cylinders (according to (3.47) and (3.48)) has not been assessed, as almost all cylinders considered are long by the definition by NACA (3.49). The length required to fulfil this claim is labelled L_L in table 6. The elastic buckling stress is shown in table 6, and is much higher than f_0 . The instability is therefore inelastic with capacity according to formula (3.52). The resistance towards local buckling is constant, regardless of length. This creates a distinctive plateau of lengths with identical capacity.

When the cylinders become longer than the length L_G (table 6), global buckling is introduced according to Jones [9]. The length is found by solving the following equation (from (3.54) and (3.35)):

$$\frac{2}{3} \sqrt{E_T^{Pl} E_S^{Pl}} \frac{t}{r} = \frac{\pi^2 E_T}{\bar{\lambda}^2} \rightarrow \bar{\lambda}_{cr,Pl} = \pi \sqrt{\frac{3r}{2t} \frac{E_T}{\sqrt{E_T^{Pl} E_S^{Pl}}}} \quad (3.62)$$

The tangent and secant moduli are functions of the plastic strain causing instability, which again is a function of the length. Because of a high radius of gyration and as well as a high local slenderness compared to the other cross-sections, A6060D127 has a larger value of L_G . The failure mode is globally inelastic until the length causes the buckling stress to decrease below the yield stress. The buckling formula is then replaced by the elastic Euler buckling (3.34) if

$$\begin{aligned} \frac{\pi^2 E}{\lambda_k^2} &< f_0 \\ \lambda_k = \frac{L_E}{i} &> \pi \sqrt{\frac{E}{f_0}} \end{aligned} \quad (3.63)$$

The length corresponding to λ_k is labelled L_E^{El} in table 6.

According to Eurocode 9, the cylinders behave differently than claimed by NACA and Jones, partially because no hardening is allowed. Any cylinders that buckle meridionally are largely defined by the C_x factor (figure 10, range 1) given in table d2. At a length L_{Cx} (table 6), this

factor becomes constant, initiating the plateau of local buckling according to the Eurocode. At this plateau (or range of cylinder lengths), all cylinders have the same capacity (figure 10, range 2). When the cylinders increase above the value L_G^{EC} , global instability given in part 1-1 is governing for the capacity, giving an elastic buckling load (figure 10, range 3). This capacity is lower than the Euler load, especially on short cylinder lengths, due to the safety margin built into formulas in the Eurocode to take residual stresses and imperfections into account.

For lengths between L_G and L_G^{EC} (table 6), theoretical approaches claims local failure modes are governing, while Eurocode says it is global.

Table 6 Limit values for different failure modes

Formula	A6060D100	A6060D127	A6082D100
$L_L [mm]$	150	105	150
$\sigma_{cr}^e [MPa]$ (3.52)	4221	1252	4221
$\sigma_{cr}^{pl} [MPa]$ ((3.54) with material parameters from chapter 6)	206.4	192.4	325.4
$L_G [mm]$	410	680	320
$L_E^{El} [mm]$	2024	2656	1580
$L_{Cx} [mm]$ (table d2) (constant $C_x=0.6$)	(no meridional buckling)	2421	986
$L_G^{EC} [mm]$ (figure 10)	406	4000	1736
Reduction factor ρ	1.0000	0.9972	1.0000

4 Finite Element Method – Modelling in Abaqus

During the last few decades, the finite element method (FEM) has been developed, improved and widely implemented to solve various engineering challenges, leading to new ways of design and provides possibilities of solving larger and more complex problems. Applying FEM includes introducing simplification of reality through discretization of several parameters, such as geometrical simplifications, element selection and material modelling.

Simulas' program Abaqus is chosen as FEA software. It is assumed that the reader has some knowledge of how this software is built up, as well as some basic knowledge of the FEM.

Three different types of models are created. This chapter aims at establishing the implications of several options in Abaqus, and the benefits and disadvantages of choices made are discussed.

All models created in relation to this project were scripted in python. This way, instead of saving a model and its possible fallacies, only the script was saved; consequently, the computer generated the model from scratch instead of loading a saved database file. This increased the robustness of the models and made the program behave more smoothly.

This chapter aims to describe how the models were created, what options were available and which consequences each choice would impose.

4.1 Geometry and boundary conditions

All cylinders modelled are based on the cross-sections and alloys described in table 2. The length of the cylinders span from short column tests with local failure modes at lengths down to 50 mm to longer tests with global failure modes, with lengths of 2000-4000mm. The only non-cylindrical geometry considered is the tension material tests, which were cut out from the cylinders, giving them a curvature. By altering lengths as well as altering between the two cross-sections and the two materials, the goal is to create a robust model that explores the elastic and inelastic global and local buckling of the cylinders.

The cylinders were in general modelled as three-dimensional cylinders, defining the outer and inner radius and applying volumetric elements. In some analyses, however, only the middle radius was defined, and a shell was implemented, having a middle surface at this radius. These analyses required using shell elements, a topic to be discussed in section 4.4.

In Abaqus, the models are loaded through the BCs, hence the tests are displacement-based (not force-based). Consequently, after maximum load is reached, the model can predict behaviour into the post-buckling area instead of collapsing. The models also better represent the

displacement-based testing done in laboratory, and the strain rates, which is closely linked to inertial effects, are controlled. While this type of BC is labelled “displacement-based”, it was modelled by applying a velocity to the desired parts of the model, ensuring a constant load rate. By recommendation of Simula through their Advanced Topics documentation [20], the quasi-static loading state was ensured by applying an amplitude. The velocity of the BC components was originally zero, then over the course of roughly one-tenth of the time span of the analysis, it was smoothly increased to its maximum value, where it was kept constant for the remainder of the analysis. This was implemented using the “smooth step” option in Abaqus, in which a fifth-order polynomial enforces zero acceleration at the start and end point of the interval while increasing the velocity the desired value. This technique for ramping up the velocity was applied to all analyses.

Boundary conditions may be established by a reference point (RP). These can be tied to nodes or analytically rigid surfaces, and applying deformation to the RP will therefore impose the boundary condition to all restrained nodes.

Two types of interactions are applied in the models created: Constraints and contacts. Constraints include tying together certain dofs of nodes, such as with the BCs established by a RP. Contact is a special kind of constraint which only activates once a certain criterion is fulfilled, such as two surfaces colliding.

4.1.1 Introducing imperfections to the FEA model

One important aspect in the modelling of cylinders, especially thin-walled cylinders, is the implementation of imperfections. Without any imperfections, the model is mathematically perfect and straight, which may cause it to obtain artificially high resistance against instability. For the cylinders considered, r/t varies between 10 and 35.

There are many ways to introduce imperfections to the Abaqus model. One way is to run a preliminary linear buckling analysis (LBA) to obtain the eigenmodes for the model as explained in Abaqus Analysis User’s Manual v6.13, section 11.3.1 [21]. These eigenmodes are then introduced to the model as imperfection with a specified amplitude, before the desired, nonlinear analysis is run. This technique is effective when the elastic buckling mode (represented by the eigenmode) is the similar to the actual (inelastic) failure mode. Another way to introduce imperfections is make the mesh irregular or to introduce a small force or displacement at some point in the model, but these methods are hard to regulate in order to study the behaviour and impact of imperfections.

A third option is to manipulate the input files before running the job in Abaqus. First, the model is written to an .inp (input) file. This file is then opened in a data treatment software (such as Matlab) that allows altering of the coordinates of the nodes to implement the desired buckling modes. Note that these coordinates are Cartesian, not cylindrical. The assumed global imperfection could be introduced as

$$\Delta x = f(z) = a_g \sin\left(\pi \frac{z}{L}\right) \quad (4.1)$$

In order to introduce local imperfections in the “vase-shape”, each x and y coordinate can be magnified by the factor F defined as

$$F(z) = \frac{\Delta x}{x_0} = \frac{\Delta y}{y_0} = \frac{a_v}{r} \sin\left(m\pi \frac{z}{L}\right) \quad (4.2)$$

Here, a_g and a_v is the amplitudes of the global and vase-shaped (local) imperfection. The translation of the cross-section in the x -direction with the given z -coordinate is represented by $f(z)$, and three different amplitudes a_g are analysed:

$$a_1 = \frac{L}{1000}, a_2 = \frac{L}{2000}, a_3 = 0 \quad (4.3)$$

In order to give the cylinder a vase-like radial (axisymmetric) imperfection as seen in figure 11, the magnification factor $1 + F(z)$ is multiplied with the radius.

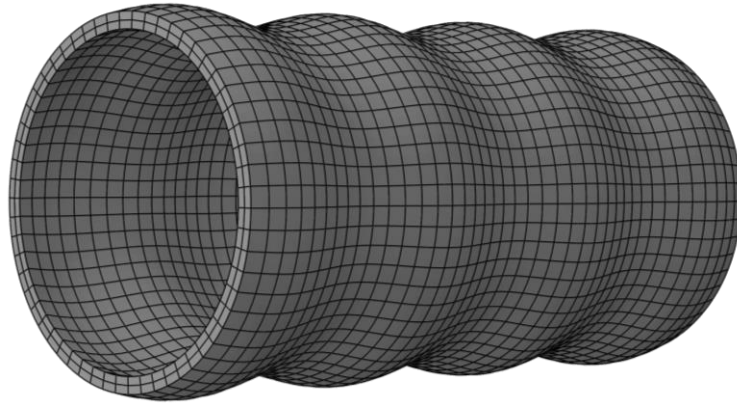


Figure 11 Local imperfections imposed by changing node coordinates

Note that the local imperfection chosen modifies the radius of each node in the cross-section with the same factor. Because the outer radius is greater than the inner radius, these nodes are moved further than their inner counterpart. The thickness of the cylinder is therefore changed slightly by imposing this imperfection. The area is consequently somewhat increased or decreased depending on the sign of $F(z)$. The imperfection is meant to induce a buckling, not

just alter the capacity due to a change of area, and the change of area should therefore be controlled. The smallest value of the area, which is found for the z -value that gives $F(z) = -\frac{a_v}{r}$, can be calculated as:

$$A = \pi \left(r^2 \left(1 - \frac{a_v}{r} \right)^2 - (r-t)^2 \left(1 - \frac{a_v}{r} \right)^2 \right) \quad (4.4)$$

$$A = \pi (r^2 - (r-t)^2) \left(1 - \frac{a_v}{r} \right)^2 = A \left(1 - \frac{a_v}{r} \right)^2$$

4.2 Material data

While only two alloys are studied, namely 6060T6 and 6082T6, these are treated as three different materials; the thin-walled and thick-walled 6060T6 alloys are treated as two different materials. The materials have three sets of properties: Elastic, plastic and physical. The elastic and physical properties found in Eurocode 9 [2] are common for all alloys, while the plastic behaviour varies, and is modelled with Voce hardening rule. Note that as the basic units kg, s and mm are chosen for the model, the density used in modelling in Abaqus is given in tonnes per cubic millimetre (table 7). In the FEA model which included detailed BC parts of steel, no yield stress was defined and the material was purely elastic. The elastic properties of steel in table 7 are taken from the book by Larsen [3].

Table 7 Elastic and physical properties of aluminium and steel

	Aluminium	Steel
E	70 000 MPa	210 000 MPa
ν	0.3	0.3
ρ	$2.7 \cdot 10^{-9} \frac{\text{tonnes}}{\text{mm}^3}$	$7.85 \cdot 10^{-9} \frac{\text{tonnes}}{\text{mm}^3}$

The plastic properties of the material was modelled to the Voce hardening law shown in equation (3.28). In the early stages of the work with this thesis shown in chapter 5, values for the parameters for alloy 6082T6 were taken from the preliminary thesis work report by Nesje [22]. In chapter 6 new parameters found for both alloys were established and verified. The material was modelled as a pure elastic-plastic material without viscous or temperature-dependant properties.

4.3 Solution algorithm and scaling

The highly non-linear behaviour of a buckling column, as well as yielding, constraints, contact and friction requires a robust solution algorithm. After some initial attempts with static solution algorithms, it is chosen to dedicate the full attention to the dynamic algorithms, as well as LBA. The dynamic solvers are divided in two categories, according to Abaqus Analysis User's Manual, section 6.3.1 [21]: explicit and implicit solvers. Both methods are based on the equation of motion:

$$[\mathbf{M}]\{\ddot{d}\} + [\mathbf{C}]\{\dot{d}\} + [\mathbf{K}]\{d\} = \{F\} \quad (4.5)$$

Here, d are the dofs of the system, \mathbf{M} , \mathbf{C} and \mathbf{K} are the mass, damping and stiffness matrices, respectively, and F is a vector containing the external loads acting on or in the direction of the dofs.

4.3.1 Implicit solution algorithm

Implicit solution algorithms solve the equation (4.5) of motion for the next time step in order to find the dofs for the current time step. This makes the method unconditionally stable, meaning that it is stable for any time step Δt . Note that stability is not the same as accuracy, and with large time steps it is possible to miss bifurcation points. Bifurcation points are the points on the load-displacement curve of which the capacity of the structure changes from one path (the original, stable path) to another (i.e. the buckling path with decreasing capacity as deformation increases) as seen in figure 12 taken from a report by Ion Leahu-Aluas [23].

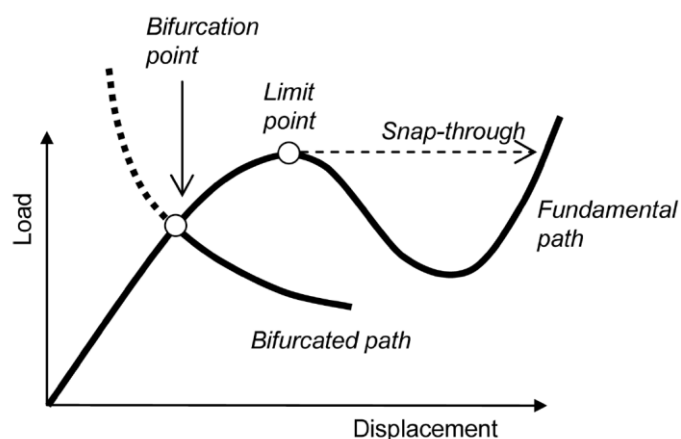


Figure 12 Main path and bifurcated (buckling) path cross at a bifurcation point

Missing a bifurcation point means that the model continues on the fundamental path and thereby predict an artificially stable solution and a too high load capacity (figure 12). Because the

buckling of the cylinder is of interest, a maximum time step Δt must be chosen so small that the bifurcation point is not missed.

The biggest drawback with the implicit method is that the stiffness matrix has to be inverted for every time step, making every time step computationally expensive. The implicit method is advantageous for analyses with long time steps and with smooth changes in stiffness, e.g. to model a material that is hardening after yielding. Implicit methods are also efficient when assessing quasi-static problems. Despite that the model is considered quasi-static and includes a hardening material, applying this algorithm can be cumbersome with regards to the local and global buckling behaviours. When buckling occurs, the implicit solver may fail because the system experiences the sudden change of stiffness.

4.3.2 Explicit solution algorithm

Explicit algorithms solve the equation of motion for the current time step. The big advantage with explicit solvers is that only the mass and damping matrix has to be inverted for every time step. Lumped mass matrix is used in place of a consistent mass matrix, giving a mass matrix that only has non-zero entries along the diagonal. This property greatly lowers the computational effort in inverting the mass matrix. Using lumped mass matrix also lowers the error in oscillation frequency displayed by the explicit solver. The damping matrix is usually represented with Rayleigh damping, meaning that it is a weighted sum of mass-proportional and stiffness-proportional damping. This can according to Cook [14] be written as:

$$[\mathbf{C}(\omega)] = \frac{a_0}{\omega}[\mathbf{M}] + a_1\omega[\mathbf{K}] \quad (4.6)$$

Here, ω is a given frequency, and a_0 and a_1 are constants. Inverting the damping matrix above means inverting both the mass and the stiffness matrices. It is undesirable to invert the stiffness matrix, but setting $a_1 = 0$ nullifies the damping of higher frequencies, which leads to high-frequency noise. It can be shown that this problem can be avoided by letting the damping lag behind half a time step, so for the n 'th time step the equation of motion becomes

$$[\mathbf{M}]\{\ddot{d}_n\} + [\mathbf{C}]\left\{\dot{d}_{n-\frac{1}{2}}\right\} + [\mathbf{K}]\{d_n\} = \{F_n\} \quad (4.7)$$

Because of this modification, sufficient damping is included in the algorithm, and the only matrix that has to be inverted is the diagonal mass matrix, meaning that each time step is calculated exceptionally rapid compared to the implicit increments.

One of the largest disadvantages with the explicit solution algorithm is that it is only conditionally stable. The time step is only stable if it is too short for information to progress from one node to an adjacent node within a single time step. This requirement can according to Cook et al [14] be written as

$$\Delta t \leq \Delta t_{cr} \leq \frac{2}{\omega_{\max}} (\sqrt{1 - \xi^2} - \xi) \leq L_e \sqrt{\frac{\rho}{E}} \quad (4.8)$$

Here, ω_{\max} is the highest eigenmode frequency and ξ is the damping related to that mode, meaning that more damping slows down the information propagation speed, allowing bigger time step. The latter expression (named the *CFL condition*) is often easier to apply for non-flexural elements (elements without rotational dofs). In this expression, L_e is the shortest characteristic element length in the model, and the density ρ and Young's modulus E gives an expression for the wave propagation speed. The values for the critical time step in the simplest analyses considered varied between 10^{-5} to 10^{-7} . Because of the short Δt , some analyses have millions of time steps. When the amount of time steps become large, the number of significant digits can highly affect the outcome of the analysis. Therefore, all explicit analyses discharged have twice the normal amount of significant digits, which is the highest setting allowable in Abaqus, and considered sufficient even for the longest analyses.

4.3.3 Scaling of the analysis

In order to achieve quasi-static results in the laboratory, the loading speed must be low, in the order of magnitude of 0.1-1 mm/s. The buckle then occurs seconds or even minutes into the analysis. If this was to be modelled in Abaqus with an explicit solver, each analysis would last for an unacceptably long time. Therefore, one of two kinds of scaling are used. The first, obvious choice is to increase the loading speed. The critical time step when scaling velocity remains the same, but the duration of the analysis in terms of seconds modelled is reduced. Higher loading speed means greater acceleration, which leads to inertial forces. The drawback of velocity scaling is that the critical time step of the whole mesh still is defined by the most critical element, consequently one tiny element (or an element with low density ρ and high stiffness modulus E) may greatly affect the analysis in terms of scaling required. All models contained a mesh that was to some degree irregular, hence velocity was discarded.

The other kind of scaling is mass scaling (MS), explained in section 11.6.1 of Abaqus Analysis User's Manual [21]. MS targets a given (desired) time step, e.g. 10^{-5} s. The critical time step is calculated for each element using formula (4.8). For the elements that has a shorter critical

time step than the target time step, the density is increased. If an element has a critical time step of $10^{-6}s$, the density has to be increased by a factor of 100 in order to obtain $\Delta t_{cr} = 10^{-5}s$. The drawback of using this method is that large densities give rise to large inertial forces, hence much scaling creates a dynamic system.

Mass scaling is used so that each element is scaled differently, according to how much that element needs to be scaled, rather than the whole model being (in practice) scaled equally toward the worst-case element. In this sense, mass scaling is more effective than velocity scaling, and the difference increases for more irregular meshes. When MS is applied, it is denoted by its target time increment, thus it has unit $[s]$. The element mass scaling factor can then be calculated as

$$EMSF = \left(\frac{\Delta t_{target}}{L_e} \right)^2 \frac{E}{\rho} \quad (4.9)$$

It is crucial to access to which degree the quasi-static loading is preserved when applying mass scaling. If the speed reaches a threshold defined partially by the length of the specimen, dynamic oscillations will alter the behaviour and capacity of the cylinder. When buckling occurs, especially globally, parts of the cylinder are moved in a transverse direction. This often rapid movement requires great acceleration of the masses to be moved, which leads to inertial forces. If the scaling is too large, these inertial forces can prevent the buckle, giving artificial high capacity to the cylinder against that governing buckling mode.

Even though explicit solution algorithms excel at finding bifurcation points due to the very low time steps, implicit solution algorithm has to be chosen for the longest cylinders analysed as they do not rely on any scaling. On the other hand, smaller models, such as the dog bone tension test, has such a low mass that even an enormous EMSF still will ensure a quasi-static solution, as seen in chapter 6.

4.4 Element type and mesh

In FEM, the choice of element is crucial as it induces several assumptions.

There are two feasible element categories available to model these axially loaded cylinders: shell elements and volumetric elements. Defining the cylinder as a shell rather than a compact volumetric element enables elements with rotational dofs, describing more detailed deformation patterns while reducing the computational time dramatically. The drawback of the shell elements is twofold: Volumetric elements are by far preferable when modelling contact,

especially when the geometry is circular/spherical. Also, when the mesh is refined and the element size gets small compared to its thickness, the solution for shell elements will not converge, but rather display a slightly different failure mode. Shell elements may sometimes be a good fit for preliminary analyses because of their low computational cost and higher-order deformation patterns.

The shell and volumetric elements used in this thesis are quadrilateral and brick elements, no triangular or tetrahedral elements are used. Triangular and tetrahedral elements have the advantage of being computationally less expensive, hence a more refined mesh can be created to allow a better discretization of complex stress and strain states. As all loading scenarios are uniaxial, with no externally applied bending forces, and most geometry modelled is regular, the authors see no motivation in modelling with these elements.

Finite Element Method only satisfies force equilibrium on an average sense, which gives a poor stress and strain distribution accuracy when the stress is sampled at the nodes of each element. To increase the accuracy of the stresses and strains, these are sampled at given integration points not located at the element nodes. All elements considered in all analyses exhibit reduced integration as explained by Cook et al [14]. This means that while displacement is measured at the all m nodes at an edge, the stresses and strains are sampled at $m - 1$ points in that direction, creating stress and strain fields of polynomial order $m - 2$. The accuracy is greatly increased because of this, but the reduced integration allows zero-energy-modes: deformation modes that occur without causing strain energy, representing a deformation field which is erroneous. Artificial stiffness is then introduced to the elements to give stiffness against said modes, damping the effect but adding artificial strain energy to the model. This parameter is recorded and evaluated, and if it is too high compared to the external work of the model, the mesh needs to be refined in order to reduce the artificial energy.

The choice of elements is strongly affected by the chosen solution algorithm. When applying an explicit solver, it is beneficial to apply lower order elements of two reasons. Because these have fewer dofs, their natural frequency is lower, increasing the critical time step. Explicit solvers tend to overestimate frequencies of dynamic oscillations, and lower-order elements tend to underestimate it, so the effect of the two partially cancel each other out, as pointed out by Cook et al [14]. For these reasons, only lower order elements are used in explicit solution algorithms.

For implicit method, the effects are reversed: The solver tend to underestimate natural frequency, hence applying higher order elements which overestimate frequency is generally

beneficial. Higher order elements require more computational effort to invert, but they generally produce higher accuracy results.

4.4.1 Shell elements

Shell elements are flexural elements, as they include rotational as well as translational dofs, according to Abaqus Analysis User's Manual, section 29.6.1 [22]. The shell elements produce excellent results when the length-to-thickness ratio is not too low, however no single strict limit exists for this ratio. As a rule of thumb $L_E \geq 4t$ can be used, but Abaqus will run the analysis with even shorter (or thicker) elements. If $L_E * 0.6 < t$, however, Abaqus has problems simulating contact problems with the shell elements.

Shell elements represent a simplification through assuming that one direction (here: the x -direction) is much smaller than the other two. The limit for how much thinner this dimension should be is discussable, both for the validity of shell elements and for the deviation between results using shell elements and volume elements. A report from Sadowski and Rotter [24] studies this deviation for cylinders subjected to global buckling and bending. In that report, Sadowski and Rotter claims that shell elements perform just as good as volume elements for $r/t=10$ and that the difference is small at $r/t=25$, both values close to the r/t relationships considered in this thesis, shown in table 2.

The lower-order shell element S4R is a four-noded element with reduced integration, a standard choice for explicit simulations. This is a general-purpose element that works well with thick and thin shell elements. In implicit analyses, the more complex S8R element is used, with three nodes per edge.

4.4.2 Volume elements

Three dimensional volume elements studied are C8R and C20R [22]. These contain only translational dofs. An advantage with volume elements is that refining the mesh makes the model converge towards a solution, both with respect to capacity and deformed shape.

4.4.2.1 C8R

C8R is an 8-noded brick with one node at each corner and three translational dofs at each node. The element exhibits reduced integration, and with two nodes per edge it only has one integration point. The strain and stress field within a single element is therefore constant. This element is chosen for all explicit analyses. Because of the simplicity of this element, many elements are required to obtain sufficient accuracy. As a rule of thumb, three elements through

the thickness of the cylinder is chosen. This way, any bending moment from an initiating buckle can be described.

4.4.2.2 C20R

C20R is a higher-order volume element which in addition to the 8 nodes in C8R also has one mid-side node on each of the 12 edges of the brick. This element is only available in the implicit solution algorithms of Abaqus, and it describes more detail C8R, although it is more computationally costly. Three elements per edge gives $(3-1)^3 = 8$ integration points, and linearly varying stresses and strains in all three directions, which gives a much better representation of the distribution of forces through the model. When an element edge with three nodes is slightly curved, for example on a cylindrical surface, the geometry is represented as a second degree polynomial rather than a straight line.

4.4.3 Mesh

The meshes in the models created are partially defined by the element length, which for this thesis is defined as the length of each element edge in the y - and z -directions. Defining the element length is therefore sufficient to describe the whole mesh if shell elements are applied.

For volumetric elements, the number of elements through thickness is labelled ETT. A mesh with cylinder thickness of 1.77, element length of 5 mm and 2 ETT will span 5.6 further in the y - and z -directions than in the x -direction. An ideal brick element (volumetric element) should have equal element lengths in its three directions. Volumetric elements with far from quadratic shape may cause ill-conditioned elements, which can lead to erroneous results. It is therefore crucial, especially for the most thin-walled cross-section, to conduct analyses of mesh sensitivity. These may establish whether or not the shape of the chosen elements leads to results deviating from that with regular elements.

4.5 Validation of analyses

Abaqus is an effective software to obtain large amounts of results. It is a purely analytical program relying on user-specified input, and does not always detect errors or deviations from the assumptions behind the model. It is the user's responsibility to ensure that the results are correct. Sensitivity analyses are one way to validate the model.

A sensitivity analysis is discharged by altering one parameter in the FEA model and noting how certain results are affected by this change. A robust model should not display large changes in results as a consequence of small changes in parameters. The results studied are the force –

displacement relationship, the axial capacity, the failure mode (local, global) and the amount of energy contained as artificial energy as well as the change of total energy in the system.

This thesis focuses on four types of sensitivity analyses:

Mesh analyses establish to what degree at change of element type, element length and (in the case of volumetric elements) change of ETT cause the simulations to render different results.

Imperfection analyses assess to what degree imperfections cause a change of failure mode.

Frictional coefficient studies assess to what degree the friction of the BCs affect the simulation.

Mass scaling analyses assess the effect of scaling up the density of the elements in order to speed up the run time of explicit analyses. The main focus is the prevention of dynamic oscillations in the reaction forces of the model.

The sensitivity analyses are focused on achieving stable results with sufficient accuracy without increasing the analysis run time needlessly.

4.6 Output data

The output data from the analyses is the basis of most plots and graphs presented. There are two types of output data available from Abaqus: field output, which saves a given variable to each node or element in the whole model at a given frequency, and history output, in which a set of nodes are chosen to record a given series of variables, at a typically higher frequency. While the former gives intuitive qualitative and quick information for validation of the model, the latter is chosen for extracting forces and displacements to give mathematical conclusions. The history is often extracted from RPs which easily track displacements and reaction forces, two key variables from most analyses. Creating graphs and manipulating data can be cumbersome in Abaqus, and Matlab is chosen for this task.

Firstly, a python script created by Marius Andersen at NTNU is used to extract all the history output data from a given analysis. These data were written into two text files, one containing the data itself and another containing the name of the variables. These files, having a general ASCII format, were then imported in Matlab as matrices and vectors. Scripts in Matlab were used for plotting graphs, for validating the model by controlling that the desired energy measurements or calculating the different responses between similar analyses or between an analysis and the laboratory test it attempted to simulate.

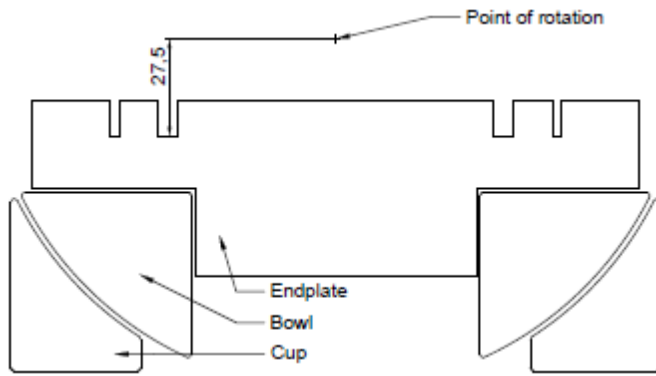
5 Laboratory Design with Spherical Hinge

The first FEA model created in relation to this thesis simulates the behaviour of long, globally slender cylinders in axial compression. The motivation was to compute the capacity and behaviour of a laboratory setup with spherical boundary conditions. Both forces and displacements should be estimated, and any hazards considering the execution should be predicted. In order to study the global buckling of a column without the interaction of local buckling patterns, the column has to be of significant length. From the formula for the Euler load (3.31) it follows that the buckling length is crucial. It is desirable to model the column with hinged BC to double the buckling length compared to clamped BC.

The laboratory equipment consisted of three parts made out of steel (figure 13), labelled the cup, the bowl and the endplate. All components in the model has an axisymmetric geometry, albeit full axial symmetry of the model in terms of forces and deformations cannot be assumed because of the global buckling. Figures in this chapter are cut with a 180-degree angle.

The endplate had two 10 mm deep circular slots customized for the two geometries considered. This piece was fitted in an opening in the bowl, which had a spherical underside. The third component, the cup, was to be bolted to the testing machine. The top of the cup had a glass fibre reinforced PTFE polymer coating and was shaped like a slot for the matching spherical underside of the bowl. The low-friction polymer surface has a coefficient of friction between 0.05 and 0.20 in connection to steel, according to the producer, SKF [25]. If required, lubrication could be applied to lower the friction even further. Because the bowl could glide more or less freely with respect to the cup, a hinged effect was ensured, according to the hypothesis behind the laboratory setup.

The point of rotation was 27.5mm from the edge of the cylinder (figure 13 (a)). Theoretically, this means that a cylinder of length L in this setup should buckle as a simply supported Euler column with length $L - 2 * 27.5mm$. The radius of the spherical surfaces was 98.5 mm.



(a) Sketch of all three components



(b) Bowl and cup components

Figure 13 Laboratory setup with SKF GX 80 F components and a customized endplate.

5.1 FEA model

The process of modelling this laboratory equipment in Abaqus was an iterative process, and it is presented as examples of how complex modelling should and should not be executed. Due to the length of the cylinders (2-4 metres), shell elements were chosen. The laboratory equipment was first modelled as three separate parts, using volumetric elements. The boundary conditions were a constant velocity applied at the cup, which was held in place in the transverse directions. This model was established for A6082D100.

Implicit solution algorithm was unable to conduct the analysis, possibly because of the complexity related to the numerous contact constraints, the size of the model and the challenging geometries. Explicit solution algorithm was then chosen as it is more robust, although this led to problems with scaling, and the inertial effects described in section 4.3.3 caused the cylinder to gain an erroneous capacity for the desired amount of mass scaling.

5.1.1 Troubleshooting and improvement of the model

The contact between different parts led to two challenges. Firstly, the contact between the bowl and the cup consisted of two discretized sphere-like surfaces, as shown for a rough mesh in figure 14. These were modelled as low-friction surfaces ($\mu = 0.05$). Because the surfaces were discretized as several straight elements, the contact was not smooth, as marked with circles in figure 14. This led to high dependency between the element size and the behaviour of the connection. The components needed to be apart at the start of the analysis to ensure that overlapping did not occur. This distance was hard to calculate analytically for the spherical surfaces. Troubleshooting was frequently done by running the analysis without any load (zero velocity) to confirm that the model was stress-free.

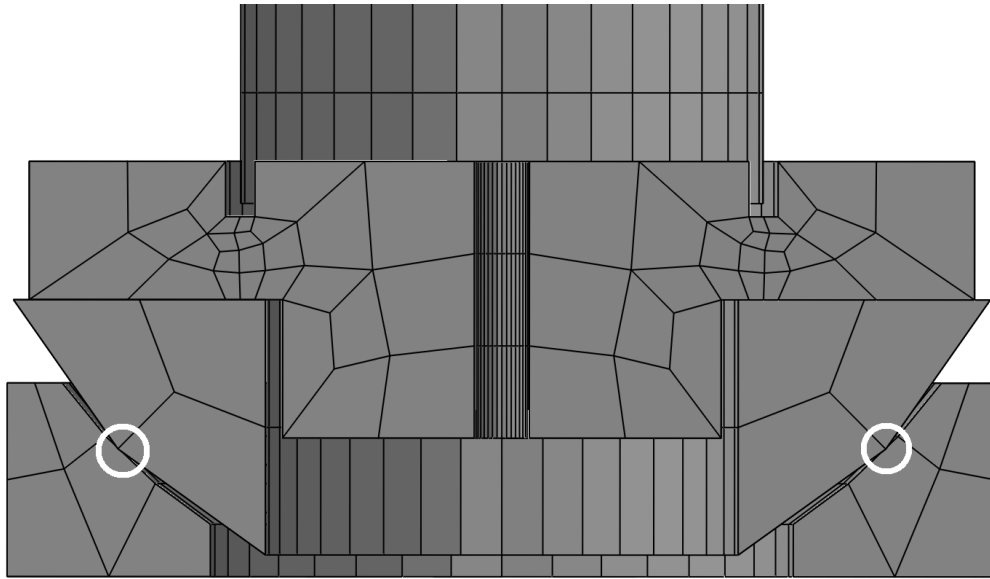


Figure 14 Spherical surfaces discretized by straight elements

The second contact problem was between the cylinder and the endplate component, modelled as a rough high-friction contact ($\mu = 0.60$). The number of nodes around the circumference of the cylinder and endplate was set equal, hence the parts were discretized similarly. Higher number of nodes resulted in more circular mesh. Abaqus required $0.6L > t$ for shell-to-volumetric-contact, which restricted the number of nodes around the circumference to 36. The slots should work as a clamped boundary condition, ensuring that the rotation occurs in the contact between the cup and the bowl. Because the slots of the endplate were 10 mm deep, contact could be initiated between the shell elements and the steel slot in the endplate. This contact constrained the transverse movement of the shell elements. The contact between the bowl and the endplate were also modelled, however this connection did not lead to any modelling challenges other than to further complexify the model.

Mass scaling towards a critical time step of 10^{-5} s pushed the limit of acceptable run time as each analysis required 10-30 hours to complete. The element mass scaling factor (EMSF) was $10^3 - 10^6$, which significantly increased the mass of the laboratory equipment from a few kg to several tonnes. As the model was loaded, inertial effects caused the BC parts to bounce back and forth, and the results were useless.

The scaled-up mass might have worked as a rotation stiffness at the end of the cylinder, since a rotation of the bowl and endplate component would require some acceleration of mass. These inertial forces would work as a rotation spring at the ends of the cylinder, causing the BCs to be less degree free to rotate. It was also evident that the model was too complex, and a

simplification was to model the endplate and bowl as one solid component, eliminating the contact between the two. In order to reduce the mass scaling and the computational effort of the model, this part was made analytically rigid. Abaqus does not easily accept contact between analytically rigid parts, hence the cup component was kept deformable. Rigid parts are not meshed with elements, which in this case made an impact in two ways. Firstly, MS scales the mass of elements, and the rigid part is consequently unmodified by the scaling of the model. Secondly, as there are no elements, the spherical and circular surfaces and edges are not discretized, but represented exactly. The spherical connection was improved, its results in terms of stresses and reaction forces contained less noise and dynamic oscillations. Discretization of the cylinder and not the now-rigid slots of the endplate gave rise to unlike geometry. With its 36 nodes, the circumference of the cylinder was modelled as a polygon with 170 degree angles. Reducing the amount of nodes led to kinematic (fitting) problems, and the mesh, despite possibly being too fine, was retained.

With the simplifications included, the complexity of the model was greatly reduced. Consequently, implicit solution algorithm became an option. A change of solution algorithm results in removing the MS. The mass of the laboratory equipment was therefore reduced from several tonnes to their correct weight, and the erroneous inertial effects were avoided.

5.1.2 Sensitivity analyses

Changing the solution algorithm permitted employing higher-order shell elements. A mesh sensitivity study was carried out with both lower and higher order elements as well as variations in mesh refinement. As pointed out in section 4.4.1, refining the mesh of shell elements does not lead to a convergence of failure mode. As a consequence of this property, it was difficult to establish what results the correct solution should display. In addition to varying meshes in the cylinder, the volumetric element mesh of the cup component was also altered. This cup mesh refinement modified at what point contact with the rigid body was made, which turned a mesh analysis challenging, as the discretization of the spherical surface of the cup was modified.

A new, simplified model was created in an attempt to establish a “correct” solution to the analyses. This model consisted of only a cylinder with shell elements and a reference point (RP) placed at 27.5 mm from each end of the cylinder. The length of 27.5 mm is meant to represent the centre of rotation from figure 13 (a). The nodes along the edges of the cylinder were then tied to that RP using an MPC-constraint, enforcing that their distance to the point was kept constant. This means that each node could rotate about the RP. It was discovered that this

simplified model gave lower capacity than the complex laboratory equipment model. The failure mode of the simplified model was also slightly different, with less localizations of deformation close to the ends of the cylinder. Because of this finding, focus was shifted towards friction.

Attempts were made to find an analytical solution to the friction problem between the two spherical surfaces. When the column deflected transversely, the end of the cylinder was rotated an angle θ . A moment $M_1 = NL_a \cos(\theta)$ would act as a driving force for a rotation of the end point of the cylinder, where L_a is the radius of the spherical surfaces. The friction would counteract this rotation with a force $M_2 = \mu c NL_a$, where μ is the frictional coefficient and c is the amount of the normal force transferred by normal stresses rather than tangential stresses. This way, the friction, normal force and geometry will act as a rotational spring, adding stiffness against rotation of the endpoint of the cylinder (figure 16 (b)). Setting $M_1 = M_2$ gives the limit value for the frictional coefficient that can resist the external force N . Dividing by NL_a on both sides gives an equation that is to a greater extent a geometrical problem than a mechanical one, and the limit value of the frictional coefficient is not directly a function of the axial force. No analytical solution was found due to the free variables c and θ , and focus was shifted to the FEM solution of the problem.

In the Abaqus model, both 2- and 4-metre-long cylinders were analysed. The friction coefficient of the PTFE polymer – steel contact was varied in order to establish at what point the friction was high enough to serve as a clamped BC rather than a simply supported one. The results indicated a lower limit frictional coefficient than anticipated (figure 16 (a)). Increasing the frictional coefficient from 0 to 0.60 for the longest column increased the capacity with a factor 3.40. This is close to the factor 4 anticipated by changing from simply supported to clamped boundary conditions, according to the formula for Euler buckling (3.31). With frictional coefficient set to zero, the shortest column had 3 percent higher capacity than the twice-as-long, high-friction column. As the frictional coefficient of the shorter column was increased, the capacity only increased by a factor of 1.63, indicating that the friction led to an inelastic buckle. It is concluded that zero friction of the spherical surfaces closely represents simply supported BC, while high friction closely represents clamped BC (figure 16 (a)). The limit coefficient for simply supported representation is in the range 0.005-0.03, depending on the length of the column. The failure mode was also slightly different because of the rotational resistance in the high-friction scenarios (figure 15).

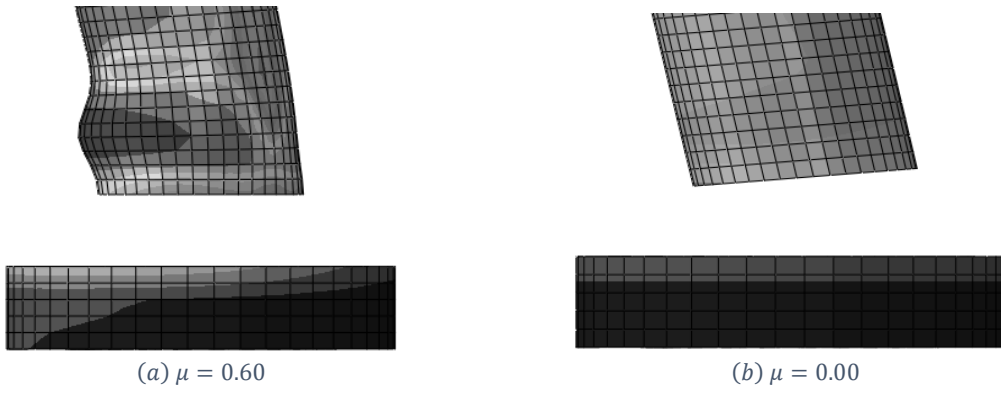


Figure 15 Failure mode with different frictional coefficients.
 Displayed deformation scaled with factor 3, rigid bowl-endplate component is not shown.

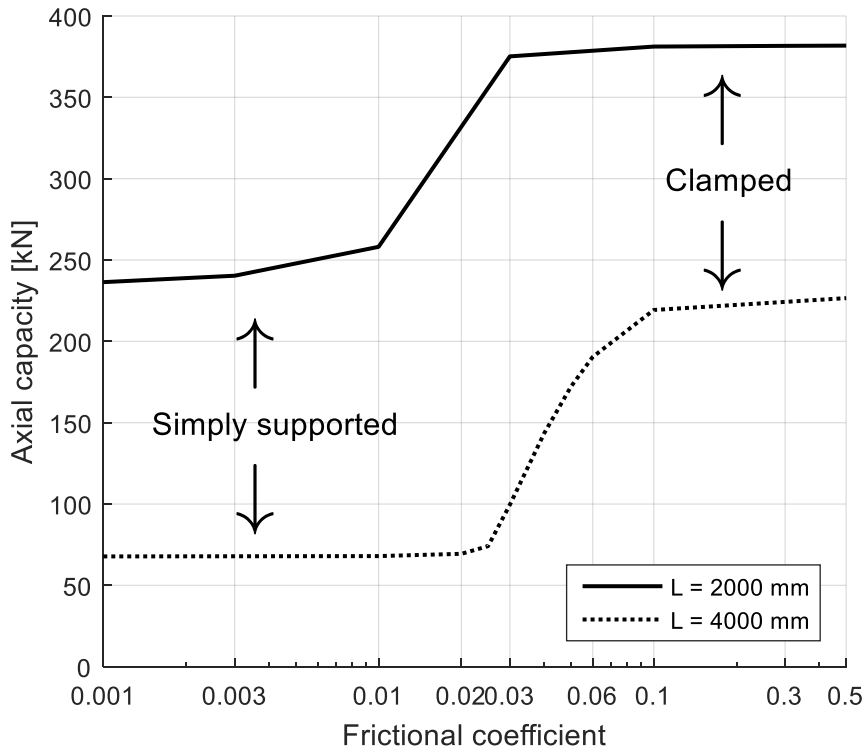


Figure 16 (a) Relation between capacity and frictional coefficient (b) Mechanical model including rotational stiffness from friction

5.1.3 Conclusions

Discovering the dependency upon the frictional coefficient and its low limit values led to the conclusion that the laboratory setup was inadequate for its purpose. The equipment was discarded and the plans for laboratory testing were cancelled, as it was deemed unrealistic to obtain sufficiently low frictional coefficients in the laboratory.

Working with the laboratory setup described served as an introduction to further FEA modelling. In the subsequent models, any new mechanical problems and assumptions will be assessed. When initiating the design of a new FEA model, it is beneficial to start with a simple model, possibly verified by hand calculations. Knowledge of how the chosen software operates can be vital, as seen in this chapter for discretizing of complex geometries in contact. In hindsight, it is evident that the frictional coefficient should have been assessed at an early stage, which would save the great amount of time that were spent on this model.

The preliminary plan for the project was to focus on globally buckling cylinders. Because the equipment was left unused and the plans abandoned, the focus was shifted to the behaviour of shorter stub column tests, which buckle locally. These are described in chapter 7, where attempts are later made to extrapolate results to the globally buckling region. In order to estimate the behaviour with sufficiently accuracy, the material is thoroughly studied in chapter 6.

6 Tension Material Test

In this chapter, the details regarding the material tests are explained and discussed in three phases. The first phase is the execution phase, where the laboratory tests are performed and raw data is generated. In the second phase, data are extracted and analysed, and several sources of error and noise are assessed. This phase results in an initial material model. In the third phase, FEM is applied to adjust and validate the material model, and alternative validations are suggested.

6.1 Phase one: Laboratory setup and DIC

The dog bone material tension test was chosen for its simplicity, as it is an accurate test with a unidimensional stress state up to necking. The dog bone test is named from the shape of the specimen, which in this case was cut out of the cylinders (figure 17 and figure 18). The cut was performed using a technique called Wire Electrical Discharge Machining (EDM), using a hot wire and water cooling. The geometry of the specimen is shown in figure 19.

The goal of these tests was to establish a true stress – logarithmic plastic strain relationship for the materials in a quasi-static state. The relationship should define yielding as well as the plastic properties. This material behaviour would later be used both as input to the FEM analyses to analyse the buckling behaviour and to calculate the axial capacity theoretically. Three series of tests were performed, one for each combination of material and cross-section. In each series, three specimens were tested. Unless written otherwise, all figures and graphs presented are taken from the same specimen, which is of type A6060D127. The two sets of cross-sections with alloy 6060T6 were treated as two different materials. This was because of the different behaviour of the tests, which is in part believed to stem from different cooling rates during extrusion due to different thicknesses. This effect is also accounted for in table 3.2 in Eurocode 9 [2].

A hydraulic Instron testing machine with 100 kN capacity was used to test the specimens. The tensile force and displacements was recorded by the testing machine, and a set of pictures of the tests was captured correlating to the logging frequency of the testing machine, 4 Hz (figure 20). Speckled dots were sprayed on the specimen (figure 21), which allowed the use of digital image correlation (DIC), using the program eCorr. Two cameras were used, but an error with the calibration process between the two cameras prevented the use of 3D DIC.



Figure 17 The dog bone specimens were slightly curved.



Figure 18 The specimens were cut out of the cylinders

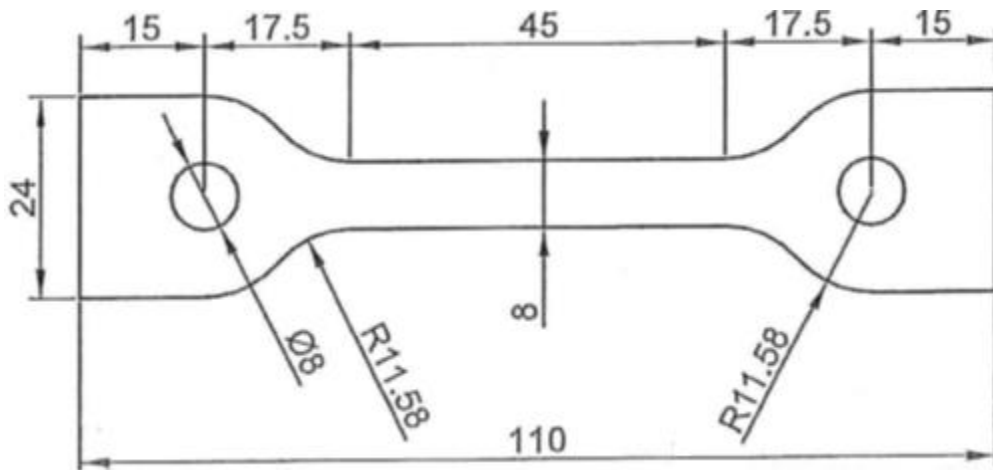


Figure 19 Geometry of the UT 110 dog bone tension specimen



Figure 20 Camera setup to allow usage of DIC technology



Figure 21 Typical speckled paint applied to the dog bone

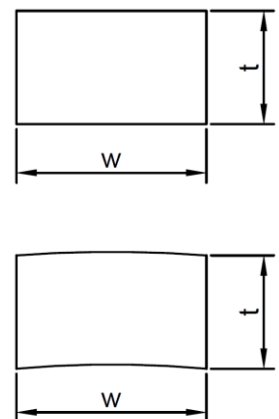


Figure 22 Rectangle and arc

In eCorr, a mesh covering the part of interest is generated from the initial picture of the specimen, in an unloaded state, as shown in figure 23. When the specimen is deformed in the subsequent images, the movement of the painted dots are traced by the program. This movement creates a displacement field, and from this field the logarithmic strains in two directions are calculated, as shown in figure 24 and figure 25. The mesh consists of constant-strain quadrilaterals (Q4 elements), which is the standard element choice in eCorr. These elements have four nodes with only translational degrees of freedom, giving a constant strain distribution within each element. The strains are then interpolated to create a strain field of higher polynomial order for the images presented, while the raw data is used in the data treatment later on. In the treatment of the DIC results, the term “column of elements” is often used. This notation is used to label the set of elements spanning across the width of the gauge.

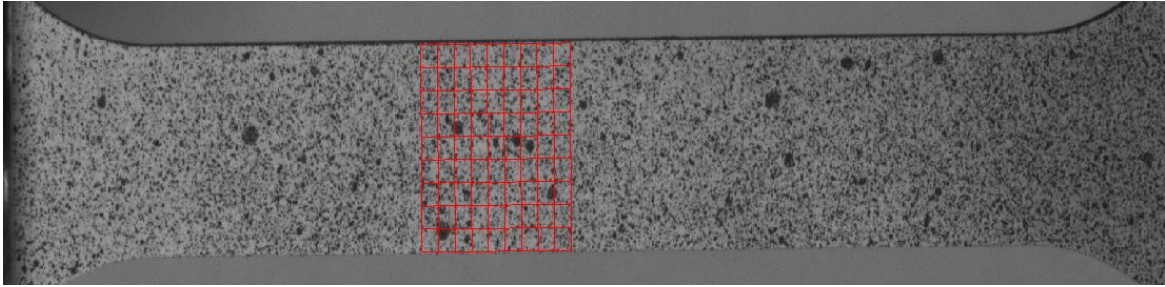


Figure 23 Mesh applied before analysis, on undeformed specimen

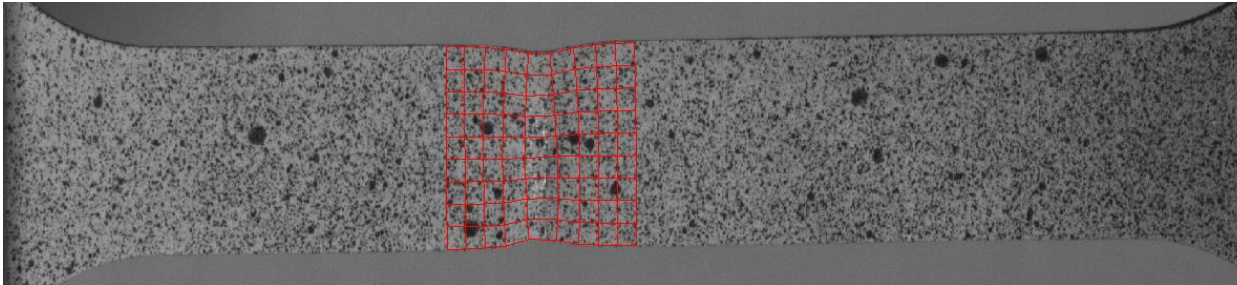


Figure 24 Deformed mesh at final stage of the test

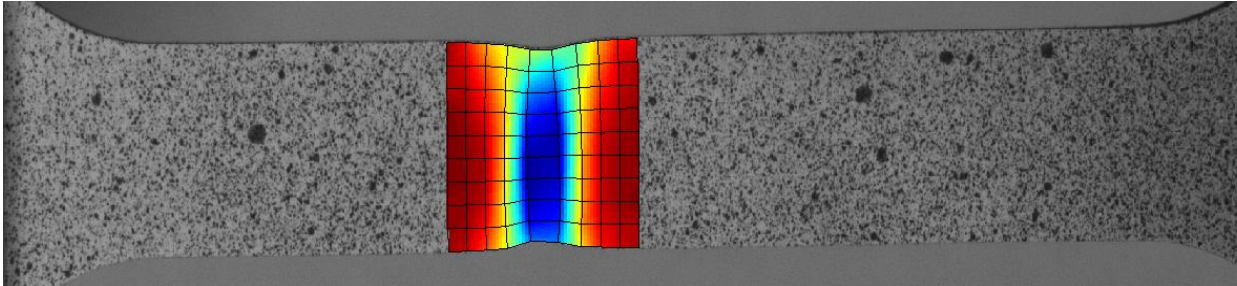


Figure 25 From the deformation, an interpolated strain field was created

When a specimen was loaded in tension, the load-displacement relationship went through four distinct stages (figure 26). Firstly, the slack between the specimen and the testing machine leads to recorded displacements without any resistance, which is assessed in section 6.3. After this, the elastic loading commences, with a linear relationship between load and displacements. When the yield stress is reached, the plastic stage and its plastic hardening initiates, increasing the stresses even further as the plastic strains are accumulated. The area of the cross-section will be reduced while the stresses are increased, and the total force will increase to the point of necking. At this point, somewhere along the length of the specimen, the cross-sectional area is reduced at a greater rate than what the strain hardening increase. This localization reduces the capacity of the specimen: dF changes sign from positive to negative. In this final stage, all specimen elongation will be taken up in the neck, which has a tri-axial stress state. The stage and the test ends when the specimen fails, often from a fracture in the middle of the neck.

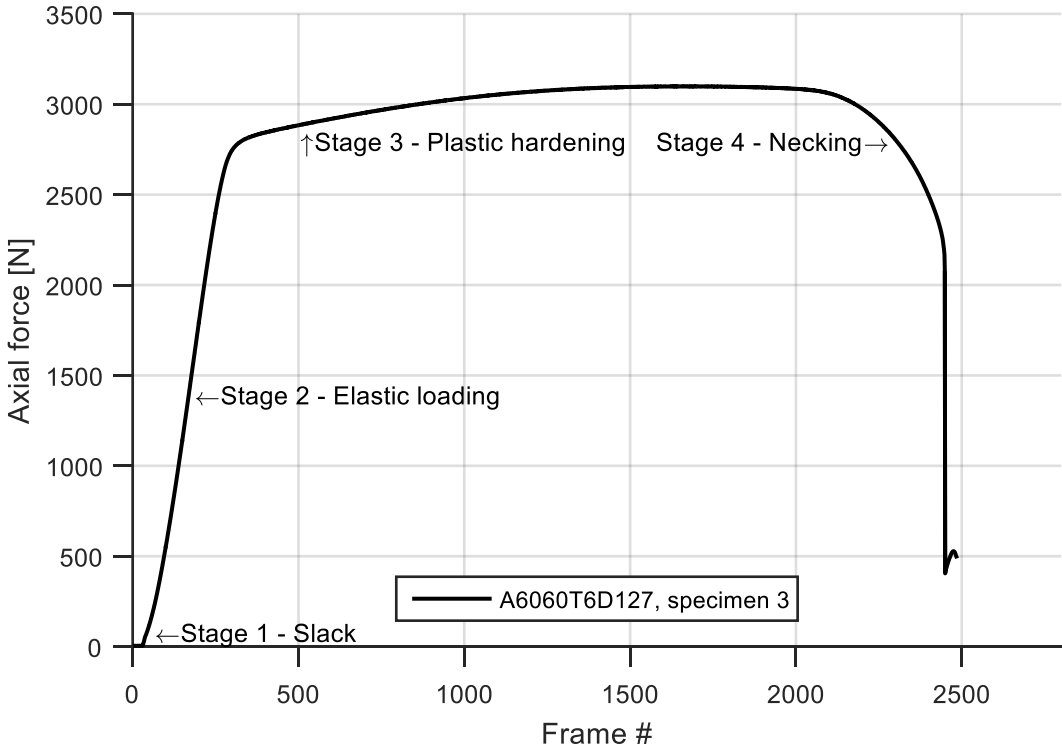


Figure 26 The four stages of tension tests

6.2 Theoretic calculations of stresses and strains

The goal of the material tests was to establish the material properties, relating stresses to strains in the elastic and plastic region. Voce hardening rule was chosen, the hardening rule as well as its derivative are stated in equations (3.28) to (3.29). From these equations as well as the formula for the plastic tangent modulus (3.19), it is seen that the stress – strain relationship as

well as its slope is continuous for $\varepsilon^{Pl} > 0$. At the point of yielding there is a drop in the slope of the stress – strain curve, unless $E_T^{Pl} \rightarrow \infty$ as $\varepsilon^{Pl} \rightarrow 0$.

In order to fit the laboratory tests to the chosen function, two parameters must be calculated from the results of the test specimen: true stress and logarithmic plastic strain.

The true stress from the tests is given in equation (3.1), where N is the axial force and A is the deformed cross-sectional area of the gauge of the specimen. While the geometry of the tests is shown in figure 19, the curved shape shown in figure 17 complexify the calculations of the initial area.

The cross-sectional area is calculated as the area between the outer and inner radius of the part of the circle considered. The y -coordinate of a circle in a Cartesian xy coordinate system can be written as

$$y^2 = r^2 - x^2 \quad (6.1)$$

The cross-section is considered to lie along the y -axis, so that the area can be integrated with respect to the x -coordinate. Note that this notation differs from the cylindrical coordinate system used in general in this thesis. The specimens were cut so that the edges were parallel to the y -axis, not to the radius of the circle, as seen in figure 17. This justifies integrating between two constant x -values.

$$A_0 = \int_{-w/2}^{w/2} \sqrt{r^2 - x^2} - \sqrt{(r-t)^2 - x^2} dx = 2 \int_0^{w/2} \sqrt{r^2 - x^2} - \sqrt{(r-t)^2 - x^2} dx \quad (6.2)$$

Solving the integral, the area is given as

$$A_0 = \left[x \left(\sqrt{r^2 - x^2} - \sqrt{(r-t)^2 - x^2} \right) + r^2 \tan^{-1} \left(\frac{x}{\sqrt{r^2 - x^2}} \right) - (r-t)^2 \tan^{-1} \left(\frac{x}{\sqrt{(r-t)^2 - x^2}} \right) \right]_{x=0}^{x=w/2} \quad (6.3)$$

Here, r denotes the outer radius of the cylinder, t its thickness and w is the width of the specimen. The impact of curvature on the area is implemented in the x terms, as a flat cross-section would have the area

$$A_0 = \int_{-w/2}^{+w/2} \sqrt{r^2} - \sqrt{(r-t)^2} dx = \int_{-w/2}^{+w/2} t dx = wt \quad (6.4)$$

The width of each specimen were measured to be 7.90 mm, which corresponds to roughly 2 percent of the circumference of the cylinder, or 7-9 degrees. The area is therefore close to that of a rectangle with area wt , where w is the width and t is the thickness of the specimen (figure 22). However, the difference of roughly 0.2 percent is still large enough to have an impact on the stresses calculated, and the simplification is discarded.

In the laboratory, an electronic caliper was used to measure the geometry of each specimen (table 8). There was some difference in the thicknesses measured on each specimen, which may stem from differences between the individual specimens or an error in measurements, for example from chippers in the material from the Water EDM cut. The largest deviation in thickness is 0.03 mm, leading to 1.7 percent larger area for specimen 3-3 compared to 1-3 and 2-3. The thickness measured has a great deviation from the thicknesses found using ultrasonic thickness gauge (table 1), which is either a systematic measuring error form due to a change of measuring equipment or wrong measuring technique, or the cylinder that is thicker than those which table 2 is based upon. This thickness deviation causes the area of the thick-walled specimen to be at most 4.0 percent and the thin-walled to be 2.5 percent larger than if they were calculated from table 2. The measured thicknesses are assumed to be correct, and the data from table 8 is used henceforth.

Table 8 Measured geometry of the dog bone specimens

Specimen ID	1-1	2-1	3-1	1-2	2-2	3-2	1-3	2-3	3-3
w [mm]	7.90	7.90	7.90	7.90	7.90	7.90	7.90	7.90	7.90
t [mm]	4.80	4.82	4.82	4.81	4.81	4.81	1.81	1.81	1.84
r_o [mm]	50	50	50	50	50	50	63.5	63.5	63.5
A [mm ²]	37.96	38.12	38.12	38.04	38.04	38.04	14.31	14.31	14.55

The deformed area is calculated based on the now known initial area. Because the DIC in these series of tests are two-dimensional, only strains in two directions are known. These strains are in the longitudinal and circumferential directions. Three assumptions were made regarding the strains: Firstly, the strain within a cross-section was assumed to be constant, and could thus be averaged over all elements in the width of the specimen. The strains did vary within the cross-section, but the variations were either random or were caused by “strain bands”, to be discussed

later. Secondly, the radial strains, which were not observable by the camera, were assumed to be equal to the circumferential strain. This assumption is equivalent to assuming that the material is isotropic, as both these directions are unloaded before necking. Thirdly, the circumferential strains were assumed equal to the transversal strains, that is, the strains in along the circumference were assumed to describe the change of the width of the gauge. The strains in the cross-section was given as

$$\varepsilon_x = \varepsilon_y = \ln\left(\frac{w}{w_o}\right) \rightarrow w = w_o \exp(\varepsilon_y) \quad (6.5)$$

The width was calculated from these strains. The deformed area of the arc is given as the initial area times the exponent of the logarithmic strains in the two directions. This is easy to see for a rectangular cross-section:

$$A = wt = w_o \exp(\varepsilon_y) t_o \exp(\varepsilon_y) = A_o \exp(2\varepsilon_y) \quad (6.6)$$

While the initial area is calculated exactly (opposed to simplified as a rectangle), as shown in equation (6.3), the relationship with the deformed area is still the same, under the assumption of equal strains along the cross-sectional axes (6.6).

Note that the stress state after necking will be tri-axial with principal stresses not necessarily in the axial direction. As a simplification, the stress state can be assumed approximately uniaxial also after necking.

Because the logarithmic strains in the longitudinal direction is given directly from eCorr, the logarithmic plastic strain is given in equation (3.10). In an ideal case, all required data would now be available and fit to insert into the formulas. It is seen in the following section, however, that data from laboratory and in particular eCorr introduces several challenges.

6.3 Phase two: Data analysis and extraction

One problem using DIC is the inevitable numerical noise, giving small random variations in the measurements in every data point in every frame. This noise in part arises from the quality of the camera equipment, from any changes in lightning (e.g. if a car with powerful headlights drives by outside the laboratory), from the size and type of the mesh chosen and from the type of paint used to spray the specimen. This noise was assessed and treated to give the FEM software a smooth, continuous stress-strain relationship.

In order to improve the results and remove noise, the data is smoothed over different variables. The strain field of the constant-strain-quadrilaterals (Q4 elements) is discontinuous across

elements. These strain values are averaged to one constant value over all the elements considered. The noise within each time step is removed and the noise between time steps are greatly reduced (figure 27). In the longitudinal direction, strain oscillations are observed at 1-3 percent strain; these are treated later in this section. The assumption of constant strain is a necessity as formula (6.6) requires one unique value for the whole cross-section at any given time of the test. After this pre-processing, smoothing with respect to time is done in Matlab. Several smoothing techniques were assessed, such as first and second degree local regressions, but in the end the simpler “moving average method” yielded the best results. In the moving average method, an odd integer (a span) is selected and the data at any point is then chosen as the mean of the data points within that span, equally weighted. For example, if span 5 is chosen, any data point after the smoothing has one fifth of the sum of the values of the current, two previous and two subsequent data points. Because each test consisted of between 2500 and 3500 frames, a rather large span could be chosen without the loss of key material characteristics. Nevertheless, smoothing data without assessing which parameters will alter the results can lead to erroneous conclusions.

Choice of mesh in the DIC software altered the results and the amount of noise. If the mesh in the DIC program was refined, the lack of pixels gave rise to numerical noise. It was also possible for some nodes to get distorted extensively out of their position, ruining the results for the rest of the analysis (figure 30). On the other hand, if the mesh was made coarser, data could get lost in the low-order constant-strain elements. In the mesh shown in figure 29 the maximum strain at the last frame before fracture was 0.15, down from 0.60 in finer meshes. Any localization, such as necking, will be underestimated if the width of the localization is smaller than the width of the element. During the data treatment phase, several different meshes were tested. Both fine and coarse meshes were tested out, these were either localized at necking or covering the whole specimen. At some point using one longitudinal and one transversal vector to extract strains were attempted without success. A mesh with 20x20 pixel elements was chosen, although 10x10 and 40x40 pixel elements were explored and compared. Initially it was stressed that one column of elements was placed where the neck would form, as seen in figure 25. All data was then taken from this column alone.

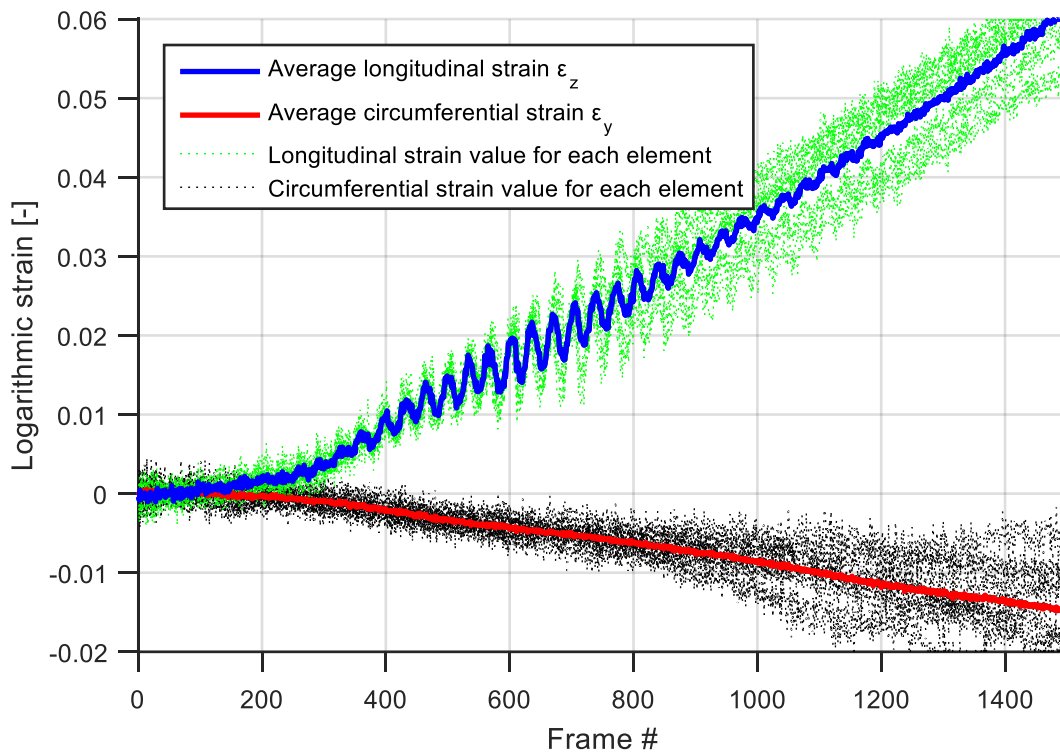


Figure 27 Strain averaging over 10 elements

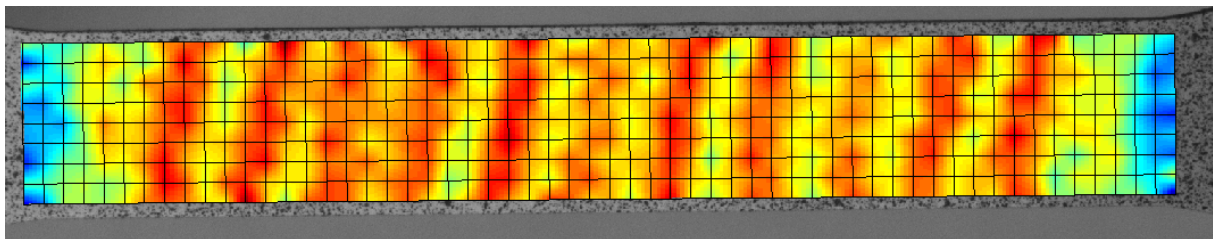


Figure 28 Typical strain bands at 1-2 % strain

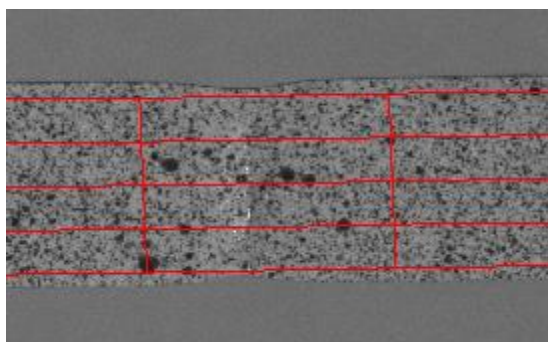


Figure 29 Very rough mesh

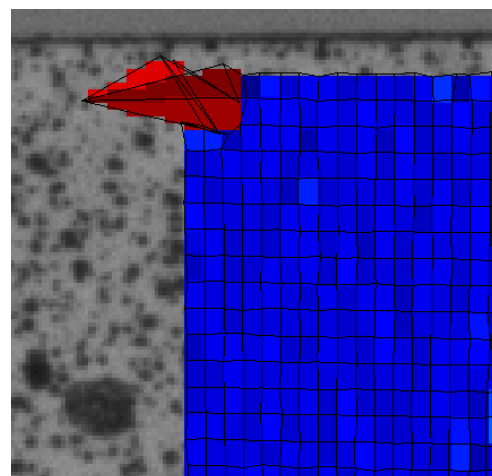


Figure 30 Very fine mesh

For many specimens, “strain bands” formed and dominated the test at low plastic strains (figure 28). These strains have similar characteristics as the Portevin-Le Chatelier effect, which gives serrations at high strain rates according to Chihab et al. [26]. However, as the strain rates are low, these strain bands stem from another effect. According to an informal report by Petter Henning Holmstrøm [27], these oscillations of longitudinal strain, named strain bands, can disturb the data around 1-2 percent strain. The source of this effect, which resemble aliasing, is not documented. One possibility is that there is a loss of data in the tiny void between the pixels in the camera sensor matrix. Only 60 percent of the lens used were covered with light-sensitive nodes, which usually is not a problem, but in this case could give rise to some aliasing. It is likely that the speckled paint as well as the ratio between deformation speed and logging frequency can give rise to further aliasing. The software and choice of elements or mesh might also be the reason why this phenomenon occurs, and some findings supported the latter claim: If the mesh was refined, the strain bands would take longer to die out, although the initial point of strain bands, their amplitude and period remained unchanged (figure 31). Rougher mesh also shortened the number of oscillation periods.

The strain bands had to be assessed, and three options were proposed: Change software or element type, use a wider mesh smoothing data over the whole specimen gauge, or just smooth the effect of the strain bands away. Regardless, some smoothing of the data was necessary, which favoured the latter approach. For each of the 9 tests, the period of the strain oscillations was recorded and used as span for the smoothing. The spans were of magnitude 15-65 frames, corresponding to 4-15 seconds, but this was deemed unproblematic due to the large amount of data. The smoothness of the results seemed satisfactory. Figure 32 shows that span 33 was adequate for this specimen, removing the impact of the strain bands. However the results using an entirely different set of elements (placed outside the neck) yielded a different set of strains in the first three stages of the test, as did the columns with finer or rougher meshes (figure 33). Choosing a column of elements placed in the middle of the neck is the only way to analyse the strains in the in the last stage of the tension test. Nevertheless, if the results in the first stages are dependent upon which column of elements is chosen then this is an unacceptable source of errors. Instead of exploring the source of the deviation of results, the strains from the last stage of the test were discarded and focus was shifted towards a broader approach. The reason for this rather significant discarding of data is that the thesis focuses on pre-buckling behaviour, hence the plastic strains of interest are unlikely to reach the strains observed at necking.

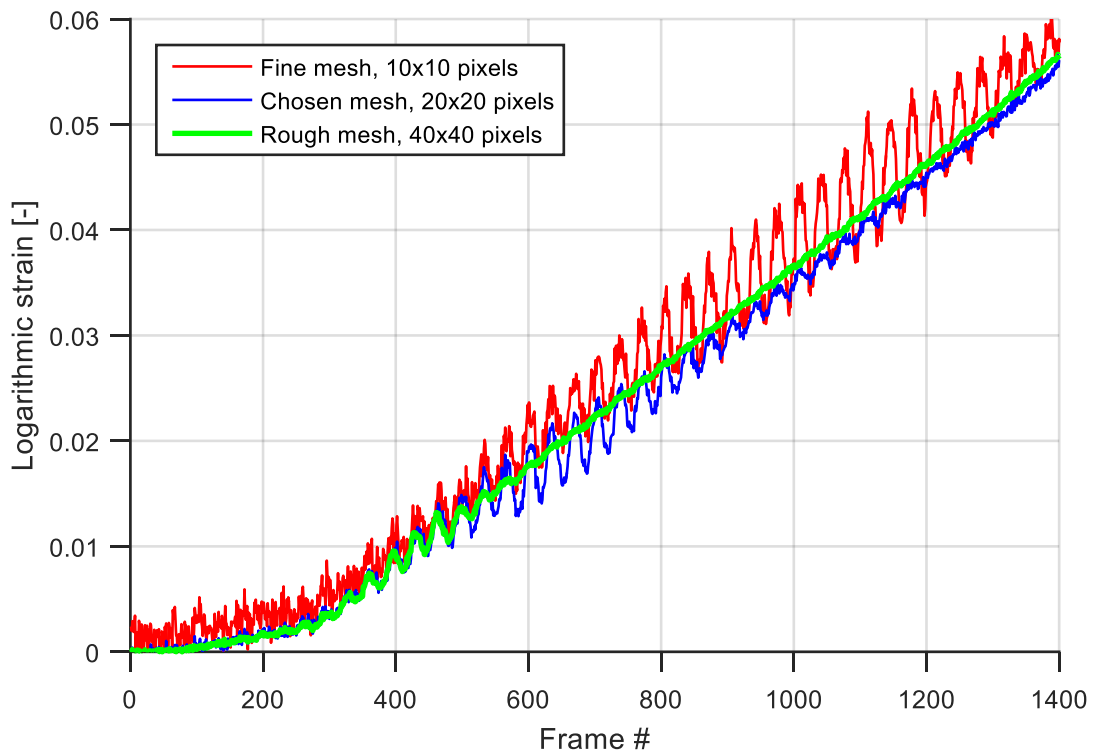


Figure 31 Dependency of element size.

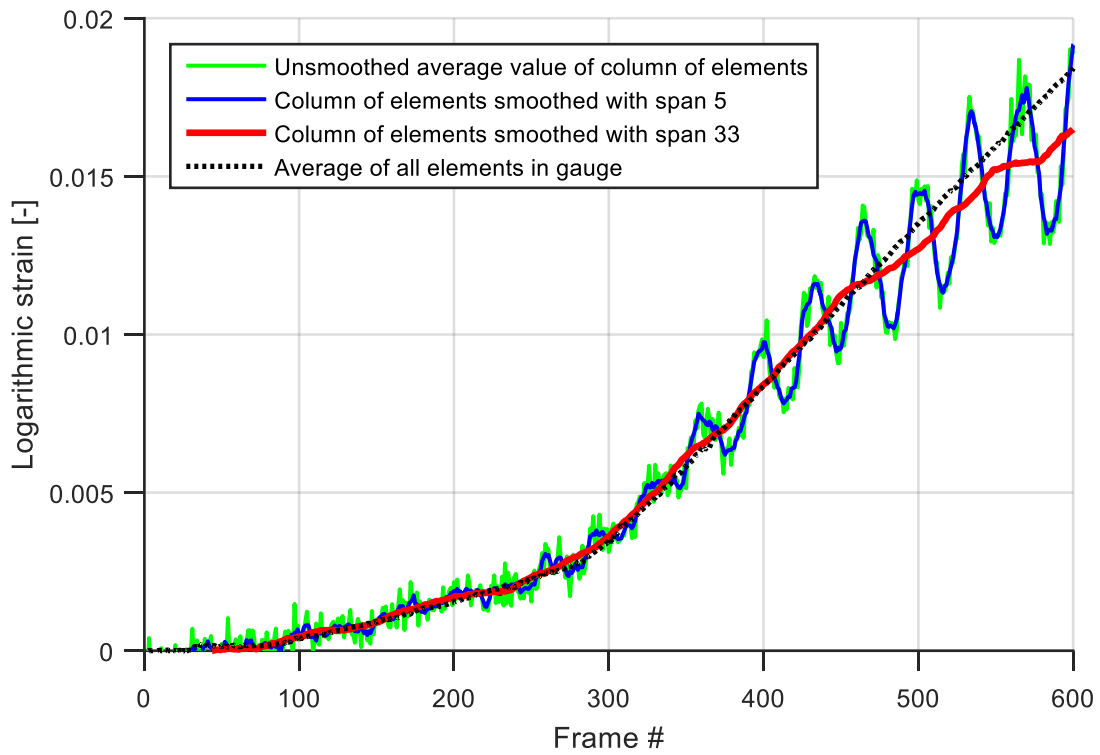


Figure 32 Smoothing of the average ϵ_z for a column of elements in the neck.

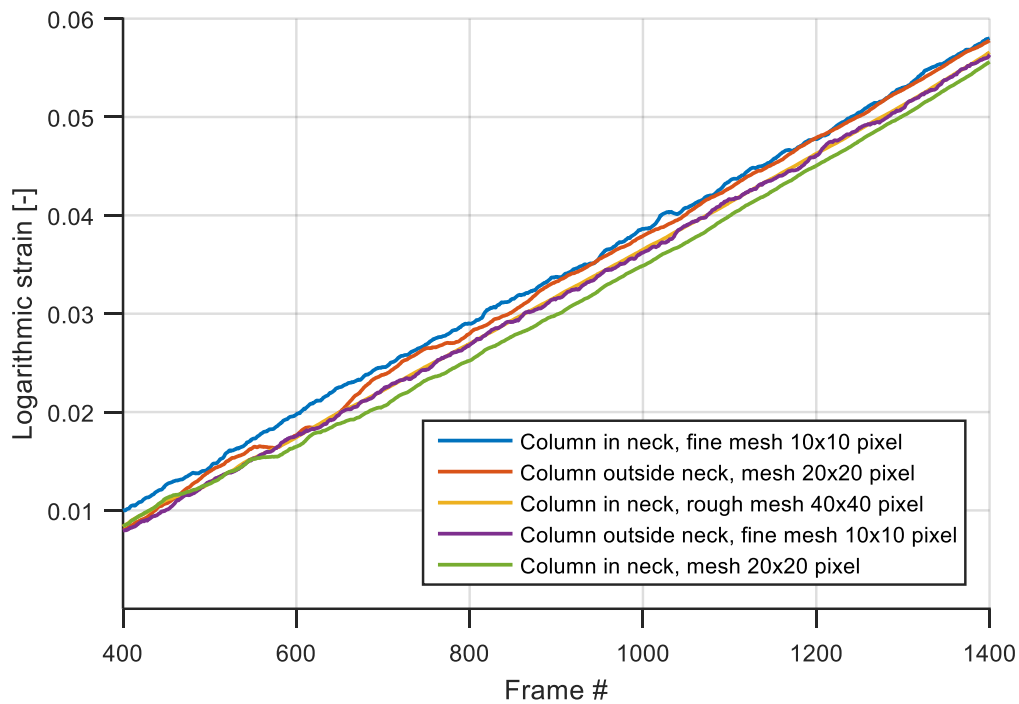


Figure 33 Smoothed columns of elements with different mesh and placement

Henceforth, the mesh was chosen to cover the whole gauge, although the outer-most elements (close to the attachment points of the machine) were often discarded due to noise from the edges. All data up to the point of maximum axial force was considered. Because the data was extracted from several hundred elements, the noise was greatly decreased. The strain bands were also nullified because both the apex and the nadir were included in the mean. The resulting curve was a smooth curve giving more trustworthy results than the former approaches (figure 32).

2D DIC has some weaknesses. As mentioned in section 6.2 it is incapable of measuring the strains in the radial direction as this direction is parallel to the camera, nor can a single camera register displacement u in the thickness direction. This inability to model strains overcome with the assumption made in the previous section; setting the radial strain equal to the circumferential strain. However, when there *is* displacement normal to the paper plane, a new source of error occurs. If for example the specimen is moved away from the camera, each element will look smaller (as it is further away), and the DIC software will treat this as compressive strains in both directions. In the start of each test, before the loading was applied, the specimen was free to move along to the attachment pins of the machine, towards or away from the cameras. This initial rigid body motion gave quite erroneous results, which in the worst cases could result in a strain error of up to 0.002 and compressive strains occurred at as much as 70 percent of

maximum tensile force (figure 34). As the applied force increased, the test specimen was in greater extent held in place, unable to move rigidly. This is also seen in the stress-strain diagrams, as the slope is close to that of the elastic solution when the load is large enough.

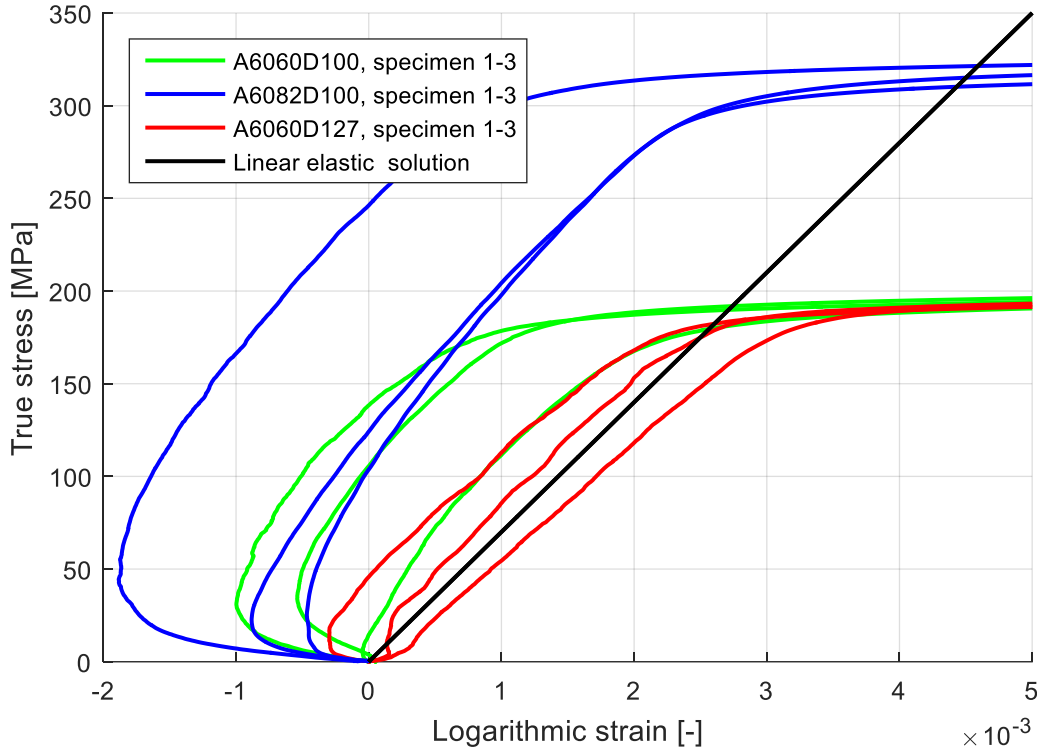


Figure 34 Compressive strains at tensile loading.

To get a good estimate of yield stress and stress-strain relationship at small plastic strains it is crucial to represent the elastic strains correctly. If the strain error in figure 34 did not occur, a natural yield criterion is defining yield as the first point where $\varepsilon > \frac{\sigma}{E}$. This cannot be used when all registered strains are wrong. A new yield criterion is proposed: Yield occurs at the *last point* 'n' where

$$E_{T,n} \approx \frac{\sigma_{n+1} - \sigma_{n-1}}{\varepsilon_{n+1} - \varepsilon_{n-1}} > 30GPa \quad (6.7)$$

Noise is magnified when the stress is differentiated as done in equation (6.7). Because of this, a down-sampling was required. A strain tensor with 800 elements is created, ranging from 0 to the maximum tensile strain value. Only tensile strains were evaluated. The stresses were interpolated to this strain vector, and for all n between 2 and 799, the tangent modulus was calculated from (6.7). The stress value corresponding to the last E_T value above 30 GPa is taken as the yield stress. The value 30 GPa was chosen because lower values would estimate yield

stress far into the plastic regime while higher values for E_T risked unclear definition of the yield stress as the tangent modulus had several local maxima and could pass the value several times (figure 35).

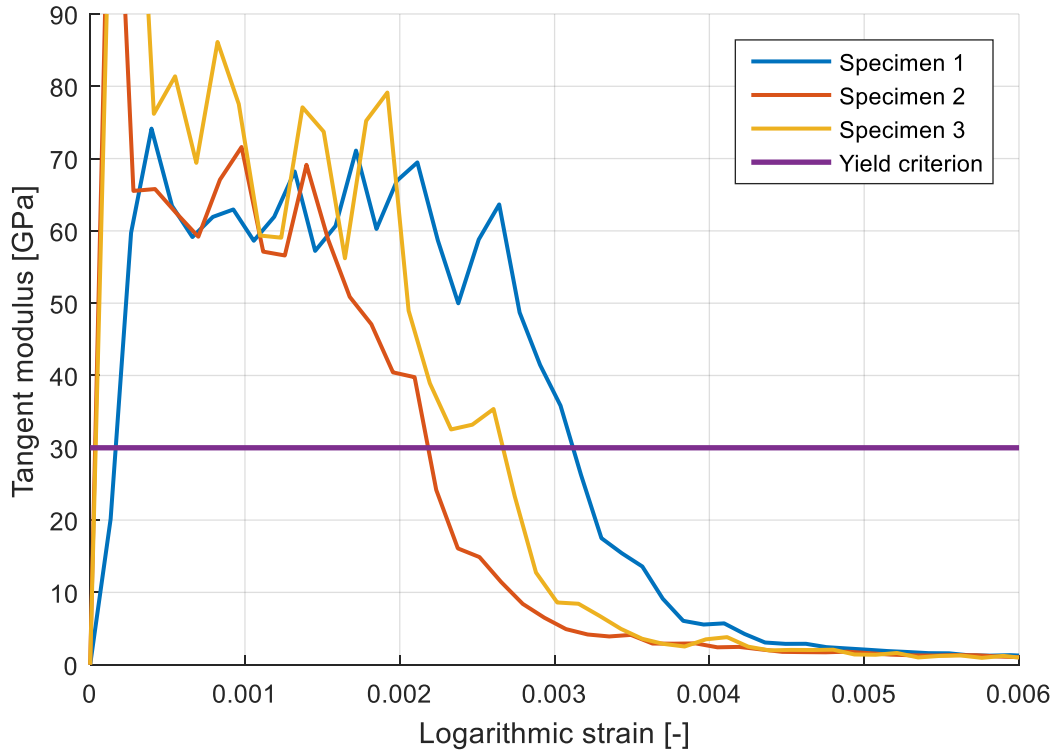


Figure 35 Tangent modulus as yield criterion - A6060D127

This down-sampling was only applied to find the yield stress. In the original (non-down-sampled) stress vector, the element closest to this stress is located. The original strain data was then shifted so that the strain at yield was exactly equal to the yield stress divided by Young's modulus, $E = 70 \text{ GPa}$ (figure 36). With this shifting of the strain values, more detailed sources of errors with less impact on the results were ready to be studied.

Camera orientation is one such source of error. It might be difficult to orient the camera so the edges of the specimen are exactly horizontal. This could be a problem, as the logarithmic strains taken from eCorr were coordinate strains, aligned to the horizontal and vertical edges of the pictures. If the camera was slightly rotated with respect to the specimen, the perceived camera axes \hat{y} and \hat{z} might not have coincided with the longitudinal and circumferential

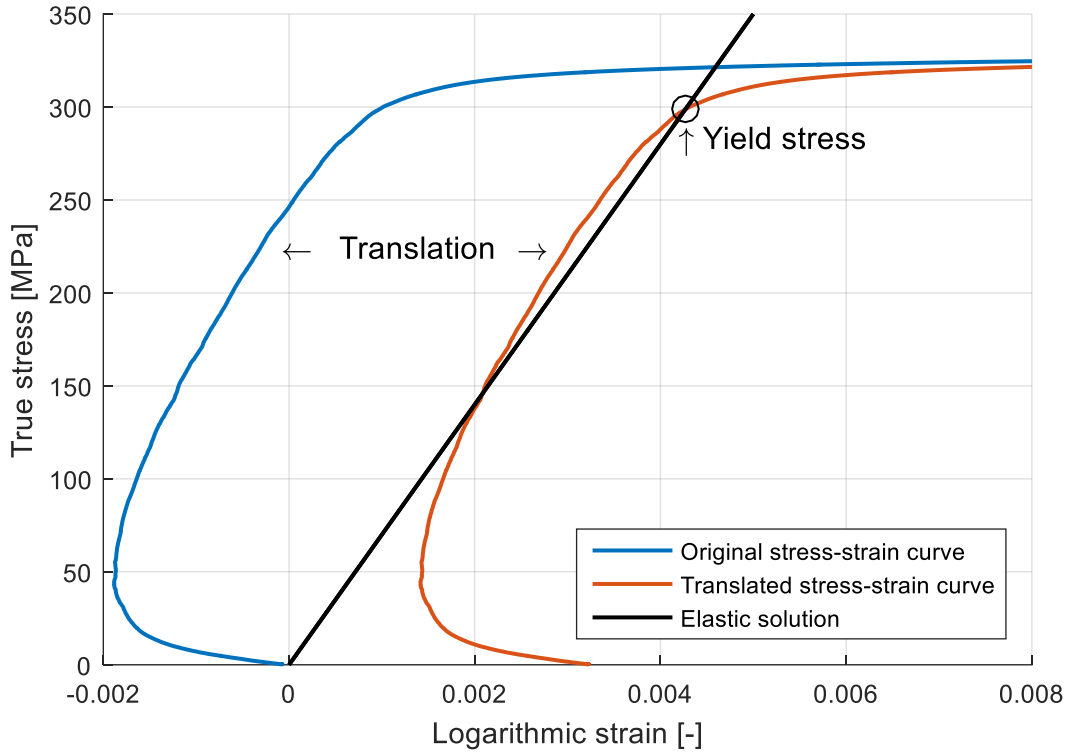


Figure 36 Translation of the stress-strain curve - A6082T6D100 specimen 1

directions y and z . Unless the camera is perfectly aligned, the shear strains $\hat{\epsilon}_{yz}$ (not to be confused with the engineering shear strains $\hat{\gamma}_{yz}$) would not be zero:

$$\hat{\epsilon}_{yz} = \frac{1}{2} \left(\frac{\delta \hat{v}}{\delta \hat{z}} + \frac{\delta \hat{w}}{\delta \hat{y}} \right) \neq 0$$

This implicates that $\hat{\epsilon}_z \neq \epsilon_1$. If the shear strains are large, the difference between $\hat{\epsilon}_z$ and the desired ϵ_z might be significant. eCorr allows extracting principal strains directly for each element, which in theory would be equal to ϵ_z up to necking. Due to noise this might not always be the case. Calculating the mean of the values of the first principal strains would mean possibly adding together values of vectors with different orientation. This is because each element in the DIC mesh might have a slight difference in principal strain orientation, thus adding them would give invalid results, albeit the error could be small.

Another approach must be found in order to establish ϵ_y and ϵ_z . One mathematically correct way to solve this problem would be to solve the system of equations

$$\det \left(\begin{bmatrix} \hat{\epsilon}_y & \hat{\epsilon}_{yz} \\ \hat{\epsilon}_{yz} & \hat{\epsilon}_z \end{bmatrix} - \begin{bmatrix} \epsilon_1 & 0 \\ 0 & \epsilon_2 \end{bmatrix} \right) = 0 \quad (6.8)$$

This system was solved for the unknown principal strains, and the rotation of the principal strains with respect to the camera coordinate system is then given as

$$\varphi = \tan^{-1} \left(\frac{\varepsilon_1 - \hat{\varepsilon}_z}{\hat{\varepsilon}_{yz}} \right) \quad (6.9)$$

The shear strains in the specimens were not zero (figure 37), however the rotation of the specimen stabilized towards a rotation of less than one degree (figure 38). The relative difference between ε_1 and $\hat{\varepsilon}_z$ is of magnitude 0 - 0.05 percent (figure 39). For these figures, initial values display noise because the low values of $\hat{\varepsilon}_z$ increases the sensitivity of changes in $\hat{\varepsilon}_{yz}$. The difference between ε_1 and $\hat{\varepsilon}_z$ in figure 39 is neglected, $\hat{\varepsilon}_z$ and $\hat{\varepsilon}_y$ is treated as equal to ε_z and ε_y , which are equal to ε_1 and ε_2 .

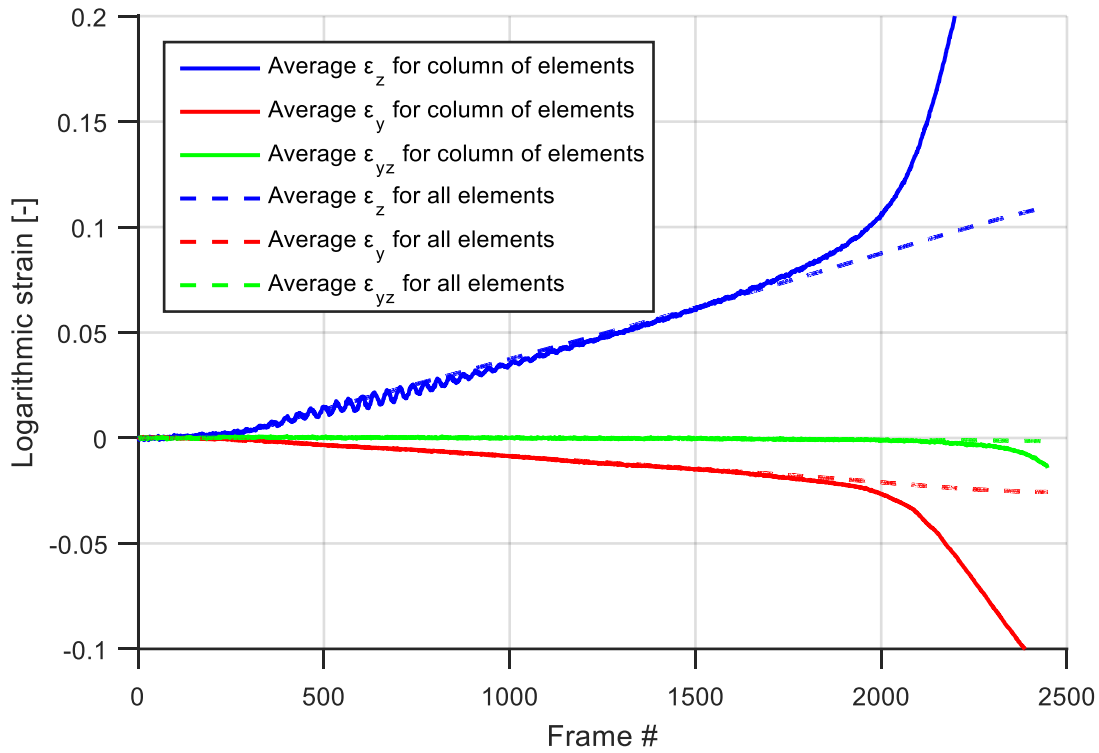


Figure 37 True strain in different directions for 20x20 pixel mesh.

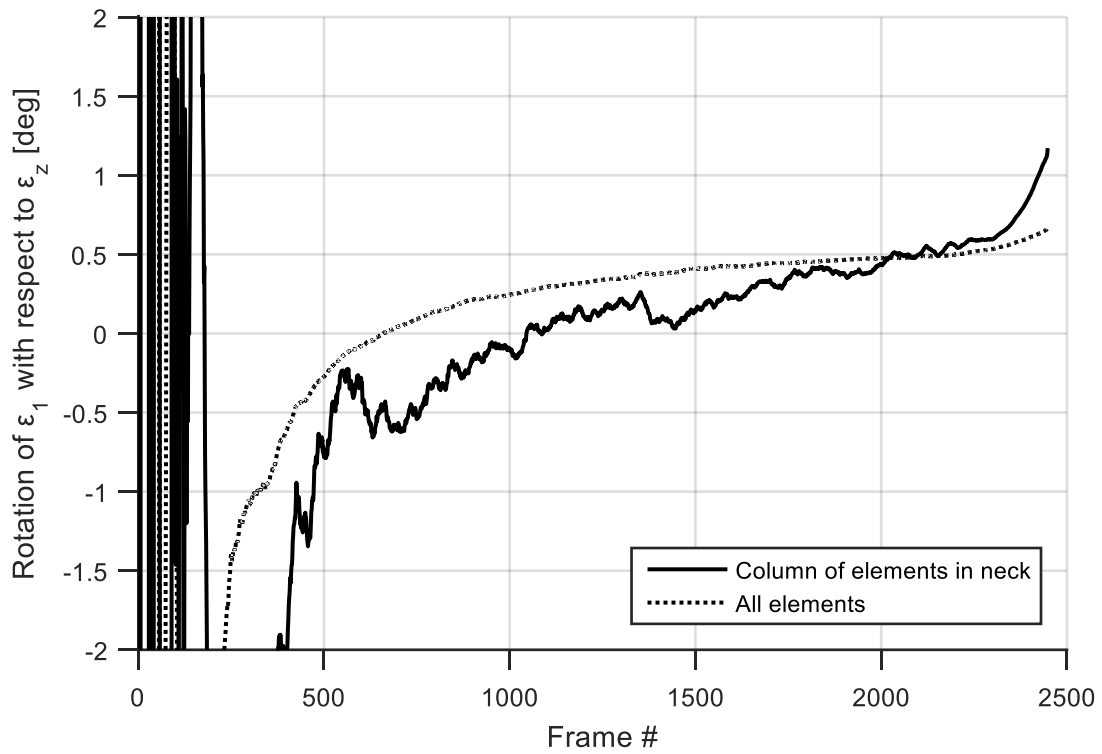


Figure 38 Rotation of principal strains, smoothed with span 33

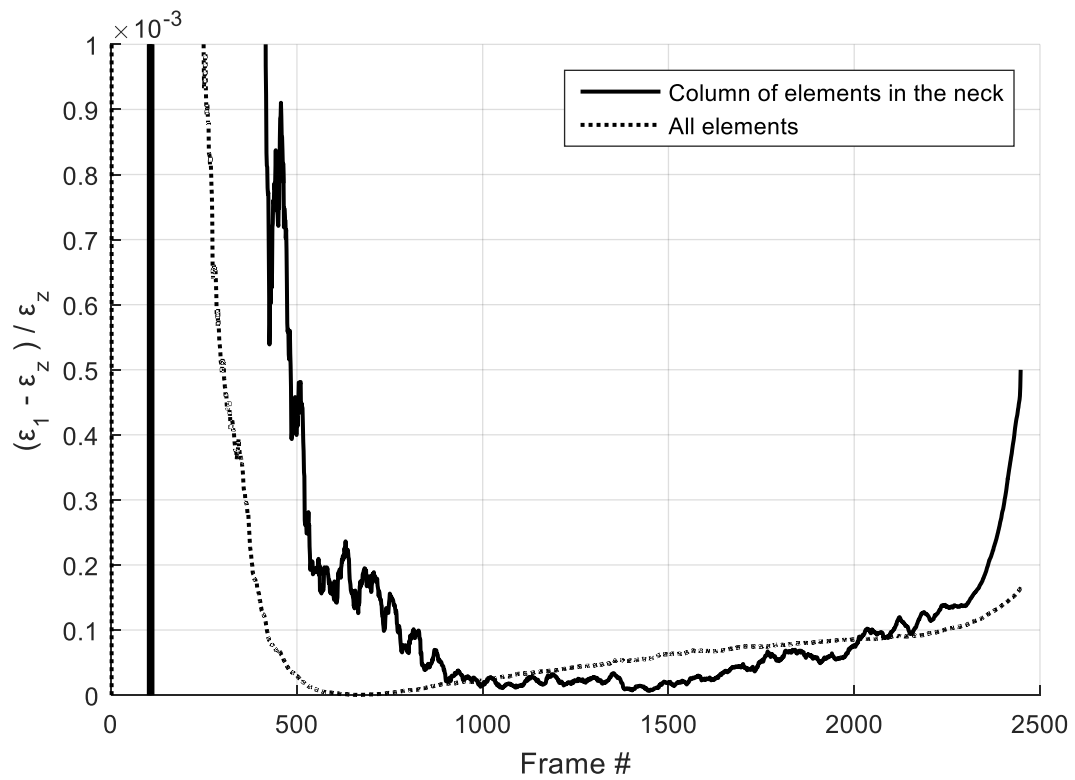


Figure 39 Difference between principal and perceived (camera) longitudinal strain

6.4 Phase three: Generation and FEM verification of stress-strain relationship

In the previous sections in this chapter, all figures and graphs (except figure 34, figure 35 and figure 36) are based on the same specimen of the type A6060D127. The other eight specimen displayed the same effects to the same or lesser extent. With the treatment of data described, each specimen was analysed with a 20x20 pixel mesh covering the whole gauge of the specimen. The data up to the point of maximum load was used to define the Voce hardening law parameters σ_0 , Q_i and C_i seen in formula (3.28). This process is described below.

In Matlab, a data set containing different chosen plastic strain values (henceforth labelled “strain vector”) was created on the form

$$\varepsilon_i^{pl} = \left(\frac{i}{500} \right)^{2.5} \quad (6.10)$$

This strain vector was chosen for its focus on low plastic strain values, with 31 data points below 0.1 percent plastic strain and 79 data points below 1 percent plastic strain. The high non-linearity of the strain vector plays a key role in correctly interpolating material behaviour at low plastic strain values, and is crucial for modelling buckling behaviour in later analyses.

The true stress of each specimen is interpolated to this strain vector using the Matlab-function “Interp1”. Each series consists of three specimens, and the mean of the three corresponding stress vectors could now be calculated as they corresponded to the same plastic strain vector.

A Voce material law with $n = 2$ is assumed, meaning that there are five unknown parameters:

$$\sigma(\varepsilon^{pl}) = \sigma_0 + \sum_{i=1}^2 Q_i (1 - \exp(-C_i \varepsilon^{pl})) \quad (6.11)$$

The Matlab function “lsqnonlin” gives an estimate for the parameters by minimizing the function

$$\left| \sigma_0 + \sum_{i=1}^2 Q_i (1 - \exp(-C_i \varepsilon^{pl})) - \bar{\sigma} \right| \quad (6.12)$$

In this equation, $\bar{\sigma}$ is the mean stress of the three specimen in a series of tests and ε^{pl} is the stress vector defined in (6.10). The minimization process requires initial parameters as a first estimate, and these are chosen so that $C_1 > C_2$. This way, the element in equation (6.11) corresponding to $i = 1$ will describe the hardening at low plastic strains.

After the true stress – logarithmic strain-curve was established, an Abaqus model was created which included the curvature. The model was simplified in the areas outside where the tension force was applied because modelling this part would not improve the model significantly and

might give rise to numerical problems (figure 40). In light of the experience from chapter 5 it was decided to rather enforce a displacement to the end surfaces of the model shown in figure 40. The shape of the dog bone specimen averts stress localization, and the failure stems from the uniform stress distribution in the slender gauge of the specimen. This justifies not putting manual and computational effort in accurately modelling the outermost parts of the specimen. The mesh was a regular cubic brick mesh in the gauge and a rougher, more non-continuous mesh near the ends (figure 41). Each end of the modelled dog bone was pulled with a constant speed of 0.05 mm/s in the longitudinal direction. This is the same loading speed as in the laboratory, to ensure a quasi-static state. The explicit dynamic solution algorithm was chosen for its robustness and simplicity. On a small-scale model the accuracy obtained using explicit algorithm is often very good compared to implicit solution algorithms. Because the whole model had a very low weight, large mass scaling (section 4.3) could be chosen without getting undesirable oscillations in the results. The mass scaling applied increased the mass by a factor of roughly 10^6 , which only led to minor oscillations after yielding, at low plastic strains.

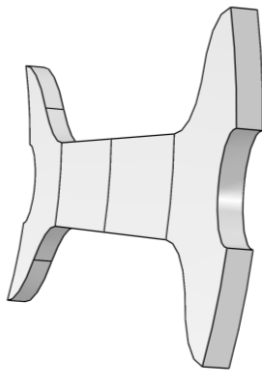


Figure 40 Model with curve A6060D127

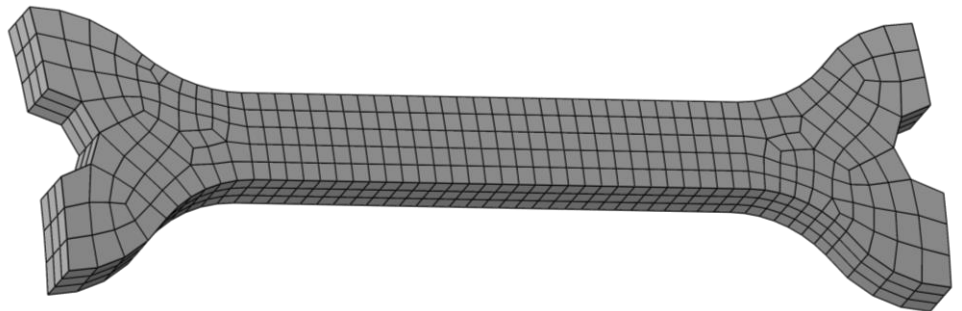


Figure 41 Mesh for A6060D100.

In order to compare the FEM analyses to the laboratory tests, the mean longitudinal engineering strain of the gauge was measured. In Abaqus, this was done by logging the displacement of the end point of the gauge, divided by the gauge length, 45mm (figure 19). In eCorr, a strain gage is created by defining the start and end point of a vector on roughly the same spot as the data points in the Abaqus model. For the thick-walled specimen, the machine in part covered the area where the gauge started, and the vector in eCorr had to cover a smaller part of the gauge. The strains would then be approximately the same, but would return larger values after necking because the DIC strain gage stretch is divided by a smaller length than the Abaqus measurements. This is taken into account when the engineering stress-engineering strain curves are compared.

The Voce parameters calculated by Matlab and used as input for Abaqus did not give satisfactory results (figure 42). The engineering stress-engineering strain curves were too different, with an increasing deviation for higher plastic strains, and all materials displayed wrong capacity and ductility.

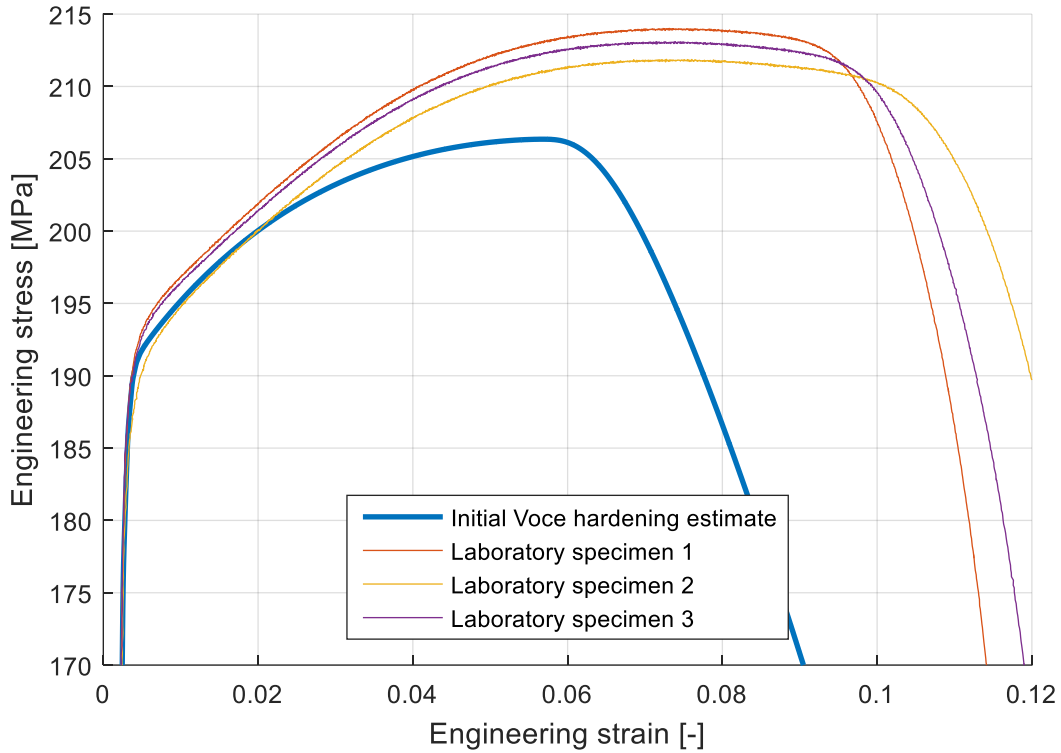


Figure 42 Initial parameters for Voce hardening - A6060D127.

A decision was made to manually add two more voce parameters, up to a total of 7. It is emphasized that the shape of the stress-strain curve of the material is crucial in modelling buckling, as seen in the formula for inelastic buckling stress (3.54). The focus of this comparison and correction of curves was therefore the shape of the curve from the FEM software. This curve is largely defined by its slope, defined in formulas (3.29) and (3.19). The plastic strain vector defined in (6.10) minimized the error of the parameters for low values of plastic strain. Yielding and initial hardening was decently modelled (figure 42). The new Voce term added would therefore focus on the hardening at high plastic strains. To ensure this, the parameter C_3 was chosen to be lower than C_1 and C_2 . The laboratory specimen reached maximum load at strain $\hat{\epsilon}$, and the difference in maximum engineering stress is denoted Δs . The parameter Q_3 was then initially estimated as

$$Q_3 = (1 - \exp(-C_3 \hat{\epsilon}))^{-1} \Delta s \quad (6.13)$$

With this second estimate for material law established, a vast series of iterations commenced to so the FEM analyses would give a satisfying shape of the stress-strain relationship. These iterations were carried out using simplified parameter analysis. As an example of the iterations carried out, consider the following case: It is desired to elevate the stress from Abaqus by a value Δs_1 at strain level e_1 , while keeping the stress constant at a strain e_2 . To solve this problem, the voce parameters in (3.28) are altered the following way:

$$\begin{aligned} \Delta Q_2(1 - \exp(-C_2 e_1)) + \Delta Q_3(1 - \exp(-C_3 e_1)) &= \Delta s_1 \\ \Delta Q_2(1 - \exp(-C_2 e_2)) + \Delta Q_3(1 - \exp(-C_3 e_2)) &= 0 \end{aligned} \tag{6.14}$$

The values ΔQ_i (typically one negative and one positive value) were then added to Q_i in formula (3.28), often resulting in a more precise behaviour in a new analysis.

With such iterations as well as parameter studies to study the behaviour of the parameters C_i (figure 43) the Abaqus analyses converged towards a satisfactory solution, presented in table 9 and figure 44. Negative values of parameters were avoided, resulting in only 5 parameters for the A6060D127-material. The A6060D100-material exhibited more hardening than its thin-walled counterpart, although low-hardening stresses were approximately equal. Higher stresses for thicker cross-sections are in good agreement with Eurocode 9 [2].

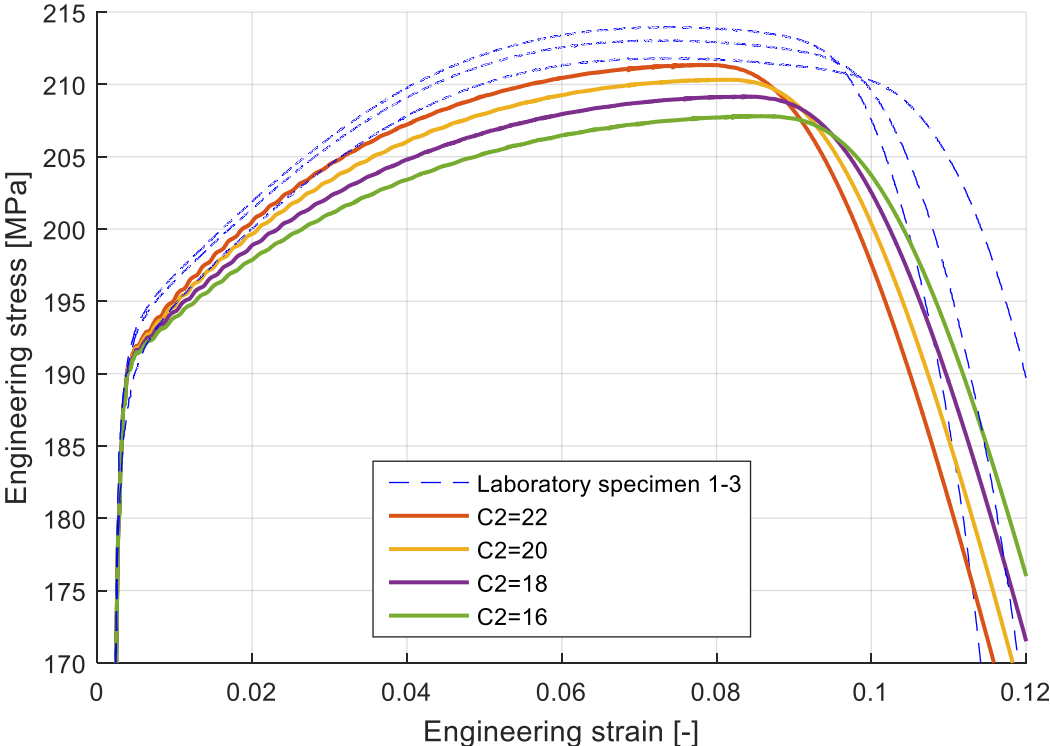


Figure 43 Effect of altering the value of C_2 – A6060D127

Note that the stress will reach $\sigma_0 + Q_1$ even at rather low plastic strains. These terms could be added together as a higher yield stress, removing the parameters Q_1 and C_1 , however since low plastic strain is of particular interest of this thesis, this simplification is avoided.

As a simplified sensitivity analysis, both rougher and finer meshes were modelled, as well as different degrees of mass scaling. The differences both in capacity, force-displacement curve and failure mode were close to identical (figure 45).

The characteristic stress f_o is defined as the stress obtained at 0.2 percent plastic engineering strain, and plays a crucial role in calculations according to Eurocode 9, as explained in section 3.5. This proof stress is given indirectly with the Voce parameters presented (table 9) as well as formulas (3.4) and (3.6), and its values are shown in table 10. Engineering stress-strain curves from the FEM software using the chosen Voce parameters is plotted together with the laboratory specimen results in figure 47, figure 49 and figure 51.

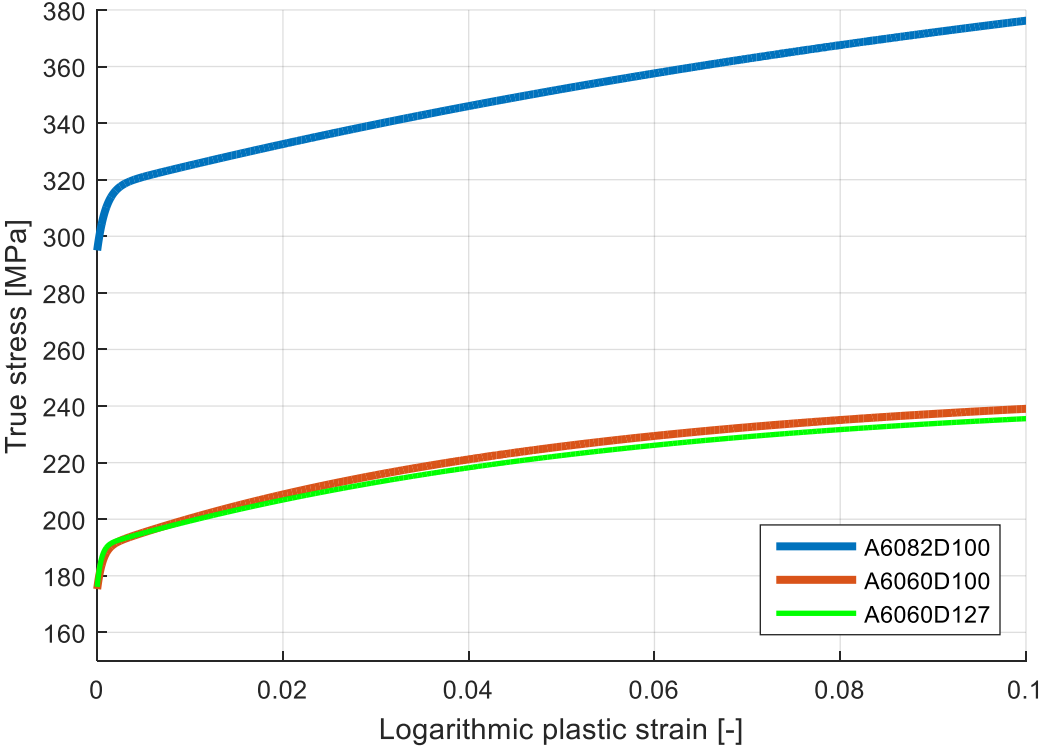


Figure 44 Voce hardening rule for the three material types

Table 9 Voce parameters for the materials.

	σ_0	Q_1	C_1	Q_2	C_2	Q_3	C_3
A6060D100	175.3	14.48	1677.6	47.678	23	35	2
A6060D127	176.09	14.378	2326.2	54	18	0	0
A6082D100	295	22	1080	33	10	85	6

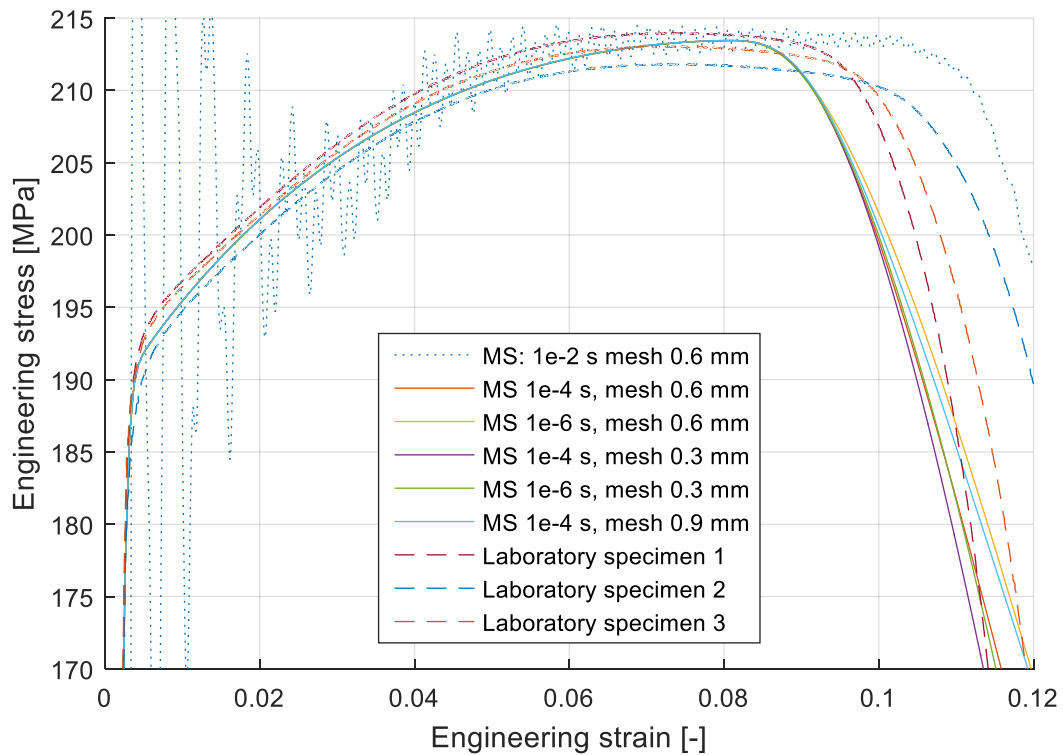


Figure 45 Sensitivity of mesh size and MS

Table 10 Characteristic stress f_0

	f_0
A6060D100	192 MPa
A6060D127	192 MPa
A6082D100	315 MPa

6.5 Verification through force-displacement correlation

Up to this point, the displacements recorded by the testing machine have not been used because of machine compliance: The machine is not indefinitely stiff, and the recorded displacements will therefore be greater than the elongation of the specimen. In order to investigate this effect, the deformation is split in two: the elongation of the gauge and the deformation from the machine and the end parts of the specimen combined (figure 46). During the elastic loading stage, the extension of the gauge of the specimen is estimated as

$$w_1 = \frac{FL_0}{A_0E} \quad (6.15)$$

The machine deformation is then defined as

$$w_2 = w - w_1 = w - \frac{FL_0}{A_0E} \quad (6.16)$$

A one-dimensional tensor with displacement values was created. The displacement w_2 of each specimen was interpolated to this displacement vector and the mean was calculated. The function $w_2(F)$ was then estimated as one linear term and one term with the same shape as the elements in Voce hardening law:

$$w_2 = Q(1 - \exp(-CF)) + \frac{1}{k}F \quad (6.17)$$

The voce term is included to describe the noise in the initial part of the test, and the spring constant k is the elastic deformation of the machine and the end parts of the specimens. w_2 includes the wider part of each specimen. The spring constant k would consequently differ from series to series, as the thickness and material varied. The thin-walled cross-section would therefore estimate a softer spring stiffness, as seen in table 11. The force-displacement curves based on w_1 are shown in figure 48, figure 50 and figure 52 with the expected difference in post-necking strain values. The results are deemed satisfactory.

Table 11 Spring stiffnesses to account for machine compliance

	<i>k from (6.17)</i>
A6060D100	10794 N/mm
A6060D127	6348 N/mm
A6082D100	12831 N/mm

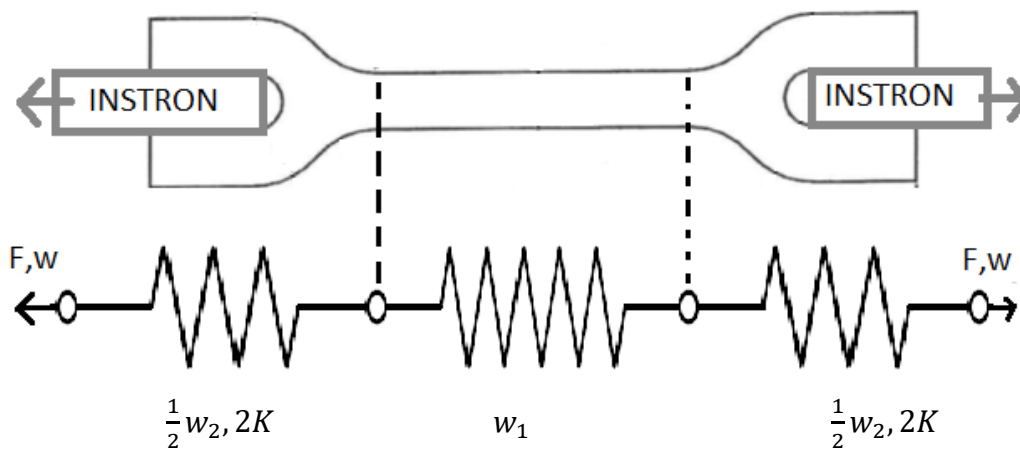


Figure 46 Mechanical model including machine compliance

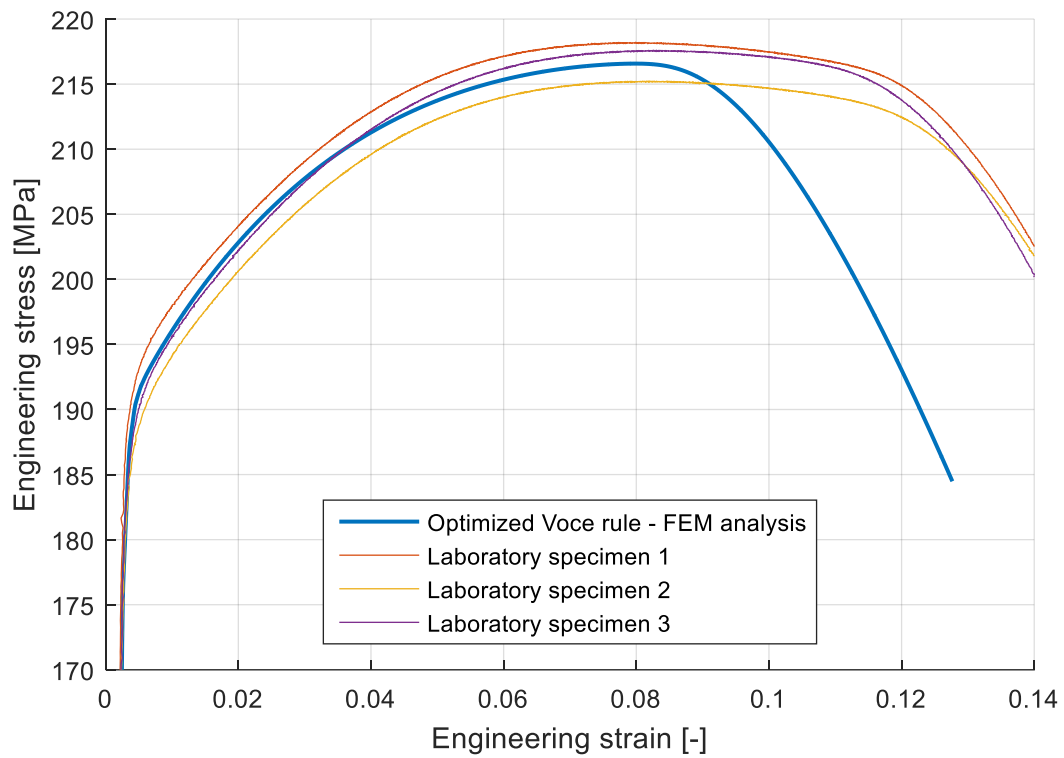


Figure 47 Chosen Voce hardening and laboratory results - A6060D100

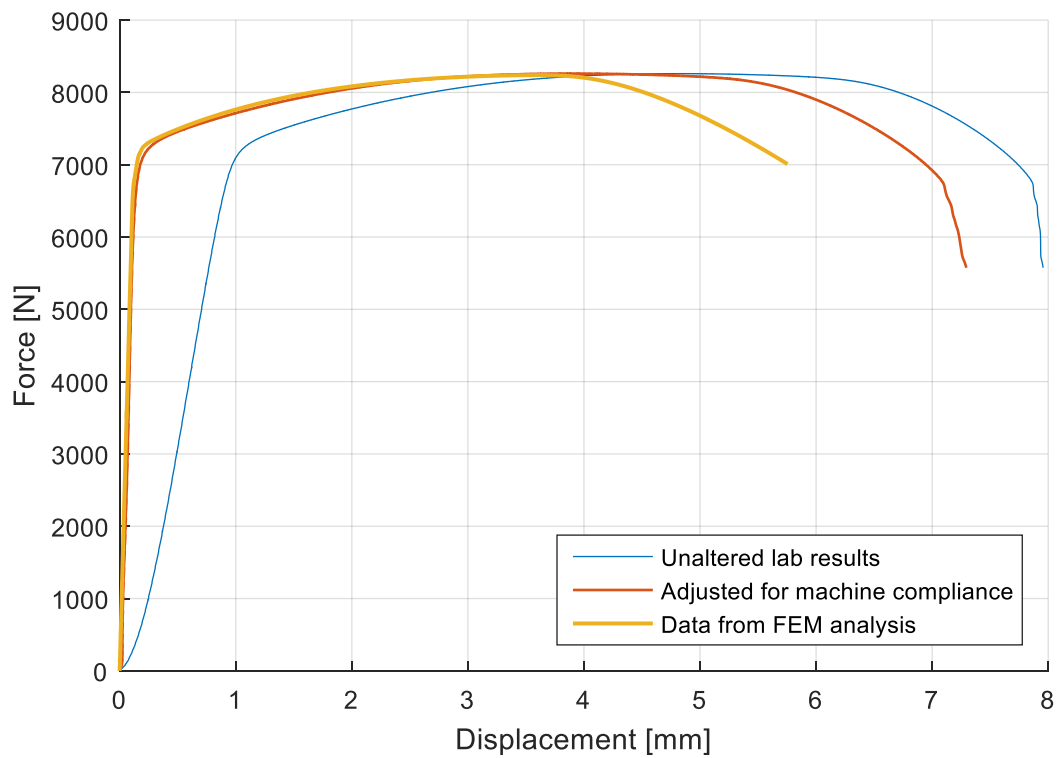


Figure 48 Force-displacement comparison - A6060D100

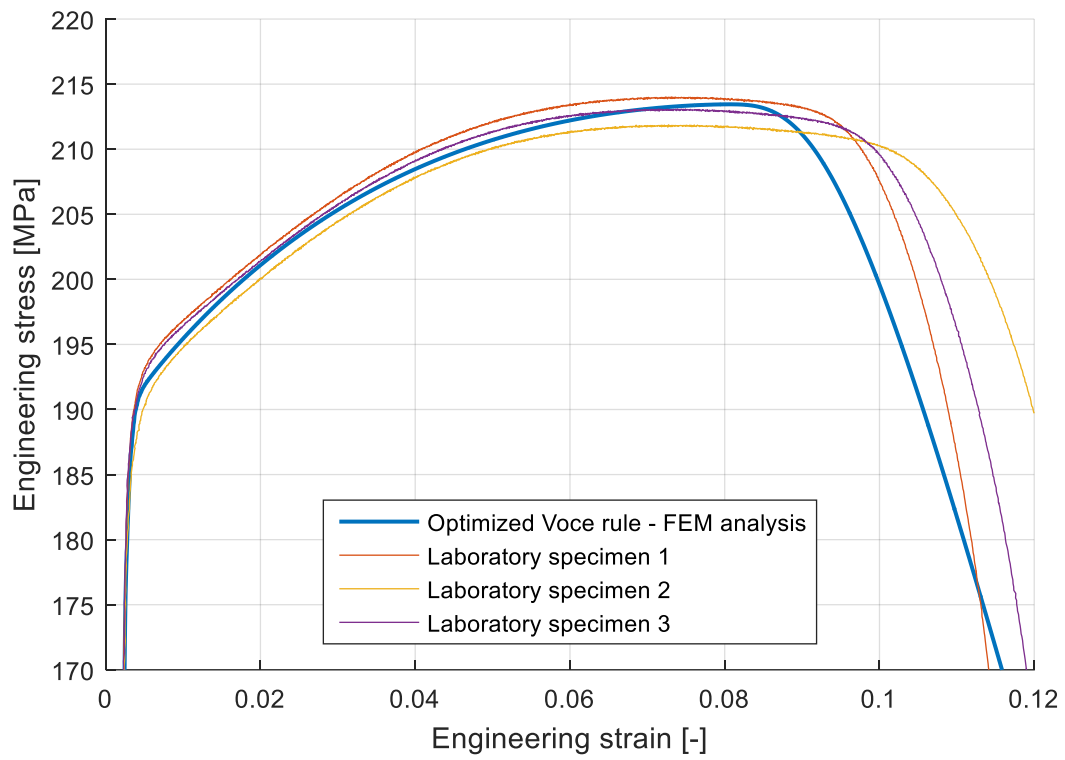


Figure 49 Chosen Voce hardening and laboratory results - A6060D127

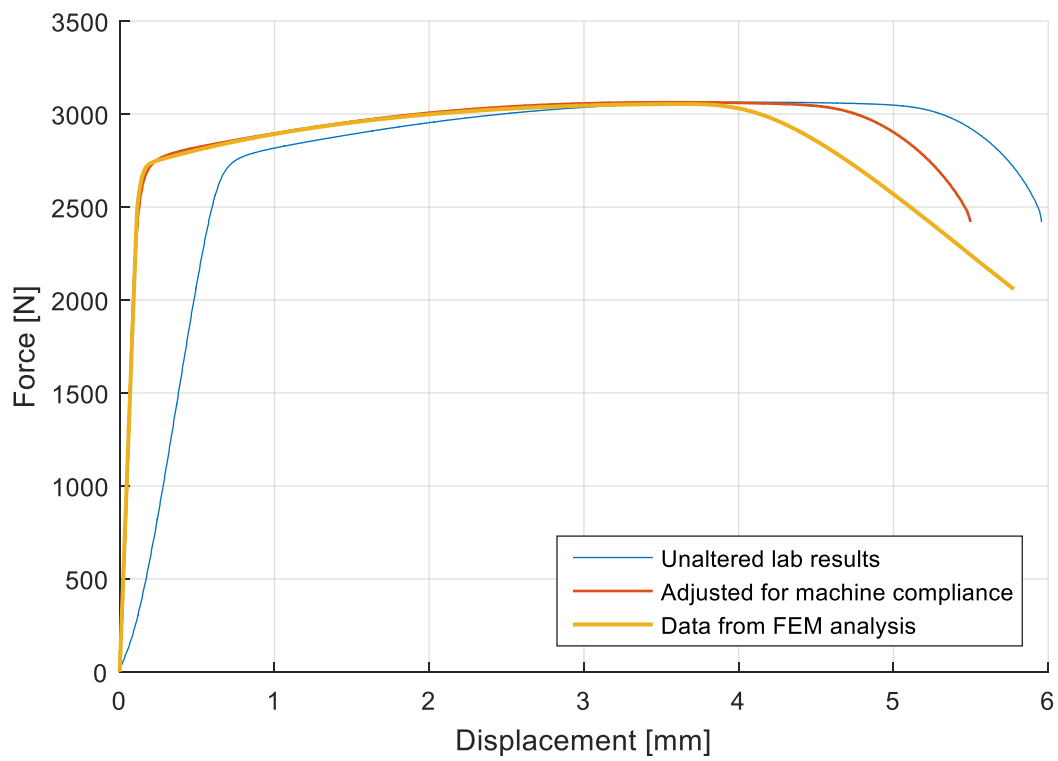


Figure 50 Force-displacement comparison - A6060D127

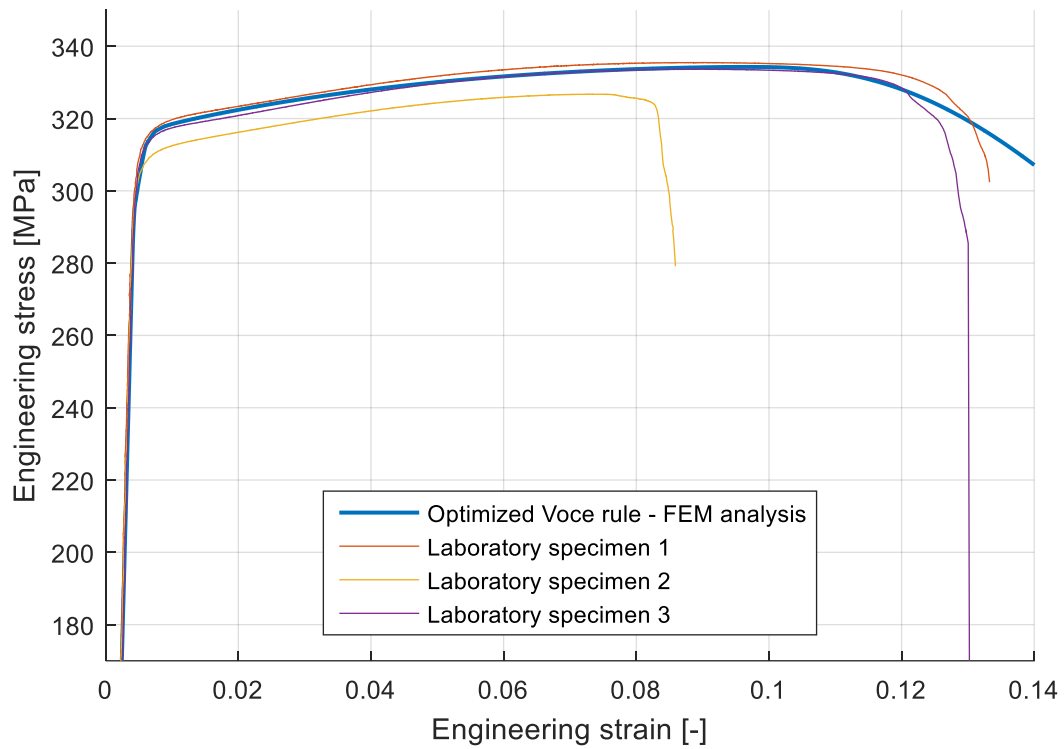


Figure 51 Chosen Voce hardening and laboratory results - A6082D100

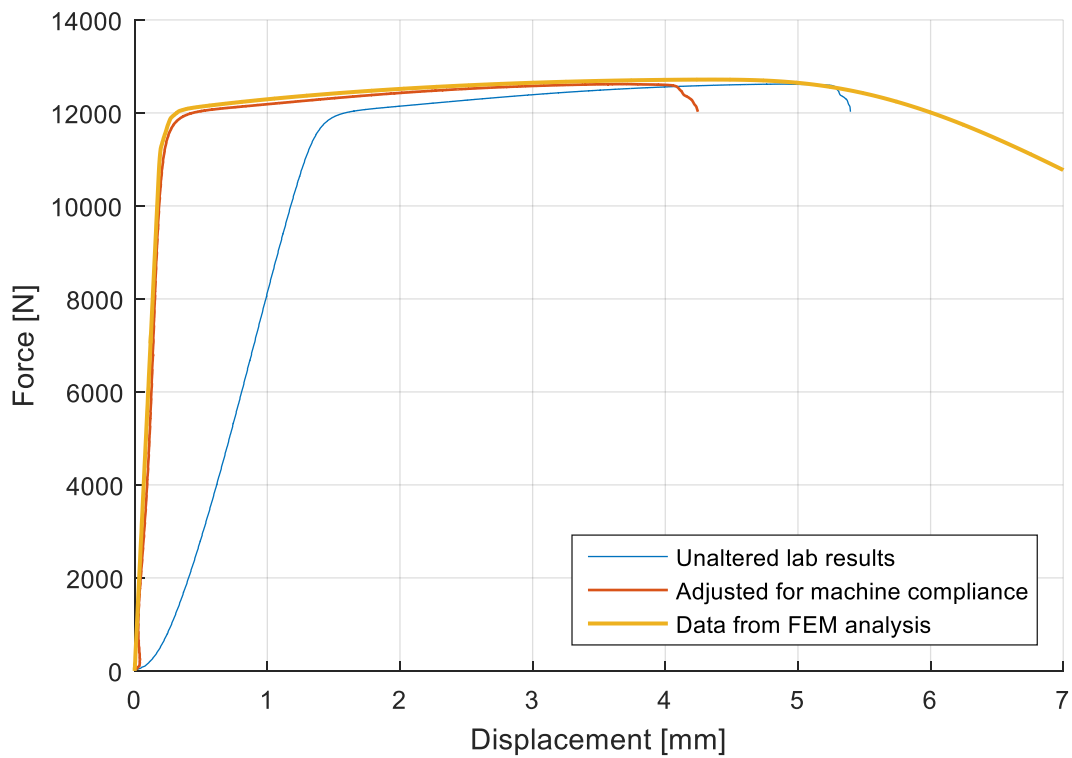


Figure 52 Force-displacement comparison - A6082D100

7 Hollow Cylindrical Columns in Compression

The behaviour of hollow cylindrical columns in axial compression are assessed in this chapter. The objective is to use results from compression tests executed in laboratory to determine the accuracy of theoretical estimates and numerical simulations at three different lengths. The main focus is the ability of the calculation method to correctly represent the axial capacity, buckling shape and force – displacement (stress – strain) relationship obtained for compression tests.

Compression tests are executed for profile A6060D100, A6060D127 and A6082D100 for lengths of 2 and 4 times the diameter and 2000 *mm* (noted L2D, L4D and L2000).

Obtained results for L2D and L4D are used to establish a robust FEM model at these lengths, which is extrapolated to lengths of 30 times the diameter. Numerous FEM analyses establish a representation of the transition from the plateau of local buckling (defined in section 3.6) to global buckling. The result of the compression test for L2000 is used to validate these extrapolated models.

The accuracy of the capacity and failure mode according to theoretical estimates and Eurocode 9 is assessed in comparison to the compression test results at L2D, L4D and L2000.

Finally, data from all sources are compared and discussed for lengths up to 30 times the diameter.

7.1 Compression test for L2D and L4D

The main objective for the first laboratory tests is to verify the behaviour of local buckling. Based on calculations from section 3.6 is anticipated that L2D and L4D buckles locally. The only exception is A6082D100L4D, which according to Jones is long enough for global buckling to affect the capacity, as $L_G = 320 < 400 \text{ mm}$ (table 6).

According to Eurocode 9, A6060D127 and A6082D100 have a slight decline in capacity as the length is increased from L2D to L4D, because $L < L_{Cx}$ (table 6). Theoretical derivations disagree on this claim for the 6060T6 alloy. Preliminary analyses in the FEM model displayed negligible decline in capacity as the length was increased from L2D to L4D, regardless of material and cross-section.

7.1.1 Laboratory setup and geometry

The column compression tests on L2D and L4D were carried out the 30th of March 2016 in the Structural Impact Laboratory (SIMLab), at NTNU. Six series of compression tests were

conducted (table 12), and three specimens were tested in each series. The 3x6 specimens are named and numbered in the tables of Appendix E. A hydraulic Dartec compression test machine with capacity of 500 kN is used. The force is applied by displacement of the upper plate seen in figure 53. In order to track the relative displacement an Opto NCDT 1700 (2 - 50 mm) laser is used. The laser is placed on a non-movable surface near the bottom plate, while an additional steel plate is mounted on to the upper moveable plate (shown to the right in figure 53). As in chapter 6, all profiles are sprayed with speckled paint (figure 54), and in order to use 3D IDC two cameras of type Nikon AF Nikkor 35-70mm are utilized.

Table 12 Material and length of column specimen

	L2D [mm]	L4D [mm]
A6060D100	200	400
A6060D127	254	508
A6082D100	200	400

The cameras, laser and compression machine were calibrated. This calibration gave one data point for each set of pictures, with data logging frequency given in table e2. The calibration allowed changing the load velocity or data frequency between and during tests without losing the correlation. The loading velocity was never change during testing, but varied between 0.1 and 0.5 $\frac{mm}{s}$ for different lengths (table e2). A low engineering strain rate was chosen to ensure quasi-static loading. In the post-buckling phase, the data frequency was reduced from 5 to 1 frames per second to decrease the amount of output data and pictures inn a less important part of the test. A mistake done in the laboratory resulted in one test with a constant frequency of 1 frame per second (ID 2-6, table e2). Plots for this test therefore contains fewer data points and give a less smooth curve than the rest. The maximum load is however rather close to the specimens in the same test series (A6060D127L2D, figure 58).

The output data from the laboratory setup is time, force, displacement and laser displacement, as well as two sets of pictures to enable DIC. It is desirable to compare laboratory testing results with FEM analysis results. In order to do this, the displacement form the laser is used, as the displacements logged by the Dartec is erroneous due to machine compliance. The force and laser displacement are extracted as text documents, logging all data with 9 significant digits.

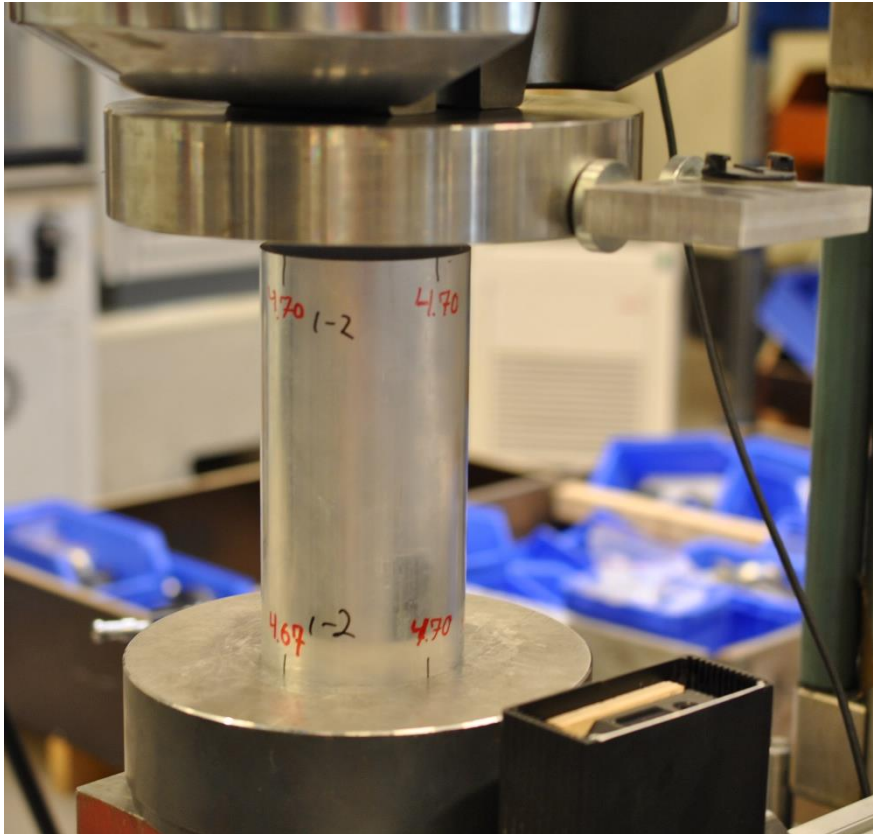


Figure 53 Setup in the laboratory before testing, with laser and mounted steel plate to the right



Figure 54 Setup in laboratory during testing with visible speckled paint

The geometry was measured prior to the execution of the tests. Length and outer diameter were gauged by an electronic caliper, while the thickness was measured by an ultrasonic thickness gauge named PosiTector. The thickness and outer diameter was measured every 90 degrees on the cross-section in both ends of the profile, as shown in figure e1 and all corresponding measurements are displayed in table e1.

The mean values (table 13) of all the thickness measurements (table e1) display little deviation from the values calculated chosen in table 2. The covariance calculated according to formulas (3.57) to (3.59), is lower than for the first measurements (table 1), despite a relatively low amount of measurements. This is believed to come from improved measuring technique, due to difficulties using the gauge on circular cross-sections, as mentioned in section 3.4.

The diameter was measured at the same locations as the thickness (table e1). Each of the three combinations of cross-section and alloy had 24 diameter measurements, a significant increase in the amount of data from the previous measurements (section 3.4). The mean diameter was similar, the value of the covariance was lower, in part because of the large amount of data (table 13).

Table 13 Measured thickness for laboratory tests on L2D and L4D

	A6060D100	A6060D127	A6082D100
\bar{t} [mm]	4.703	1.764	4.680
s_t [mm]	0.045	0.028	0.045
CoV_t	0.965 %	1.577 %	0.970 %
\bar{D} [mm]	99.94	99.91	126.96
s_D [mm]	0.055	0.121	0.325
CoV_D	0.055 %	0.121 %	0.256 %

In calculations of the data from the compression test, the mean of the measurements for each specimen is used rather than the generalized geometry of table 2. Consequently, each specimen within a series of tests might have a slight difference in area (figure e3). The lengths of the cylinders deviated less than 0.1 percent (figure e2). This deviation is neglected and its intended length (table 12) is applied in all calculations.

7.1.2 Compression test results

Laboratory settings for each specimen with corresponding measurements and calculations are given in Appendix E. Table 14 contains a brief summary of mean values for each test series.

The results are presented in two types of graphs: force – displacement (figure 55, figure 58 and figure 61) and engineering stress – engineering strain (figure 56, figure 59 and figure 62).

eCorr is used with its 3D DIC calibration to estimate the transverse movement of points on the cylinders. DIC images for one representative specimen from each test series at maximum load is shown in figure 57, figure 60 and figure 63. The final deformed shape (figure e5 to figure e10) and transversal movement (figure e2 to figure e4) for all specimens (except ID 2-4) is shown in Appendix E.

Table 14 Results from compression tests for L2D and L4D profiles

	$\bar{\epsilon}$	\bar{D}_o	\bar{A}	\bar{N}_{max}	CoV_N	\bar{S}_{max}
Profile	[mm]	[mm]	[mm ²]	[kN]	[%]	[MPa]
A6060D100L2D	4.70	99.9	1407.12	311.41	0.67	221.16
A6060D100L4D	4.70	99.9	1407.12	311.48	0.56	221.55
A6060D127L2D	1.76	127.0	693.81	138.15	0.31	199.98
A6060D127L4D	1.76	127.0	693.81	138.23	0.40	198.32
A6082D100L2D	4.68	99.9	1400.13	505.58	0.57	360.74
A6082D100L4D	4.68	99.9	1400.13	499.34	1.13	357.01

7.1.2.1 A6060D100

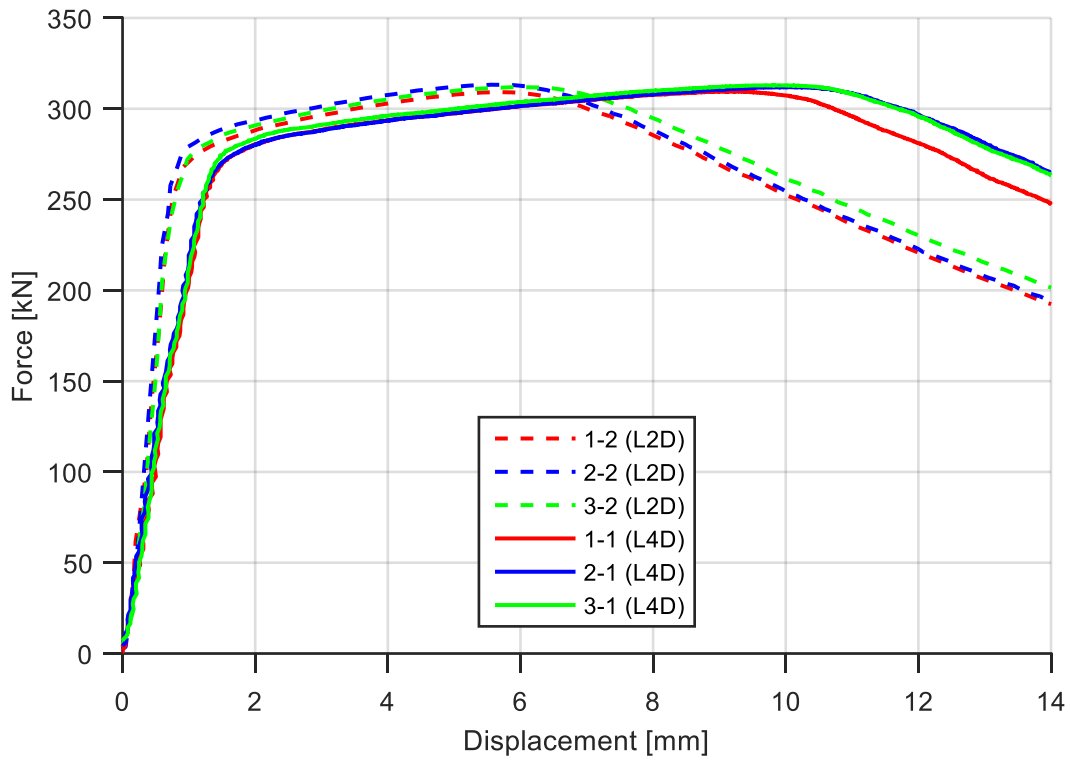


Figure 55 Force – displacement curves from compression tests of profile A6060D100L2D and A6060D100L4D

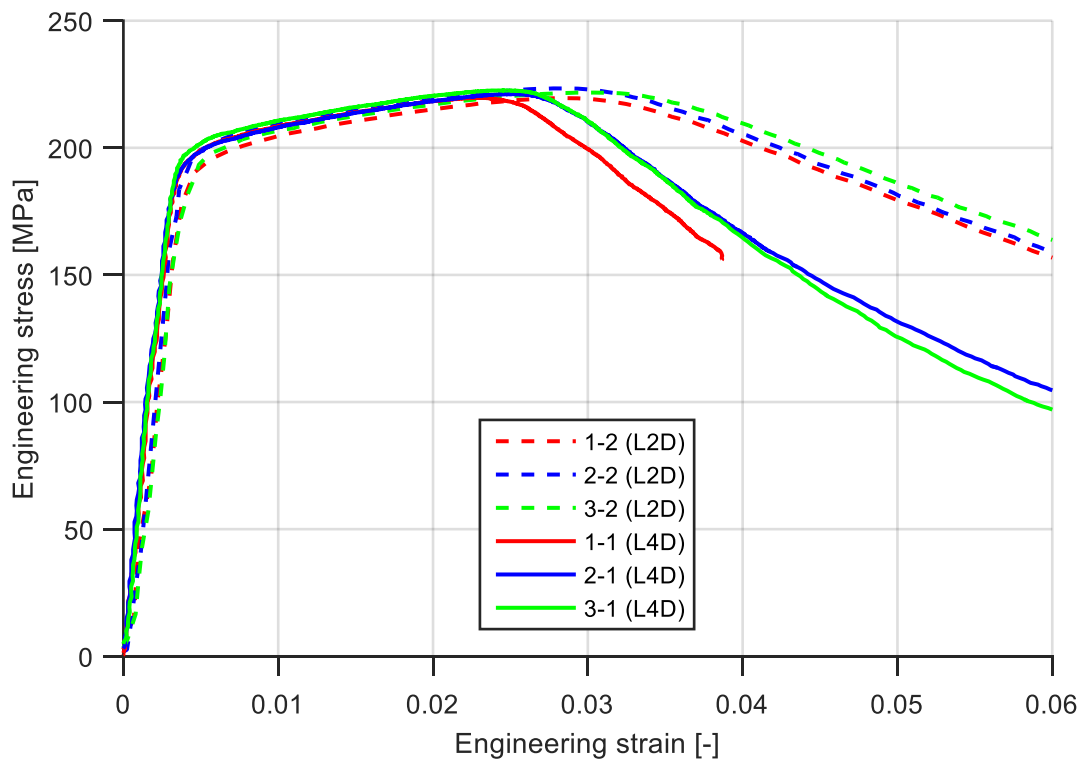
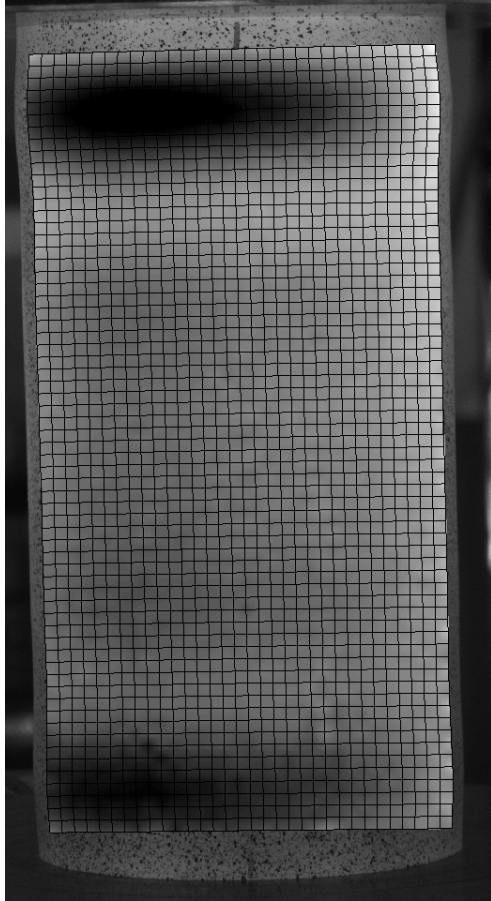
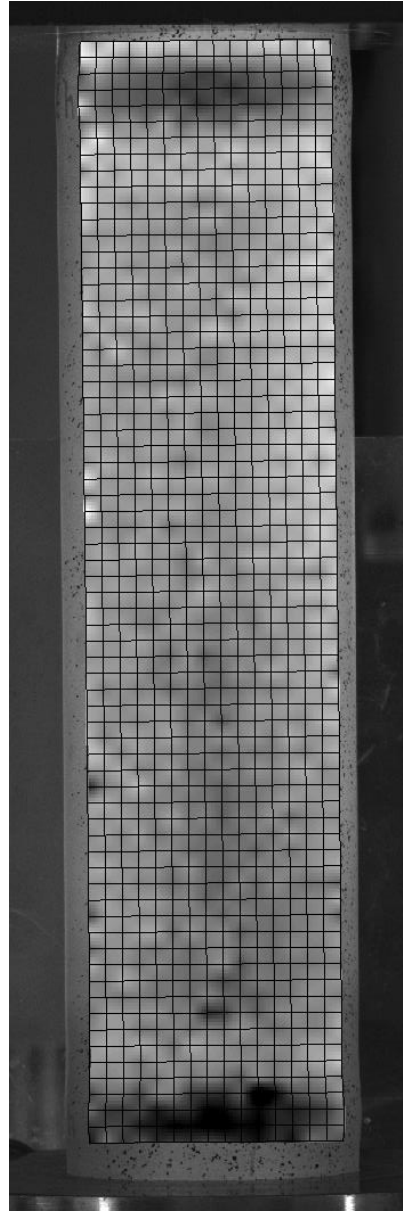


Figure 56 Stress – strain curves from compression tests of profile A6060D100L2D and A6060D100L4D



(a)



(b)



(c)

Figure 57 Deformation in transverse direction (towards camera) at maximum load. Pictures generated in eCorr, (a) A6060D100L2D (b) A6060D100L4D (c) scale [mm]

7.1.2.2 A6060D127

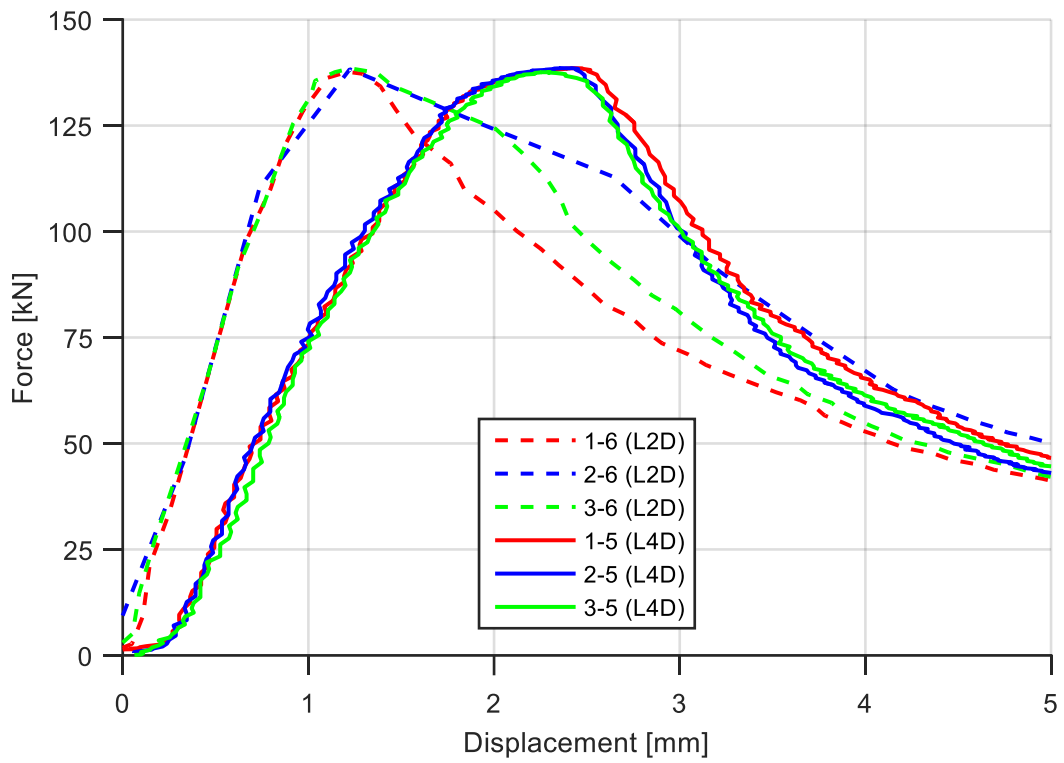


Figure 58 Force – displacement curves from compression tests of profile A6060D127L2D and A6060D127L4D

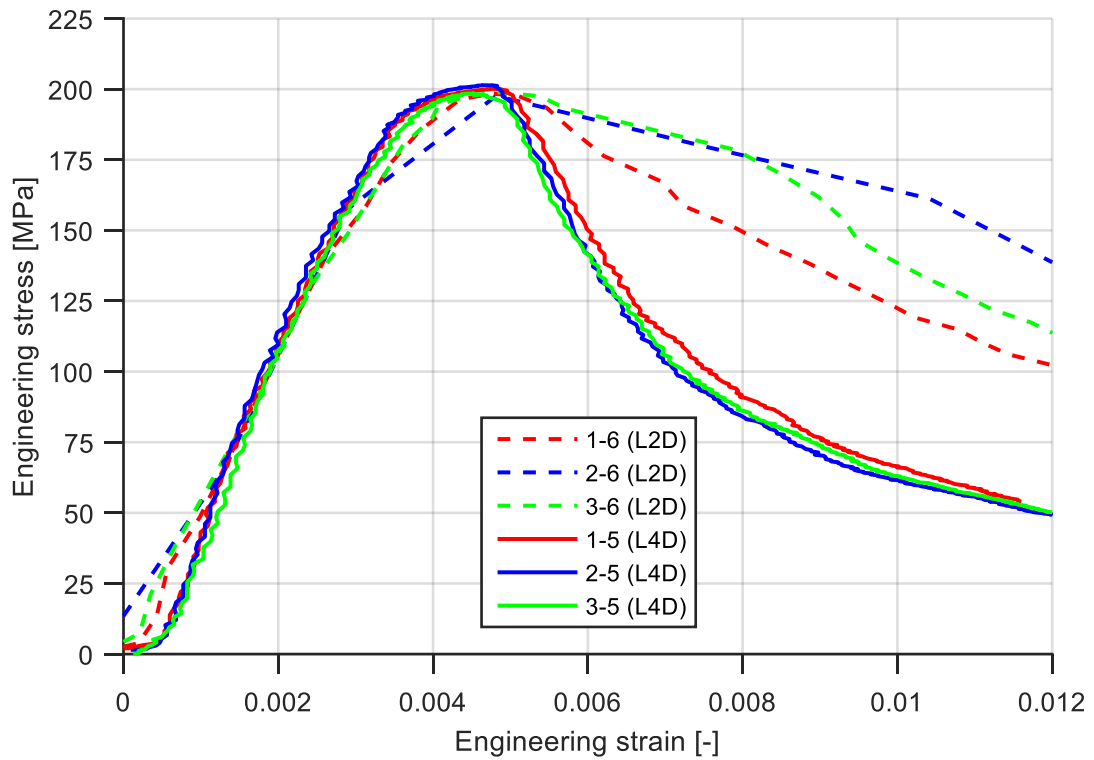


Figure 59 Stress – strain curves from compression tests of profile A6060D127L2D and A6060D127L4D

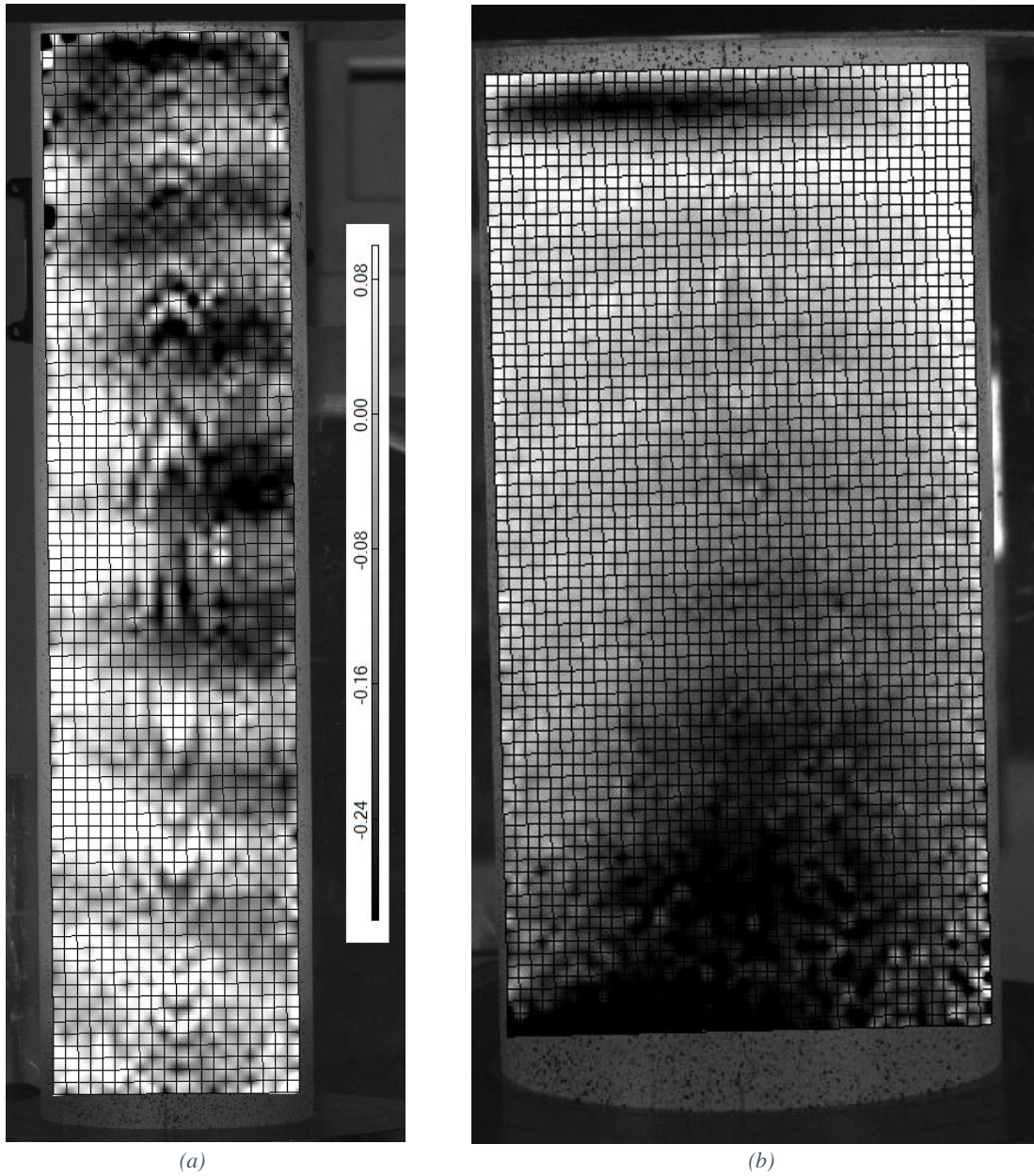


Figure 60 Deformation in transverse direction (towards camera) at maximum load. Pictures generated in eCorr, (a) A6060D127L2D with scale [mm] (b) A6060D127L4D

7.1.2.3 A6082D100

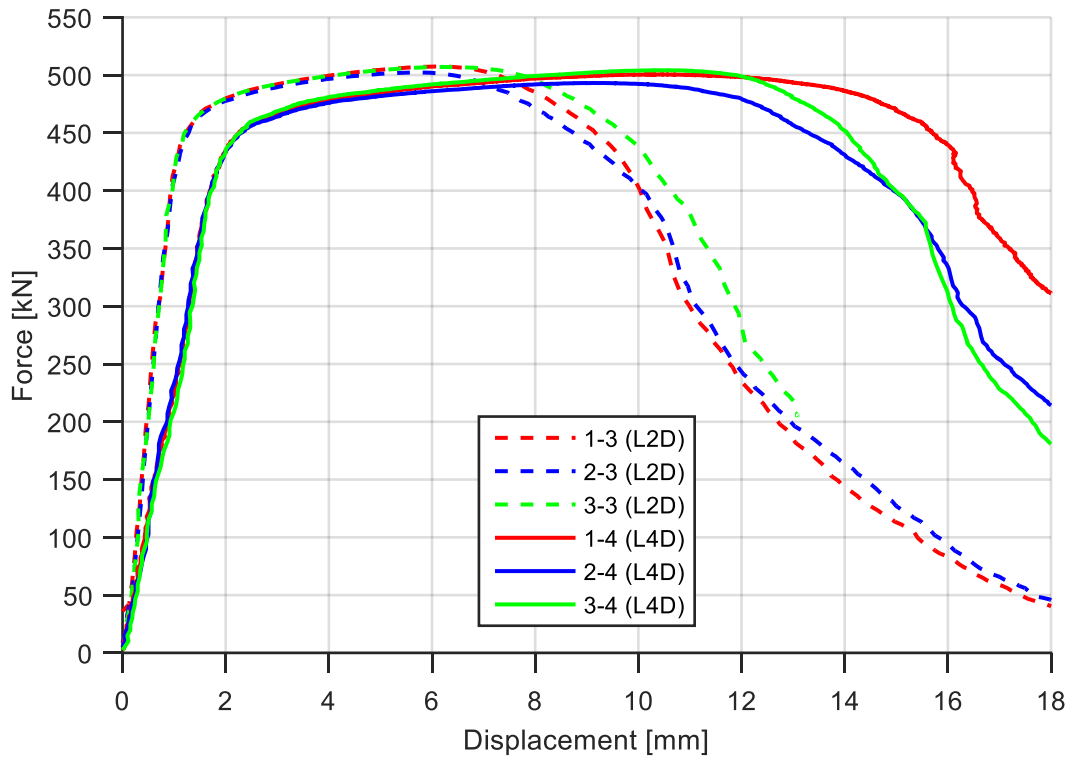


Figure 61 Force – displacement curves from compression tests of profile A6082D100L2D and A6082D100L4D

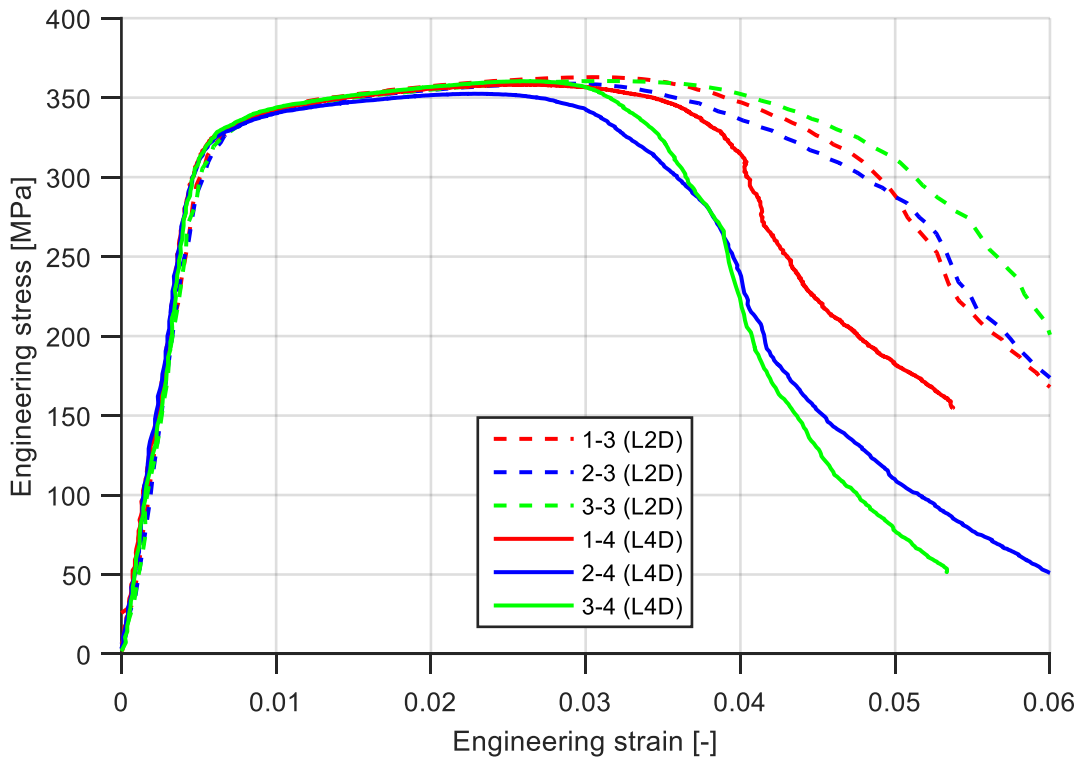
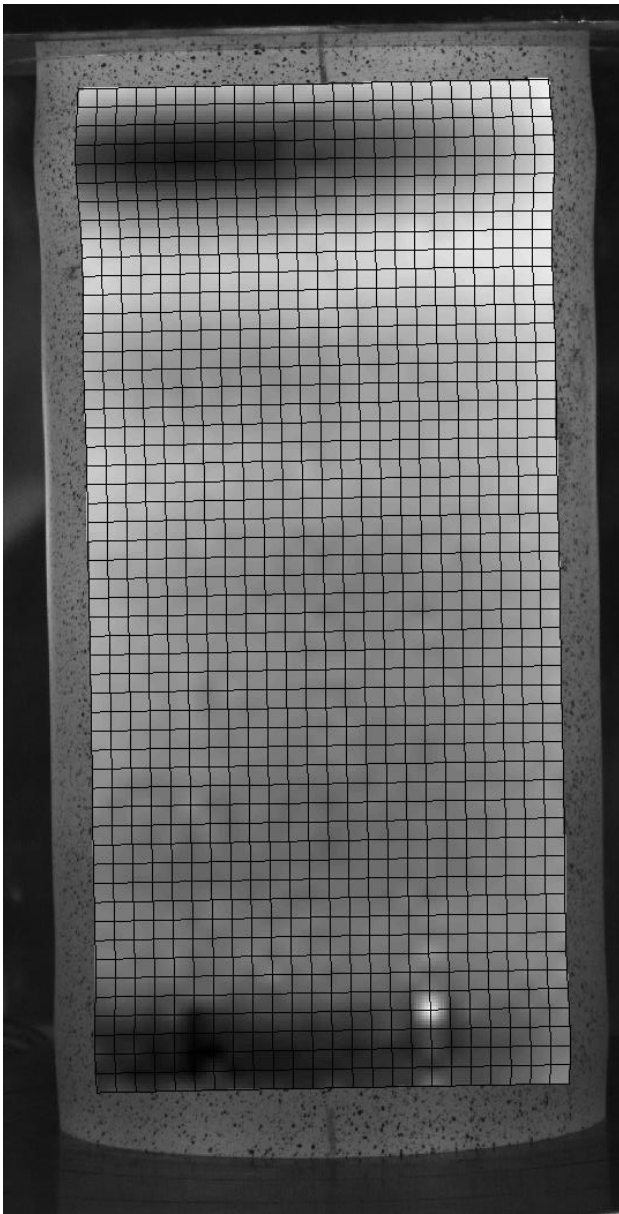
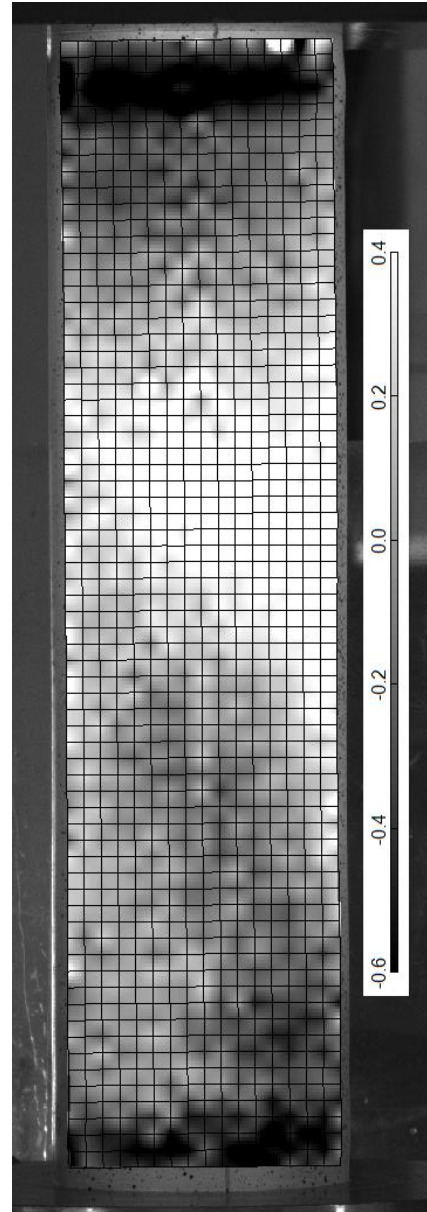


Figure 62 Stress – strain curves from compression tests of profile A6082D100L2D and A6082D100L4D



(a)



(b)

Figure 63 Deformation in transverse direction (towards camera) at maximum load. Pictures generated in eCorr, (a) A6082D100L2D (b) A6082D100L4D

7.1.2.4 Comparison of compression test results of L2D and L4D

A6060D100 and A6082D100 display two major buckles, one close to each cylinder end at maximum load. In the post-buckling phase, one of these buckles absorbs all additional deformation (figure e5 to figure e10).

The two series of A6060D127 did not display any major buckle before reaching maximum load, but rather many small ones (figure 60).

The variation in capacity within each series was adequately low (table 14). This coincides with the assumption of small variation of imperfection (section 3.4.1). A6082D100L4D has the largest scatter in capacity with a distinct deviation in CoV compared to the other five series. The brittle alloy properties discussed in section 3.4 may partly explain this difference.

It is seen from the force – displacement curves (figure 55, figure 58 and figure 61) that columns with twice the length require approximately twice the deformation to reach the capacity. The differences in the mean capacity for the two lengths were negligible

$$\epsilon = \frac{\bar{N}_{L4D} - \bar{N}_{L2D}}{\bar{N}_{L2D}} \quad (7.1)$$

$$\epsilon_{A6060D100} = \frac{311.48 - 311.41}{311.41} * 100\% = 0.023\%$$

$$\epsilon_{A6060D127} = \frac{138.23 - 138.15}{138.15} * 100\% = 0.058\%$$

$$\epsilon_{A6082D100} = \frac{499.39 - 505.58}{505.58} * 100\% = -1.2\%$$

These results indicate that L2D and L4D are at the plateau of local buckling mentioned in section 3.6. A slight reduction of capacity is displayed for A6082D100, which might indicate that L4D is at the initiation of the transition towards the global buckling range, as predicted by the theories of NACA and Jones.

The slope of the force – displacement curves for L2D and L4D are different. The elastic axial stiffness defined as

$$k = \frac{EA}{L} \quad (7.2)$$

gives a steeper curve for shorter specimens. In the elastic range the relationship between the force and deformation is given as

$$w = \frac{N}{k} = \frac{NL}{EA} \quad (7.3)$$

The engineering strain (3.4) can then be written as

$$e = \frac{w}{L} = \frac{N}{EA} \quad (7.4)$$

Note the assumption of $L \approx L_0$. The engineering strain is not a function of the length of the cylinder, hence the engineering stress – strain curves (figure 56, figure 59 and figure 62) display yield stress at the same engineering strain, corresponding to twice the deformation. However, L4D reaches maximum load at lower engineering strain for all series. It is believed that this effect stems from the amount of strain energy. Longer columns has approximately twice the amount of strain energy, as the volume is twice as large and the strain energy per volume given in equation (3.7) is approximately the same.

The engineering strain of the thick-walled cross-sections at maximum load is approximately 6 times larger than for thin-walled cross-sections. The internal energy is lower in A6060D127 than A6060D100, but the energy required to initiate buckling is also much lower as the cross-section is slenderer.

Pictures of the post-buckling shape off all specimens are displayed in Appendix E.

7.2 Compression test for L2000

The laboratory tests on two metres long cylinders were performed the 26th of May 2016, only two weeks before the delivery of this thesis. The results are discussed and analysed, but the consequence of the findings were only partially implemented due to the lack of time. DIC was discarded due to the large amount of data and long processing time.

The laboratory setup was similar to the previous laboratory session (figure 64). Three specimens of each series led to 3x3 tests, which are labelled in Appendix G. The failure mode of A6060D100 and A6082D100 were anticipated to be global, as seen by both L_G and L_G^{EC} in table 6. For A6060D127, L_G^{EC} (based on Eurocode 9) claimed local instability failure up to four metres, while estimates by the tangent-modulus global buckling predicted global buckling for all lengths above $L_G = 680 \text{ mm}$.



Figure 64 Laboratory setup for L2000mm

The cylinders tested in the laboratory were measured similarly to L2D and L4D, albeit a technical error with the ultrasonic thickness gauge resulted in the use of electronic calipers for thickness measurements. Measuring circular shapes with flat caliper jaws causes a slight overestimation of the thickness. The width of the caliper jaws was measured (with another electronic caliper) to be 3.4 mm, and a correction to the thickness is taken as

$$\Delta t = -r \left(1 - 2 \cos \left(\frac{2\pi(0.5 * 3.4mm)}{2\pi r} \right) \right) \quad (7.5)$$

Despite correlating for this error, the measured geometry (table g1) exhibited a thickness deviation of more than 2 percent compared to earlier measurements (table 2 and table 13) indicating a systematic error (figure 5). The covariance was small (0.4-1.5 percent), hence the random error was acceptable. The measurements were discarded because of the systematic error, in favour of the simplified geometry in table 2.

Of reasons unknown, the laser displacement measurements rendered erroneous results with noise. These data had to be discarded, and all force – displacement data (and hence the stress – strain data) is taken from the recorded machine displacement. Modification due to machine

compliance is necessary, and this is done in a similar, yet simpler manner than in section 6.5. The total stiffness of the system can be written as

$$\frac{1}{k_{tot}} = \frac{1}{k_m} + \frac{1}{k_s} \quad (7.6)$$

where k_m is the machine stiffness and k_s is the specimen stiffness. The relationship between any stiffness i and their corresponding deformation is

$$N = k_i w_i \quad (7.7)$$

The stiffness of the specimen in the elastic region is given in equation (7.2). One data point was chosen from the force – displacement graph in the early part of the elastic regime and one at the end. These points gave a measure of the total stiffness:

$$k_{tot} = \frac{N_2 - N_1}{w_2 - w_1} \quad (7.8)$$

Through equation (7.6) the machine stiffness was estimated. Each of the 9 series rendered different values for the machine stiffness (in the range between 252 *kN/mm* and 614 *kN/mm*). This scatter is large, perhaps an indication that the assumption of a linear spring was not necessarily a good enough fit. The error in machine compliance could lead to a steeper or flatter force-displacement relationship than the correct one. Nevertheless, as this error is assumed to be low, the algorithm is kept. Since the machine compliance should be the same regardless of test specimen, the mean value was used. In later comparisons to simulations, the curves are slightly shifted so that a straight line between the two mentioned points – with a stiffness given in (7.2) – will end up in the origin. The initial slack of the tests will therefore cause the force-displacement graphs to start at $w = 0, N > 0$ (figure 100).

7.2.1 Compression test results

All laboratory settings, obtained capacities and corresponding stresses are shown in table g2. The force – displacement curves and stress – strain curves from the laboratory are shown in figure 65 to figure 70. The buckling shape of A6060D100 and A6082D100 was a slowly progressing global instability, while the buckling shape of A6060D127 was local and the buckling propagation was sudden, possibly due to the excessive stored internal energy. The post-buckling shape of the specimens is shown in Appendix G.

7.2.1.1 A6060D100

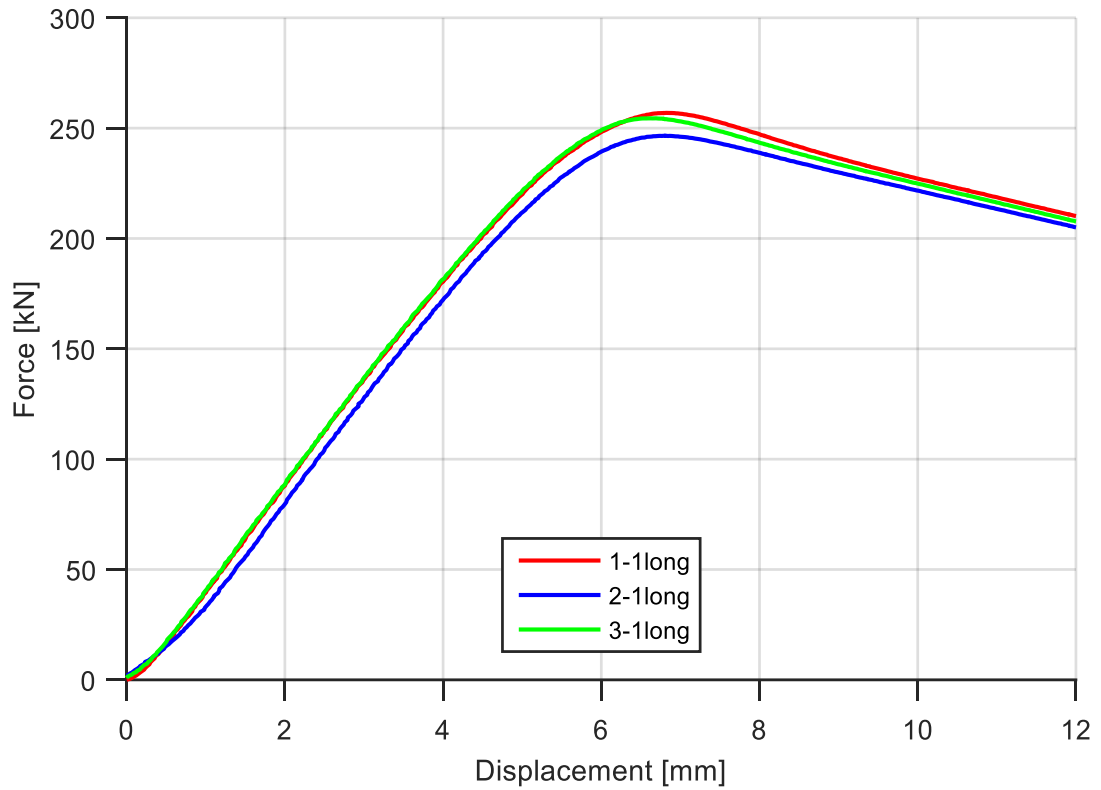


Figure 65 Force – displacement curves from compression tests of profile A6060D100L2000

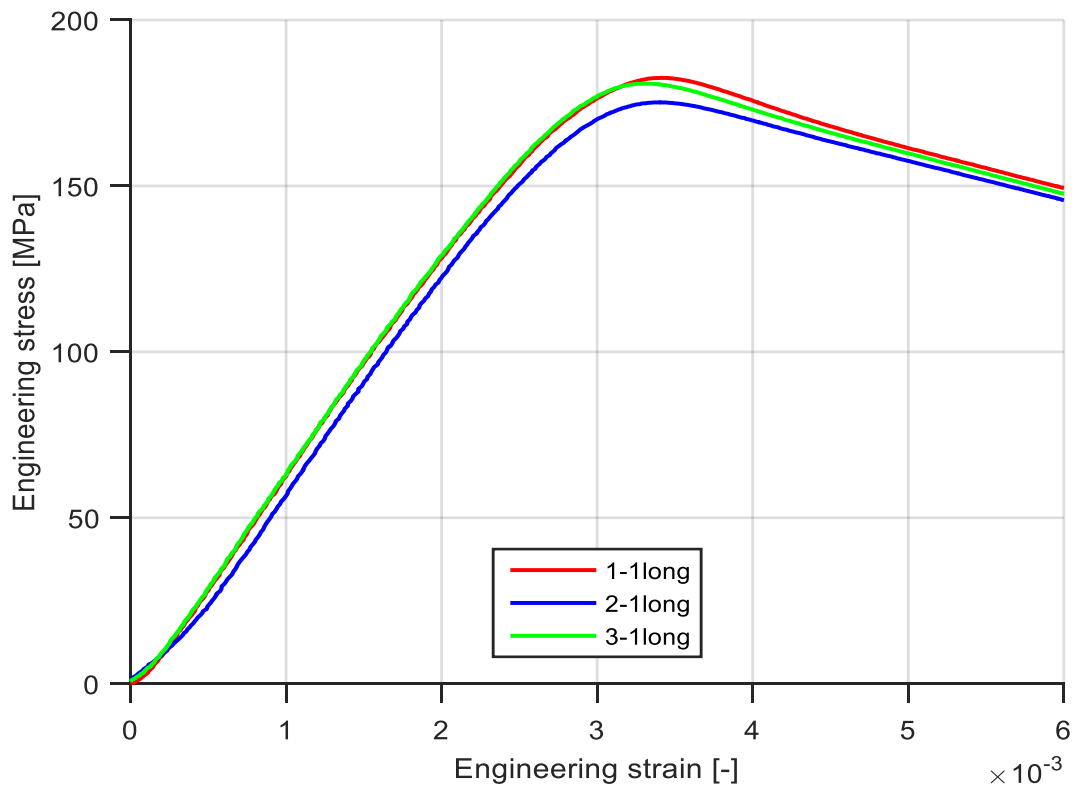


Figure 66 Stress – strain curves from compression tests of profile A6060D100L2000

7.2.1.2 A6060D127

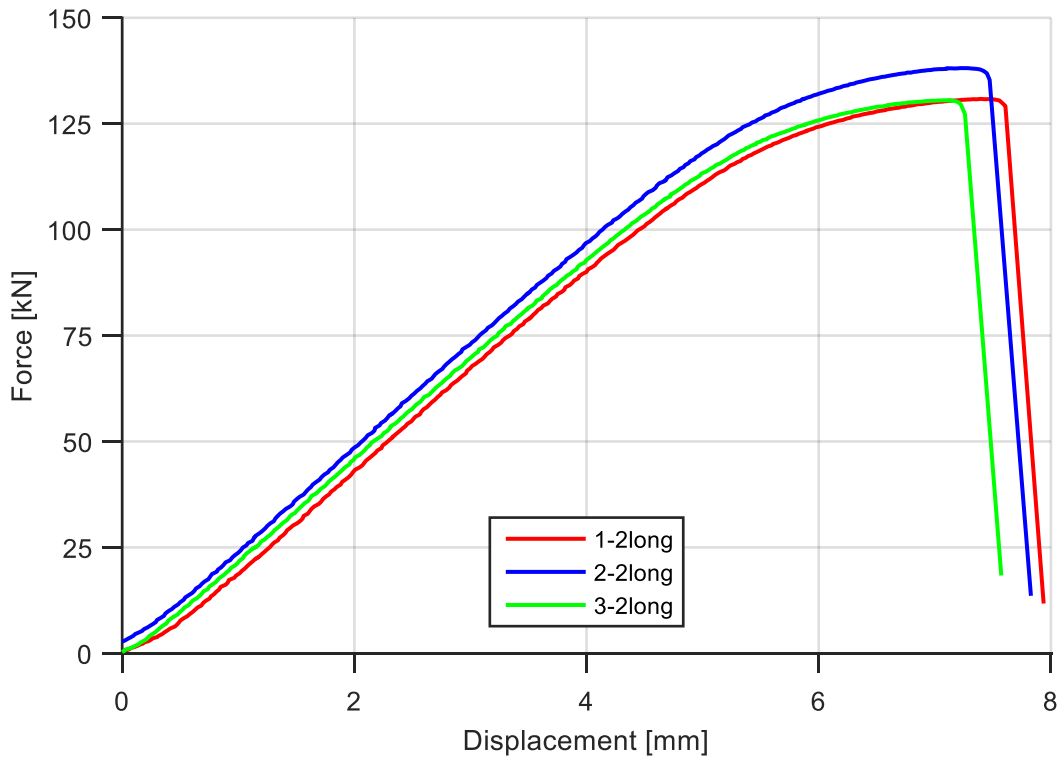


Figure 67 Force – displacement curves from compression tests of profile A6060D127L2000

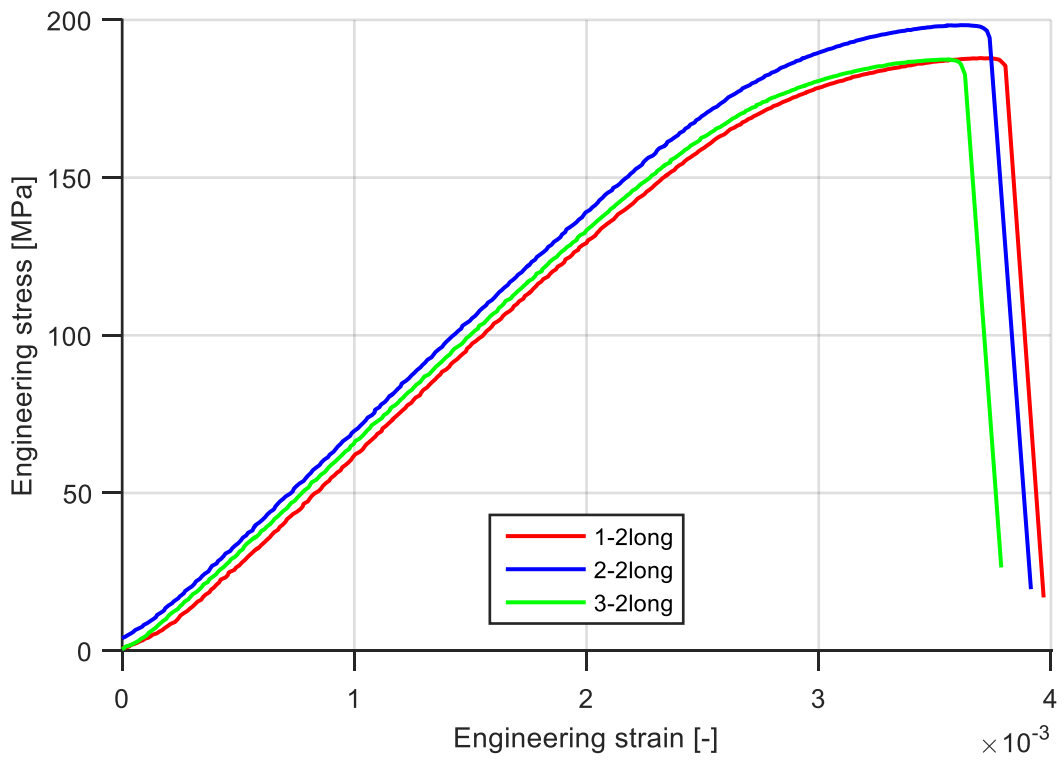


Figure 68 Stress – strain curves from compression tests of profile A6060D127L2000

7.2.1.3 A6082D100

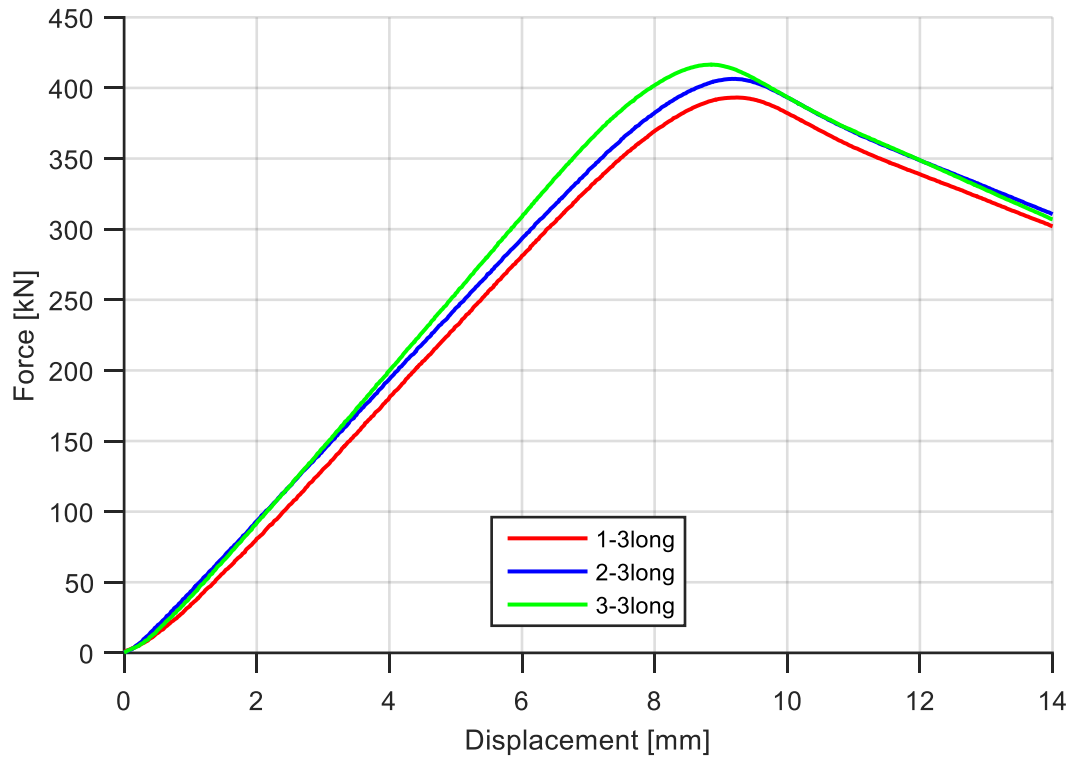


Figure 69 Force – displacement curves from compression tests of profile A6082D100L2000

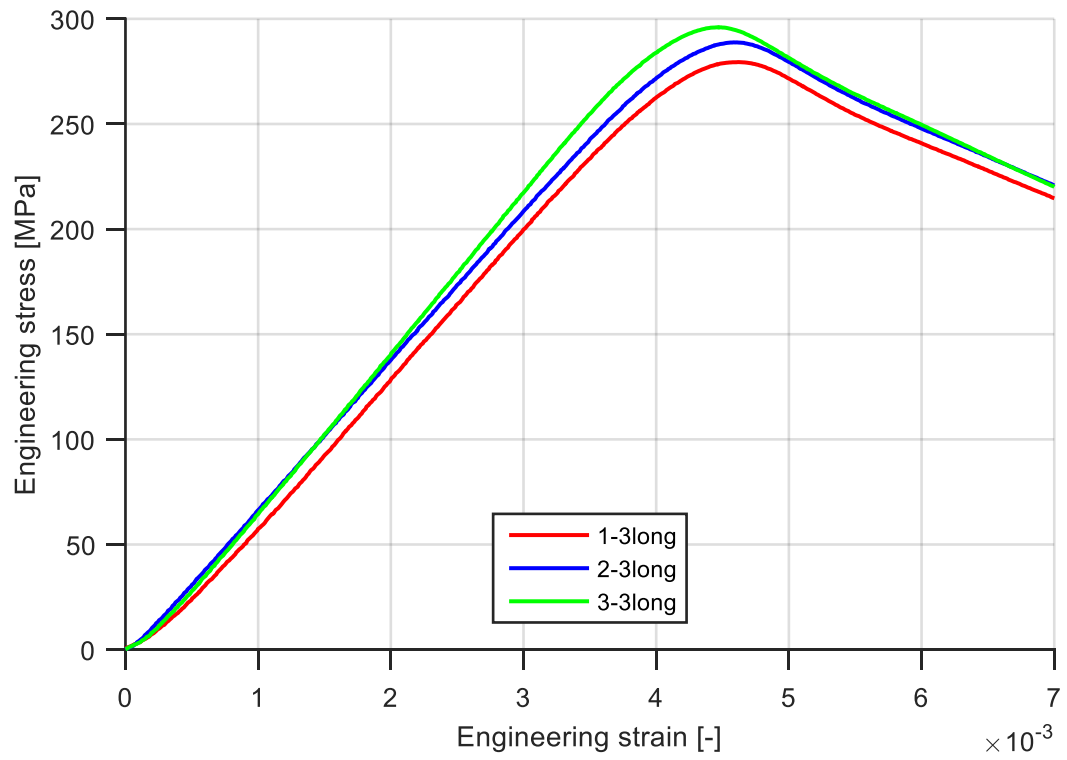


Figure 70 Stress – strain curves from compression tests of profile A6082D100L2000

7.2.1.4 Comparison of compression tests

Table g2 shows that A6060D127 has the highest covariance (3.22 percent). The local buckling mode is induced when the internal strain energy U_0 from formula (3.9) exceeds a certain limit in order to make an imperfection propagate into a buckle. It is believed that the imperfections of the cylinders to some extent can dictate at which load the cylinders fails, leading to a slight increase in covariance for this series.

Table g2 displays a noticeable high covariance for A6082D100 (2.88 percent). This covariance comes in part because one of the cylinders (specimen 3-3) was cut 19 mm shorter than the target length of 2000mm. The capacity against global buckling (which is the failure mode observed in laboratory), scales against the length squared (3.31). The change in length should therefore lead to an increased capacity:

$$N_{1981} \approx N_{2000} \left(\frac{2000}{1981} \right)^2 \approx 1.02 N_{2000} \quad (7.9)$$

As the length was increased from L4D to L2000, the reduction of mean capacity in each series was 19 percent for both thick-walled cross-sections, while A6060D127 only exhibited a reduction of 3.6 percent (table 14 and table g2). One specimen of the latter series had larger capacity than any of the L4D specimens, hence this reduction might be partially due to scatter in results. Local instability dominates the failure mode, but at this length, some interaction with global buckling can affect the result, giving a slight reduction of capacity.

Note that the covariance in table 13 and table g2 are based on the standard deviation given in (3.58), which might be a bad measurement for deviation when the number of samples is low. The sample size of each series of tests was 3. In order to ensure consistency and due to the low scatter of results, the measurement for standard deviation is not altered.

7.3 The FEA model for compression tests

The main objective for the Abaqus modelling is to create a robust FEA model that can represent results (force – displacement and buckling shape) up to maximum load for all three profiles for lengths up to 30 times the diameter. The procedure is an iterative process that started in section 6.4 with correct representation of the material. Laboratory results from compression tests at L2D and L4D are used to optimize and validate the FEA model. Results from the compression test at L2000 are only used as a validation as the tests were executed two weeks before the delivery of this thesis.

7.3.1 Basis for the FEA model

7.3.1.1 Solving algorithm

The dynamic implicit solving algorithm is selected in order to ensure quasi-static loading by avoiding scaling. Choosing an implicit solver is justified by the simple geometry as well as the possibility to extend the model to long columns.

When implicit solution algorithm is applied to bifurcation problems, a strict time limit has to be set for the maximum time step. If not, the bifurcation point initiating the buckle might not be detected by the solver. In all analyses except in section 7.3.2.1, identification of the bifurcation point was ensured by defining a maximum time step corresponding to 0.05 mm deformation. Finer time step increment was found to not alter the result.

Because implicit solution algorithm was chosen, it was possible to employ higher-order elements S8R and C20R in addition to the lower-order S4R and C8R.

7.3.1.2 The assembly

The cylinder is modelled between two analytical rigid plates (figure 71), with the geometry given in table 2. In order to impose and track the displacement, each plate contains a rigid connected reference point with a given initial velocity. The RP placed at $z = 0$ is used to track the total reaction force and deformation of the system. A surface-to-surface contact is established between the plates and the column. Because the post-buckling behaviour was not of interest, self-contact was not modelled.

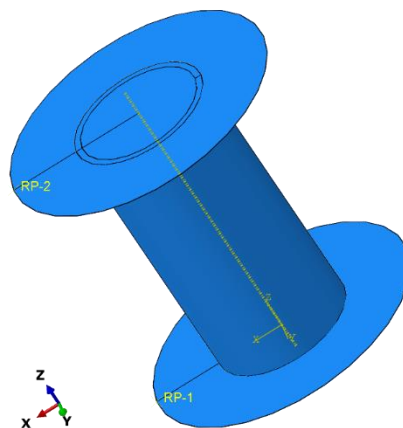


Figure 71 Assembly in Abaqus model used for compression test

7.3.2 Sensitivity analyses

To ensure that the models are able to represent a correct solution, sensitivity analyses of mesh, friction and imperfection are conducted.

7.3.2.1 Mesh analysis - L2D

Selection of element type, shape and size can affect the solution to the FEA. In order to ensure that the mesh is able to represent the correct resistance, deformation and buckle pattern up to reached capacity, three mesh-related parameters are studied: element length, ETT and element type. Criteria used for validation are: force – displacement curves, axial load capacity, buckling shape and amount of artificial energy up to the point of maximum axial load. In order to assure a robust model, it is chosen that the mesh should exhibit the same properties and capacity as a refined mesh.

The analyses are conducted on the profiles A6060D100L2D and A6060D127L2D. Material hardening is assumed to not alter the mesh sensitivity of the model. Due to long processing time of the material data from chapter 6, mesh sensitivity for A6060D100L2D and A6060D127L2D was analysed with preliminary material parameters. The results for A6060D100 are extrapolated to A6082D100.

As a simplification of the model in the early stages of the parameter study, the volumetric elements are analysed with a maximum time step of 1 second. This corresponds to 1 *mm* deformation, and causes the represented data to appear less smooth. In subsequent analyses, the maximum time step is adjusted down to 0.05 seconds. It is assumed that the mesh sensitivity of the model is unaffected by this down-adjustment.

The shell elements S4R and S8R and volume element C8R and C20R are evaluated. The volume elements are analysed with 1 and 3 ETT, and the higher-order elements are also studied with 2 ETT. The element lengths analysed are 2.5, 5, 10 and 20 *mm*.

The behaviour of the analyses were dependent upon the mesh, as seen in the force – displacement graphs in Appendix F. For some element types, the axial capacity of the cylinder also differed as the mesh was refined, as seen in figure 72 and figure 73 for A6060D100 and figure 74 and figure 75 for A6060D127. In these figures it is seen that the capacity of the shell elements converges to a different, slightly lower value than the volume elements. From figure f1, figure f2 (A6060D1100) and figure f8, figure f9 (A6060D127) it is observed that the shell elements do not well display the force-displacement relationship observed in laboratory, and that refining the mesh for A6060D100 leads to worse representation of force – displacement relationship. The C8 elements do not converge with 1 ETT (figure f3 and figure f10) and has a very low rate of convergence for 3 ETT (figure f4 and figure f11). C8 1 ETT is also unable to represent the correct buckling mode for all meshes.

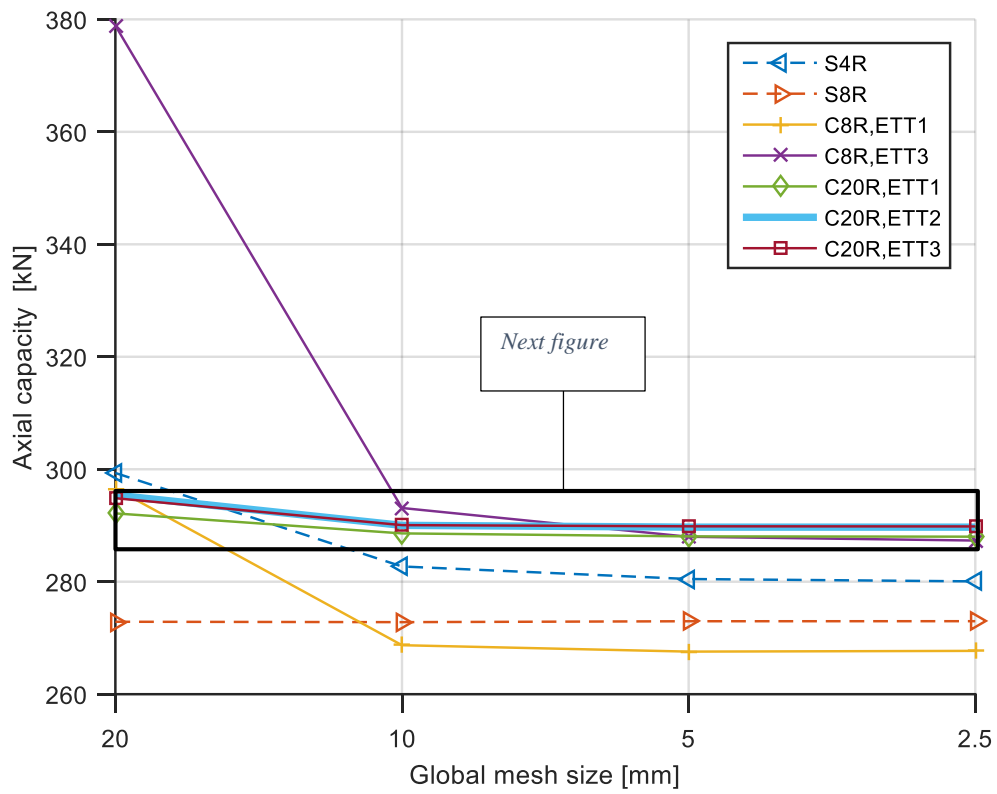


Figure 72 Sensitivity of mesh for A6060D100L2D

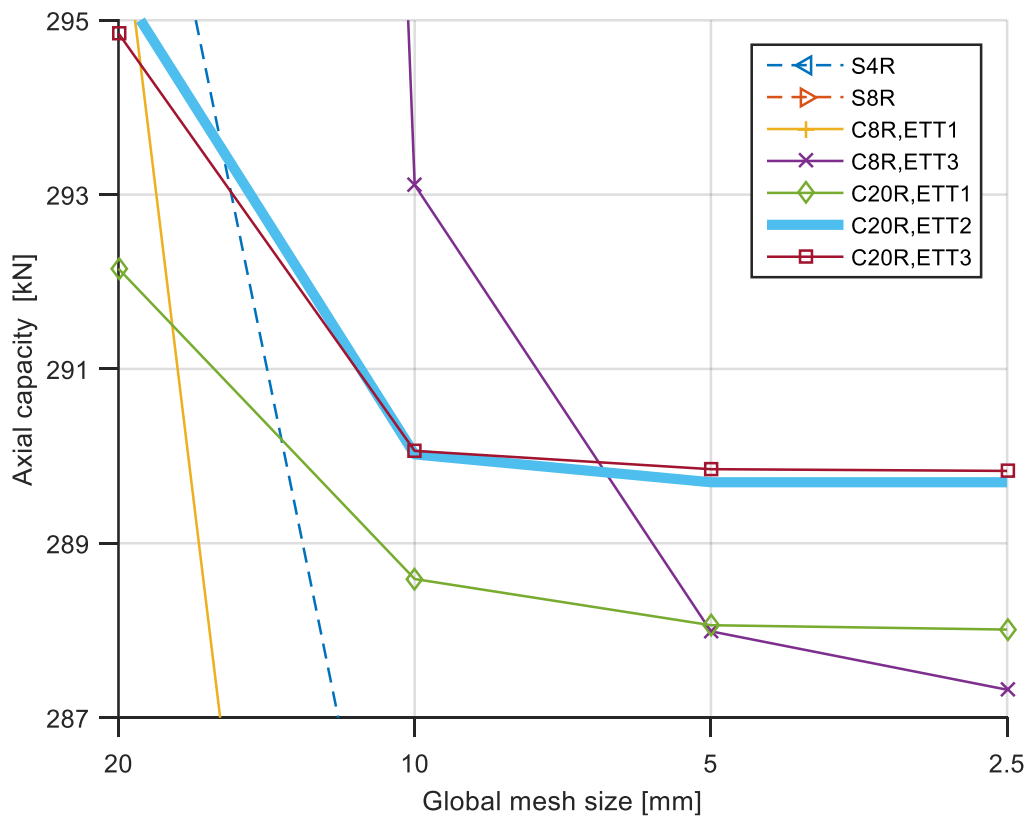


Figure 73 Sensitivity of mesh for A6060D100L2D (zoomed)

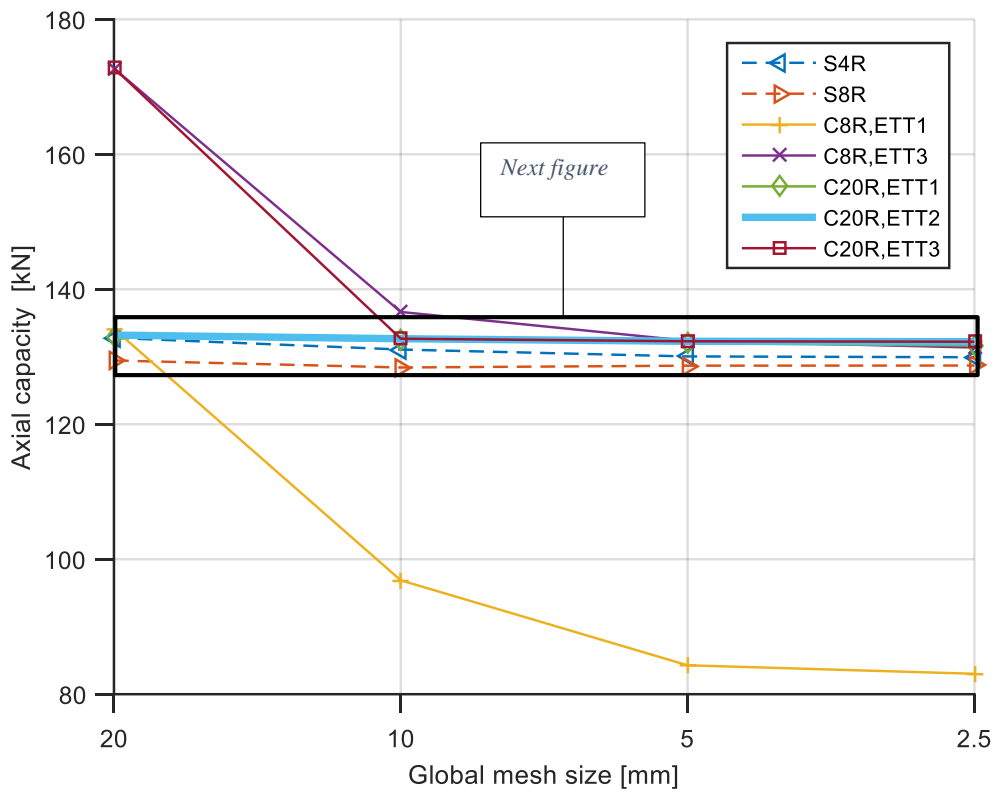


Figure 74 Sensitivity of mesh for A6060D127L2D

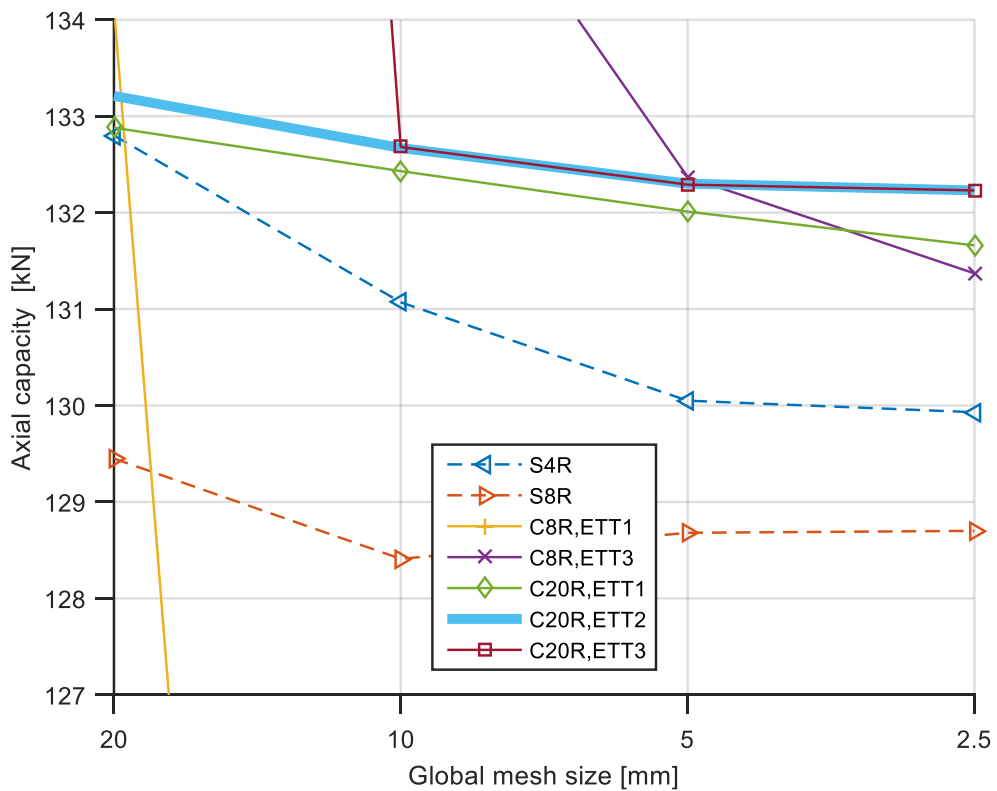


Figure 75 Sensitivity of mesh for A6060D127L2D (zoomed)

As 20-noded C20R higher-order elements are introduced, a linear stress gradient is modelled within every element, and 1, 2 and 3 ETT gives good results even for the coarsest mesh. With 3 ETT the A6060D127 elements becomes very distorted for the roughest mesh, with a length-to-thickness-ratio of 34. This ill-conditioning gives rise to artificial stiffness, but is drastically reduced as the element length shortens. The amount of elements needed for a robust model, however, is so large that the computational cost far exceeds what is preferable, and 3 ETT for this cross-section is therefore discarded. It is desired, although not an absolute necessity, to have the same number of ETT for the two different cross-sections.

In order to quantify the effect of ill-conditioning on A6060D127L2D, mesh with element length 2.5 mm 1 ETT is compared to element length 10 mm 2 ETT (figure 76). Their respective length-to-thickness-ratios are 1.4 and 11.3. The force-displacement curves were similar up to the point of maximum load, which deviated by 0.77 percent. Element length 5 mm 2 ETT is introduced (figure 76), with a length-to-thickness-ratio of 5.6. Its deviation in maximum load is reduced to 0.28 percent. Based on this information, ill-conditioning is assumed to affect the capacity only in a negligible way as long as the length-to-thickness ratio is kept below 10.

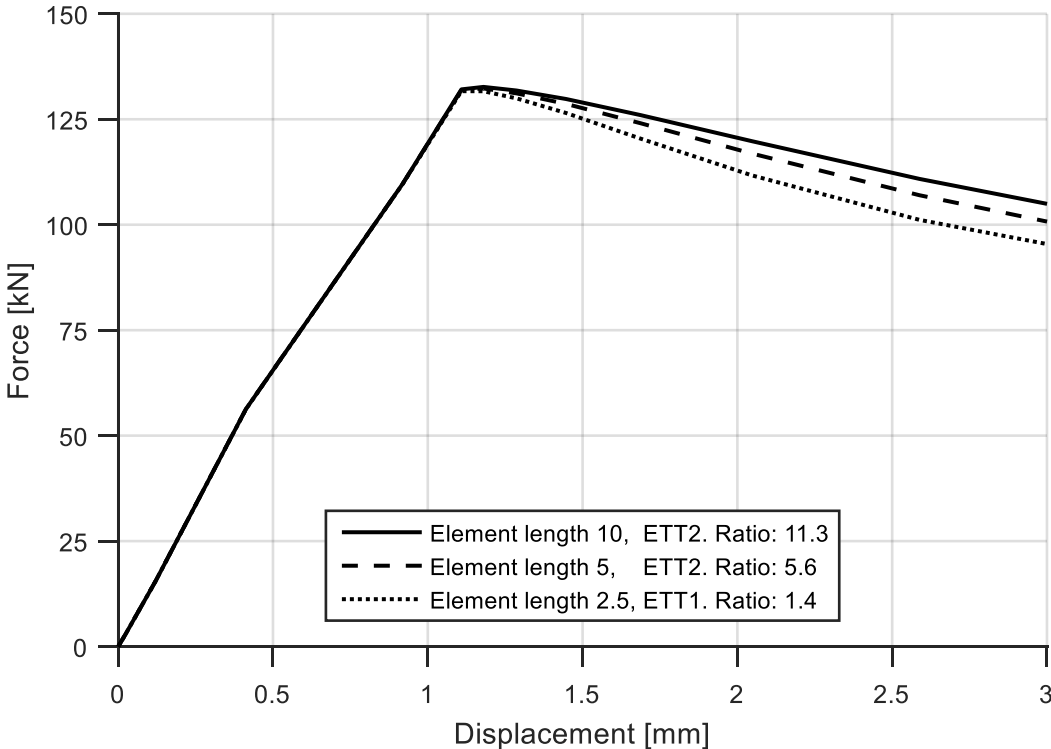


Figure 76 Study of the effect of ill-conditioning for different ratios of element length to element thickness A6060D127L2D, C20R elements

Only one ETT could be sufficient for tests with linear variation in stress. Two ETT is preferred in order to create a robust FEA that can model local and global buckling modes of cylinders with different lengths. Especially short column tests are believed to be better modelled by 2 ETT due to the tri-axial stress state close to the frictional plates. One ETT may lead to numerical problems, which for A6060D127L2D caused the artificial energy to take up over 10 percent of the energy of the whole mode, even for fine meshes. 1 ETT is therefore discarded and 2 ETT is chosen for all meshes.

The element length 5 mm is chosen based on the convergence of the solutions seen in figure 73 and figure 75. The deviation from the results for 10 mm mesh and 2.5 mm mesh indicates that the model with this mesh is robust with respect to element size. The thickness-to-length ratios of the elements are 5.6 and 2.1 for A6060D127 and A6060D100 respectively, and are considered adequately low. An element size of 10 mm might have been sufficient (if ill-conditioning did not void the results), but in order to extrapolate the model to different lengths, a safety margin is included in the choice of element length.

As a result of the mesh parameter study, element type C20R is chosen and all cylinders are modelled with an element length of 5 mm and two elements through the thickness.

7.3.2.2 Validation of mesh - L2000

The mesh is validated for a length corresponding to the last laboratory session, in order to ensure that a change of length and possibly a change failure mode do not affect the robustness of the model. This validation is done for some chosen meshes with C20R elements, and the objective is solely to confirm that small changes in element size do not cause significant changes in capacity or buckling mode. The results presented in table 15 and figure 77 show that the model is robust and that a change of mesh is unlikely to alter the behaviour up to the point of maximum load for the most slender cross-section. The artificial energy was also adequately low. The previously chosen mesh of C20R elements with 2 ETT and element length 5 mm is judged robust and validated.

Table 15 Axial capacity [kN] from mesh sensitivity analyses at L2000

ETT	1	2				3
Element length [mm]	5	20	10	5	2.5	5
A6060D100L20D	247.6	247.6	247.6	247.6	247.6	247.6
A6060D127L20D	124.0	124.1	124.1	124.0	124.0	124.0

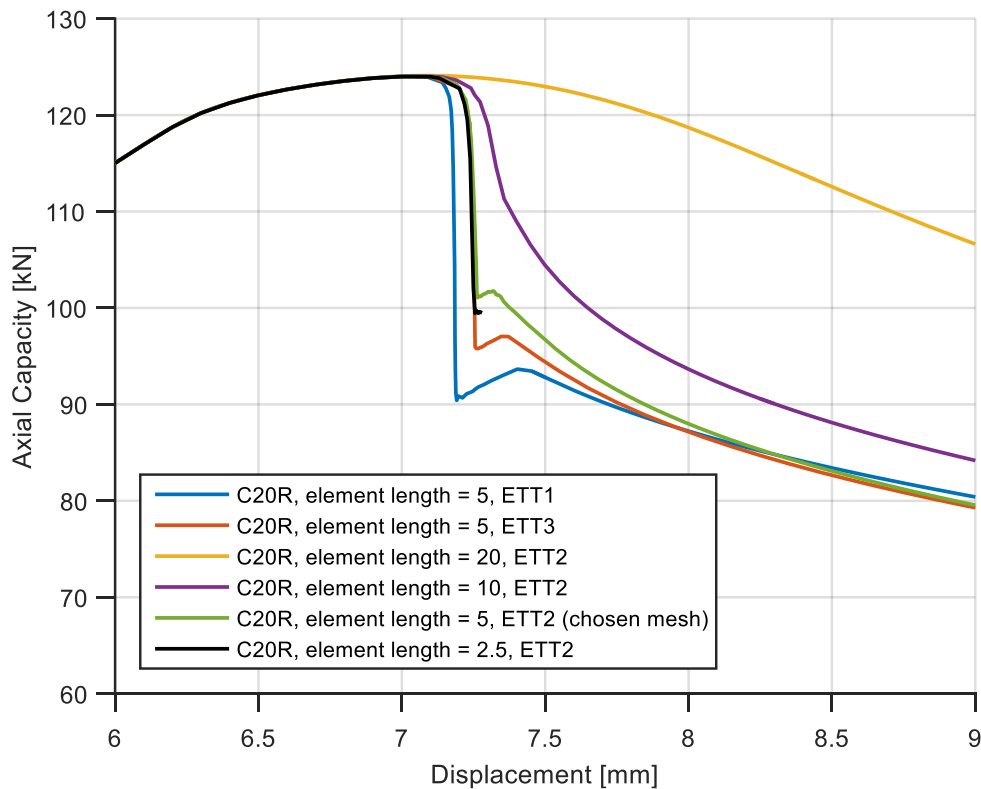


Figure 77 Mesh sensitivity - A6060D127L20D

7.3.2.3 Friction coefficient analysis - L2D

The analytically rigid end plates apply the load to the cylinder, and it is desirable to achieve clamped BCs by applying friction to the contact. In light of chapter 5, the frictional coefficient is analysed in order to define whether or not the laboratory setup will give fully clamped BCs. The frictional coefficient between aluminium and steel on untreated surfaces is typically close to 0.61 [28]. From figure 78 and figure 79 it is concluded that slight deviations from $\mu = 0.6$ will not alter the capacity or behaviour of the cylinder significantly. Frictional coefficient of 0.61 is chosen for the model.

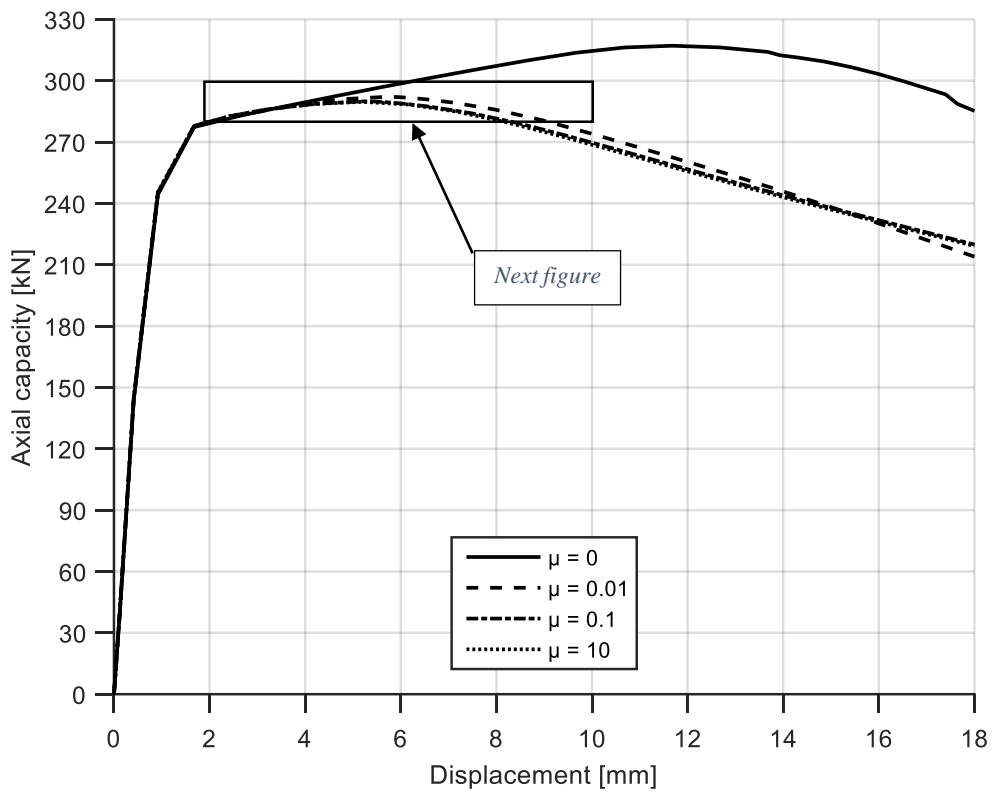


Figure 78 Sensitivity tests of friction - A6060D100L2D

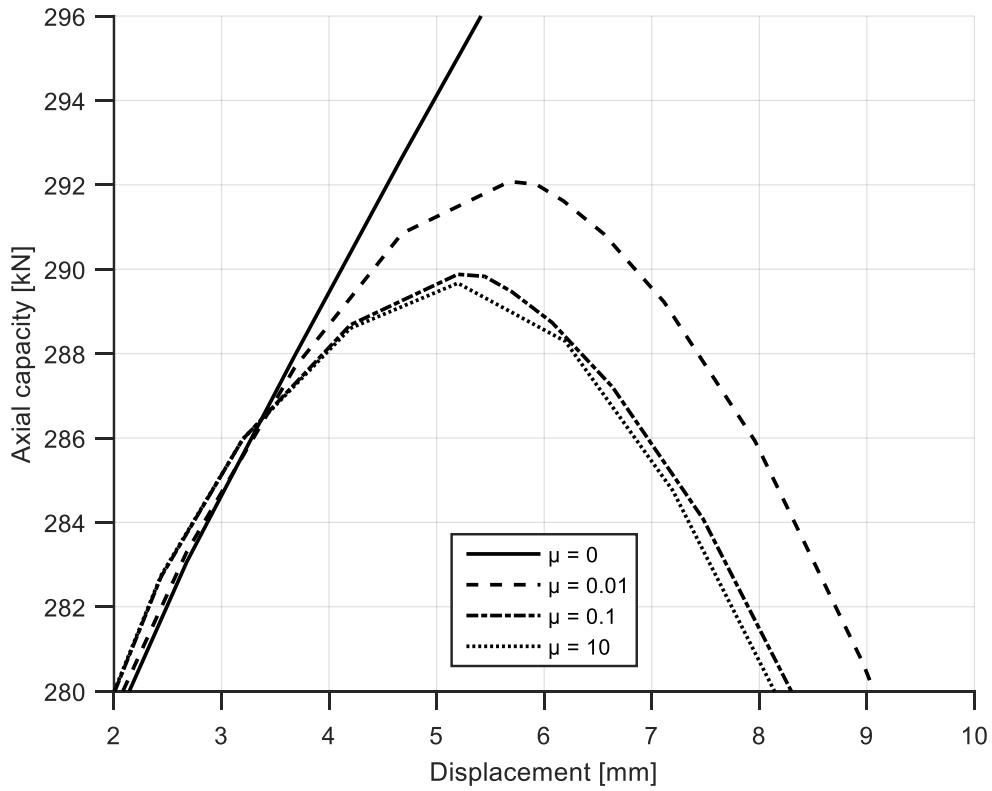


Figure 79 Sensitivity tests of friction - A6060D100L2D (zoomed)

7.3.2.4 Imperfection analysis - L2D

In this section, the imperfection types shown in figure 6 are introduced to the FEM model as described in section 4.1.1. The objective is to establish to what degree different types of imperfections influence the force – displacement relationship and failure mode. Note that the analyses were carried out on L2D, and discharged before the execution of the compression tests of L2000.

The capacity without imperfections were lower than what observed in compression tests, and the buckling shape was correct, but as mentioned, modelling a mathematically straight and geometrically perfect cylinder can reduce the robustness of the model and may give rise to erroneous buckling resistance.

In order to introduce eigenmode imperfections, the first eigenmode from an LBA analysis in the FEA model is calculated and imposed on the model with a given amplitude. In addition to eigenmodes from LBA, tests with the vase-shaped imperfection and the global imperfection from section 4.1.1 are discharged. In order to implement the vase-shaped imperfections, the number of buckles is calculated from equation (3.56) and rounded to the nearest integer. The results from (3.56) and the change of area according to formula (4.4) is shown in table 16.

Table 16 Basis for introducing vase-shaped imperfections

	E_T^{pl} [MPa]	E_S^{pl} [MPa]	m	$\frac{A}{A_0}$ ($a=0.5t$)	$\frac{A}{A_0}$ ($a=0.1t$)	$\frac{A}{A_0}$ ($a=0.15mm$)
A6060D100	810	12149	7	0.908	0.981	0.994
A6060D127	1160	89495	9	0.972	0.994	-
A6082D100	777	31477	5	0.908	0.981	0.994

The results displayed in figure 80 and figure 81 show that the eigenmode imperfection barely alters the capacity unless unrealistically large imperfections were introduced. The eigenmodes at L2D were not axisymmetric, and predicted an elastic buckling load much higher than the actual capacity. Amplitude increased to 0.1 times the thickness did not cause significant changes in failure mode or force – displacement relationship.

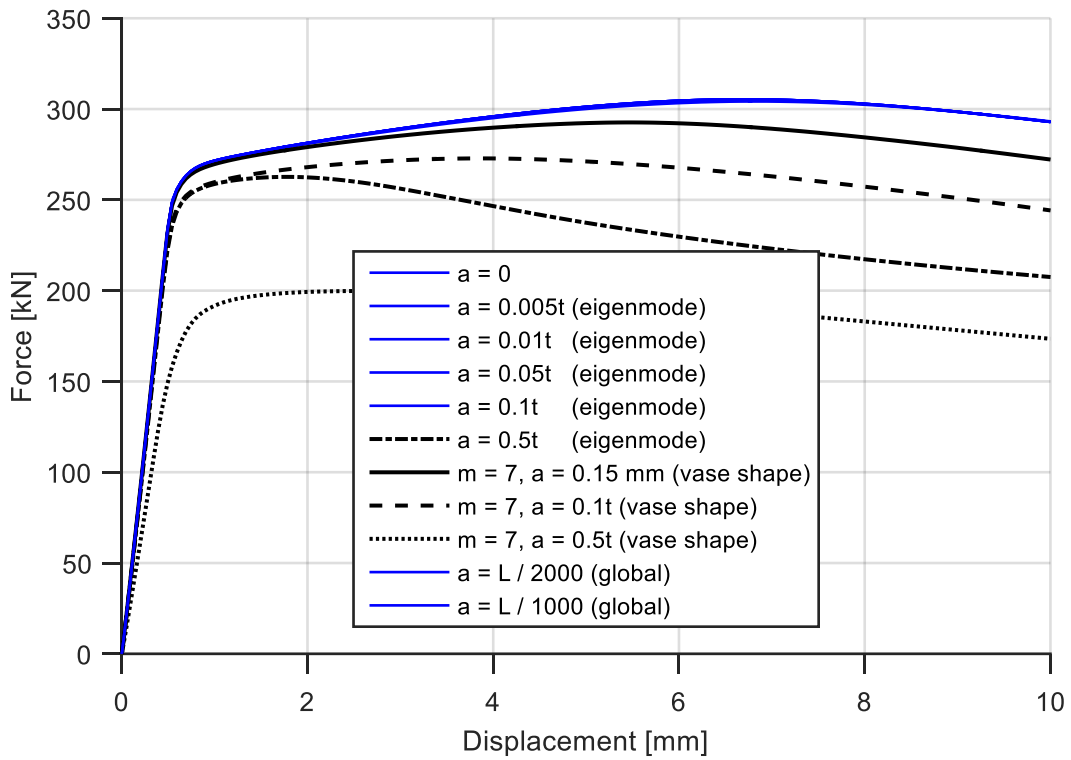


Figure 80 Influence of imperfection for the profile A6060D100L2D

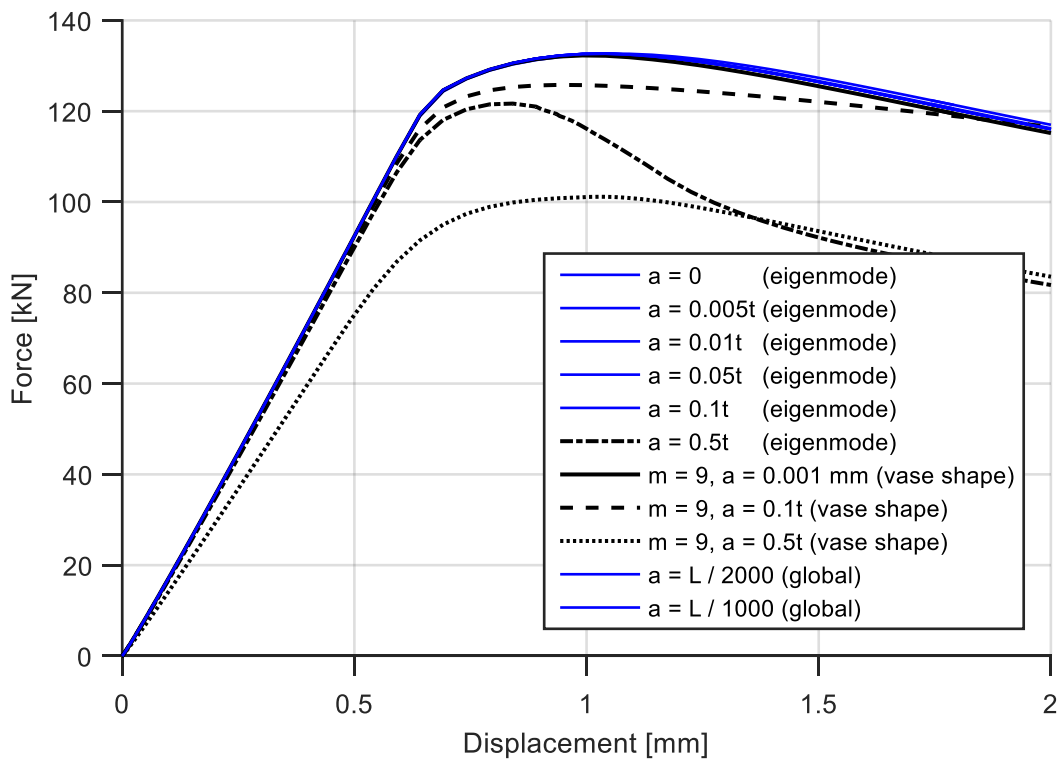


Figure 81 Influence of imperfection for the profile A6060D127L2D

The FEM model was sensitive towards vase-shaped imperfections, which lowered the capacity even for small imperfections (figure 80 and figure 81). This type of imperfection caused the failure mode of the model (figure 82) to deviate from what was seen in the laboratory (Appendix E). The difference between the resulting shapes might stem from the assumptions made in the NACA report [7], described in section 3.3.2: No friction in the BC plates, axisymmetric deformation pattern and no elastic strains. The assumption of no friction affects the assumed buckling shape upon which the formulas are derived. This may be the cause of the erroneous buckling shape exhibited when introducing the imperfection through this theory. No further inspection of the vase-shaped imperfection is discharged.

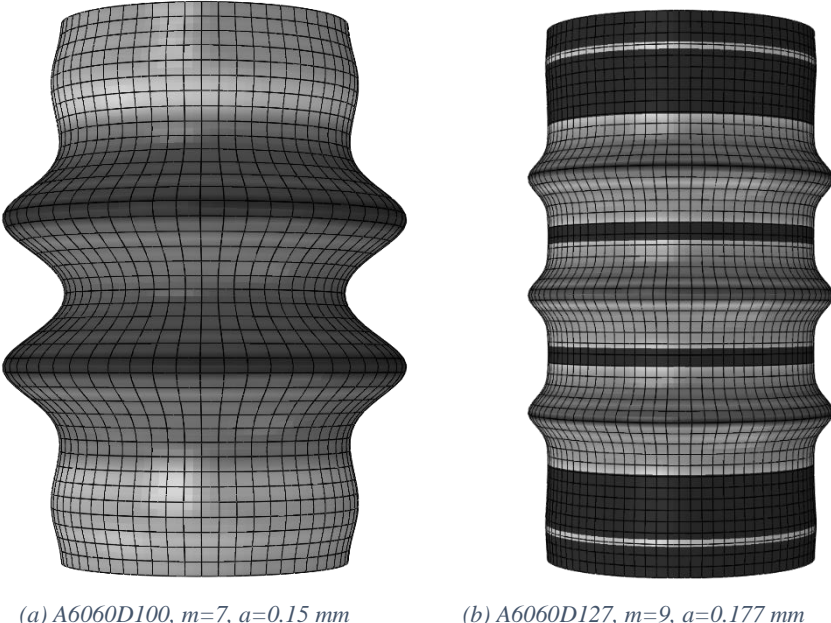


Figure 82 Failure mode from vase-shaped imperfection

One last imperfection was attempted. The cylinder was modelled as the area between two circles, and the inner circle was moved relatively to the outer circle (figure 83). When this movement was 0.15 mm, A6060D100L2D showed no change of capacity but a slight localization of deformation on the most thin-walled side. The imperfection was increased to 2.35 mm = $t/2$, hence the “cylinder” had a varying thickness, from $t/2$ on the thin side to $3t/2$ on the thick side, where t denotes the original thickness. This is much more than what was measured in from the laboratory specimens. Introducing this imperfection altered the failure mode to a more one-sided buckle, but the capacity was only reduced by 2 percent, despite the amplitude of the imperfection. This imperfection was discarded similarly to the other two local imperfection types.

The global imperfection was assumed to not affect the capacity or behaviour of the cylinder, both because the imperfection given as a multiple of the length was low and because the failure modes were assumed local. The difference was negligible, albeit the global imperfection was not discarded as it was believed to be important for longer cylinders.

The consequence of not inducing local imperfections on longer specimens, as well as the impact from the compression test results at L2000, is assessed and discussed in section 7.4.3.

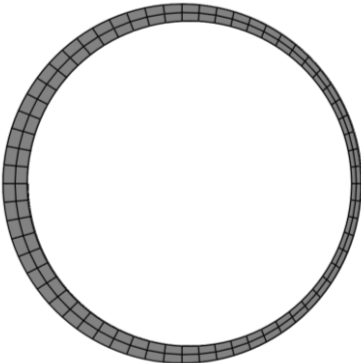


Figure 83 Cross-section with translated inner circle

7.4 Comparison of FEA model and executed compression tests

7.4.1 FEM Analyses of L2D and L4D

As the chosen parameter studies are discharged and the choices of the model is established, FEM analyses on the laboratory lengths are discharged for L2D and L4D. The mesh is chosen as 5 mm long C20R elements, with depth corresponding to two elements through thickness.

In section 7.3.2.4, the deviation with different imperfections for L2D and L4D was small, hence only imperfections a_1 and a_3 from (4.3) is presented. The stress – strain curves from laboratory tests and their FEA counterpart are shown in figure 84 to figure 86 and the corresponding force – displacement graphs are shown in Appendix H.

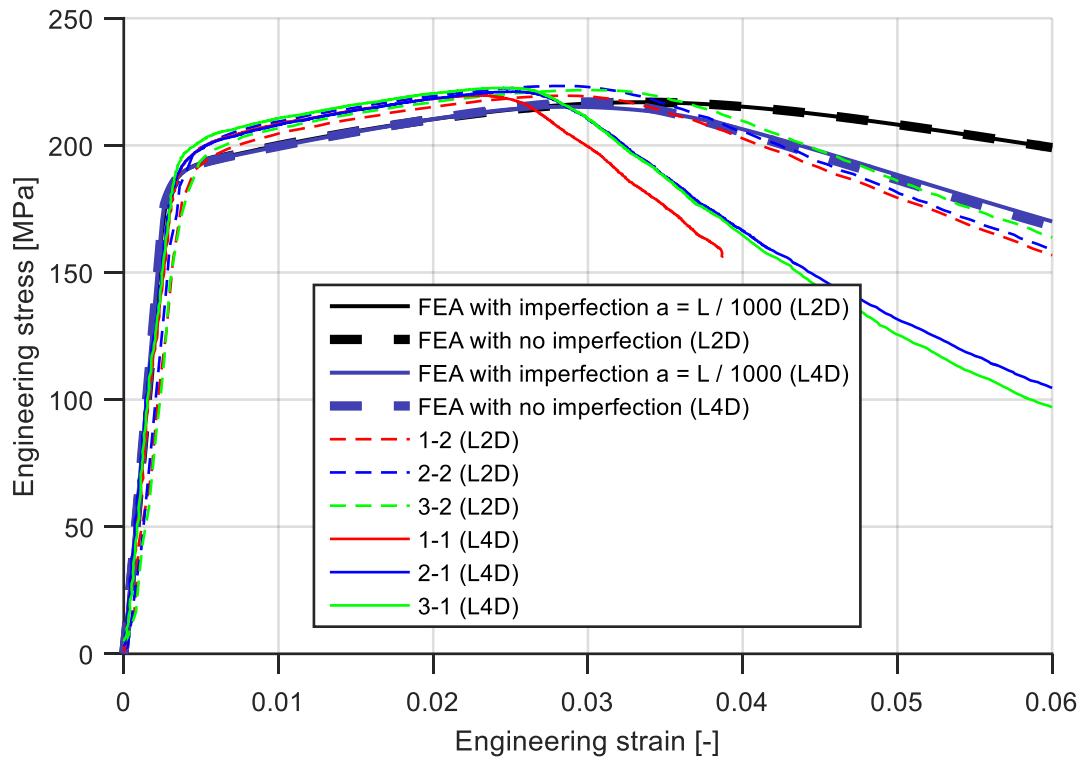


Figure 84 Stress – strain graphs from compression tests and FEA analyses for A6060D100L2D and A6060D100L4D

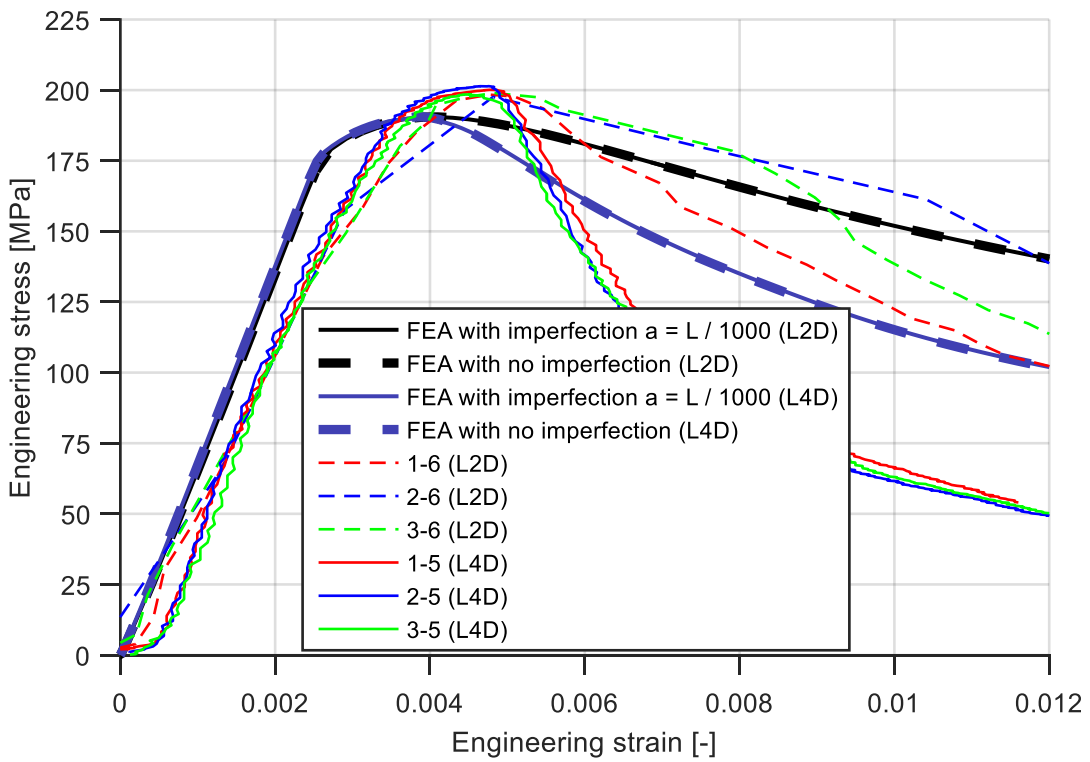


Figure 85 Stress – strain graphs from compression tests and FEA analyses for A6060D127L2D and A6060D127L4D

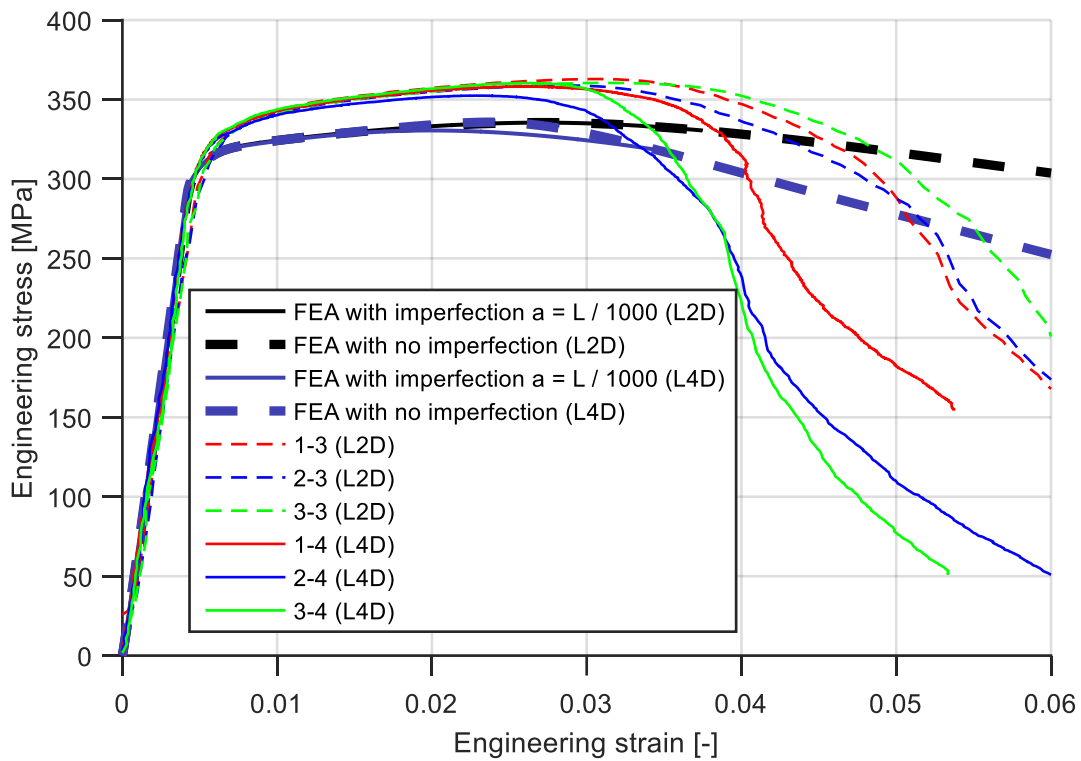


Figure 86 Stress – strain graphs from compression tests and FEA analyses for A6082D100L2D and A6082D100L4D

The general trends displayed are that the FEA results yields at slightly lower capacity compared to the compression tests (table 17), and the imperfections caused negligible differences in capacity. The plastic hardening spans across the same strain values, and buckling occurs at roughly the same strain but at lower stress (figure 84 to figure 86). The reasons for this underestimation of force may stem from wrong material modelling.

Table 17 Capacity of short column compression tests [kN]
FEA model with different imperfections and compression test results

	A6060 D100L2D	A6060 D100L4D	A6060 D127L2D	A6060 D127L4D	A6082 D100L2D	A6082 D100L4D
FEA, a_1	305.3	302.8	132.7	132.3	472.0	465.1
FEA, a_3	305.3	305.5	132.7	132.7	472.1	472.5
Compression tests	311.41	311.48	138.15	138.23	505.58	499.34

With no imperfections introduced to the FEA model, the deformation pattern at maximum load (figure 87) was similar to that seen in the laboratory for all profiles. Up to the point of maximum load, the deformation of the laboratory specimens was more or less symmetric, similar to the FEA solution. In post-buckling the largely symmetric FEA models deviated, as laboratory specimens buckled only on one end of the cylinder. Post-buckling behaviour is assumed to not affect capacity or pre-buckling behaviour, and is neglected herein.

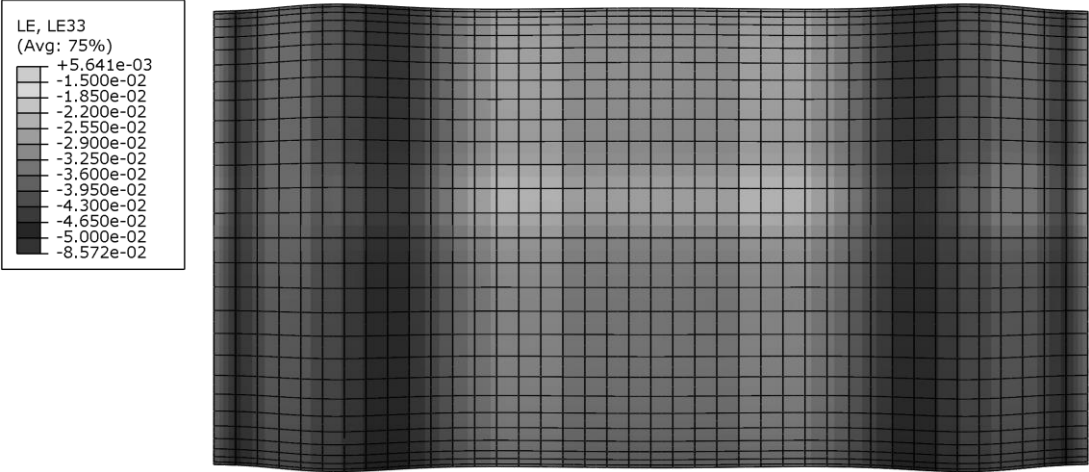


Figure 87 FEM contour plot of logarithmic strain at maximum load for A6060D100L2D

7.4.1.1 Tracking of radial displacement

A new way of comparing FEA results with laboratory tests is suggested: comparison of radial displacement. By applying 3D DIC to the tests, it is possible to compute the movement towards the camera for each node. One row of nodes spanning across the length of the cylinder is analysed – the row closest to the camera is chosen, so that any movement towards the camera is a radial displacement. At each end of the cylinder, there was an area that only one camera could observe throughout the test. The mesh in eCorr could only cover the part which was visible to both cameras, hence the outer-most parts of the mesh was not included. No marks were made on the specimen to specify where the mid-point of the specimen were, so there was no way to know if the mesh was placed symmetric or not. In order to plot the deformation of the surface an assumption was made: The pre-buckling deformations were symmetric, so that the two major buckles had equal distance to their closest end plates. With this correction, the deformation from eCorr could be plotted, and an example of this is shown in figure 88. The top and bottom buckle is of similar magnitude up to the point of maximum load.

One key finding in this figure is that the cylinder displays many tiny buckles before maximum load, as assumed in the derivations behind local buckling formulas in section 3.3.2. At

approximately 50 percent of the deformation of at maximum load, when the load was 97 percent of maximum, the major buckles at the ends of the cylinder started forming.

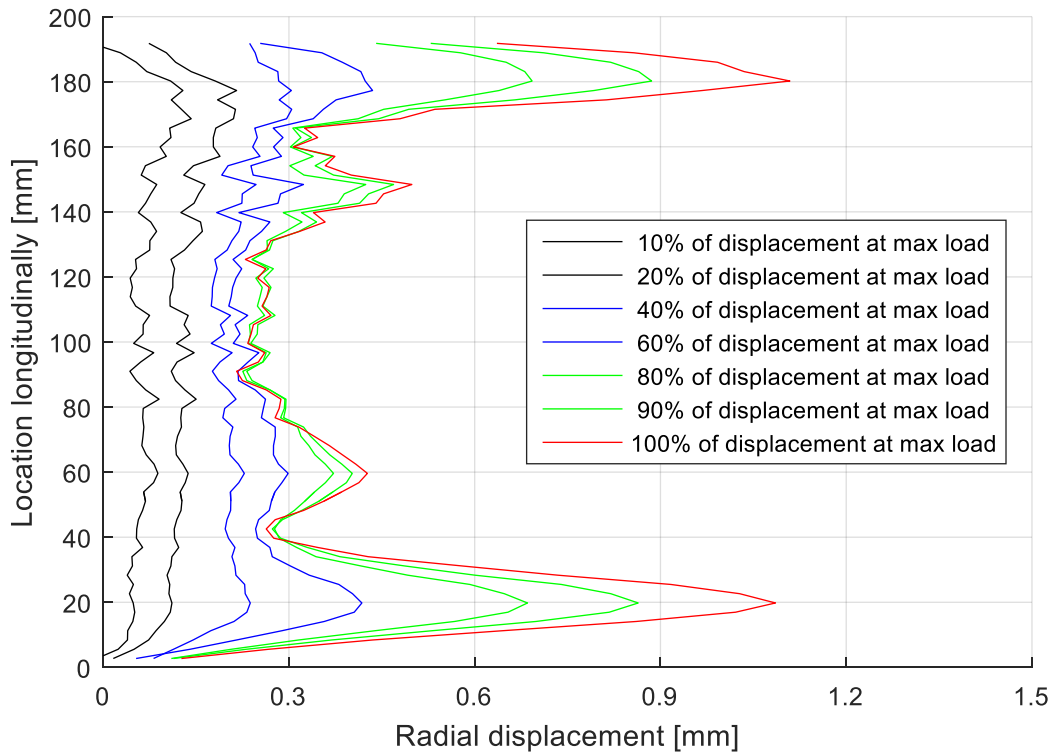


Figure 88 Radial displacement from DIC - A6082D100L2D.

As the post-buckling shape as well as the deformation of the equivalent nodes in Abaqus is introduced, it is seen that the FEM model is unable to represent the distance between the major buckles and the ends of the cylinder, however the buckle amplitude from DIC and FEA is of similar magnitude (figure 89). Greatly refining the mesh as well as lowering the friction coefficient did not cause a noticeable change of deformation pattern.

This type of graphs may in future work be helpful in assessing to what degree imperfections succeed at representing the correct failure mode from laboratory testing. High-quality cameras and a large variation in imperfection types could improve this process. For this thesis, however, these radial graphs are not used any further.

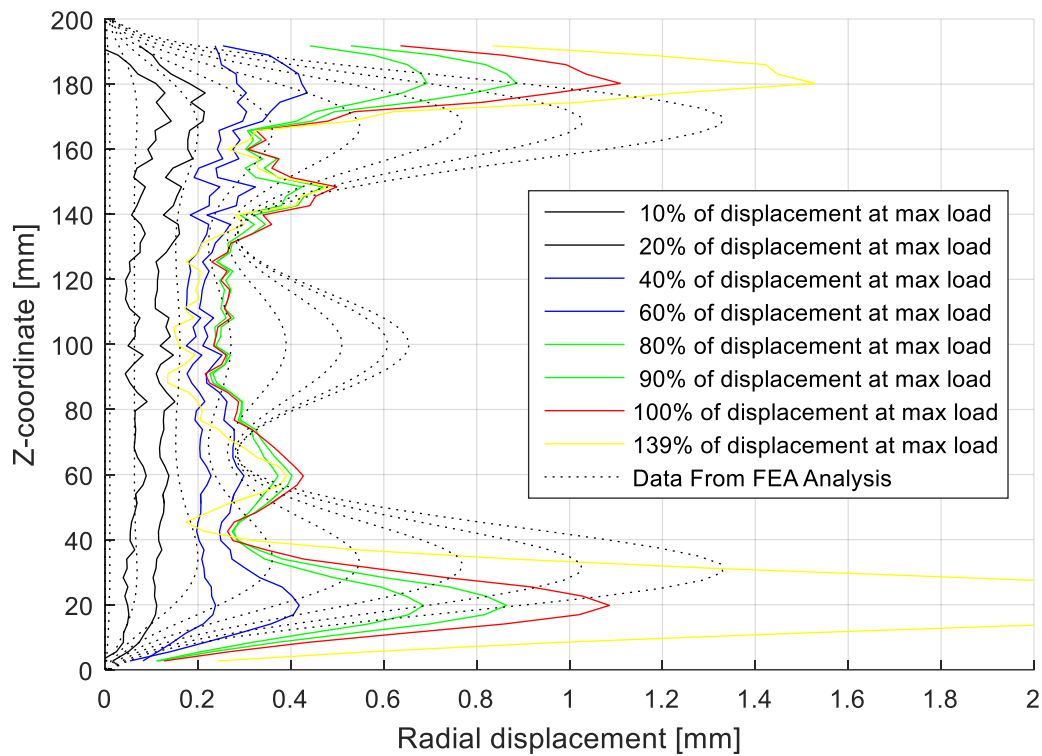


Figure 89 Radial displacement from DIC and FEA - A6082D100L2D

7.4.2 FEA model extrapolation

The established FEA model is extrapolated to find the capacity for lengths up to thirty times the diameter. This extrapolation into the globally buckling range (figure 10, range 3) requires the introduction of imperfections, as mentioned in section 4.1.1. These imperfection amplitudes are a_1 to a_3 from formula (4.3), implemented as global sinusoidal imperfections according to (4.1) for all series considered.

The relationship between the capacity of the FEM analyses and the length of the cylinders is shown in figure 90 and figure 91 for A6060D100, figure 93 and figure 94 for A6060D127 and figure 96 and figure 97 for A6082D100. These figures also show the capacity of the cylinders tested in the laboratory. Tabular data is shown in table h1.

For imperfection a_1 , the obtained deformed shape at maximum load is shown in figure 92, figure 95 and figure 98. The deformations are scaled up in the transverse directions. In order to give a good representation of the failure modes, different scaling is chosen for each analysis.

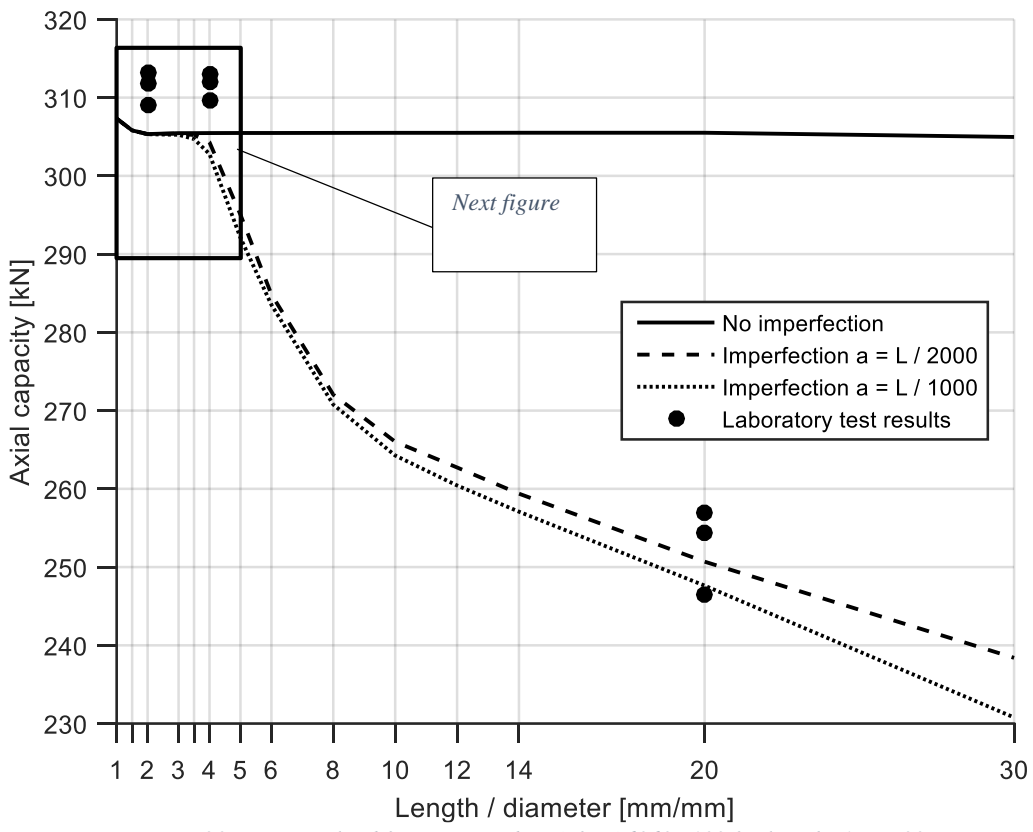


Figure 90 Maximum load from tests and FEA for A6060D100 for lengths 1D to 30D

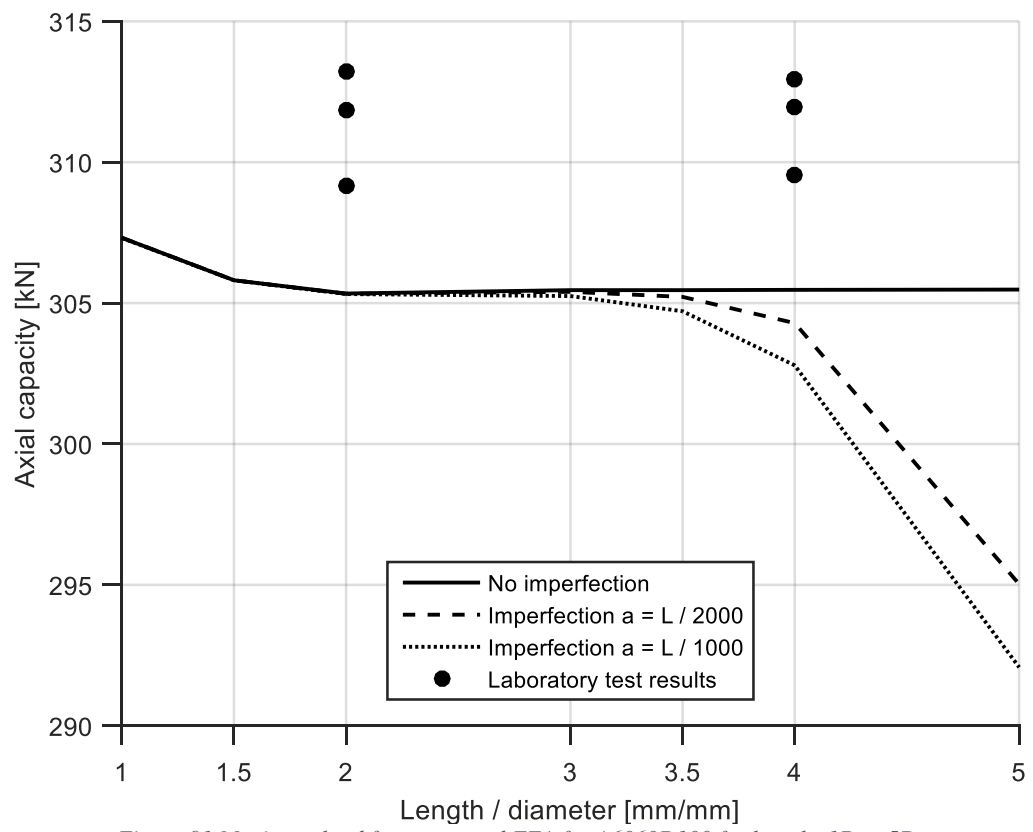


Figure 91 Maximum load from tests and FEA for A6060D100 for lengths 1D to 5D



Figure 92 Buckling-shape at maximum load for A6060D100 with imperfection $a = L/1000$

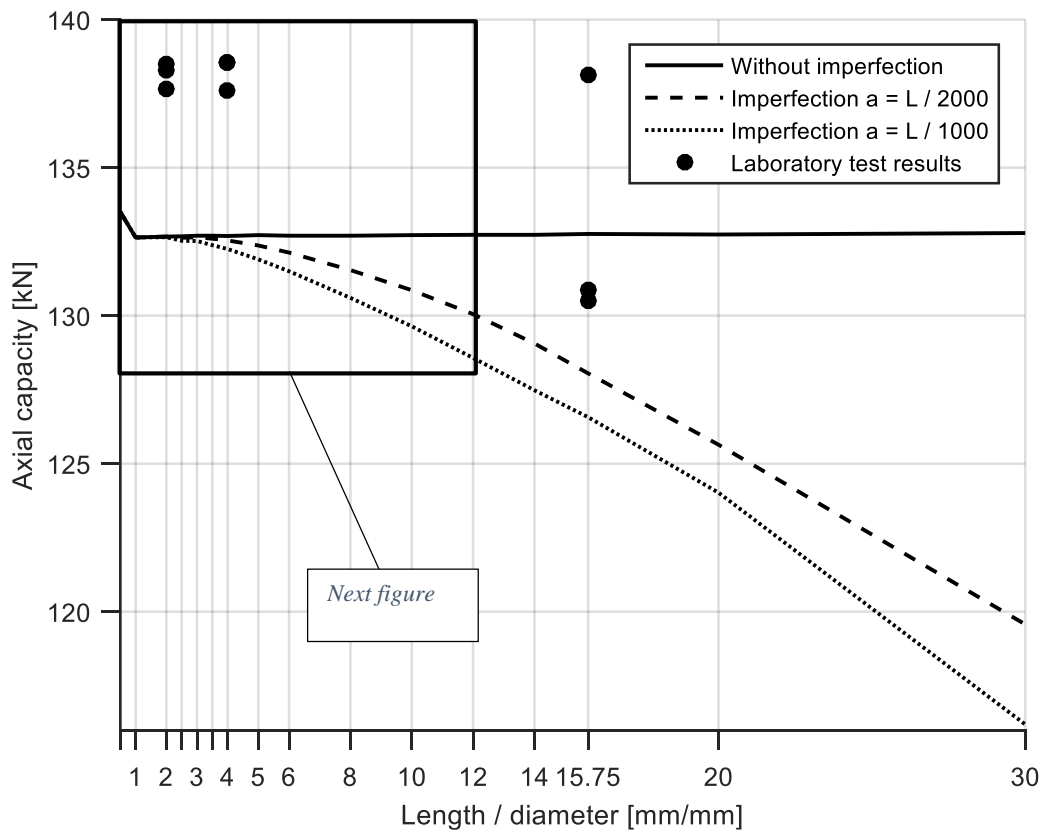


Figure 93 Maximum load from tests and FEA for A6060D127 for lengths 0.5D to 30D

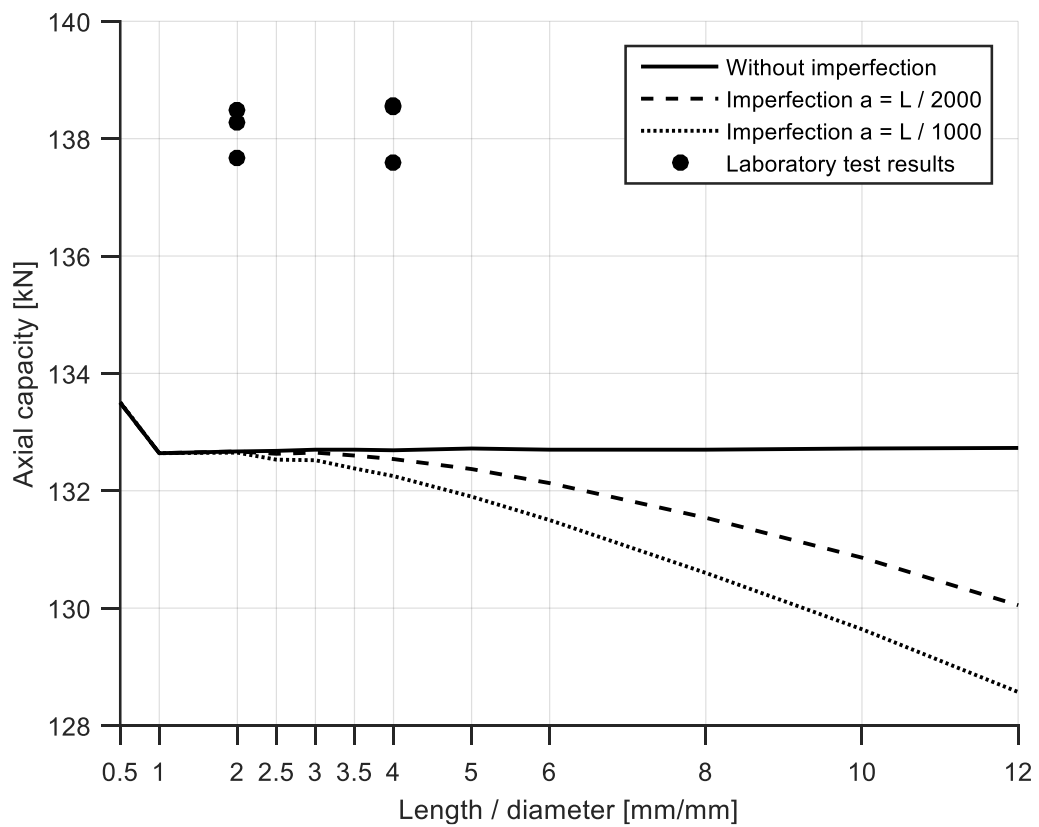


Figure 94 Maximum load from tests and FEA for A6060D127 for lengths 0.5D to 12D



Figure 95 Buckling-shape at maximum load for A6060D127 with imperfection $a = L/1000$

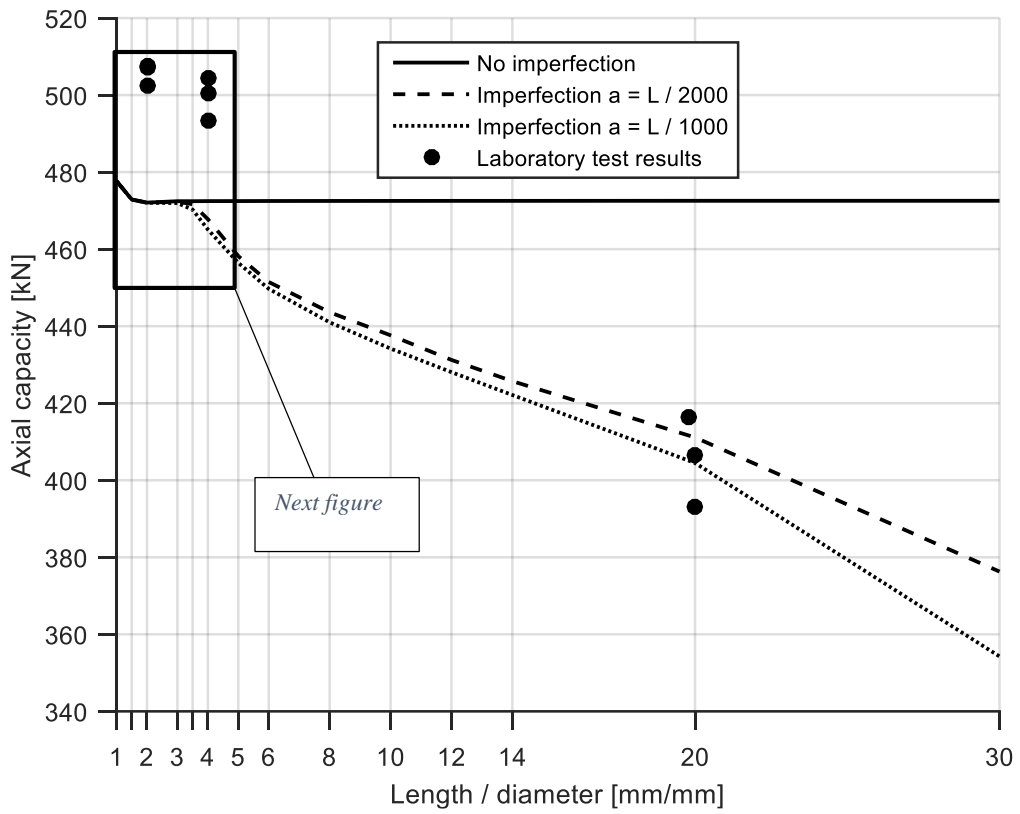


Figure 96 Maximum load from tests and FEA for A6082D100 for lengths 1D to 30D

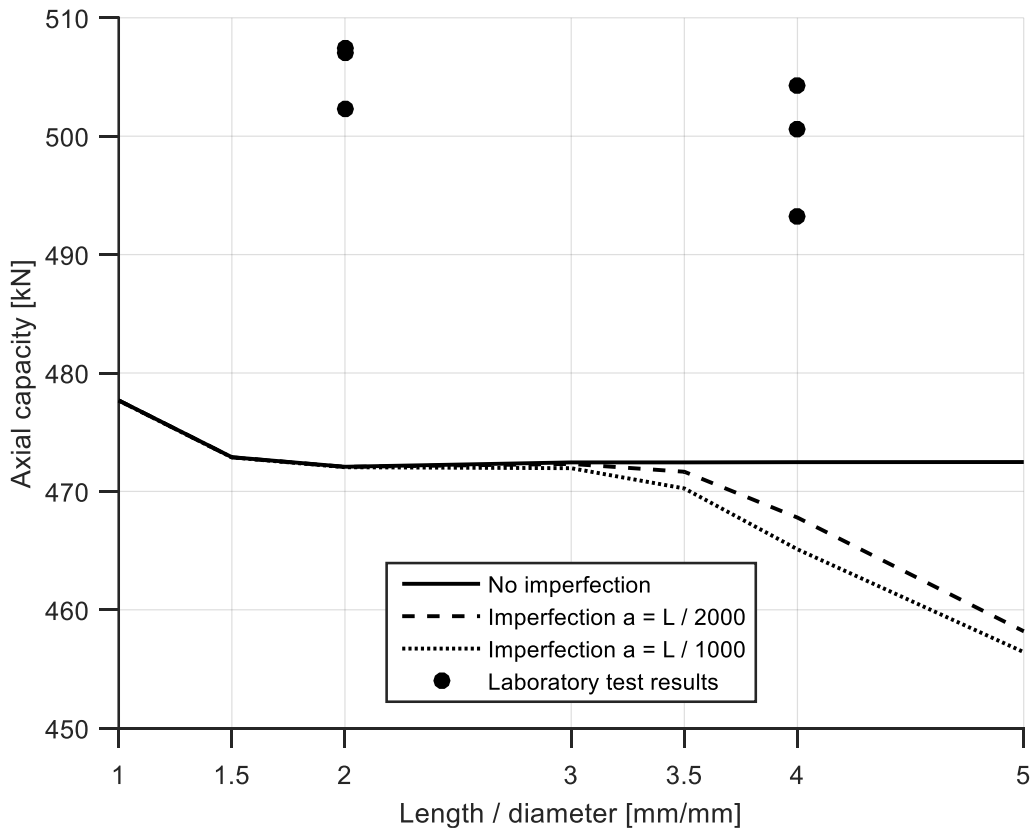


Figure 97 Maximum load from tests and FEA for A6082D100 for lengths 1D to 5D

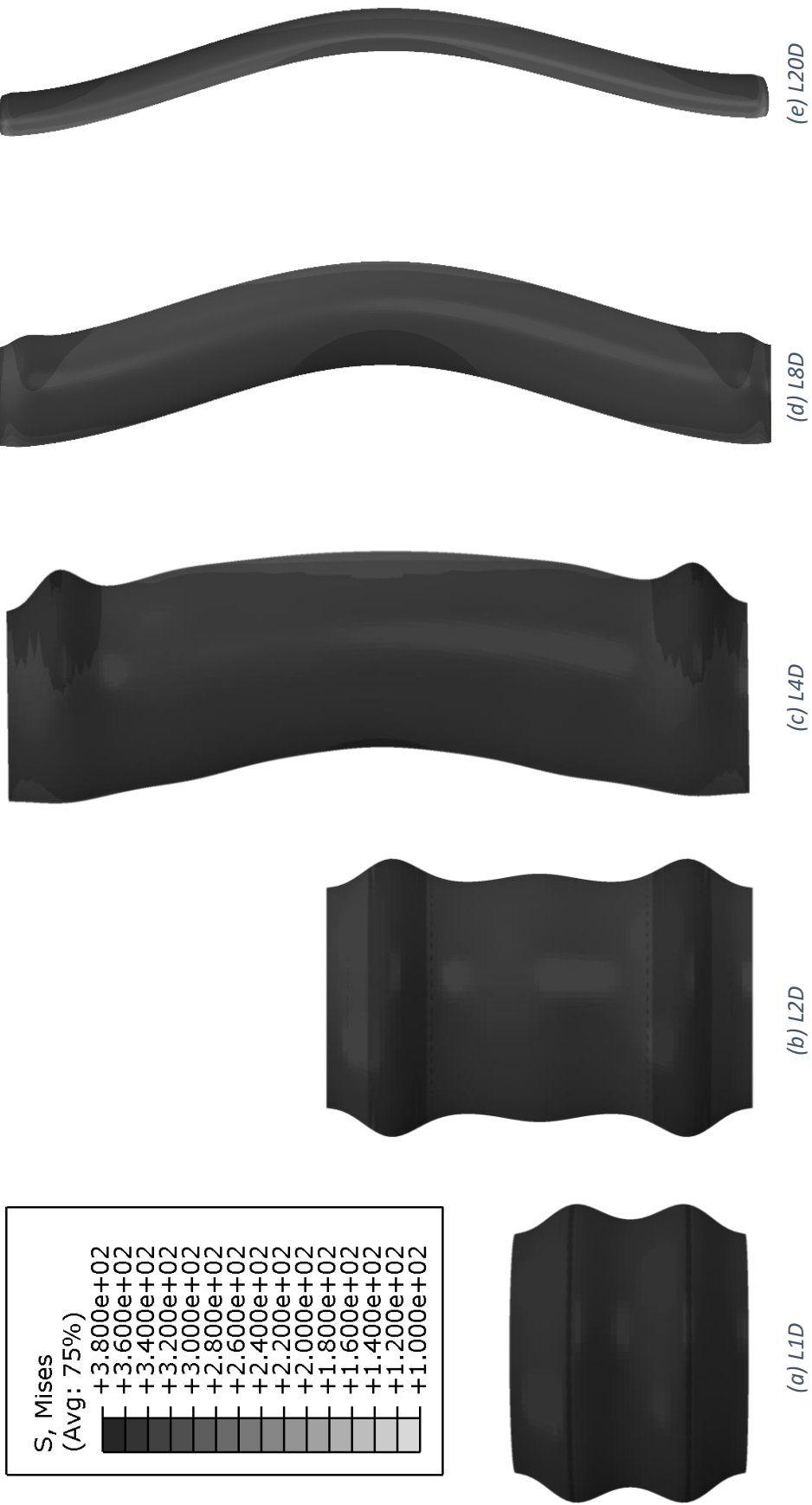


Figure 98 Buckling-shape at maximum load for A6082D100 with imperfection $a = L/1000$

The failure modes from the FEM analyses for L4D are local, but global imperfection still affect the capacity. A6060D100L4D has 1.6 percent lower capacity for L/1000 than for no imperfection, although both failure modes are dominated by local instability modes.

The FEA model generally fails at obtaining as much compression resistance as the laboratory specimens for L2D and L4D. For thick-walled cylinders, the accuracy of the FEA model was highest at L2000, indicating a good simulation of globally buckling columns. Local failure is largely dependent upon the plastic material properties, such as yield stress and hardening, while the global failure to a greater extent is dependent upon stiffness and geometry, and occurs at low plastic strains. The cause of the lack of accuracy on short columns therefore might be due to deficits in material modelling.

In figure 99 it is seen that the engineering yield stress for A6082T6 is lower for the tension test than the compression test, an indication that the material model based on tension test results is not well suited for modelling compression. The difference is roughly 5 percent, which is of the same magnitude as the capacity error for 6082D100L2D.

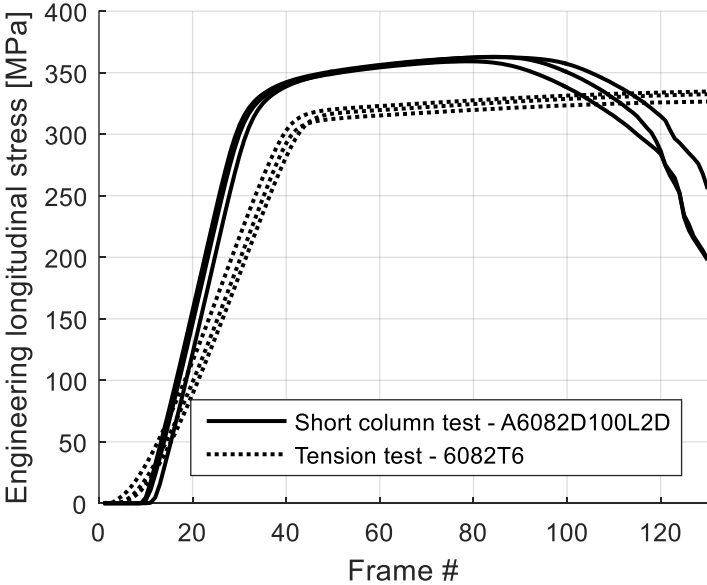


Figure 99 Comparison of stresses. Tension test results have been down sampled (fewer frames) for easier graph comparison

There are at least 5 sources of errors that might have caused this deviation:

1. As mentioned in section 3.2.4.1, the alloys might exhibit a strength differential effect which increases the strength in compression by several percent compared to tension. If this is the case, the tension tests are not suited for modelling compression properties.
2. Wire EDM was used to cut the tension test specimens. The area close to the cut might have been heat affected by the cut. Heat affecting lowers the ductility and strength of aluminium. If a heat affected zone was established during the cut, the mean strength measured from the tension test would be slightly lower than from a non-cut specimen.
3. The thickness of the tension specimens was measured by electronic calipers, which may have resulted in an overestimation of thickness, and consequently an underestimation of stress. The correction described in (7.5) was not applied, hence some overestimation took place.
4. The amount of tension tests was low, making the model prone to scatter among specimens. The seam welds may have affected some specimens, increasing the random error, thus leading to a deviation between the measured mean strength and the actual behaviour.
5. Some degree of human error might have affected the results. Great effort was put in double-checking calculations, derivations, scripts and measurements, but this source of error cannot be completely ruled out.

From figure 92 and figure 98 it is seen that the thick cross-sections display a pure global buckling shape at L8D, while L4D has a combined failure mode, indicating that this length is in the transition range for the FEA model. For A6060D127, the pure global buckling pattern is obtained for L20D, while L8D seems to be in the transition range (figure 95).

As insinuated in section 7.3.2.4, not introducing imperfections to the model can alter its behaviour. As seen in table 6, it was anticipated that A6060D127 would buckle locally for slightly longer specimens than the thick-walled cross-sections. The FEA model is highly dependent upon global imperfection for longer specimens. These imperfections were seen to be crucial for correct representation of A6060D100 (figure 90 and figure 91) and A6082D100, but caused faulty representation of A6060D127, which estimated global buckle prematurely. This effect is further studied in section 7.4.3.2.

7.4.3 FEM analyses of L2000

7.4.3.1 Analyses of A6060D100L2000 and A6082D100L2000

For L2000, the force-displacement graphs from laboratory tests is shown in figure 100 and figure 101, together with FEA results with imperfections a_1 , a_2 and a_3 .

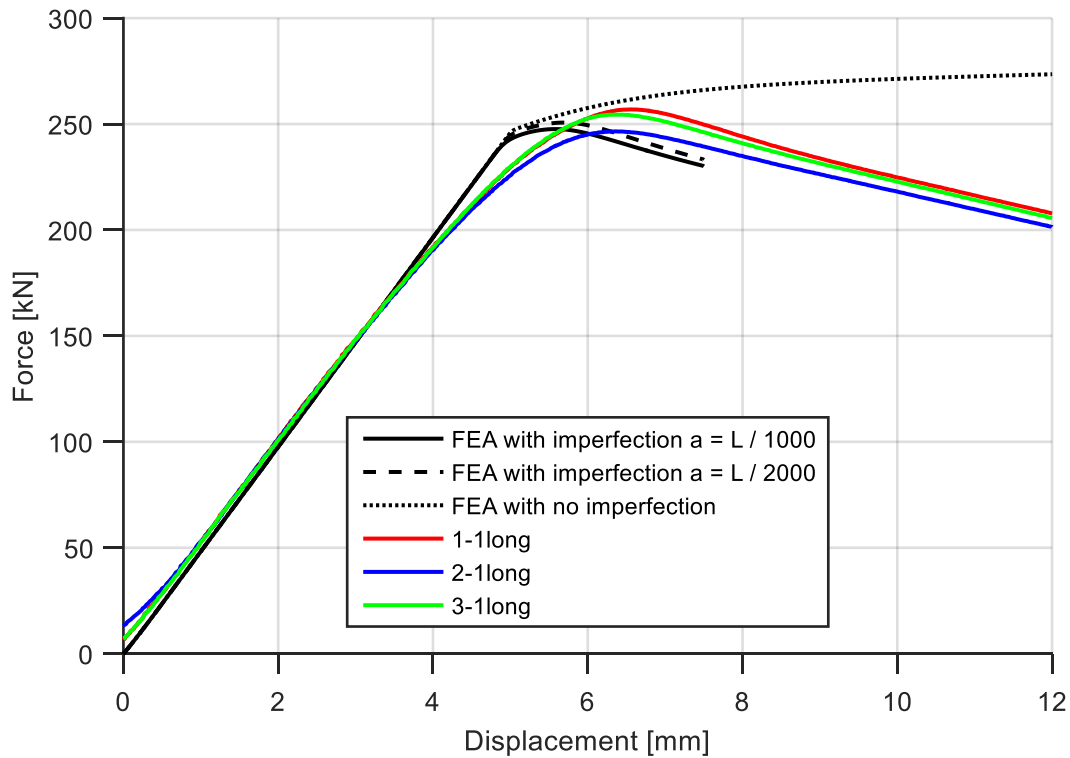


Figure 100 Force – displacement from compression tests and FEA, A6060D100L2000

A6060D100 and A6082D100 managed to accurately imitate the laboratory behaviour at L2000 with an imperfection of $a_2 = L/2000 = 1 \text{ mm}$, which is in good accordance to the recommendation from Mazzolani (section 3.4.1). The buckling mode of the model with imperfections was global, and the FEA results showed close resemblance to the behaviour of the test specimens. Before reaching maximum load there is a deviation in the force – displacement relationship, where the FEA solution is stiffer than the laboratory test specimen (figure 100 and figure 101). This effect is most noticeable on A6060D100, which has a lower yield stress than A6082D100.

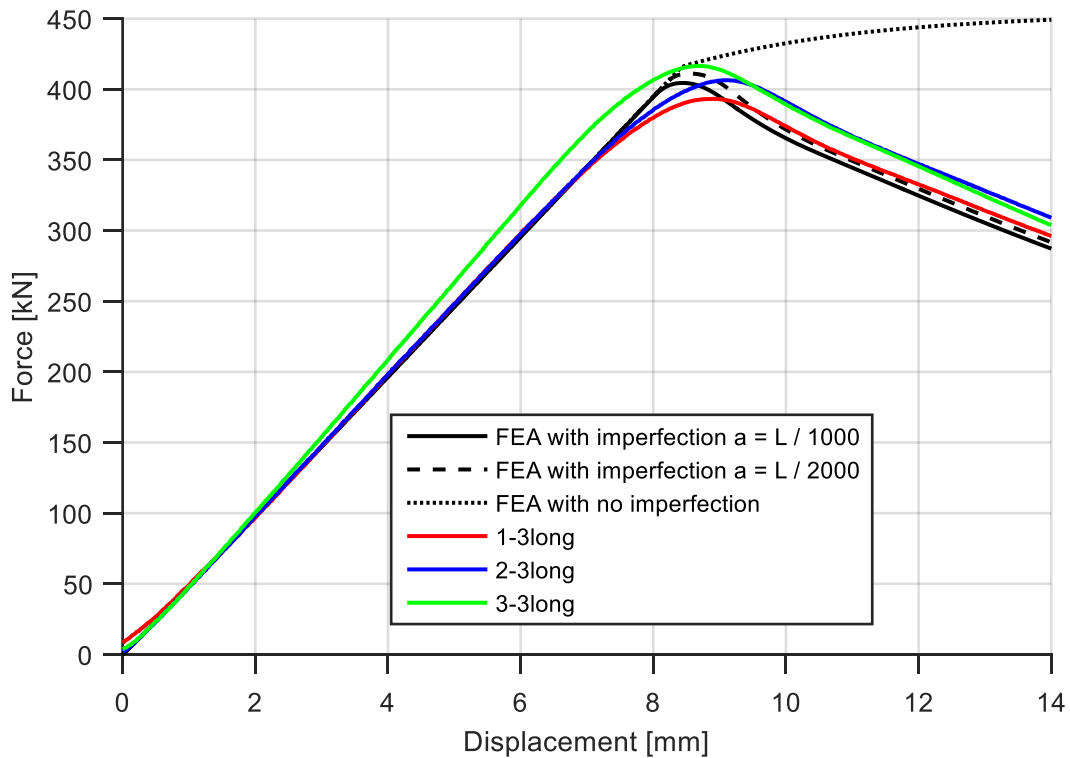


Figure 101 Force – displacement from compression tests and FEA, A6082D100L2000

An important discovery is the large deviation between low imperfection and no imperfection. Without any imperfection for A6060D100, the axial capacity was estimated 21.9 percent higher with a_3 than for a_2 , and this load was reached at 9.6 times as much deformation. The thick-walled cross-sections therefore require imperfection in order to correctly model global buckling.

Note that specimen 3-3 is somewhat stiffer and reaches a slightly higher capacity than the other specimens and analyses of type A6082D100 (figure 101). This might be because the length of this specimen was 1981 mm, not 2000 mm.

7.4.3.2 Imperfection analysis – A6060D127L2000

Compression tests of the profiles A6060D127L2000 exhibited local instability. FEA with imperfections a_1 and a_2 led the model to exhibit global buckle (similar to figure 95 (e)) and slight underestimation of capacity (figure 102). Analyses with no imperfection (a_3) gave buckling shape localized close to the end of the cylinder, closely corresponding to the observed failure mode from the compression tests. This analysis closely followed the force – displacement relationship seen in compression tests (figure 102). Modelling without any imperfection is not a robust solution, as any bifurcation (local or global) is hard to determine.

This is readily seen from the lack of reduction of capacity in figure 93. In order to predict the correct buckling shape, the slender A6060D127 would perhaps require a lower imperfection than the thick-walled cross-sections, due to a lower value of $\frac{t}{r}$.

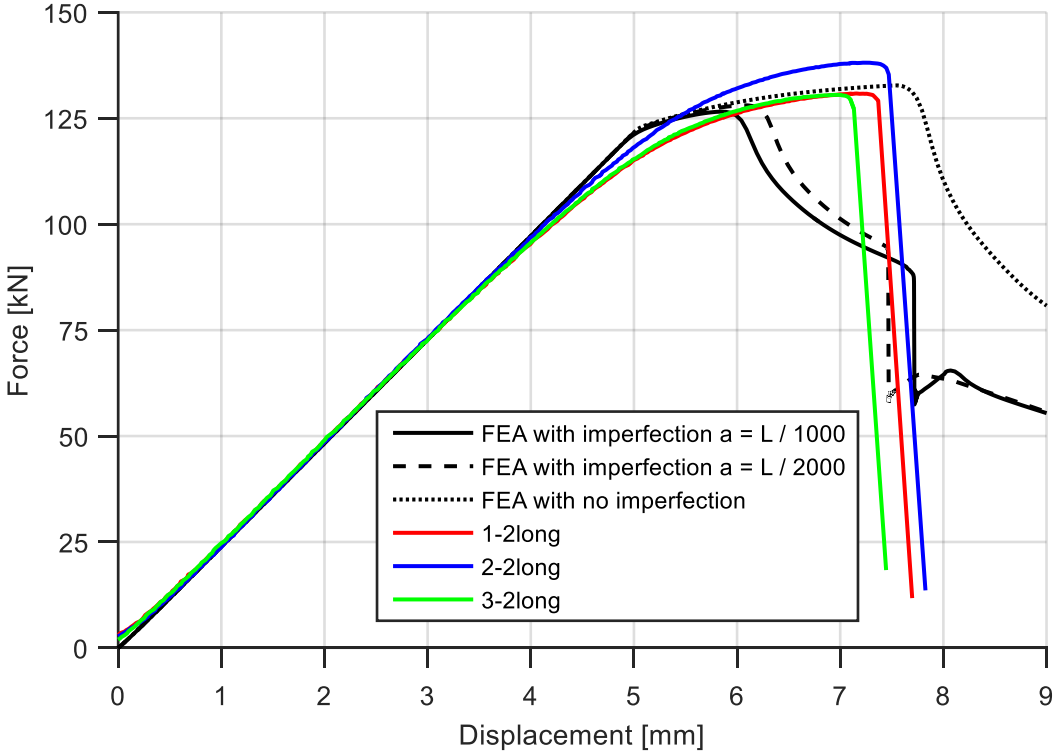


Figure 102 Force - displacement from compression tests and FEA, A6060D127L2000

New analyses with global imperfections $\frac{L}{5000}$, $\frac{L}{10000}$, $\frac{L}{20000}$ and $\frac{L}{100000}$ are carried out. All imperfections led to global buckling pattern, underestimating capacity and predicting failure at a lower deformation (figure 103). Lowering the amplitude of the imperfection resulted in higher capacity (figure 104), but the model is far from robust when an imperfection of $\frac{L}{100000}$ can change the failure mode into an erroneous one.

In order to improve the model for A6060D127, another measure of imperfection could be implemented. A modification of the vase-shaped imperfection can perhaps solve this problem. Global imperfection seems to be necessary to model global failure modes correctly, but as displayed in figure 103, the global mode can override the local mode erroneously. In section 7.3.2.4 it was seen that small local imperfections did not alter the capacity at L2D. For longer, locally buckling columns such as A6060D127L2000, these imperfections (in combination with

the necessary global imperfection) may suppress premature estimations of global buckling, possibly leading to the correct failure mode but not increasing the capacity. This interaction might require a thorough study of the mechanisms occurring in cylinders up to the point of buckling. This may be complex as the governing imperfection mode is not necessarily identical to the post-buckling shape, hence finding a good imperfection from compression test results may be difficult. After the longest compression tests were carried out, there was not enough time for the authors to test out this new hypothesis on imperfections.

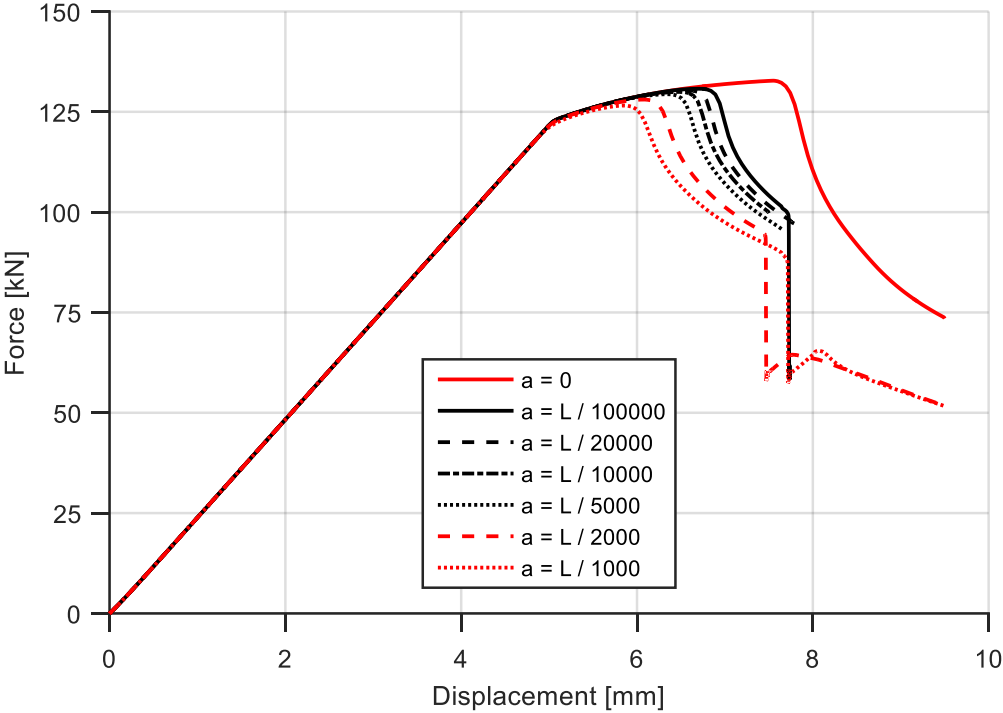


Figure 103 Global imperfection amplitude study for A6060D127L2000

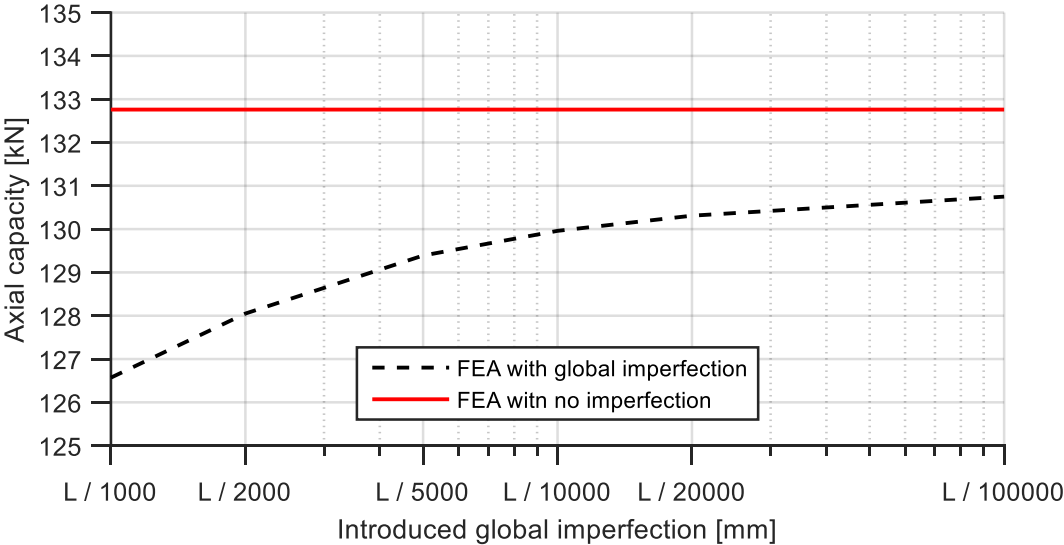


Figure 104 Reduction of global imperfection in FEA model for A6060D127L2000

Premature global instability in the FEA model was only observed for the thin-walled cross-section for the lengths tested in laboratory. In order to establish whether or not this occurs for the thicker cross-sections, more laboratory tests in the transition range (5-8 times the diameter) could be carried out.

It is possible that the interaction between local and global buckling modes on thin cross-sections is best carried out with flexural shell elements, such as S8R. Explicit solution algorithm would perhaps improve the simulations due to its short time increments. These topics are not further investigated.

7.5 Comparison of Eurocode 9 and laboratory

The capacity estimates from Eurocode 9 were lower than the observed capacity from compression tests. The deviation was largest on the shortest cylinders; this lack of accuracy is assumed to stem from two sources. Firstly the Eurocode does not allow stresses above f_0 . This constraint can cause significant underestimations on cross-sections that obtain the most plastic strain. From figure 56, figure 59 and figure 62 as well as the cross-sectional slenderness factor β , it is concluded that this underestimation affect A6060D100 and A6082D100 the most.

The second source of underestimation on short lengths is the conservative formulas in Eurocode 9 part 1-5, predicting a very low membrane buckling stiffness for shells. Its main deviation from other theoretical sources is the reduction factor C_x , causing a reduction of the critical meridional buckling stress by up to 40 percent. This led to estimated capacity of the cylinders to be slightly lower than observed in laboratory (table 18). This underestimation is most prominent in the cross-section which is most prone to meridional buckling, which is the cross-section with the highest local slenderness factor β : A6060D127.

Eurocode 9 anticipates only a low reduction of capacity as the length is increased from L2D to L4D, in good accordance to laboratory tests. The lack of accuracy is similar on L2D and L4D (table 18).

The globally buckling cylinders do not obtain as much hardening, which may explain why the underestimation from Eurocode 9 (table 18) is lower than for the other predictions.

The accuracy of the Eurocode varies with length; hence it is not only caused by a constant safety margin. This reduces the precision of the Eurocode, which at short lengths cause the code to exploit only an amount of the strength of the structural member.

Table 18 Axial capacity and buckling mode according to Eurocode 9 part 1-1, part 1-5 and compression tests

	A6060D100			A6060D127			A6082D100		
	L2D	L4D	L2000	L2D	L4D	L2000	L2D	L4D	L2000
$N_{b, rk, part1-1}$ [kN]	270.2	270.2	245.3	133.3	133.3	125.3	443.3	440.9	381.2
$N_{x, rk, part1-5}$ [kN]	-	-	-	119.2	118.5	112.1	420.0	415.2	394.7
EC 9 predicted buckling mode	X	X	G	L	L	L	L	L	G
$\bar{N}_{laboratory}$ [kN]	311.4	311.5	252.6	138.2	138.2	133.2	505.6	499.3	405.4
Laboratory test buckling mode	L	L	G	L	L	L	L	L	G

The buckling modes assumed from Eurocode 9 and the compression tests are also seen in table 18 (based on L_G^{EC} from table 6) where G indicates global buckling mode, L a local mode and X indicates that buckling does not affect capacity. In the latter case, Eurocode assumes that the cross-section reaches its capacity, and that buckling occurs in the subsequent deformation, which does not increase the axial resistance of the cylinder. The post-buckling mode of this model is corresponding to the local failure mode. Eurocode 9 therefore predicts correct failure mode for all laboratory specimens.

7.5.1 Local slenderness

The local slenderness according to Eurocode 9 defined in formula (C.6), with $C_1 = 32$ and $C_2 = 220$ (table c1). For short thin-walled cylinders without welds, the axial capacity can be written as

$$N_R = \rho_c f_0 A_0 \quad (7.10)$$

For the laboratory tests at L2D and L4D, this reduction factor is estimated by

$$\rho_c = \frac{N_{cr}}{A_{eff} f_{0.2}} = \frac{\sigma_{cr}}{f_{0.2}} \quad (7.11)$$

Note that this reduction factor is only valid when global instability does not reduce the capacity. The results are shown in figure 105, the difference between the laboratory results and the Eurocode is explained mainly by the inability of plastic hardening in the code.

The estimates according to Eurocode 9 are somewhat conservative, as seen by A6060D127 which is of cross-sectional class 4 but obtains $\rho_c > 1.0$. A hypothetical extrapolation of the class 4 curve seems to fit with the points plotted, but Eurocode is restricted to $\sigma \leq f_0$, therefore not allowing $\rho_c > 1.0$.

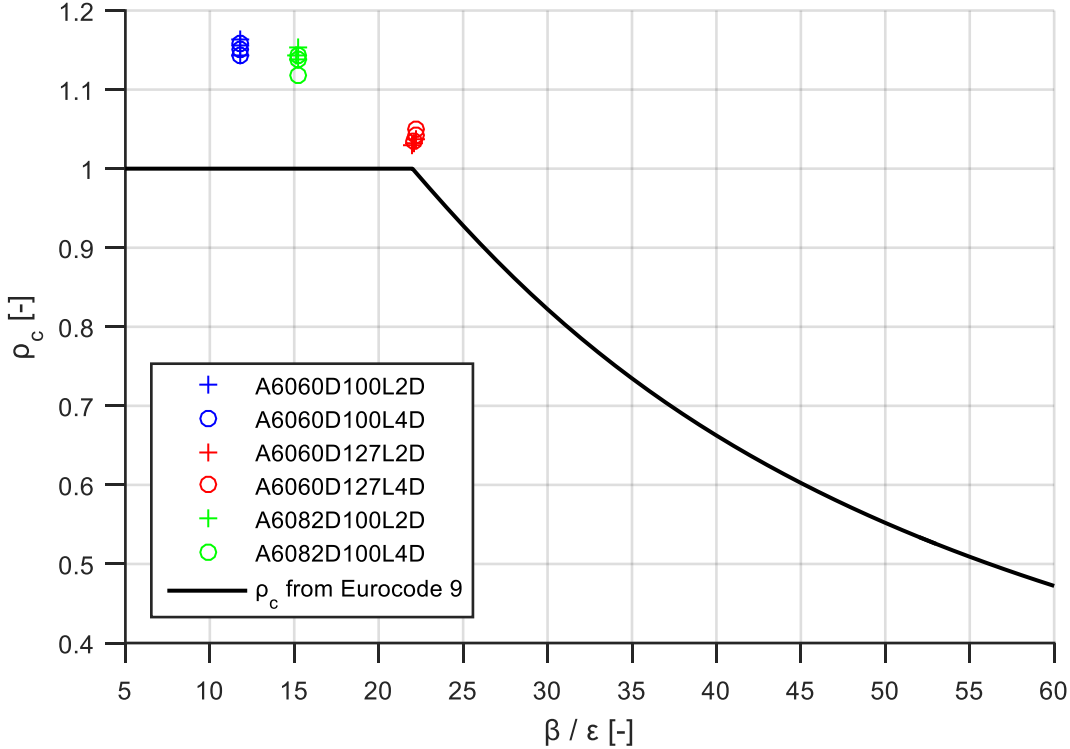


Figure 105 Buckling reduction factor according to Eurocode 9 and estimated from compression tests L2D and L4D

7.6 Comparison of theoretic approaches and compression tests

Based on the compression tests, the accuracy of the formulas and equations from chapter 3 can be studied. Data from table 6 predicts inelastic buckling modes for the cylinder lengths tested in laboratory, and the capacity of the cylinders are governed by formulas for local (3.54) and global (3.35) buckling.

Instability is defined as the point where the cylinder stress is equal to the critical stress from either one of these two formulas. Because of the inelasticity, both the cylinder stress and the buckling stresses are function of the strains. The local buckling criterion relates to the moduli based on plastic strains while the global criterion relates to the tangent modulus based on the

total strains. The Voce hardening curve (figure 44) is given as a function of the plastic logarithmic strain, but plotted against the total engineering strain. Formula (3.10) is applied to calculate ε from ε^{Pl} and σ , then formulas (3.4) and (3.6) are used to calculate e and s from ε and σ .

Stresses and strains are calculated from the force and displacement recorded from compression tests. Based on these data sets, the plastic secant stiffness was calculated from formula (3.15) and a plastic tangent stiffness was calculated similar to that in chapter 6:

$$E_{T,n}^{Pl} \approx \frac{\sigma_{n+1} - \sigma_{n-1}}{\varepsilon_{n+1}^{Pl} - \varepsilon_{n-1}^{Pl}} \quad (7.12)$$

From these data points, at any strain ε_n^{Pl} a corresponding critical buckling stress $\sigma_{cr,Pl,n}$ was calculated from formula (3.54) for each specimen. These results were smoothed using the moving average method, and are shown in figure 106 to figure 108. In these figures, an analytical result is shown as well, obtained by using parameters from the Voce hardening rule (table 9) and formula (3.29). The global inelastic buckling stress is calculated from the Voce parameters as well, but only shown for the lengths L4D and L2000, as L2D rendered too high capacity to be shown in the figure.

The global and local instability formulas relate to the longitudinal stresses and strains. Voce hardening rule relates the equivalent Mises stress σ_{Eq} from formula (3.26) to the accumulated plastic strain p defined in formula (3.27). In a uniaxial stress state, these would be equal to the longitudinal components. Simulations from FEA shows that the hoop stress in general is low and the radial stress is negligible. For short, locally buckling cylinders, the most critical elements (placed in the middle of the buckle) accumulates some hoop stress, increasing the equivalent stress by 20-30 percent. As a simplification, this effect is neglected. The graph displaying Voce hardening stress as a function of plastic strain therefore only relates to the longitudinal components.

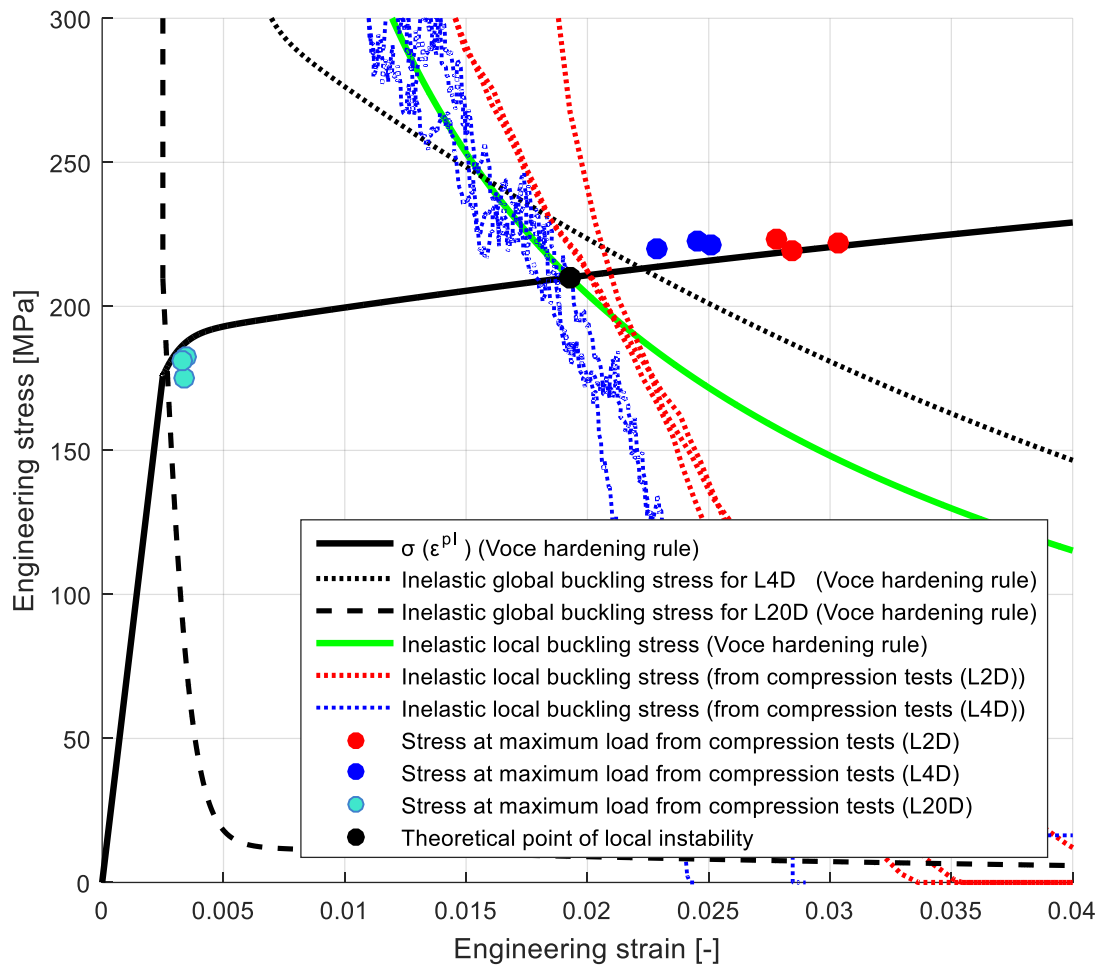


Figure 106 Inelastic instability criteria and laboratory results - A6060D100

Based on data at the point of maximum load for each specimen tested in laboratory, the stress and strain is plotted as points in the graphs. The intersection between the Voce stress curve and the smooth theoretical inelastic local buckle is shown with a black filled circle, this stress was given as σ_{cr}^{pl} in table 6.

The full summary of obtained stresses and failure modes (as in section 7.4.3) are shown in table 19.

The accuracy in terms of estimated failure strain was best for A6060D127, which missed with at most 0.15 percent of the engineering failure strain observed in tests.

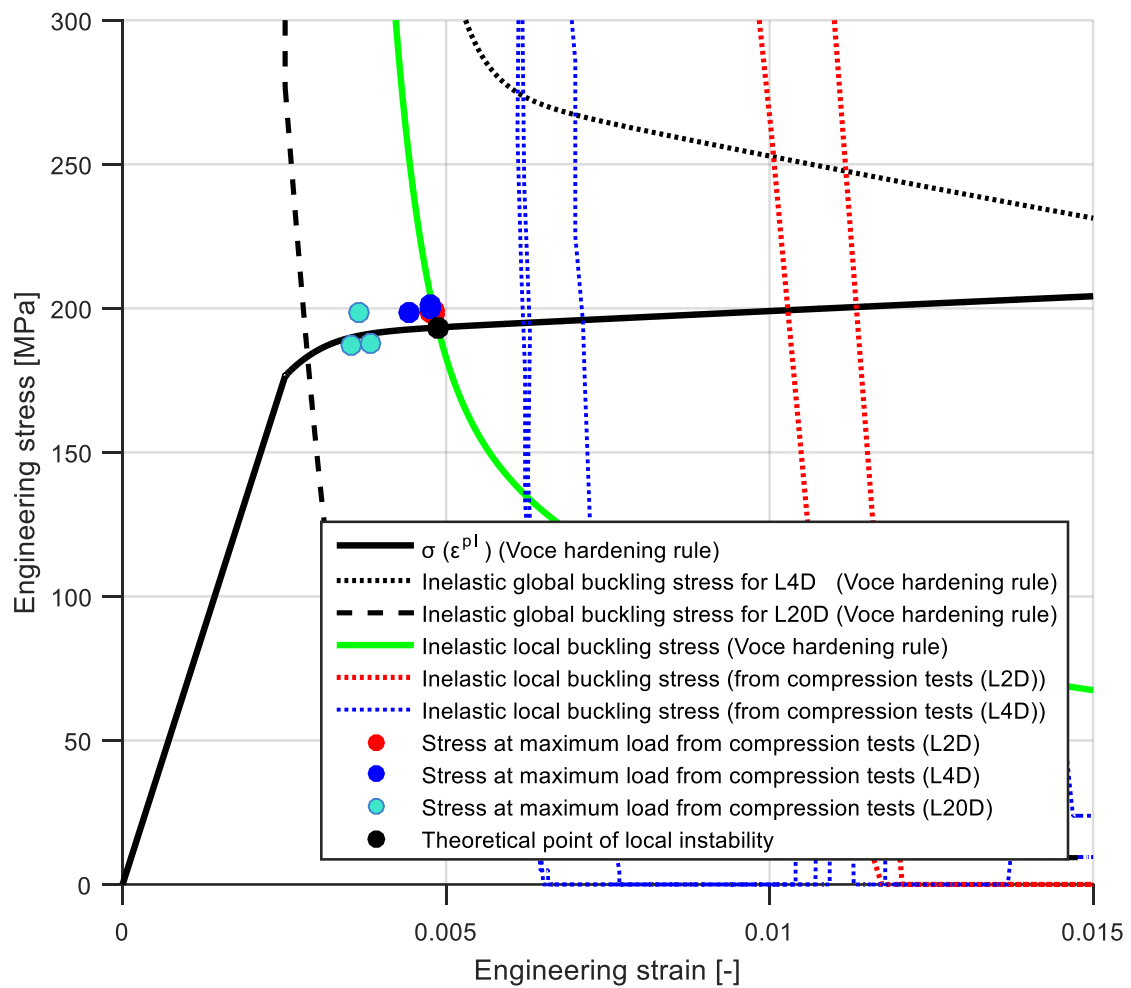


Figure 107 Inelastic instability criteria and laboratory results – A6060D127

For the longest specimens, the graph showing the criterion for global buckling crosses the stress graph at lower stresses than the local buckling graph. This is the graphical proof that the theoretical approaches estimate global buckling at this length. The accuracy regarding capacity was high for all L2000 specimens, and for A6082D100 the capacity was overestimated (table 19). This accuracy is believed to stem from the dependency upon elastic properties rather than plastic, as the failure occurs at very low plastic strains. Global buckling was also predicted for A6082D100L4D, but the accuracy of this estimate was flawed as it estimated global buckling at an engineering strain of 0.8 percent, while the observed failure mode is local with roughly 2.5 percent.

The observed failure modes for A6082D100L4D and A6060D127L2000 were local, hence the predictions were wrong.

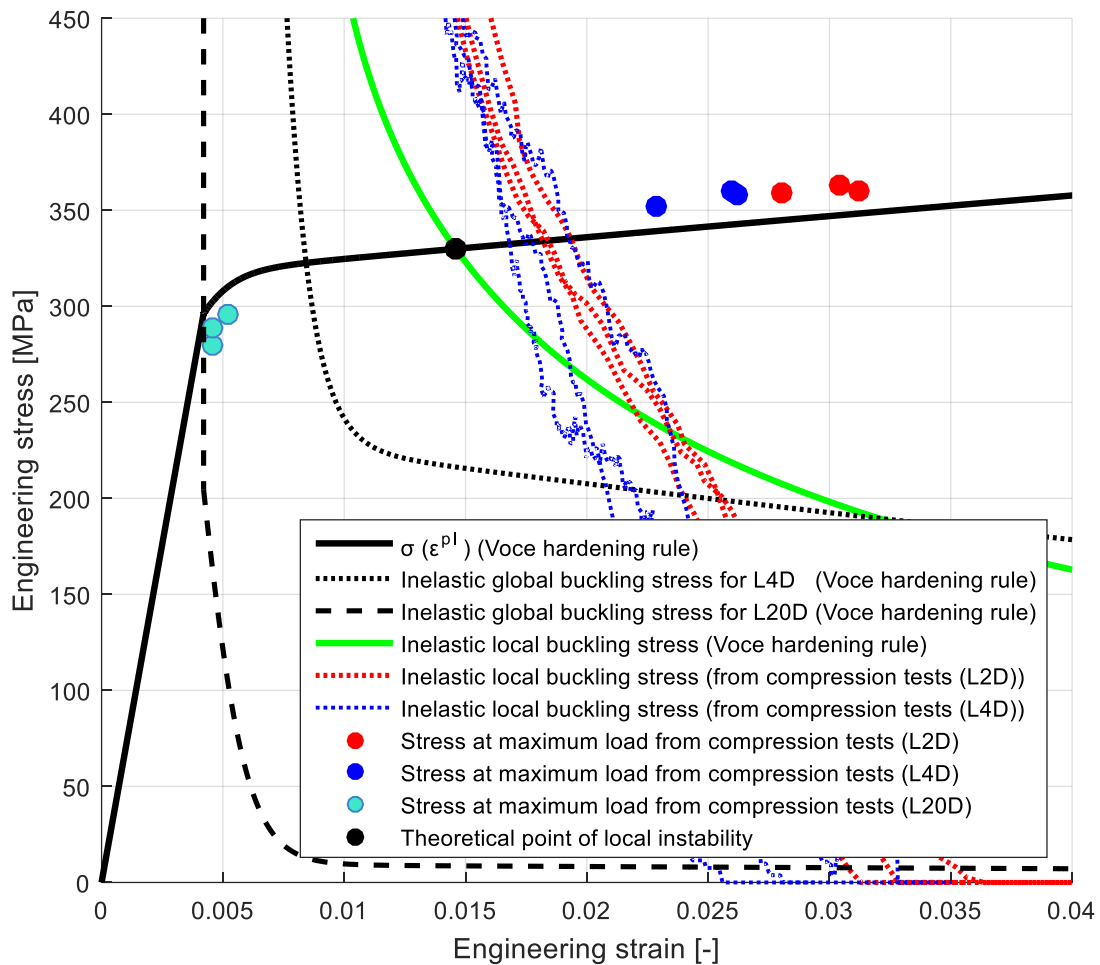


Figure 108 Inelastic instability criteria and laboratory results - A6082D100

The theoretical approach chosen models inelastic local buckling through formula (3.54) and gives the most accurate results for the cross-section most prone to local buckling, A6060D127 (table 19). The accuracy declines to a deviation of roughly 5 percent as the cross-section becomes thicker (A6060D100) and misses by almost 10 percent (table 19). for the strongest material (A6082D100). Deviations could indicate wrong material modelling, as mentioned in section 7.4.1. Applying formula (3.54) with empirical data from the compression tests by using formula (7.12) did not increase the accuracy except for A6082D100. Formula (3.54) therefore underestimates capacity for the given laboratory specimens.

According to NACA (section 3.3.2), the pre-buckling phase is characterized by m small buckles (formula (3.56)) spread evenly across the length of the cylinder. At buckling, one of these will dominate in an instability failure. Equation (3.56) estimated $m = 9$ half buckles L2D (4 or 5 outwards buckles) and twice as many for L4D, but figure 60 show 7-8 buckles for both lengths.

This error might be due to the erroneous assumptions behind the formulas derived by NACA, such as frictionless BCs.

Table 19 Estimated and observed capacity and failure mode

	A6060 D100 Estimated	A6060 D100 Observed	A6060 D127 Estimated	A6060 D127 Observed	A6082 D100 Estimated	A6082 D100 Observed
L2D capacity [kN]	295.5	311.4	134.6	138.2	464.2	505.6
L2D failure mode	X	L	L	L	L	L
L4D capacity [kN]	295.5	311.5	134.6	138.2	454.0	499.3
L4D failure mode	L	L	L	L	G	L
L2000 capacity [kN]	251.6	252.6	127.7	133.2	416.8	405.4
L2000 failure mode	G	G	G	L	G	G

7.7 Comparison of all approaches

7.7.1 Results for L2D, L4D and L2000

This section aims to analyse and compare the four sources of information: the compression test results, theoretical estimates, characteristic capacity from Eurocode 9, and FEA results. The engineering stress at maximum load shown in table 20 displays to what degree the different approaches succeed in predicting laboratory behaviour. The stresses at maximum load are presented in table 20 with an error measurement chosen as:

$$\epsilon_i = \frac{\sigma_{\max,i} - \sigma_{\max,lab}}{\sigma_{\max,lab}} * 100\% \quad (7.13)$$

Table 20 Measured and predicted buckling stress (engineering longitudinal stress)

	A6060D100			A6060D127			A6082D100		
	L2D	L4D	L2000	L2D	L4D	L2000	L2D	L4D	L2000
$\bar{S}_{max,laboratory} [MPa]$	221.29	221.36	179.51	198.45	198.45	191.27	359.3	354.82	288.09
$S_{max,FEA} (a = 0) [MPa]$	216.98	217.1	217.1	190.5	190.5	190.6	335.5	335.8	335.8
$\epsilon_{S_{max,FEA}} (a = 0) [\%]$	-1.946	-1.936	20.942	-4.001	-3.987	-0.33	-6.63	-5.374	16.564
$S_{max,FEA} (a = L / 2000) [MPa]$	217.0	216.2	178.1	190.5	190.3	183.9	335.5	332.4	292.1
$\epsilon_{S_{max,FEA}} (a = L / 2000) [\%]$	-1.949	-2.315	-0.756	-4.001	-4.096	-3.866	-6.632	-6.311	1.4085
$S_{max,Eurocode 9} [MPa]$	192.01	192.01	174.32	171.17	170.16	160.97	298.47	295.05	270.89
$\epsilon_{S_{max,Eurocode 9}} [\%]$	-13.23	-13.26	-2.89	-13.75	-14.25	-15.84	-16.93	-16.84	-5.969
$S_{max,theory} [MPa]$	210.0	210.0	178.8	193.3	193.3	183.3	329.9	322.6	296.2
$\epsilon_{S_{max,theory}} [\%]$	-5.102	-5.133	-0.393	-2.595	-2.595	-4.167	-8.181	-9.08	2.8152

In general, all approaches displayed good accuracy at predicting maximum load. Eurocode was the only theoretical source that accurately predicted the buckling mode obtained from the compression tests, although the predicted stress was inaccurate compared to FEM analyses and the results from theoretical formulas. Its deviation is seen in the local slenderness reduction factor from figure 105, hence if the graph for ρ_c was extended, the accuracy of the code would be greatly improved.

All sources of predictions gave good estimates of the global buckling pattern and capacity for long, thick-walled cylinders (table 20).

No global buckling shape was observed for A6060D127, and the high local slenderness might have been the cause for lower accuracy on this cross-section from all sources except NACA, which deviated with only 4.2 percent.

The largest scatter in capacity estimates are found for A6082D100, which both included the least accurate estimate and the only overestimations of capacity (not considering FEA without imperfections). The theoretic approach wrongly predicted global buckling at L4D, and all estimates for capacity at L2D and L4D missed by more than 6 percent. The material modelling was possibly worse for this material than for the other two.

The highest accuracy is in general found for A6060D100, where FEM simulations displayed roughly two percent deviation from compression tests results.

7.7.2 Results for all lengths

Figure 109 to figure 111 shows the calculated capacity according to Eurocode 9 from section 3.5.3, and display results from three series of FEM analyses (7.4.2) and the nine laboratory tests for each cross-section and alloy, described in 7.1 and 7.2. In these figures, the gap between estimates from Eurocode 9 and FEA is initially large on short columns, but as the column length increases, the gap shrinks. For the slenderest cross-section, this gap is persisted for lengths above two metres, compared to the FEA results which seem to only give a slight underestimation of laboratory tests (figure 110). From this figure, if ignoring the L2000-specimen with highest capacity, it would seem like $a_2 = \frac{L}{2000}$ is a good fit, underestimating the laboratory results with the same amount on all lengths. However, as pointed out in section 7.4.3 and 7.4.2, the failure mode is global instead of local and the results are therefore not reliable.

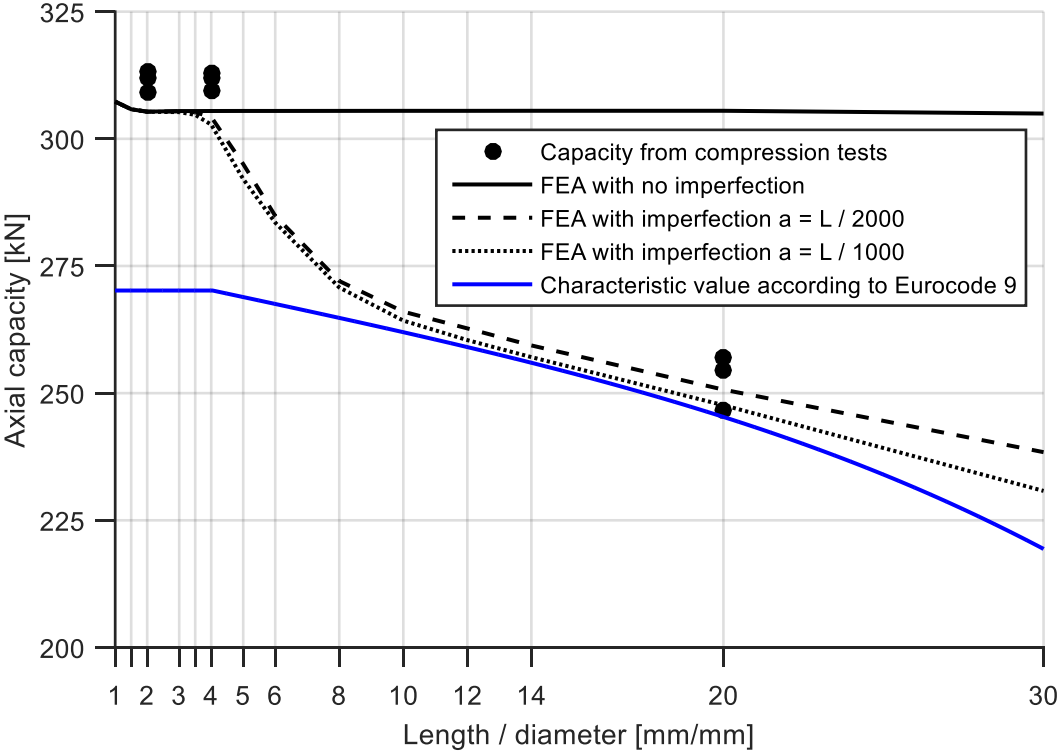


Figure 109 Comparison of results for A6060D100

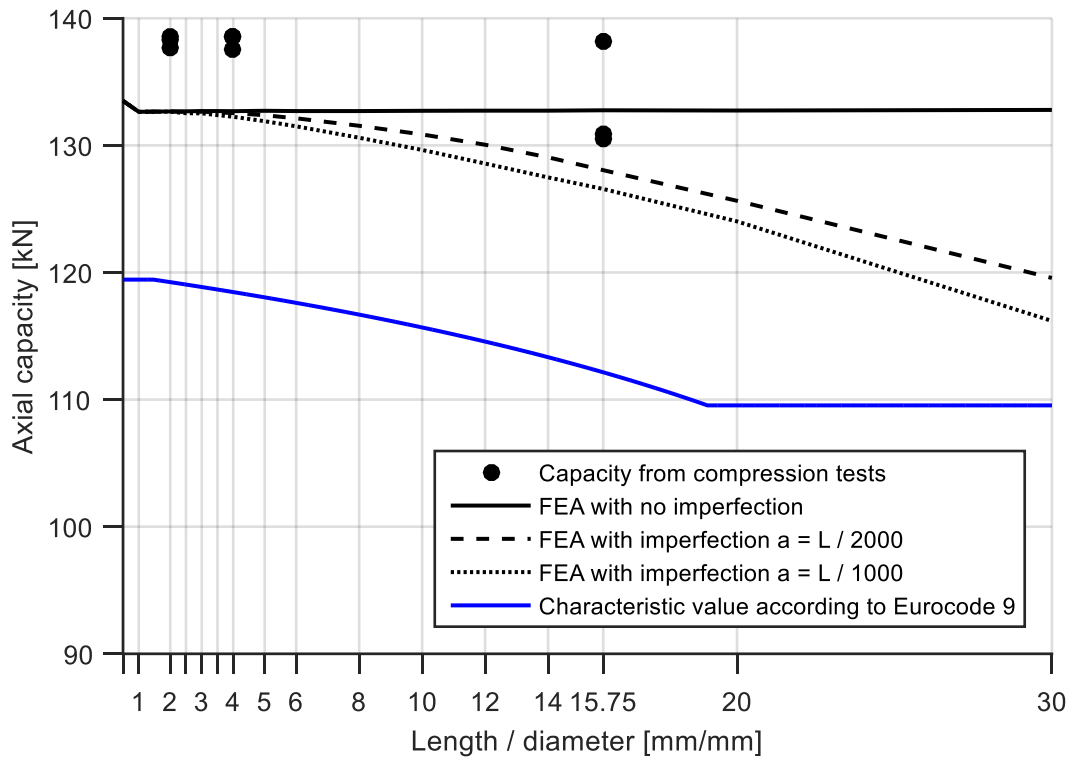


Figure 110 Comparison of results for A6060D127

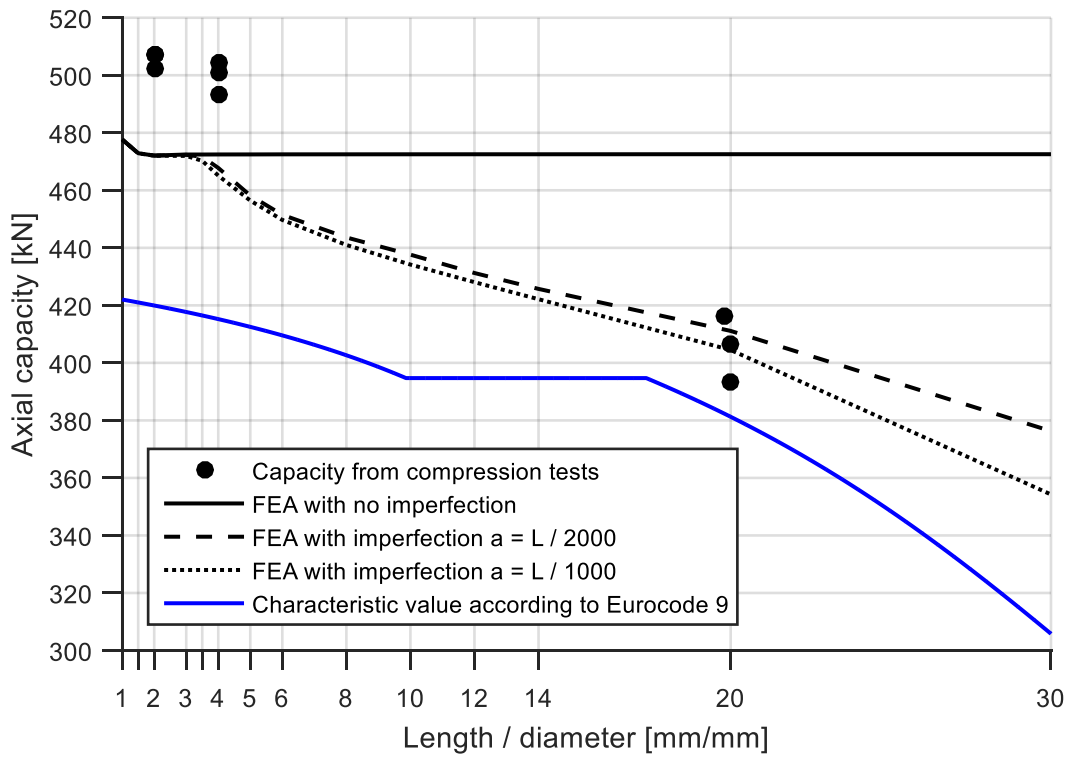


Figure 111 Comparison of results for A6082D100

The Eurocode has in general been most accurate in its predictions of buckling mode. Hence, any disagreement between Eurocode 9 and the FEA model regarding buckling mode should be investigated. It is assumed that the estimate of where the transition range between local and global buckling initiates in the FEA model, to some degree should coincide with the Eurocode estimations. The Eurocode is not as close to the correct capacity on shorter columns as the FEA model (table 20), but it can be used as an indicator of the buckling mode, and for short columns an extension of the local slenderness reduction factor ρ_c seen in figure 105 into the plastic regime could modify the results to become more accurate.

A6060D100 does not buckle meridionally according to the code. The plateau of local buckling (mentioned in section 3.6) ends at roughly the same length for Eurocode and the FEA model.

For A6060D127 there was no such consistency, as the FEA model initiated global interaction of buckling shape at roughly L8D (figure 110 and figure 95) while the Eurocode assumed local dominated failure mode on all lengths considered. The same effect is to some degree seen for A6082D100 (figure 111)

In figure 112, the figures presented above are normalized and compared. It is seen from this graph that as the Eurocode predictions generally obtain increased accuracy for longer specimens with larger global slenderness λ . The low predictions from Eurocode 9 is an indication of its safety margins, built into the material model.

According to the FEA model, decreasing the length of a thick-walled high-strength profile to a global slenderness below 10-20 greatly increases its axial capacity (figure 112). This limit slenderness may in reality be larger due to premature buckling modes in the FEA model, initialized by the chosen global imperfection (as discussed in section 7.4.3). This increased axial capacity may be an important aspect in design of modules of truss systems in power pylons in order to fully exploit the strength of the structural components. Taking this effect into account can increase the utilization of the material by optimizing the length of the members, which may to a larger extent enable economically competitive power pylons. Note that in order to apply the results from FEA to a design situation, a larger safety margin has to be applied than in the Eurocode, as the FEA model may be less documented and contain larger uncertainties.

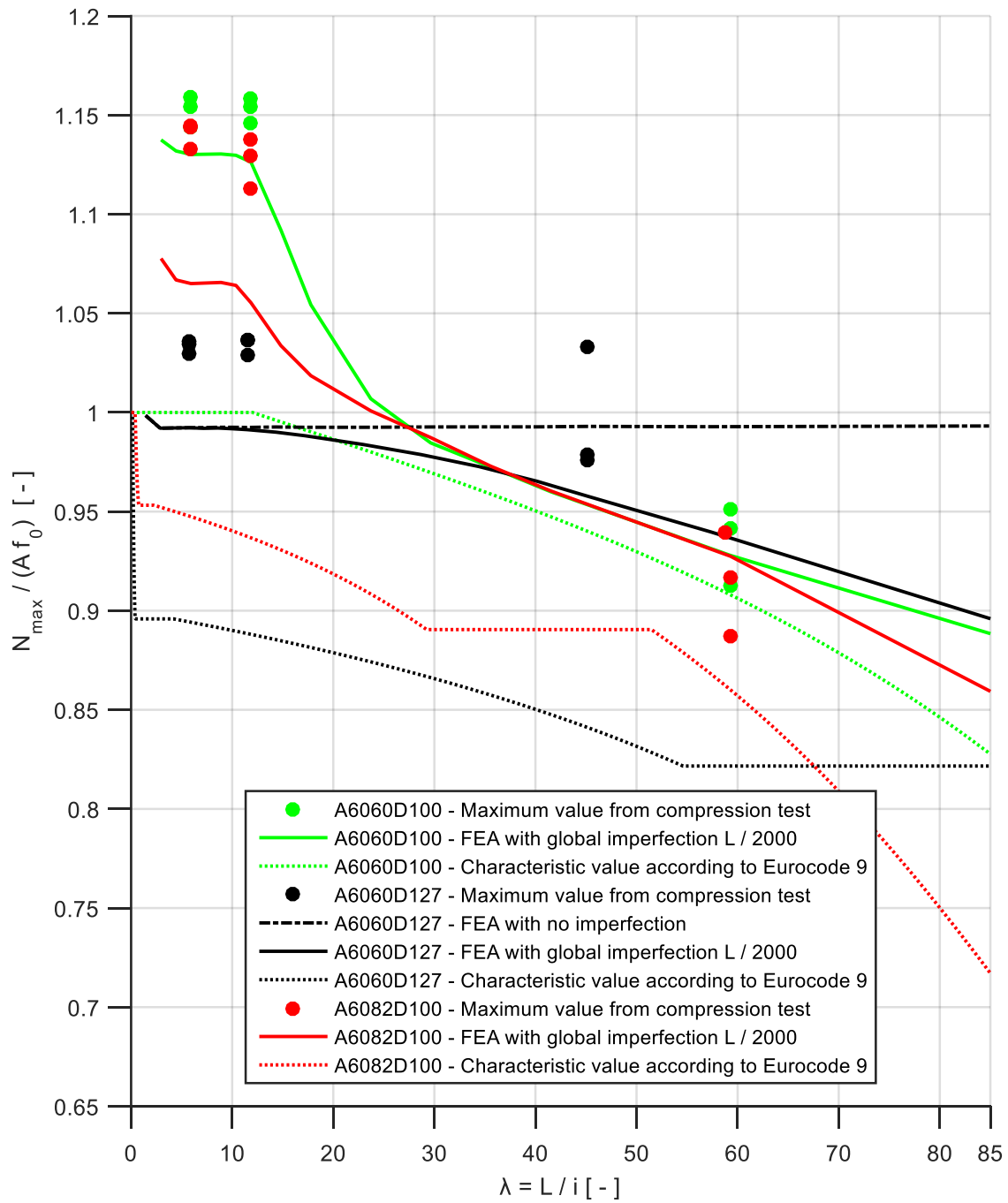


Figure 112 Normalized capacity as a function of global slenderness from compression tests, FEA and Eurocode 9.

8 Conclusions

Material and mechanical behaviour of hollow cylinders in aluminium has been studied under inelastic local and global instability. Analytical and empirical theories and guidelines from literature has been expounded, their accuracy assessed in comparison with compression test results. These compression tests were executed on lengths L2D, L4D and L2000 and displayed small scatter in behaviour and capacity.

A planned laboratory setup with low-friction spherically shaped boundary conditions was discarded when FEA modelling revealed a dependency of frictional coefficient which was unachievable in laboratory.

Material inelastic properties of aluminium alloys 6060T6 and 6082T6 are adapted to Voce hardening law. This adaption was based on tension tests and only partially succeeded in modelling the compressive strength of the materials in FEM analyses, despite a good fit in tension modelling. The deviation in compressive capacity was 2-4 percent for alloy 6060T6 and 6-7 percent for 6082T6.

The implicit dynamic FEA model representing the axially compressed hollow cylinders from laboratory tests simulated the behaviour with high accuracy when modelling short, locally buckling columns. Introducing a global imperfection with amplitude $L/2000$ rendered excellent results for the longest columns with thick-walled cross-section, but induced erroneous global buckling mode for A6060D127 with imperfections as low as $L/100000$.

The thick cross-sections displayed a drastic drop in axial capacity as the global slenderness is increased above 10-15. Exploiting this result may enable economically competitive solutions to the design of power pylons.

9 Future Work

As of June 2016, the project on power pylons in aluminium is still in its early stages. This thesis has created a basis for calculations of material and stability which may be improved by further implementation of suggested improvements.

Regarding the material model, additional tests should be performed, not only to reduce the random error, but to explore the possibility of the sources of error discussed. Hopkinson-bar tests can assess the compressive and tensile strength of the cylinders, through testing of specimen turned out of the cylinder wall. The tension tests from these bars can help assess to what degree heat affected zones from the Wire EDM cut affected the previous tension tests. The difference between Hopkinson-bar tension and compression tests can assess the strength differential effect. Correctly applying DIC calibration during laboratory testing to allow 3D DIC might improve the data treatment process of the material tests. Hardness tests on ring specimen might identify to which degree seam welds affect the ductility and strength of the cylinders. At the time when this thesis was published, both types of tests were planned and ordered but not performed.

Future work on this project should try to exploit the potential of the radial displacement graphs comparing 3D DIC with FEM analysis results. These graphs can help the modelling process by providing a basis of comparison of the local and, through improvement of the method, global failure mode. The modelling of imperfections was found to be an area of challenge. When assessing this problem, the radial displacement graphs may be an important tool to help the FEM analyses simulate and quantify the correct behaviour.

Improving the FEA model requires improving how and to what degree imperfections are introduced. This may require a combination of global and local imperfections, a study which may lead to a deeper understanding of the behaviour of the columns in the last load increments leading up to instability and buckle.

Options to the compression test FEA model that was not thoroughly explored in this thesis includes usage of shell elements and explicit solution algorithm. These may improve the models' ability to buckle correctly.

In chapter 5 the laboratory setup with a spherical hinged connection was analysed but deemed unsuited to study the effects of interest. A new laboratory setup is planned, and showed in figure 113. This setup might provide additional data to further improve the Abaqus model on globally slender columns.



(a)



(b)

Figure 113 New hinged laboratory setup to analyse globally buckling cylinders

The theoretic approaches in this thesis are not necessary the best approximation. Parameters such as amplitude and type of imperfection, plastic parameters and ductility may affect to what degree formulas succeed in predicting material and geometrical behaviour. In chapter 7 predicting the correct failure mode was a key aspect in assessing the accuracy of estimates and predictions. Based on calculations carried out, it is evident that the criterion in formula (3.35) is too conservative, assuming global instability affects the capacity to a greater degree than what was found in laboratory. Future work might explore other global instability criterions, such as the Reduced-Modulus Theory, the Transcendental Plastic Buckling approach or some energy-based iterative schemes, all presented by Jones [9]. The theory behind Gerard's local inelastic buckling formula (3.54) is based on the assumption of no elastic strains, hence it gives erroneously high capacity at low plastic strains. Future work may include deriving an improved formula for local inelastic buckling, perhaps similarly as done by Jones [9].

As the understanding of the behaviour of aluminium is improved, the study might be oriented more towards the design of power pylons, for example by optimizing truss systems with respect to capacity and economy in compliance with the vision of the project.

Bibliography

1. Tryland, T., *Design av aluminiummast tilpasset automatisert produksjon*. 2015, SINTEF: Powerpoint.
2. Standard Norge, *Norsk Standard NS-EN 1999-1-1:2007+A1:2009+NA:2009*, in *Eurokode 9: Prosjektering av aluminiumskonstruksjoner. Del 1-1: Allmenne regler*. 2007.
3. Larsen, P.K., *Dimensjonering av stålkonstruksjoner*. 2010, Trondheim: Akademika forlag.
4. Standard Norge, *Norsk Standard NS-EN 1993-1-1:2005+A1:2014+NA:2015*, in *Eurokode 3: Prosjektering av stålkonstruksjoner. Del 1-1: Allmenne regler og regler for bygninger*. 2008, Standard Norge.
5. *Abaqus Unified FEA*. 2016; Available from: <http://www.3ds.com/products-services/simulia/products/abacus/>.
6. Batdorf, S.B., M. Schildcrout, and M. Stein, *Critical stress of thin-walled cylinders in axial compression (NACA Technical note 1343)*. National Advisory Committee For Aeronautics, 1947.
7. Gerard, G., *NACA technical note 3726 - Compressive and tensional buckling of thin-walled cylinders in yield region*. 1956, NACA: Washington.
8. Gerard, G. and H. Becker, *Handbook of Structural Stability, Part III - Buckling of Curved Plates and Shells (NACA Technical Note 3783)*. 1957, National Advisory Committee for Aeronautics/NASA.
9. Jones, R.M., *Buckling of bars, plates and shells*. 2006, Blacksburg, Virginia, USA: Bull Ridge Publishing.
10. Standard Norge, *Norsk Standard NS-EN 1999-1-5:2007+NA2010*, in *Eurocode 9: Prosjektering av aluminiumskonstruksjoner. Del 1-5: Skallkonstruksjoner*. 2007.
11. Rørvik, T., *Aluminiumskonstruksjoner, Innføring i material- og konstruksjonslære*. 1997: BYGGFORSK.
12. Hoppestad, O.S. and T. Børvik, *Lecture Notes Material Mechanics Part 1*. 2013.
13. Nixon, M.E., O. Cazacu, and R.A. Lebensohn, *Anisotropic response of high-purity alpha-titanium: Experimental characterization and constitutive modeling*. International Journal of Plasticity, 2010. **26**(4): p. 516-532.
14. Cook, R.D., et al., *Concepts and applications of finite element analysis*. Vol. Fourth Edition. 2002, United States: Publication Services, Inc.
15. e-education.psu.edu, *The Nature of Geographic Information, Systematic_vs_Random_Error*, Editor. 2016, e-education: <https://www.e-education.psu.edu>.
16. Borrego, L.P., et al., *Analysis of low cycle fatigue in AlMgSi aluminium alloys*. Engineering Failure Analysis, 2004. **11**(5): p. 715-725.
17. Mazzolani, F.M., *Aluminium Alloy Structures*. 1995, London, United Kingdom: E & FN Spon.
18. Standard Norge, *Norsk Standard NS-EN 1993-3-1:2006+NA:2009*, in *Eurokode 3: Prosjektering av stålkonstruksjoner. Del 3-1: Tårn og master*. 2009, Standard Norge.
19. Standard Norge, *Norsk Standard NS-EN 1990:2002+NA:2008*, in *Eurocode: Grunnlag for prosjektering av konstruksjoner*. 2008.
20. *Abaqus - Lecture 5 - Quasi-static analyses*. Abaqus/Explicit: Advanced Topics 2005.
21. *Abaqus Analysis User's Manual*. 2013 [cited 2016; Available from: <http://129.97.46.200:2080/v6.13/books/usb/default.htm>].

22. Nesje, A.V., *Aksialkapasitet for aluminiumssylindere*. 2015, NTNU: Trondheim.
23. Leahu-Aluas, I. and F. Abed-Meraim, *A proposed set of popular limit-point buckling benchmark problems*. *Structural Engineering and Mechanics*, 2015. **38**: p. 767-802.
24. Sadowski, A.J. and J.M. Rotter, *Solid or shell elements to model cylindrical tubes and shells under global bending*. *International Journal of Mechanical Sciences*, 2013. **74**: p. 143-153.
25. skf. *Friction*. 2016; Available from: <http://www.skf.com/uk/products/bearings-units-housings/spherical-plain-bearings-bushings-rod-ends/general/friction/index.html>.
26. Chihab, K., et al., *The Kinetics of the Portevin-Le Chatelier Bands in an Al-5at%Mg Alloy*. *Scripta Metallurgica* 1987. **21**: p. 203-208.
27. Holmstrøm, P.H., *Strain bands*. 2016.
28. Toolbox, E. *Friction and Friction Coefficients*. 2016; Available from: http://www.engineeringtoolbox.com/friction-coefficients-d_778.html.

Appendix A NACA reports

NACA has given the following figures explaining the relationship between the length parameter Z_L (also called Z) and the buckling factor k_c . Figures are taken from NACA report 3783 [8].

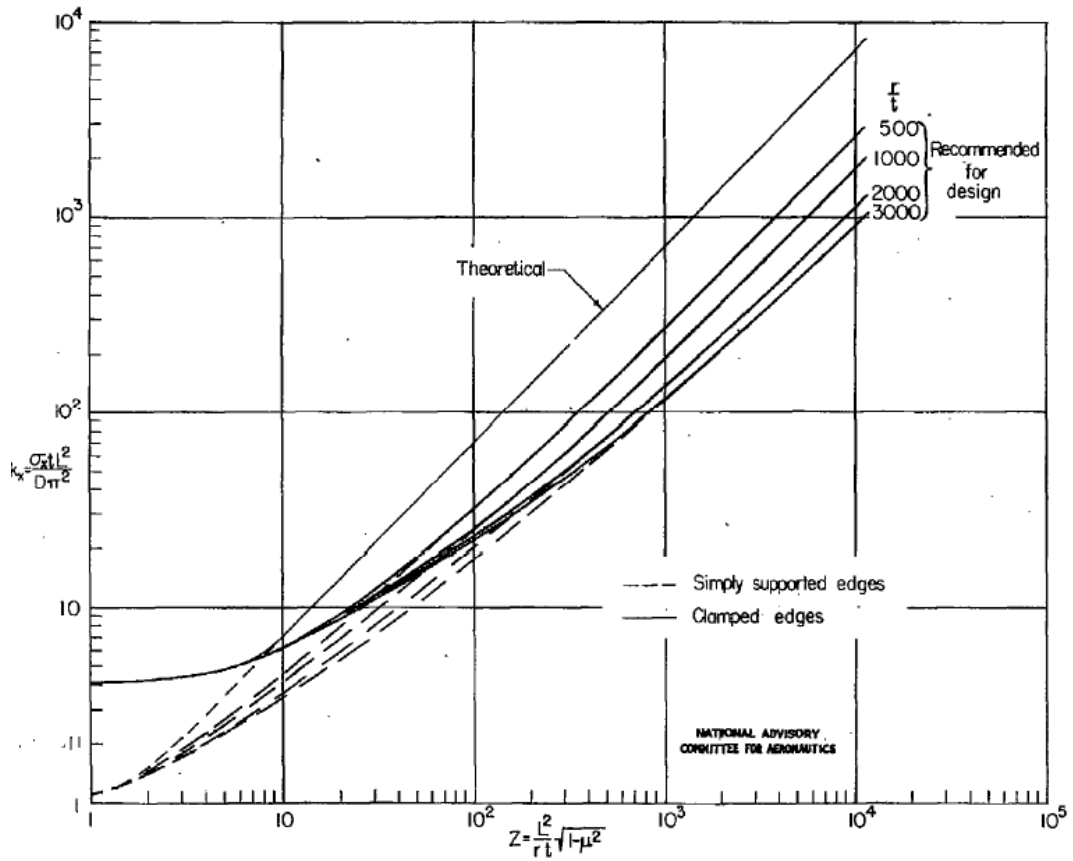


Figure 2.- Critical stress coefficients for thin-walled circular cylinders subjected to axial compression.

Figure a1 k_c as a function of Z_L , different slenderness

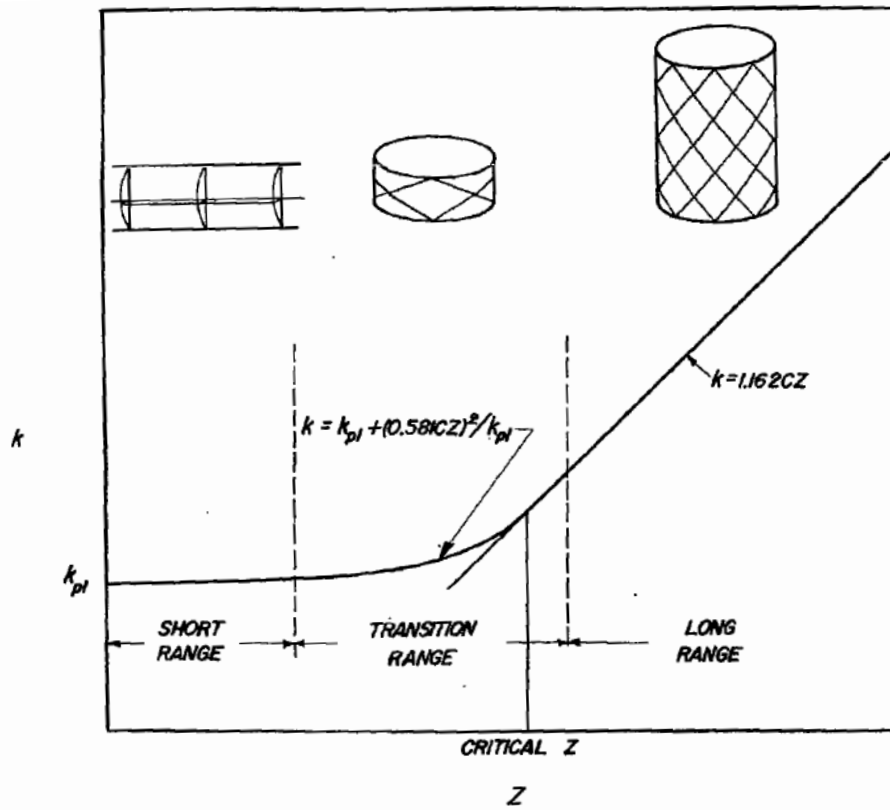


Figure 5.- Method of construction of curve for k as a function of Z . Typical buckle patterns shown for cylinder in each range of Z .

Figure a2 k_c as a function of Z_L , different buckling patterns

Appendix B Laboratory: Premeasurement of geometry

Table b1 Measured diameters for initial cylinder measurements

	i	6082D100	6060D100	6060D127
D (first end)	1.00	99.80	-	126.56
	2.00	99.79	-	126.72
	3.00	98.80	-	126.93
	4.00	99.76	-	126.84
D (second end)	1.00	99.98	99.95	126.62
	2.00	98.15	100.04	127.03
	3.00	99.82	99.80	126.69
	4.00	99.83	99.67	126.84

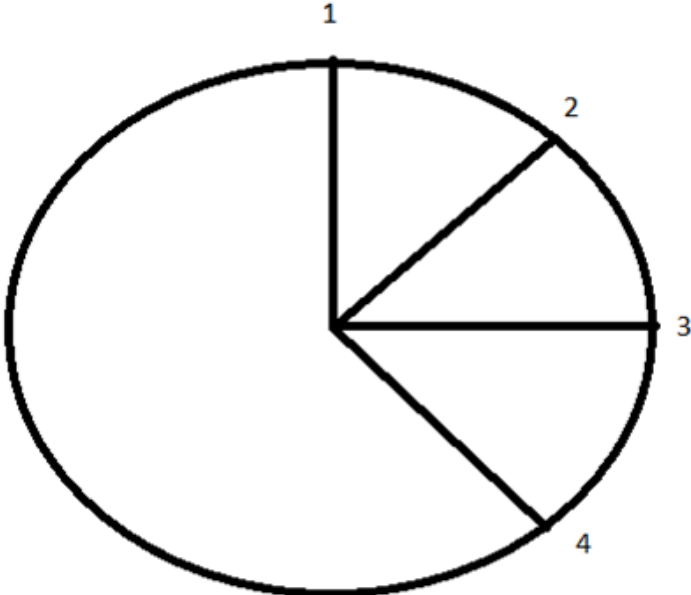


Figure b1 Points of measurement for diameter

Table b2 Measured thickness [mm] for initial cylinder measurements

	i	6060D100				6060D127				6082D100			
		0°	90°	180°	270°	0°	90°	180°	270°	0°	90°	180°	270°
Length: 250mm	1	4.65	4.65	4.70	4.70	1.72	1.72	1.77	1.75	4.65	4.65	4.70	4.70
	2	4.65	4.65	4.70	4.62	1.82	1.75	1.77	1.77	4.72	4.65	4.65	4.70
	3	4.60	4.65	4.75	4.75	1.77	1.85	1.82	1.85	4.70	4.65	4.65	4.75
	4	4.70	4.72	4.75	4.70	1.77	1.80	1.77	1.87	4.80	4.65	4.65	4.82
Length: 750 mm	1	4.65	4.65	4.75	4.65	1.77	1.77	1.77	1.92	4.75	4.67	4.65	4.70
	2	4.70	4.75	4.89	4.67	1.82	1.82	1.80	1.90	4.77	4.65	4.65	4.77
	3	4.65	4.70	4.80	4.65	1.87	1.82	1.82	1.82	4.77	4.70	4.65	4.80
	4	4.62	4.70	4.62	4.65	1.87	1.82	1.80	1.82	4.75	4.70	4.65	4.80
Length: 1250 mm	1	4.65	4.65	4.70	4.65	1.75	1.77	1.72	1.80	4.65	4.65	4.70	4.75
	2	4.65	4.70	4.75	4.65	1.82	1.77	1.77	1.72	4.65	4.65	4.75	4.80
	3	4.62	4.67	4.77	4.65	1.82	1.72	1.80	1.70	4.70	4.70	4.70	4.70
	4	4.70	4.70	4.77	4.65	1.82	1.72	1.80	1.70	4.75	4.65	4.80	4.77
Length: 1750 mm	1	4.65	4.70	4.70	4.65	1.72	1.75	1.77	1.80	4.70	4.65	4.65	4.75
	2	4.65	4.65	4.70	4.70	1.92	1.47	1.80	1.80	4.70	4.72	4.67	4.80
	3	4.65	4.65	4.75	4.84	1.72	1.72	1.85	1.82	4.75	4.65	4.70	4.75
	4	4.72	4.70	4.75	4.67	1.75	1.77	1.77	1.77	4.70	4.65	4.67	4.77
Length: 2250 mm	1	4.70	4.67	4.70	4.67	1.72	1.82	1.82	1.70	4.60	4.70	4.65	4.70
	2	4.70	4.70	4.70	4.75	1.80	1.77	1.72	1.77	4.67	4.70	4.65	4.70
	3	4.65	4.65	4.70	4.70	1.77	1.77	1.77	1.77	4.65	4.75	4.65	4.70
	4	4.75	4.65	4.70	4.65	1.72	1.85	1.77	1.77	4.75	4.70	4.65	4.70
Length: 2750 mm	1	4.70	4.70	4.70	4.94	1.72	1.72	1.82	1.72	4.72	4.67	4.65	4.70
	2	4.70	4.70	4.70	4.80	1.75	1.75	1.77	1.77	4.72	4.65	4.65	4.75
	3	4.65	4.65	4.70	4.75	1.77	1.72	1.77	1.82	4.80	4.62	4.67	4.77
	4	4.60	4.70	4.70	4.80	1.77	1.70	1.77	1.70	4.72	4.67	4.65	4.70
Length: 3250 mm	1	4.65	4.75	4.80	4.72	1.82	1.77	1.72	1.77	4.75	4.60	4.70	4.70
	2	4.75	4.65	4.80	4.70	1.82	1.77	1.72	1.75	4.70	4.65	4.67	4.75
	3	4.70	4.65	4.82	4.72	1.80	1.80	1.72	1.72	4.80	4.65	4.70	4.72
	4	4.70	4.65	4.75	4.80	1.82	1.80	1.77	1.72	4.75	4.62	4.65	4.77
Length: 3750 mm	1	4.70	4.65	4.70	4.65	1.77	1.82	1.77	1.72	4.65	4.65	4.65	4.75
	2	4.70	4.67	4.75	4.70	1.77	1.72	1.72	1.77	4.70	4.65	4.65	4.70
	3	4.72	4.65	4.70	4.75	1.75	1.82	1.77	1.70	4.67	4.67	4.70	4.70
	4	4.70	4.65	4.72	4.72	1.87	1.67	1.72	1.72	4.67	4.65	4.65	4.70
Length: 4250 mm	1	4.72	4.65	4.70	4.65	1.77	1.85	1.72	1.72	4.67	4.70	4.70	4.75
	2	4.70	4.60	4.70	4.65	1.72	1.72	1.77	1.72	4.70	4.70	4.65	4.72
	3	4.65	4.65	4.70	4.65	1.82	1.80	1.77	1.82	4.67	4.67	4.65	4.72
	4	4.65	4.65	4.80	4.65	1.72	1.77	1.77	1.77	4.65	4.65	4.65	4.70
Length: 4750 mm	1	4.65	4.67	4.75	4.72	1.87	1.75	1.72	1.77	4.65	4.70	4.70	4.75
	2	4.65	4.65	4.70	4.75	1.92	1.75	1.77	1.75	4.65	4.75	4.67	4.82
	3	4.65	4.70	4.70	4.80	1.87	1.75	1.77	1.87	4.65	4.70	4.65	4.75
	4	4.65	4.65	4.75	4.75	1.80	1.72	1.72	1.77	4.65	4.70	4.70	4.77

Appendix C Eurocode 9 part 1-1

All point references and figures in appendix C are taken from Eurocode 9 part 1-1 [2] unless specified.

Chapter 6 Ultimate limit states for members

6.3.1 Members in compression

6.3.1.1(2) The design buckling resistance of a compression member $N_{b,Rd}$ should be taken as:

$$N_{b,Rd} = \kappa \chi A_{eff} \frac{f_0}{\gamma_{M1}} \quad (C.1)$$

- χ reduction factor for relevant buckling mode
- κ factor to allow for the waekening effects of welding
- A_{eff} effective area allowing for local buckling for class 4 cross-section
- f_0 characteristic value of 0.2% proof strength
- γ_{M1} partial safety factor for ultimate limit state

however, in order to estimate the accuracy of the Eurocode the only interest is the characteristic buckling resistance that don't include partial safety factor.

$$N_{b,Rk} = N_{b,Rd} * \gamma_{M1} = \kappa \chi A_{eff} f_0 \quad (C.2)$$

Due to no welding:

$$\kappa = 1 \quad (C.3)$$

6.1.5(1) Local buckling in class 4 members is generally allowed for by replacing the true section by an effective section. The effective section is obtained by employing a local factor ρ_c to factor down the thickness, viz.

$$t_{eff} = \rho_c t \quad (C.4)$$

6.1.5(2) The factor ρ_c is given by

$$\rho_c = 1.0 \text{ if } \beta \leq \beta_3 \quad (C.5)$$

$$\rho_c = \frac{C_1}{\beta / \varepsilon} - \frac{C_2}{(\beta / \varepsilon)^2} \text{ if } \beta > \beta_3 \quad (C.6)$$

where C_1 and C_2 are taken from table c1

Table c1 Constants C_1 and C_2 from table 6.3 in Eurocode 9

Material classification according to Table 3.2	Internal part		Outstand part	
	C_1	C_2	C_1	C_2
Class A, without welds	32	220	10	24
Class A, with welds	29	198	9	20
Class B, without welds	29	198	9	20
Class B, with welds	25	150	8	16

The slenderness factor β for hollow circular cross-section is calculated after (3.43) and classified with slenderness parameters from table c2.

Table c2 Slenderness parameters β_1/ε , β_2/ε and β_3/ε from table 6.2 in Eurocode 9

Material classification according to Table 3.2	Internal part			Outstand part		
	β_1/ε	β_2/ε	β_3/ε	β_1/ε	β_2/ε	β_3/ε
Class A, without welds	11	16	22	3	4,5	6
Class A, with welds	9	13	18	2,5	4	5
Class B, without welds	13	16,5	18	3,5	4,5	5
Class B, with welds	10	13,5	15	3	3,5	4

$\varepsilon = \sqrt{250/f_0}$, f_0 in N/mm^2

The area of a circular cross-section then becomes

$$A_{eff} = \frac{\pi}{4} ((D_m + t_{eff})^2 - (D_m - t_{eff})^2) \quad (\text{C.7})$$

6.3.1.2(1) For axial compression in members the value χ for the appropriate value of $\bar{\lambda}$ should be determined from the relevant buckling curve according to:

$$\chi = \frac{1}{\phi + \sqrt{\phi^2 + \bar{\lambda}^2}} \quad \text{but } \chi \leq 1 \quad (\text{C.8})$$

where:

$$\phi = 0.5(1 + \alpha(\bar{\lambda} - \bar{\lambda}_0)) + \bar{\lambda}^2 \quad (\text{C.9})$$

$$\bar{\lambda} = \sqrt{\frac{A_{eff} f_0}{N_{cr}}} \quad (\text{C.10})$$

α imperfection factor

$\bar{\lambda}_0$ the limit of the horizontal plateau

N_{cr} the elastic critical force for the relevant buckling mode based on the gross cross-sectional properties

α and $\bar{\lambda}_0$ is taken from table c 3.

Table c 3 Values of α and $\bar{\lambda}_0$ from table 6.6 in Eurocode 9

Material buckling class according to Table 3.2	α	$\bar{\lambda}_0$
Class A	0,20	0,10
Class B	0,32	0,00

N_{cr} are equal to N_E given in (3.31) with corresponding critical length for clamped column

$$L_E = 0.5L \quad (C.11)$$

Note that this is a deviation from table 6.8 in part 1-1 [2], which claims that $0.7L$ should be used to take “*various deformations in the connection between different structural parts*” [2] into account. The mechanical setup in laboratory is assumed to ensure fully clamped boundary conditions, justifying formula (C.11).

The partial safety factor from NA.6.1.3(1) is given as

$$\gamma_{M1} = 1.10 \quad (C.12)$$

Appendix D Eurocode 9 part 1-5

All point references in appendix D are related to Eurocode 9 part 1-1 [10] unless otherwise is specified.

A.1.2(1) Cylinders need not be checked against meridional shell buckling if they satisfy:

$$\frac{r}{t} \leq 0.03 \frac{E}{f_0} \quad (\text{D.1})$$

r radius of cylinder middle surface

t thickness of shell

E Young's modulus

f_0 characteristic value of 0.2% proof strength

6.2.3.2(1) The design buckling resistance should be obtained from:

$$\sigma_{x,Rd} = \alpha_x \rho_{x,w} \chi_{x,perf} \frac{f_0}{\gamma_{M1}} \quad (\text{D.2})$$

α_x imperfection reduction factor

$\rho_{x,w}$ reduction factor due to heat-affected zones

$\chi_{x,perf}$ reduction factor due to buckling of a perfect shell

γ_{M1} partial safety factor

The buckling resistance force then becomes:

$$F_{x,Rd} = \sigma_{x,Rd} A \quad (\text{D.3})$$

$$F_{x,Rk} = \sigma_{x,Rd} A \gamma_{M1} \quad (\text{D.4})$$

No welds entails:

$$\rho_{x,w} = 1 \quad (\text{D.5})$$

6.2.3.2(2) The reduction factor due to buckling for a perfect shell is given by:

$$\chi_{x,perf} = \frac{1}{\varphi_x + \sqrt{\varphi_x^2 + \bar{\lambda}_x^2}} \text{ but } \chi_{x,perf} \leq 1,00 \quad (\text{D.6})$$

with:

$$\varphi_x = 0.5 \left((1 + \mu_x (\bar{\lambda}_x - \bar{\lambda}_{x,0})) + \bar{\lambda}_x^2 \right) \quad (\text{D.7})$$

where:

μ_x parameter depending on the alloy and loading case

$\bar{\lambda}_{x,0}$ the squash limit relative slenderness

Both parameters are taken from table d1.

Table d1 Values of $\bar{\lambda}_{x,0}$ and μ_x for meridional compression from table A.4 in Eurocode 9

Material buckling class	$\bar{\lambda}_{x,0}$	μ_x
A	0,20	0,35
B	0,10	0,20

6.2.3.2(3) The shell slenderness parameter component should be determined from:

$$\bar{\lambda}_x = \sqrt{\frac{f_0}{\sigma_{x,cr}}} \quad (D.8)$$

A.1.2.1(3) The critical meridional buckling stress should be obtained from

$$\sigma_{x,cr} = 0.605 E C_x \frac{t}{r} \quad (D.9)$$

using values for C_x in table d2

Table d2 Values for critical meridional buckling stress C_x from table A.1 in Eurocode 9

Cylindrical shell	$\omega = \frac{l}{\sqrt{rt}}$	Factor C_x
Short	$\omega \leq 1,7$	$C_x = 1,36 - \frac{1,83}{\omega} + \frac{2,07}{\omega^2}$
Medium-length	$1,7 < \omega < 0,5 \frac{r}{t}$	$C_x = 1$
Long	$\omega \geq 0,5 \frac{r}{t}$	$C_x = 1 - \frac{0,2}{C_{xb}} \left(2\omega \frac{t}{r} - 1 \right)$ but $C_x \geq 0,6$ where C_{xb} is given in Table A.2

A.1.2.1(1) ω is the length of the shell segment and is characterized in terms of the dimensionless parameter:

$$\omega = \frac{l}{\sqrt{rt}} = \sqrt{\frac{Z_L}{\sqrt{1-\nu^2}}} \quad (D.10)$$

C_{xb} is given in table d3 with boundary conditions defined in table d4.

Table d3 Parameter C_{xb} for the effect of boundary conditions for long cylinders from table A.2 in Eurocode 9

Case	Cylinder end	Boundary condition	C_{xb}
1	end 1 end 2	BC 1 BC 1	6
2	end 1 end 2	BC 1 BC 2	3
3	end 1 end 2	BC 2 BC 2	1

NOTE BC 1 includes both BC1f and BC1r

Table d4 Boundary conditions for shells from table 5.1 in Eurocode 9

Boundary condition code	Simple term	Description			Normal displacements	Meridional displacements	Meridional rotation
		radially	meridionally	rotation			
BC1r	Clamped	restrained	restrained	restrained	$w = 0$	$u = 0$	$\beta_\phi = 0$
BC1f		restrained	restrained	free	$w = 0$	$u = 0$	$\beta_\phi \neq 0$
BC2r		restrained	free	restrained	$w = 0$	$u \neq 0$	$\beta_\phi = 0$
BC2f	Pinned	restrained	free	free	$w = 0$	$u \neq 0$	$\beta_\phi \neq 0$
BC3	Free edge	free	free	free	$w \neq 0$	$u \neq 0$	$\beta_\phi \neq 0$

NOTE The circumferential displacement v is very closely linked to the displacement w normal to the surface so separate boundary conditions are not needed.

A.1.2.2(1) The meridional imperfection factor should be obtained from:

$$\alpha_x = \frac{1}{1 + 2.6 \left(\frac{1}{Q} \sqrt{\frac{0.6E}{f_0}} (\bar{\lambda}_x - \bar{\lambda}_{x,0}) \right)^{1.44}} \text{ but } \alpha_x \leq 1.00 \quad (\text{D.11})$$

Q meridional compression tolerance parameter as defined in table d5

Table d5 Tolerance parameter Q from table A.3 in Eurocode 9

Tolerance class	Value of Q for boundary conditions	
	BC1r, BC2r	BC1f, BC2f
Class 1	16	
Class 2	25	
Class 3	40	
Class 4	60	50

Appendix E Executed laboratory test and measurements for L2D and L4D

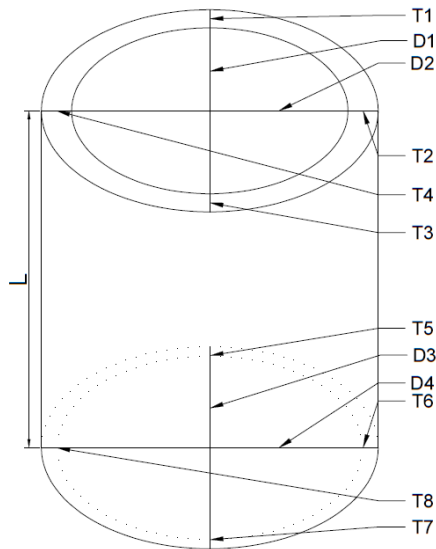


Figure e1 The location of measurers for thickness and diameters

Table e1 Measured and calculated geometry of the columns specimens for L2D and L4D

A6060D100L2D	T ₁	T ₂	T ₃	T ₄	T ₅	T ₆	T ₇	T ₈	T _m	D ₁	D ₂	D ₃	D ₄	D _m	A
1-2 L = 200.08mm	4.70	4.70	4.75	4.70	4.67	4.70	4.75	4.67	4.71	100.0	100.0	100.0	100.0	100.0	1408
2-2 L = 199.99mm	4.70	4.70	4.72	4.67	4.65	4.70	4.70	4.65	4.69	99.9	100.0	99.9	100.0	99.9	1402
3-2 L = 199.98mm	4.67	4.70	4.70	4.70	4.70	4.72	4.72	4.70	4.70	100.0	99.9	100.0	99.9	99.9	1407
A6060D100L4D	T ₁	T ₂	T ₃	T ₄	T ₅	T ₆	T ₇	T ₈	T _m	D ₁	D ₂	D ₃	D ₄	D _m	A
1-1 L = 400.04mm	4.68	4.70	4.73	4.71	4.70	4.70	4.74	4.72	4.71	99.9	100.0	99.8	100.0	99.9	1409
2-1 L = 399.98mm	4.72	4.75	4.67	4.67	4.73	4.75	4.70	4.70	4.71	100.0	100.0	100.0	100.0	100.0	1410
3-1 L = 399.94mm	4.67	4.72	4.70	4.70	4.67	4.75	4.70	4.70	4.70	99.8	99.9	99.9	99.9	99.9	1406
A6082D100L2D	T ₁	T ₂	T ₃	T ₄	T ₅	T ₆	T ₇	T ₈	T _m	D ₁	D ₂	D ₃	D ₄	D _m	A
1-3 L = 200.00mm	4.65	4.65	4.70	4.70	4.65	4.67	4.70	4.67	4.67	100.0	99.8	99.9	100.0	99.9	1398
2-3 L = 200.01mm	4.67	4.65	4.65	4.72	4.70	4.65	4.65	4.75	4.68	99.8	99.9	99.8	100.0	99.9	1400
3-3 L = 200.01mm	4.70	4.70	4.65	4.67	4.70	4.70	4.76	4.76	4.71	100.0	99.8	99.8	99.9	99.9	1407
A6082D100L4D	T ₁	T ₂	T ₃	T ₄	T ₅	T ₆	T ₇	T ₈	T _m	D ₁	D ₂	D ₃	D ₄	D _m	A
1-4 L = 400.14mm	4.65	4.70	4.65	4.67	4.70	4.70	4.65	4.67	4.67	99.7	99.8	100.1	99.8	99.9	1398
2-4 L = 400.09mm	4.67	4.70	4.65	4.67	4.67	4.70	4.67	4.67	4.68	99.7	100.0	100.1	100.0	100.0	1399
3-4 L = 400.02mm	4.65	4.70	4.65	4.65	4.70	4.70	4.65	4.67	4.67	100.1	99.9	100.0	100.1	100.0	1399
A6060D127L2D	T ₁	T ₂	T ₃	T ₄	T ₅	T ₆	T ₇	T ₈	T _m	D ₁	D ₂	D ₃	D ₄	D _m	A
1-6 L = 253.93mm	1.72	1.80	1.77	1.77	1.72	1.80	1.77	1.77	1.77	127.1	126.8	127.0	126.9	126.9	694
2-6 L = 253.98mm	1.80	1.80	1.77	1.77	1.80	1.77	1.77	1.77	1.78	127.1	126.5	127.3	126.5	126.8	700
3-6 L = 253.98mm	1.75	1.77	1.77	1.80	1.72	1.77	1.77	1.77	1.77	127.3	126.9	127.2	127.8	127.3	696
A6060D127L4D	T ₁	T ₂	T ₃	T ₄	T ₅	T ₆	T ₇	T ₈	T _m	D ₁	D ₂	D ₃	D ₄	D _m	A
1-5 L = 507.99mm	1.75	1.72	1.75	1.77	1.77	1.75	1.77	1.80	1.76	127.1	126.8	127.4	126.6	127.0	692
2-5 L = 508.03mm	1.75	1.72	1.72	1.82	1.75	1.72	1.72	1.80	1.75	126.7	127.1	127.0	126.8	126.9	688
3-5 L = 508.07mm	1.75	1.77	1.72	1.77	1.82	1.77	1.75	1.77	1.77	126.6	127.2	126.8	126.7	126.8	693

Table e2 Laboratory settings and values at maximum load for L2D and L4D

Profile and intended length	ID	Measured length [mm]	Velocity [mm/s]	Data frequency [Hz]	N_{max} [kN]	\bar{N}_{max} [kN]	S_N [kN]	CoV [%]	\bar{S}_{max} [Mpa]
A6060D100L2D	1-2	200.08	0.5	5	309.14	311.41	2.08	0.67	221.16
	2-2	199.99	0.5	5	313.23				
	3-2	199.98	0.5	5	311.86				
A6060D100L4D	1-1	400.04	0.1	5	309.55	311.48	1.75	0.56	221.55
	2-1	399.98	0.1	5	311.93				
	3-1	399.94	0.1	5	312.96				
A6060D127L2D	1-6	253.93	0.5	5	137.68	138.15	0.42	0.31	199.98
	2-6	253.98	0.5	1	138.28				
	3-6	253.98	0.5	5	138.50				
A6060D127L4D	1-5	507.99	0.1	5	138.55	138.23	0.56	0.40	198.32
	2-5	508.03	0.1	5	138.56				
	3-5	508.07	0.1	5	137.59				
A6082D100L2D	1-3	200.00	0.5	5	507.45	505.58	2.87	0.57	360.74
	2-3	200.01	0.5	5	502.27				
	3-3	200.01	0.5	5	507.02				
A6082D100L4D	1-4	400.14	0.1	5	500.63	499.34	5.63	1.13	357.01
	2-4	400.09	0.2	5	493.17				
	3-4	400.02	0.2	5	504.21				

Table e3 Calculations of β , ϵ and i for each specimen of L2D and L4D

A6060D100L2D	T_m	Do	A	β	ϵ	β/ϵ	i
1-2 L = 200.08mm	4.71	99.97	1408.85	13.49	1.14	11.82	33.71
2-2 L = 199.99mm	4.69	99.9	1410.46	13.49	1.14	11.82	33.62
3-2 L = 199.98mm	4.70	99.9	1405.81	13.50	1.14	11.83	33.72
A6060D100L4D	T_m	Do	A	β	ϵ	β/ϵ	i
1-1 L = 400.04mm	4.71	99.9	1408.06	13.50	1.14	11.83	33.71
2-1 L = 399.98mm	4.71	100.0	1402.28	13.53	1.14	11.85	33.83
3-1 L = 399.94mm	4.70	99.9	1406.55	13.50	1.14	11.83	33.68
A6060D127L2D	T_m	Do	A	β	ϵ	β/ϵ	i
1-6 L = 253.93mm	1.77	126.9	692.33	25.30	1.14	22.18	44.31
2-6 L = 253.98mm	1.78	126.8	687.99	25.37	1.14	22.23	44.60
3-6 L = 253.98mm	1.77	127.3	693.39	25.25	1.14	22.13	44.47
A6060D127L4D	T_m	Do	A	β	ϵ	β/ϵ	i
1-5 L = 507.99mm	1.76	127.0	693.97	25.26	1.14	22.14	44.22
2-5 L = 508.03mm	1.75	126.9	699.85	25.14	1.14	22.03	43.87
3-5 L = 508.07mm	1.77	126.8	696.04	25.30	1.14	22.17	44.13
A6082D100L2D	T_m	Do	A	β	ϵ	β/ϵ	i
1-3 L = 200.00mm	4.67	99.9	1398.28	13.54	0.89	15.20	33.71
2-3 L = 200.01mm	4.68	99.9	1399.73	13.53	0.89	15.19	33.70
3-3 L = 200.01mm	4.71	99.9	1406.54	13.49	0.89	15.14	33.68
A6082D100L4D	T_m	Do	A	β	ϵ	β/ϵ	i
1-4 L = 400.14mm	4.67	99.9	1397.55	13.54	0.89	15.20	33.69
2-4 L = 400.09mm	4.68	100.0	1399.30	13.54	0.89	15.20	33.73
3-4 L = 400.02mm	4.67	100.0	1399.19	13.55	0.89	15.21	33.75

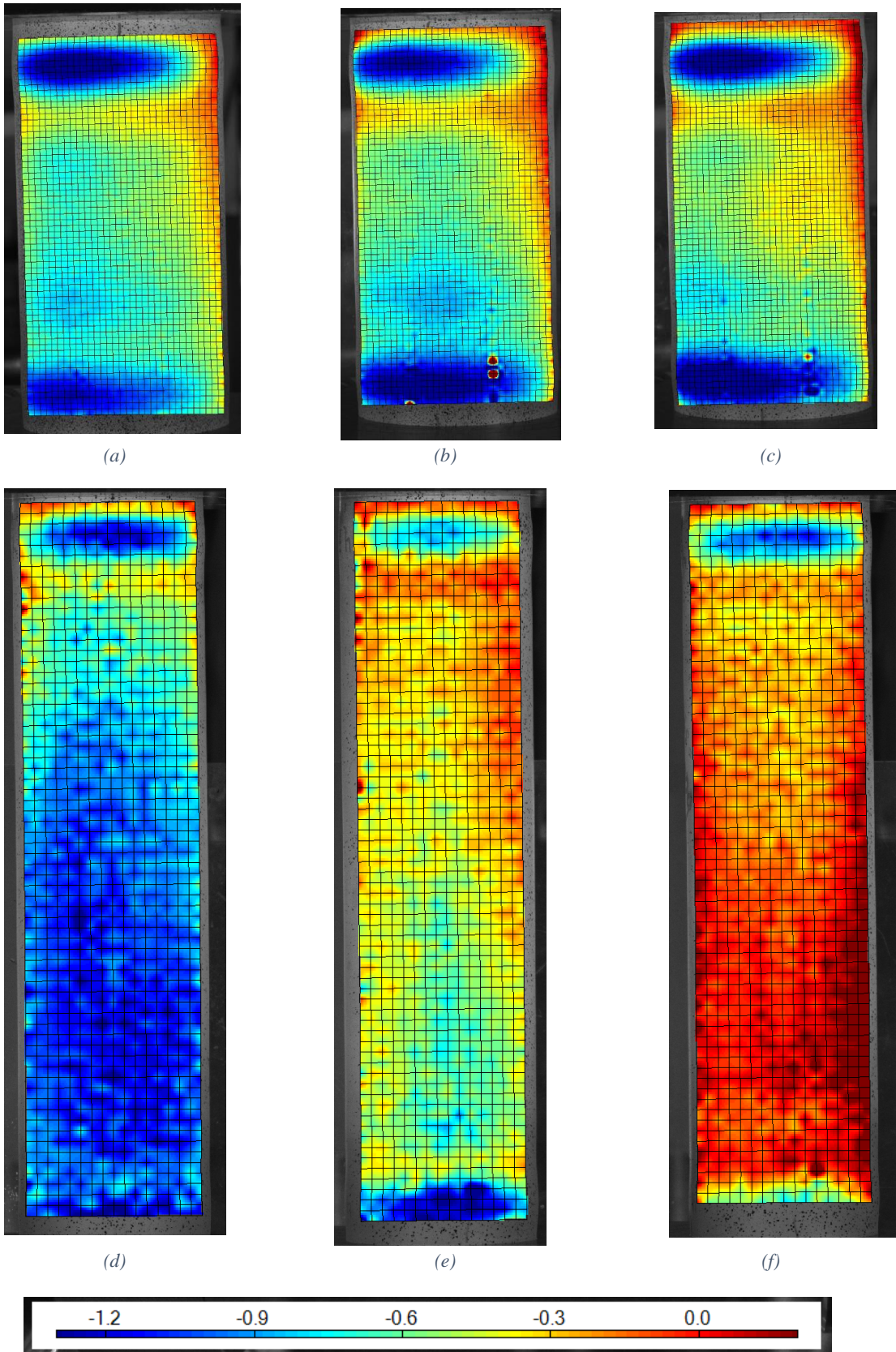
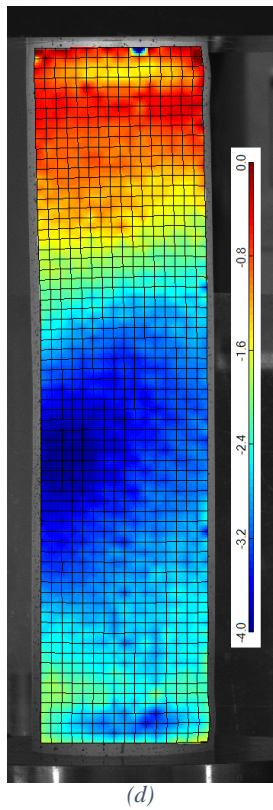
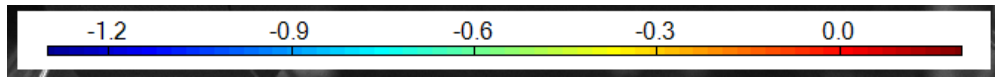
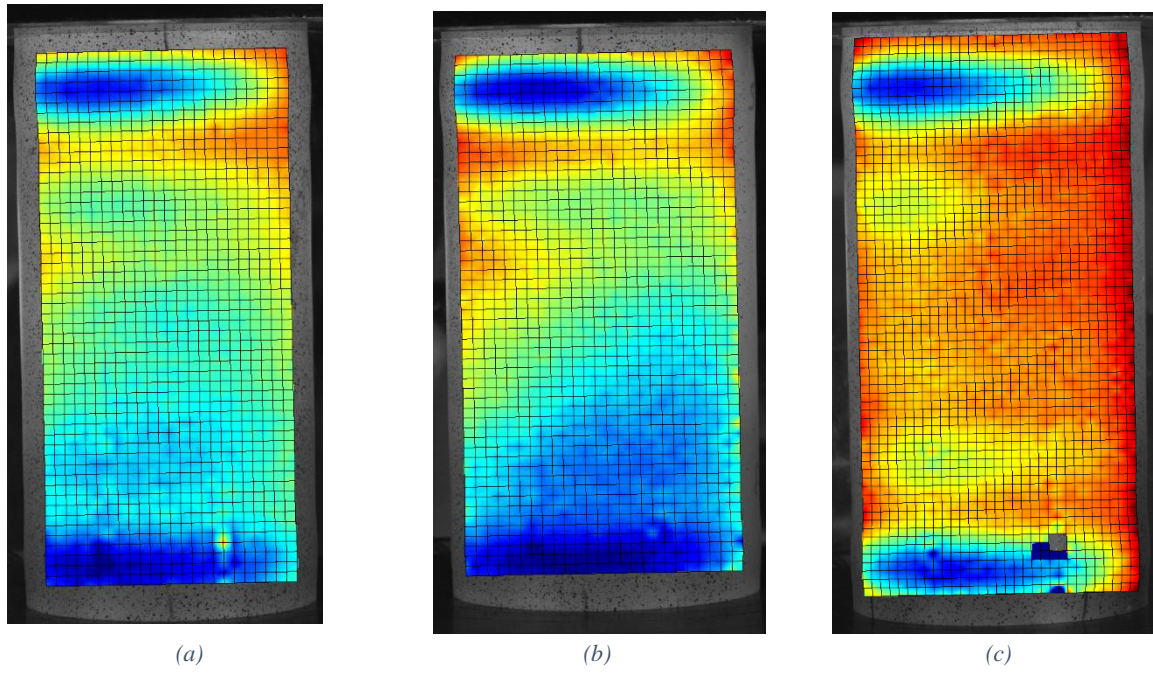


Figure e2 Displacement away from camera at maximum load. (a)-(c): 6060D100L2D. (d)-(f): 6060D100L4D



Missing specimen due to loss of data

(e)

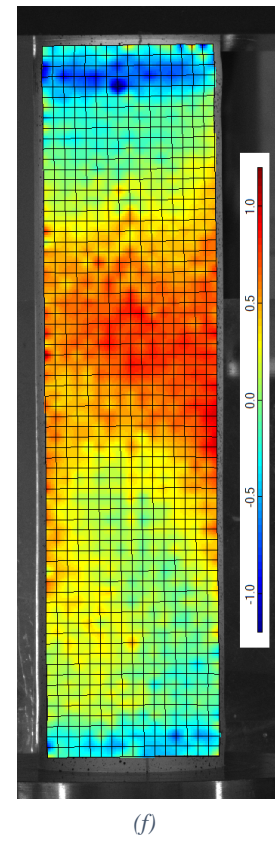


Figure e3 Displacement away from camera at maximum load. (a)-(c): 6082D100L2D. (d),(f): 6082D100L4D

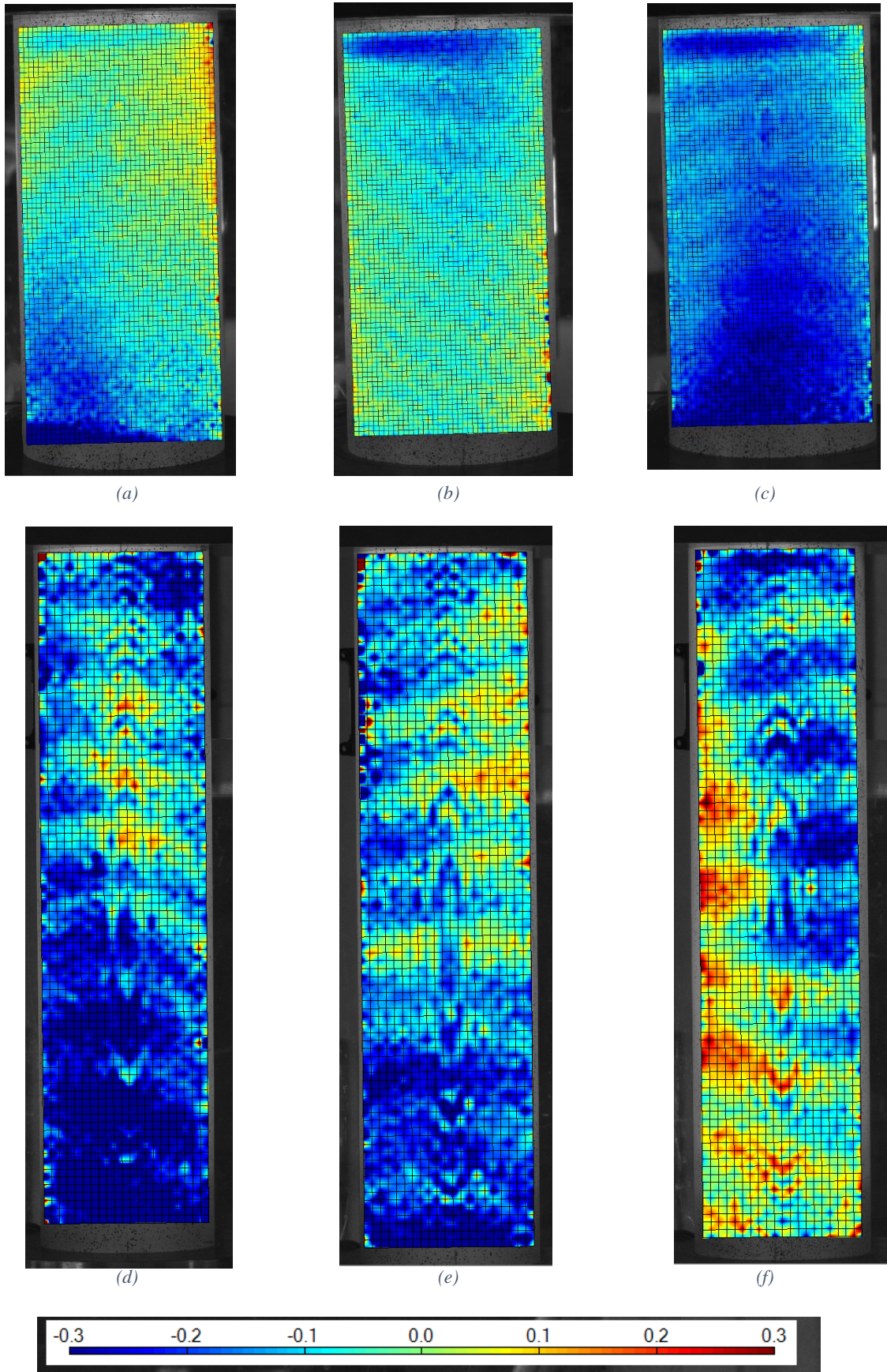


Figure e4 Displacement away from camera at maximum load. (a)-(c): 6060D127L2D. (d)-(f): 6060D127L4D



Figure e5 Post-buckling shape specimen 1-2, 2-2 and 3-2 (A6060D100L2D)

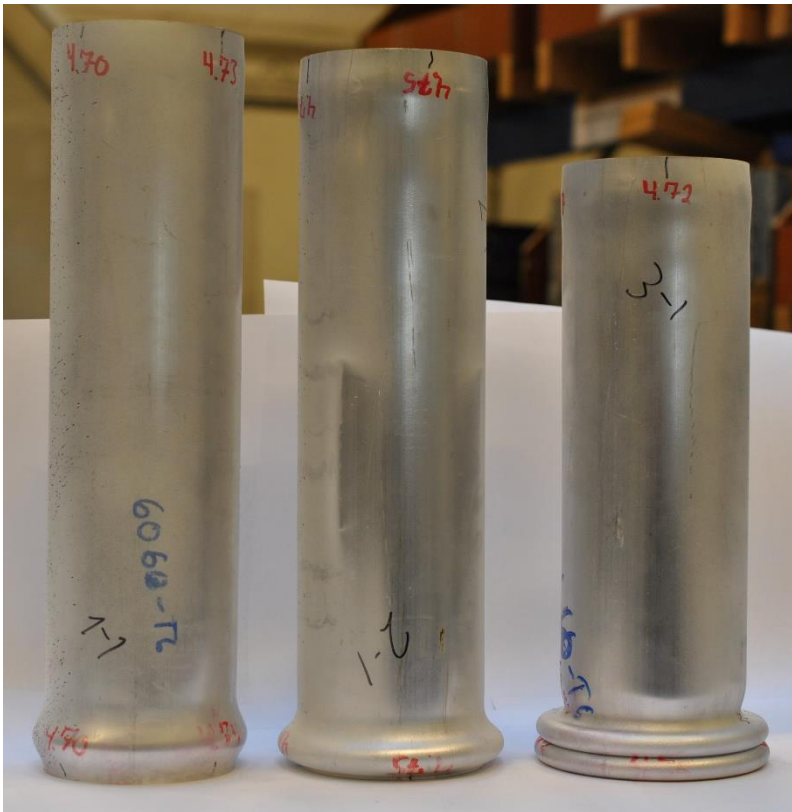


Figure e6 Post-buckling shape specimen 1-1, 2-1 and 3-2 (A6060D100L4D)



Figure e7 Post-buckling shape specimen 1-6, 2-6 and 3-6 (A6060D127L2D)

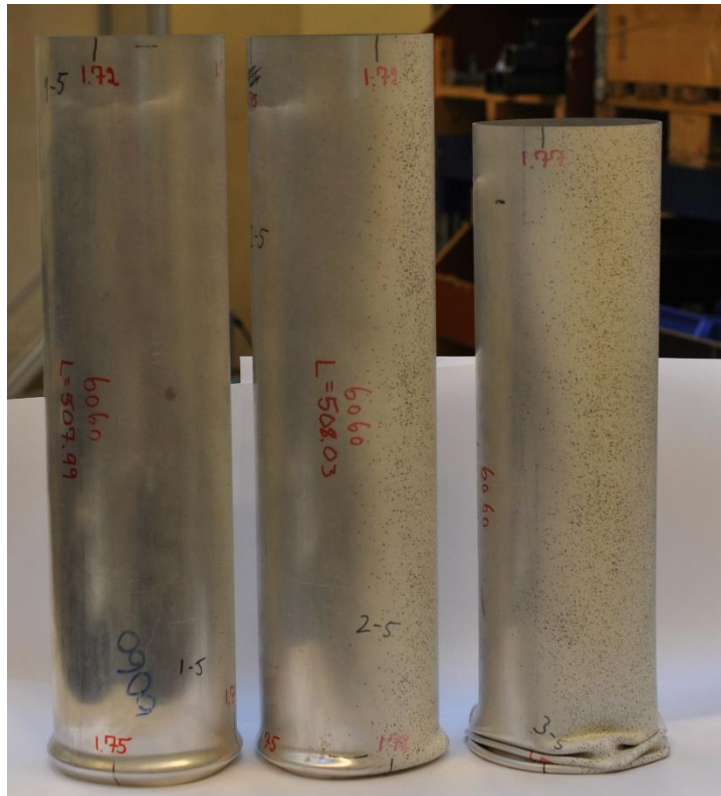


Figure e8 Post-buckling shape specimen 1-5, 2-5 and 3-5 (A6060D127L4D)

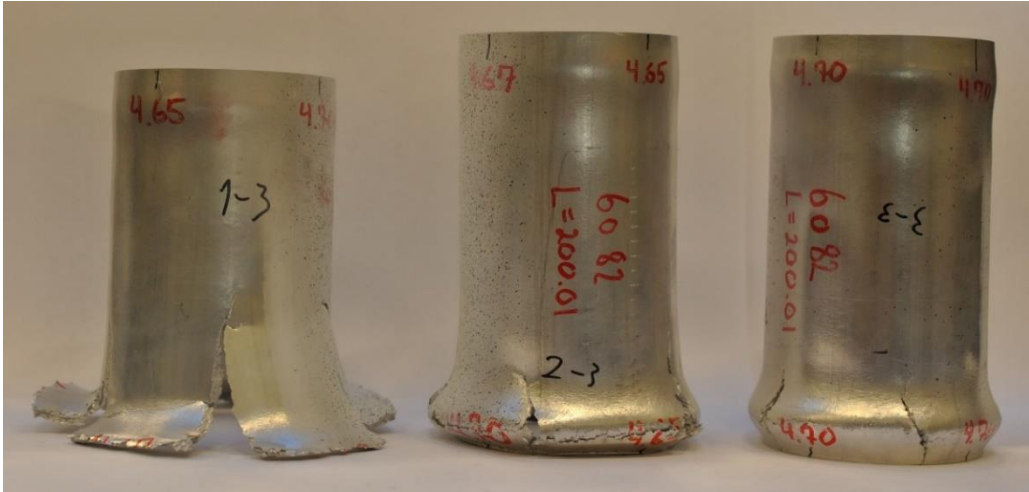


Figure e9 Post-buckling shape specimen 1-3, 2-3 and 3-3 (A6082D100L2D)

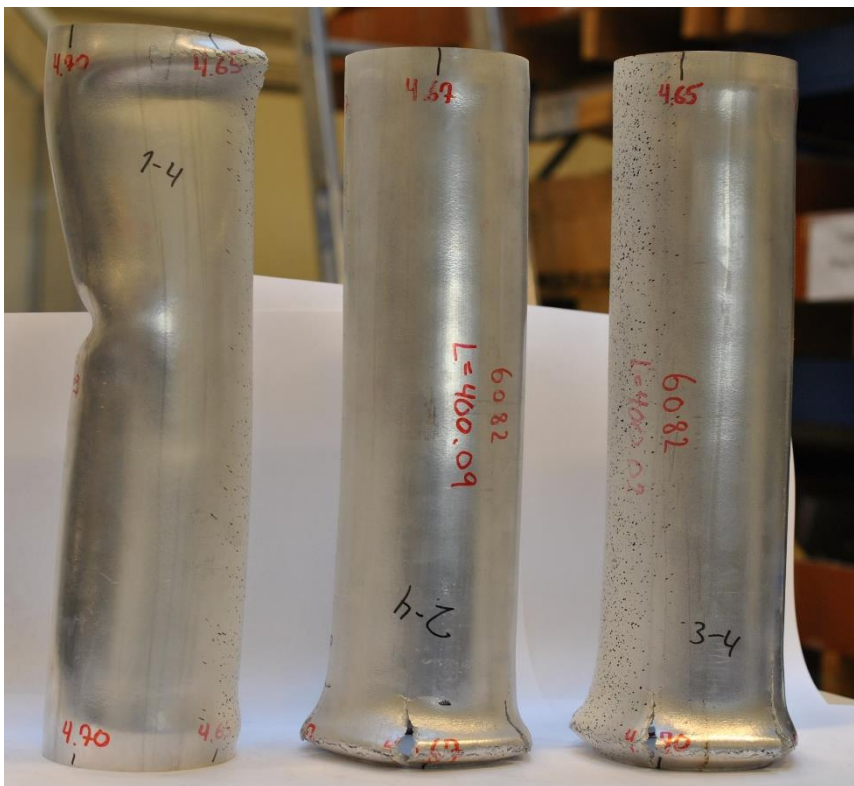


Figure e10 Post-buckling shape specimen 1-4, 2-4 and 3-4 (A6082D100L4D)

Appendix F Mesh sensitivity L2D

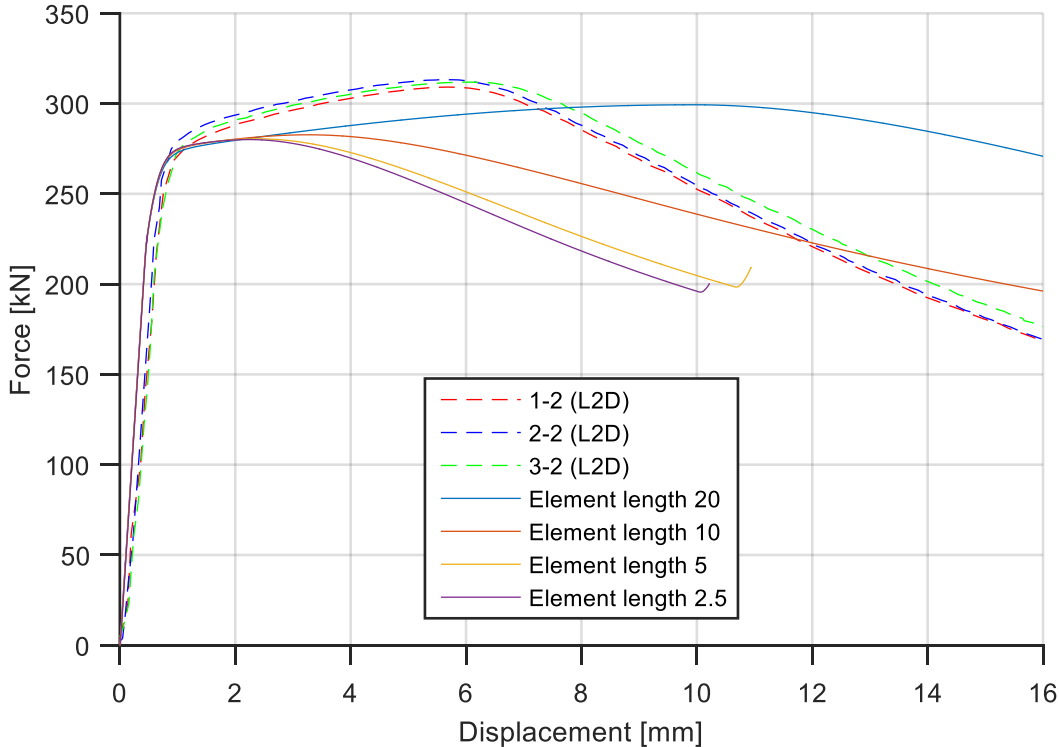


Figure f1 Mesh sensitivity for element S4R – A6060D100L2D

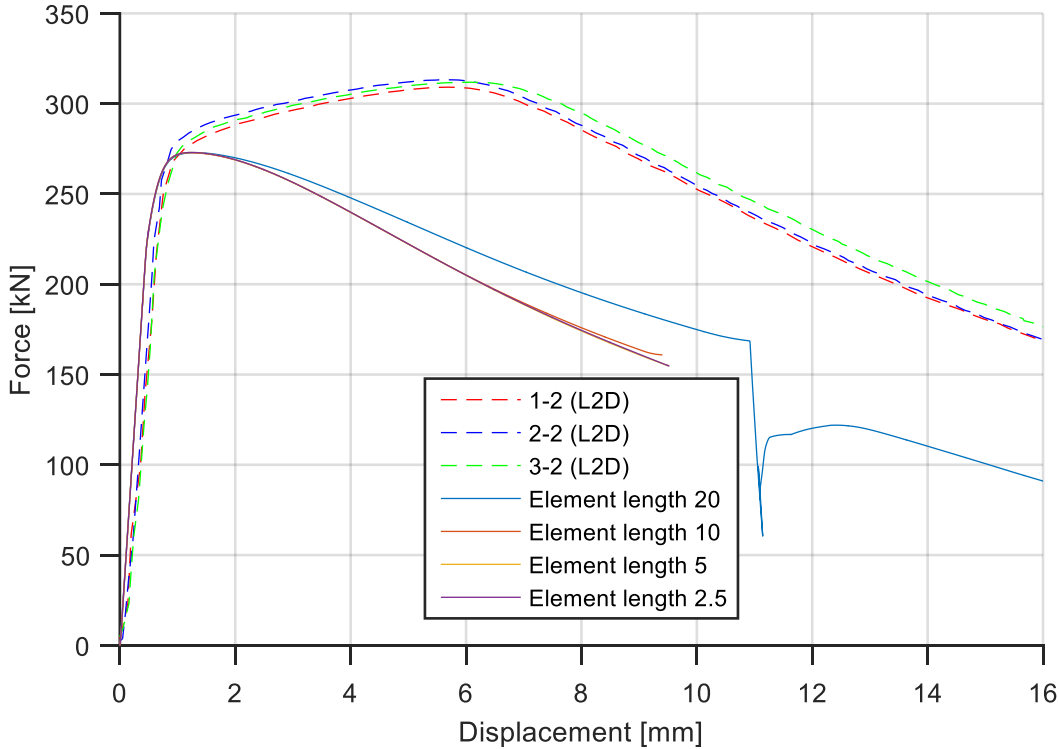


Figure f2 Mesh sensitivity for element S8R – A6060D100L2D

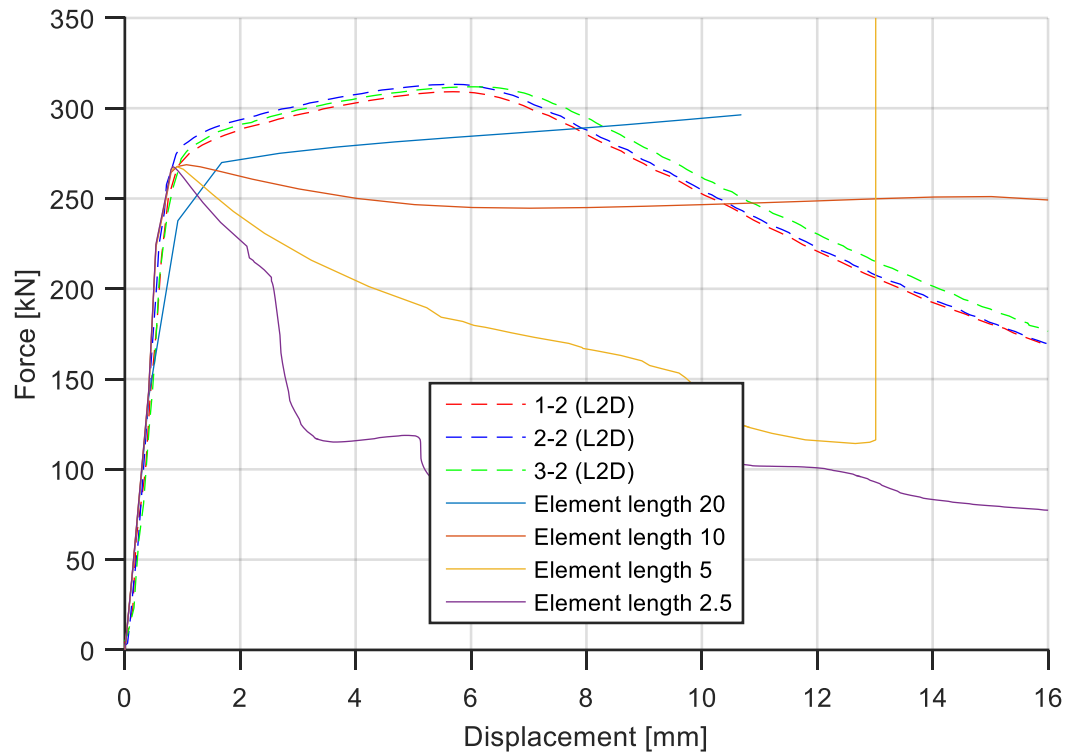


Figure f3 Mesh sensitivity for element C8R with 1 ETT – A6060D100L2D

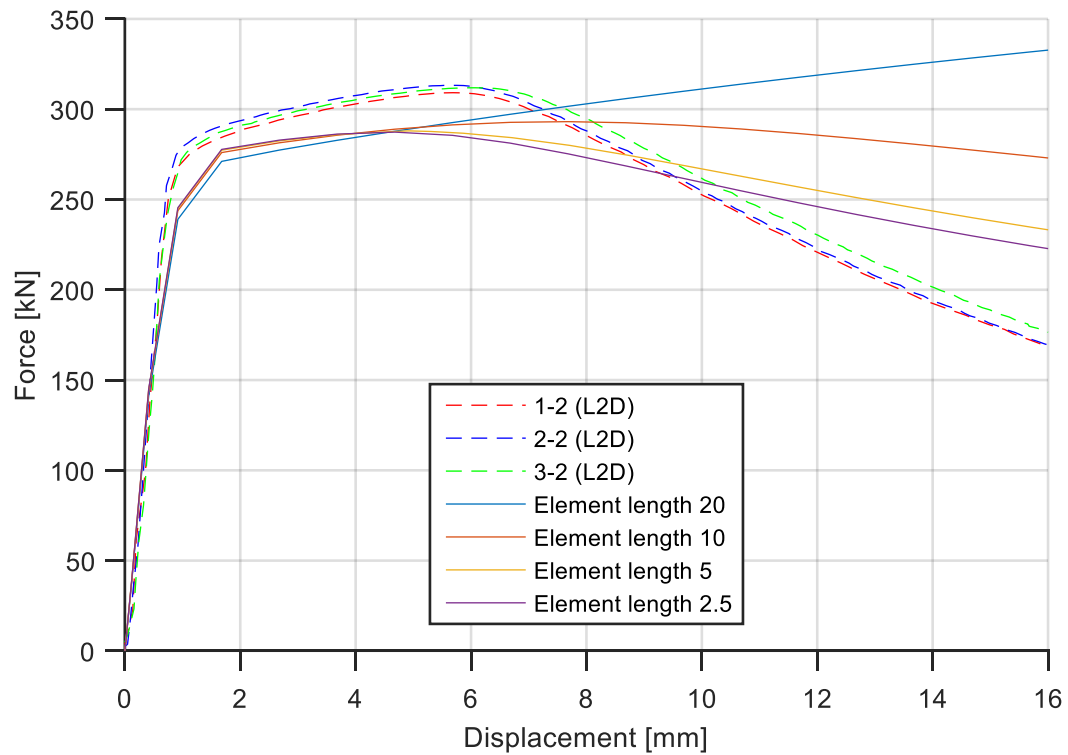


Figure f4 Mesh sensitivity for element C8R with 3 ETT – A6060D100L2D

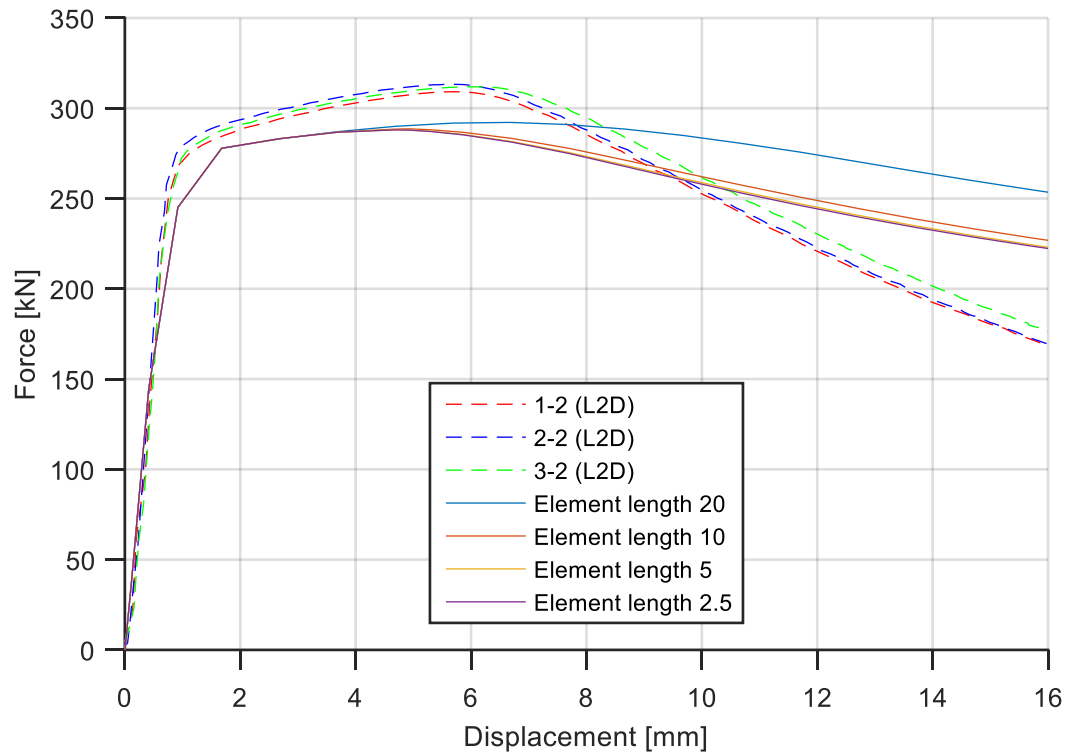


Figure f5 Mesh sensitivity for element C20R with 1 ETT – A6060D100L2D

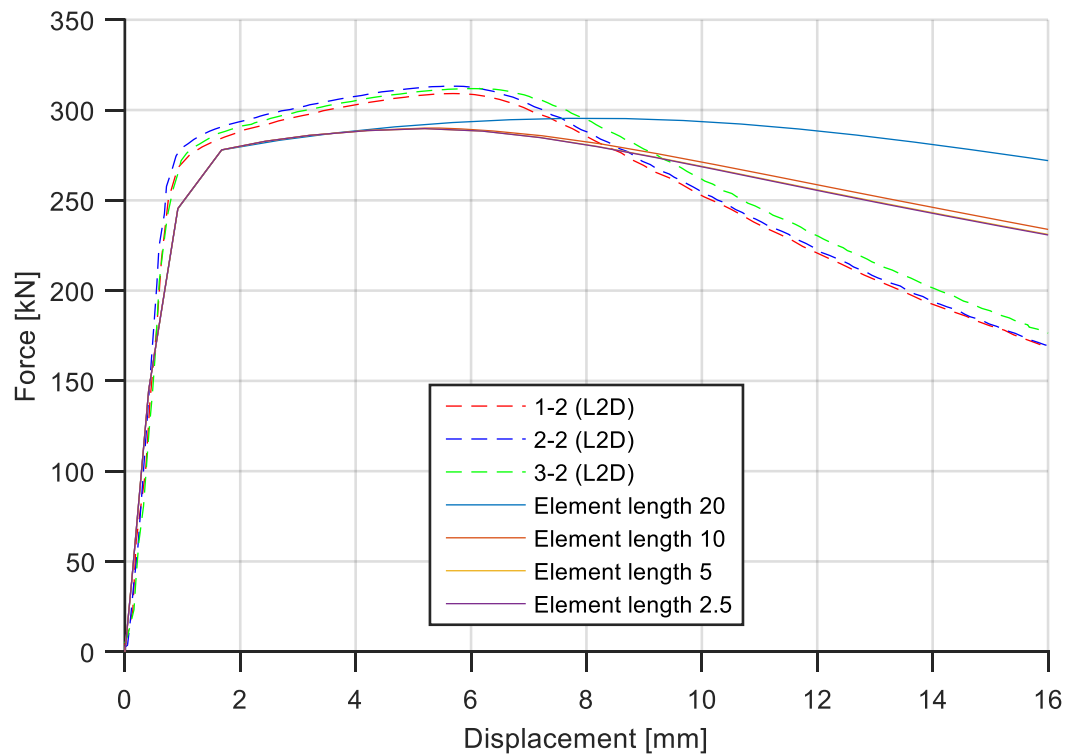


Figure f6 Mesh sensitivity for element C20R with 2 ETT – A6060D100L2D

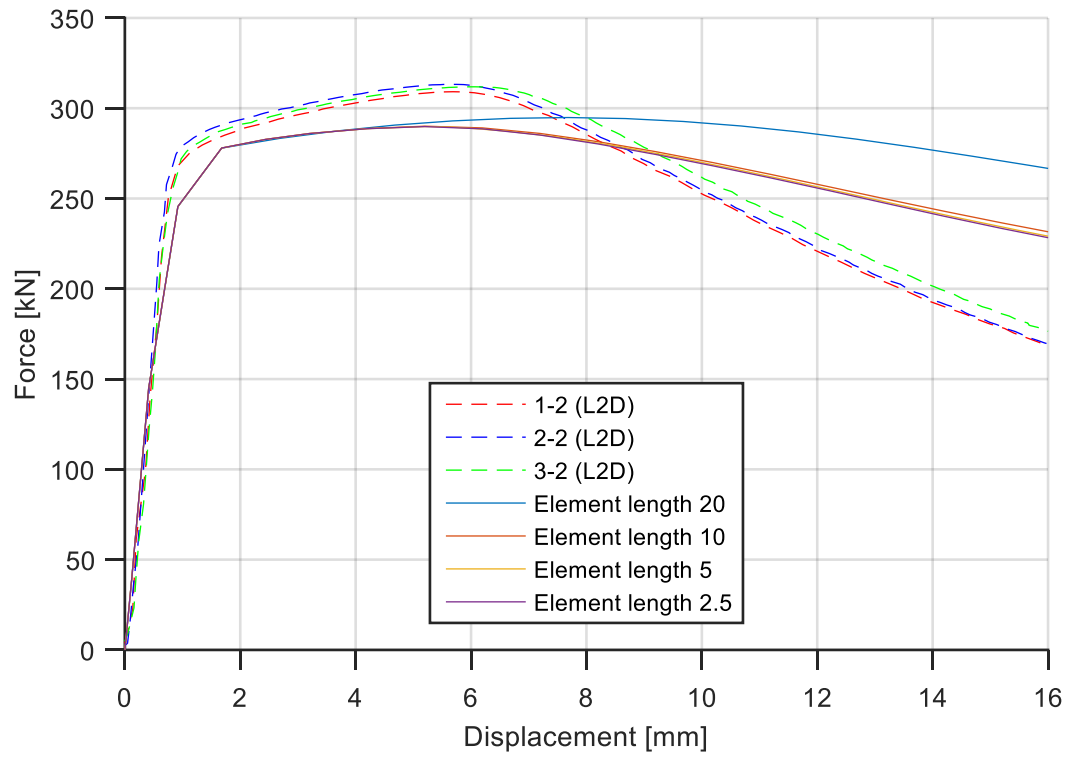


Figure f7 Mesh sensitivity for element C20R with 3 ETT – A6060D100L2D

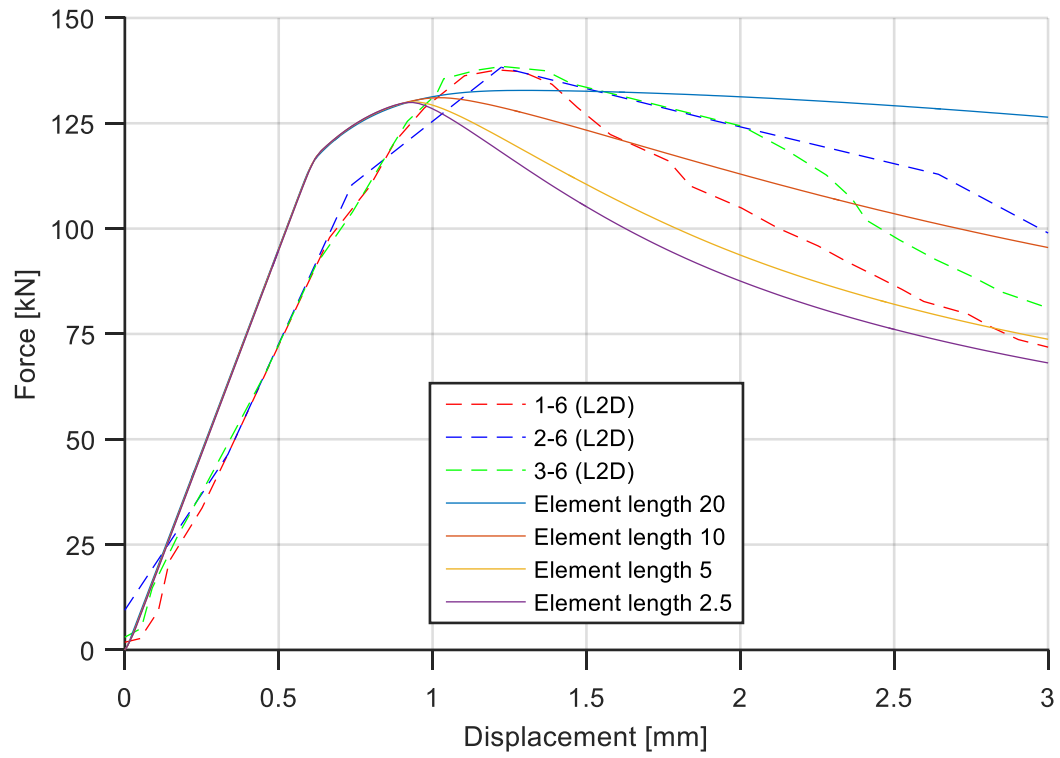


Figure f8 Mesh sensitivity for element S4R – A6060D127L2D

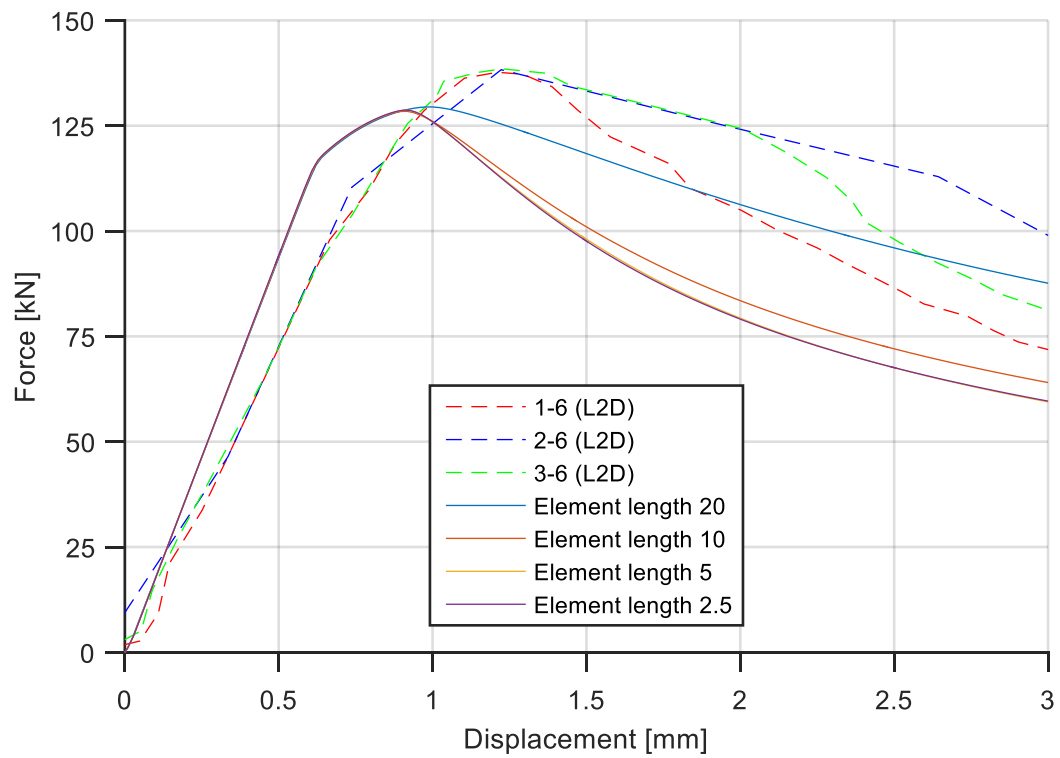


Figure f9 Mesh sensitivity for element S8R – A6060D127L2D

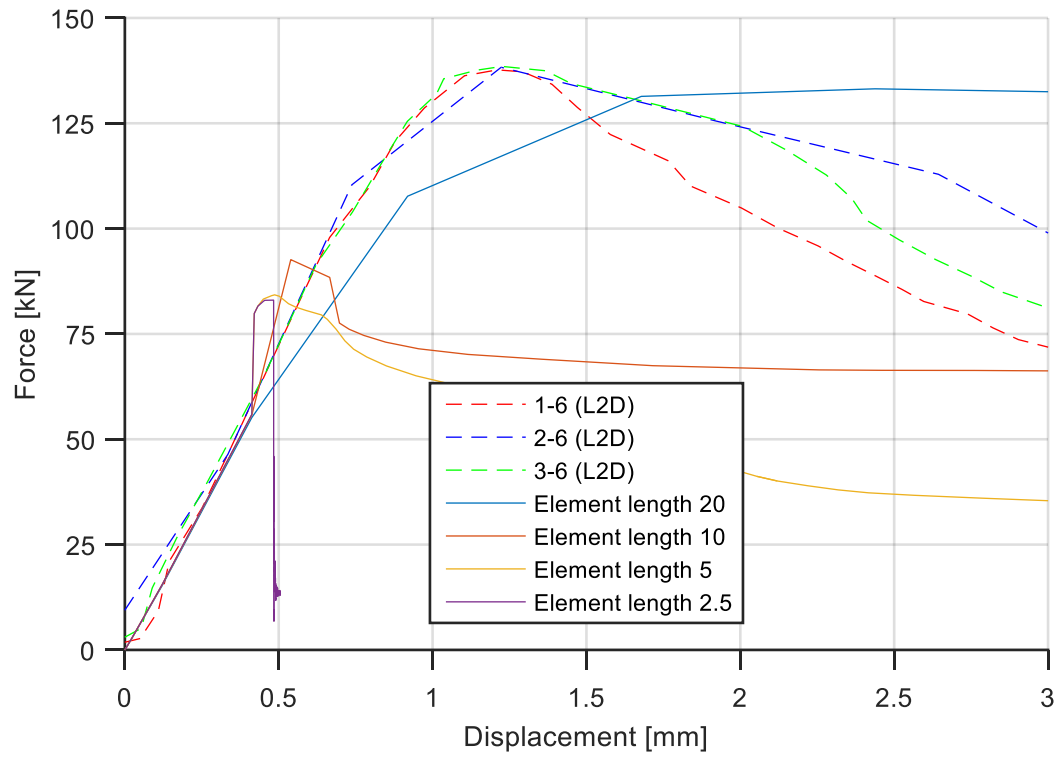


Figure f10 Mesh sensitivity for element C8R with 1 ETT – A6060D127L2D

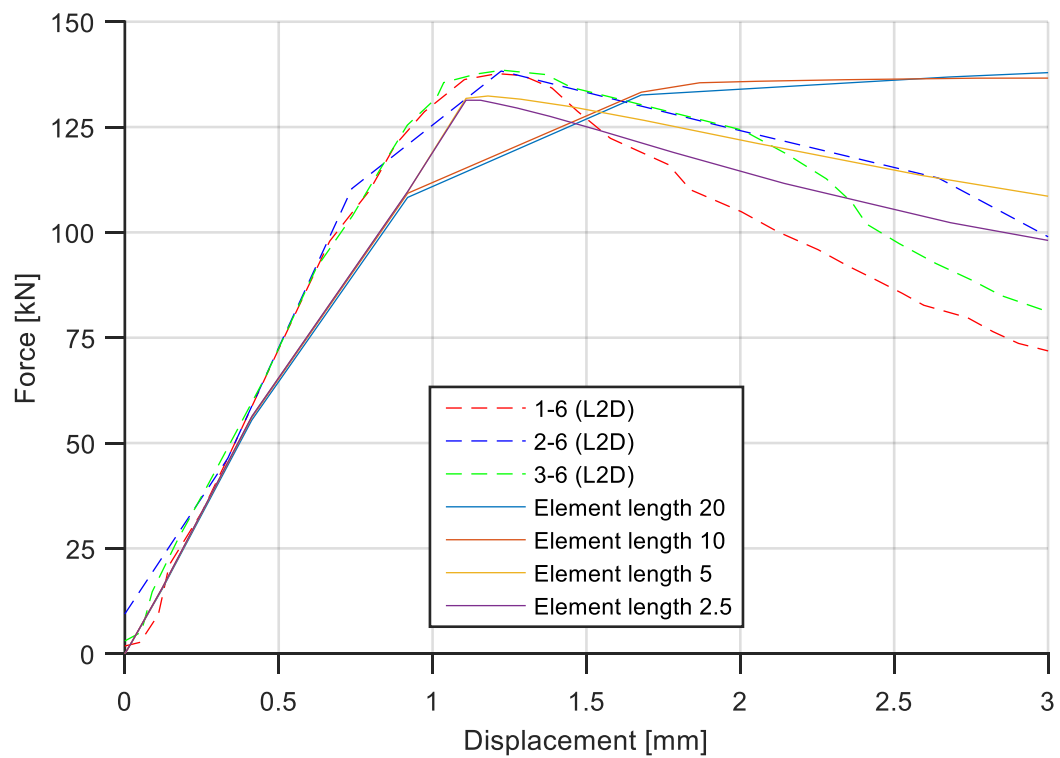


Figure f11 Mesh sensitivity for element C8R with 3 ETT – A6060D127L2D

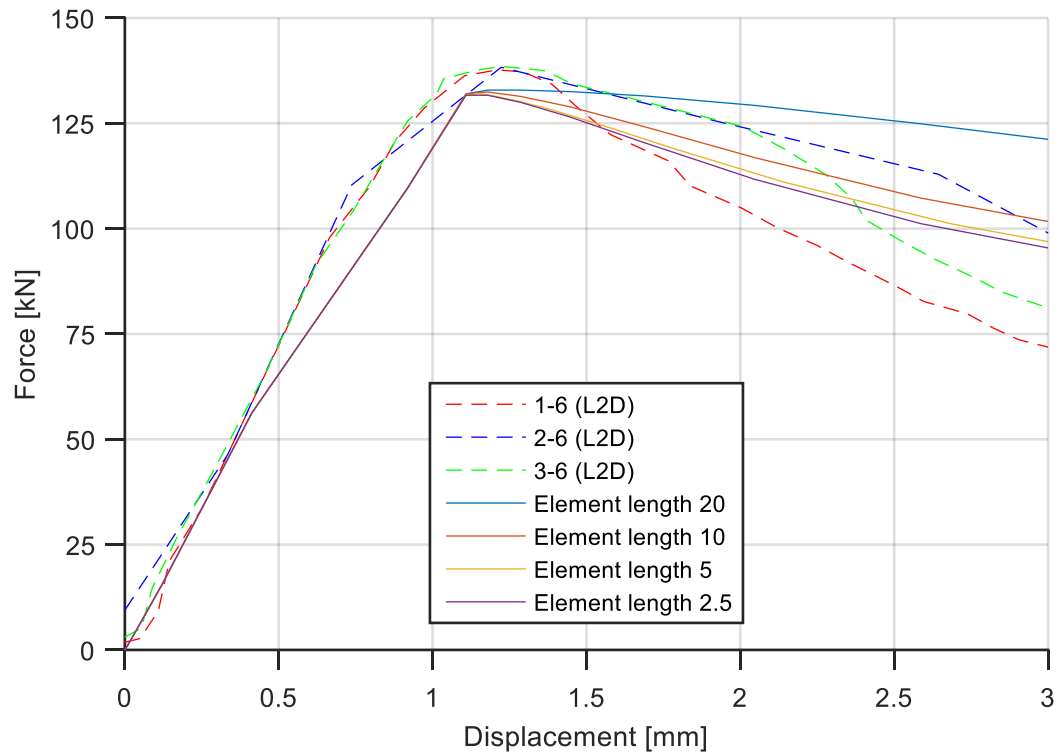


Figure f12 Mesh sensitivity for element C20R with 1 ETT – A6060D127L2D

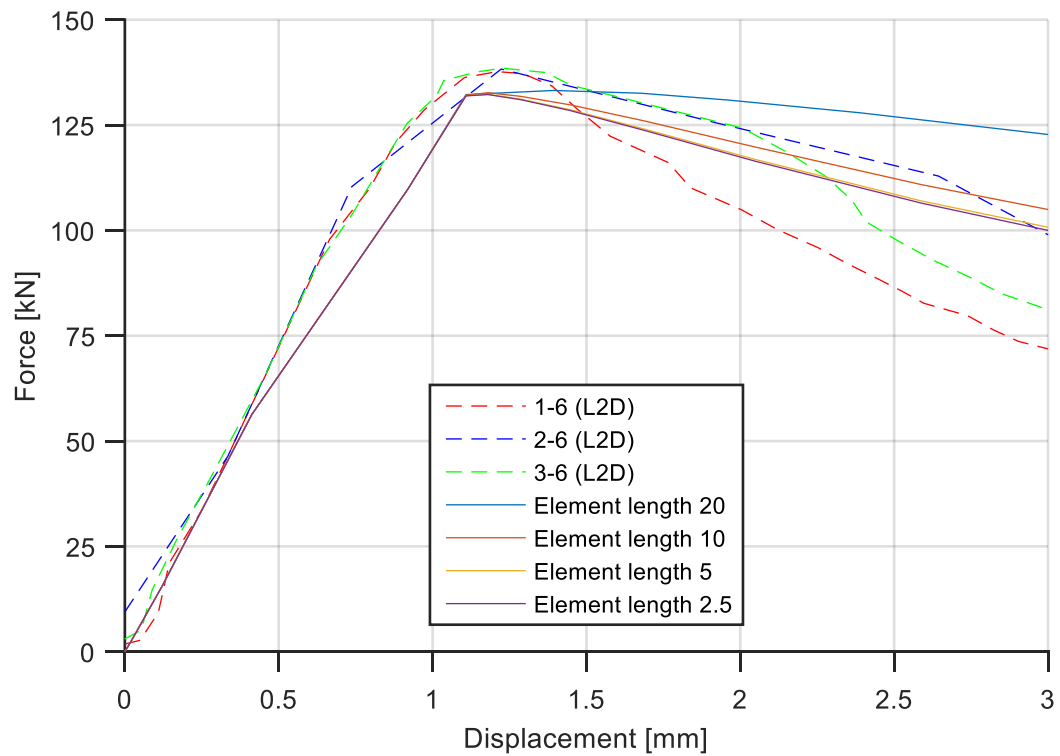


Figure f13 Mesh sensitivity for element C20R with 2 ETT – A6060D127L2D

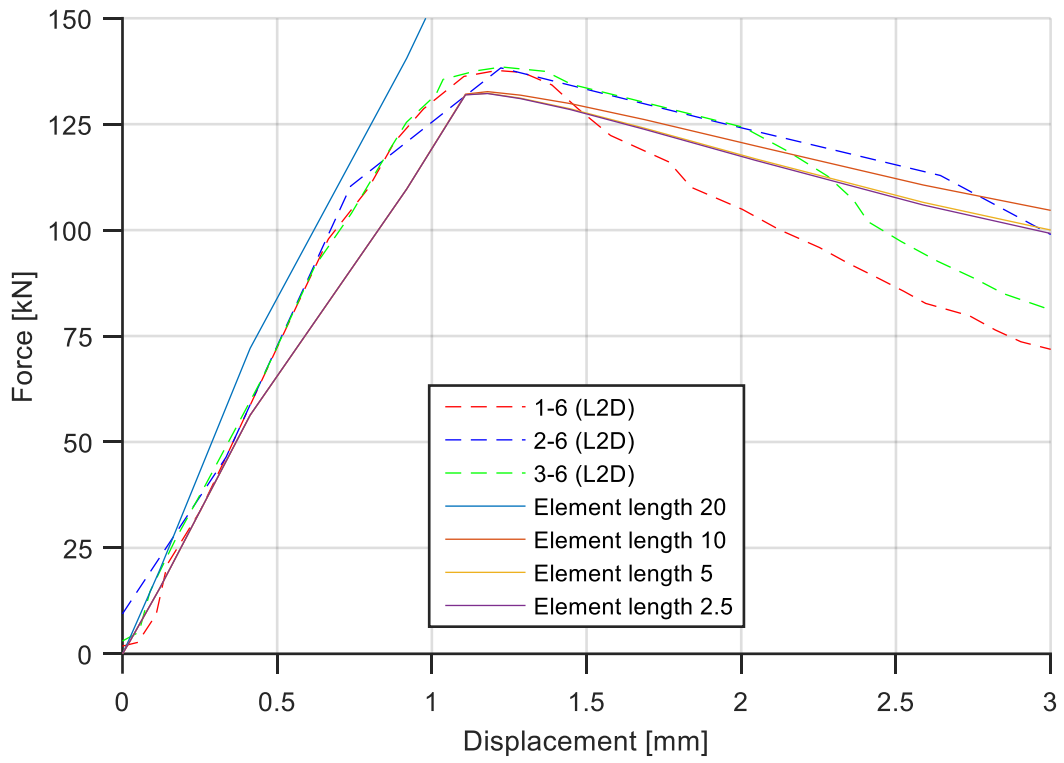


Figure f14 Mesh sensitivity for element C20R with 3 ETT – A6060D127L2D

Appendix G Laboratory L2000mm

Table g1 Measured and calculated geometry of the columns specimens for L2000

6060D100L2000	Length [mm]	D1	D2	D9	D10	D5	D6	T1	T2	T3	T4	T5	T6	T7	T8	Dm	Tm	Am
1-1long	2001.0	99.82	99.82	99.89	99.84	99.87	99.90	4.81	4.83	4.81	4.82	4.83	4.85	4.84	4.83	99.86	4.79	1430.8
2-1long	2000.0	99.79	99.78	99.83	99.82	99.85	99.86	4.80	4.77	4.83	4.84	4.76	4.80	4.81	4.82	99.82	4.77	1423.6
3-1long	2001.0	99.82	99.78	99.82	99.73	99.79	99.77	4.83	4.79	4.83	4.83	4.79	4.81	4.83	4.82	99.79	4.78	1426.5
6060D127L2000	Length [mm]	D1	D2	D9	D10	D5	D6	T1	T2	T3	T4	T5	T6	T7	T8	Dm	Tm	Am
1-2long	2002.0	126.6	127.3	126.6	126.9	126.3	126.9	1.85	1.80	1.81	1.83	1.85	1.84	1.81	1.85	126.8	1.81	709.6
2-2long	2001.0	126.9	127.0	127.1	126.9	126.9	127.0	1.86	1.89	1.90	1.87	1.87	1.90	1.87	1.87	127.0	1.86	729.5
3-2long	2000.0	127.2	126.7	126.9	127.2	126.7	126.8	1.82	1.85	1.86	1.81	1.82	1.82	1.86	1.82	126.9	1.81	711.3
6082D100L2000	Length [mm]	D1	D2	D9	D10	D5	D6	T1	T2	T3	T4	T5	T6	T7	T8	Dm	Tm	Am
1-3long	2003.0	99.98	99.82	99.81	99.79	100.53	99.33	4.79	4.79	4.79	4.81	4.83	4.80	4.80	4.82	99.88	4.77	1424.4
2-3long	2001.0	99.53	99.67	99.67	100.03	99.71	99.97	4.77	4.73	4.75	4.78	4.80	4.82	4.81	4.78	99.76	4.74	1415.9
3-3long	1981.0	99.84	99.81	99.72	99.83	99.75	99.88	4.79	4.75	4.80	4.80	4.78	4.77	4.79	4.81	99.81	4.75	1418.3

Table g2 Results from compression test of L2000 in laboratory

Profile	ID	Measured length [mm]	Velocity [mm/s]	Data frequency [Hz]	t [mm]	D _o [mm]	N _{max} [kN]	\bar{N}_{max} [kN]	S _N [kN]	CoVN [%]	S _{max} [MPa]	\bar{S}_{max} [MPa]
A6060D100L2000	1-1long	2001.00	0.05	2	4.70	100	256.90	252.63	5.42	2.15	182.56	179.53
	2-1long	2000.00	0.05	2			246.53				175.19	
	3-1long	2001.00	0.05	2			254.45				180.82	
A6060D127L2000	1-2long	2002.00	0.05	2	1.77	127	130.85	133.16	4.29	3.22	187.89	191.21
	2-2long	2001.00	0.05	2			138.12				198.33	
	3-2long	2000.00	0.05	2			130.52				187.42	
A6082D100L2000	1-3long	2003.00	0.05	2	4.70	100	393.23	405.38	11.67	2.88	279.44	288.08
	2-3long	2001.00	0.05	2			406.41				288.81	
	3-3long	1981.00	0.05	2			416.51				295.98	



Figure g1 Post-buckling shape specimen 1-1long, 2-3long and 3-3long (A6060D100L2000mm)



Figure g2 Post-buckling shape specimen 1-2long, 2-2long and 3-2long (A6060D127L2000mm)



Figure g3 Closeup post-buckling shape for A6060D127L2000mm



Figure g4 Post-buckling shape specimen 1-2long, 2-2long and 3-2long (A6082D100L2000mm)

Appendix H Results from FEA

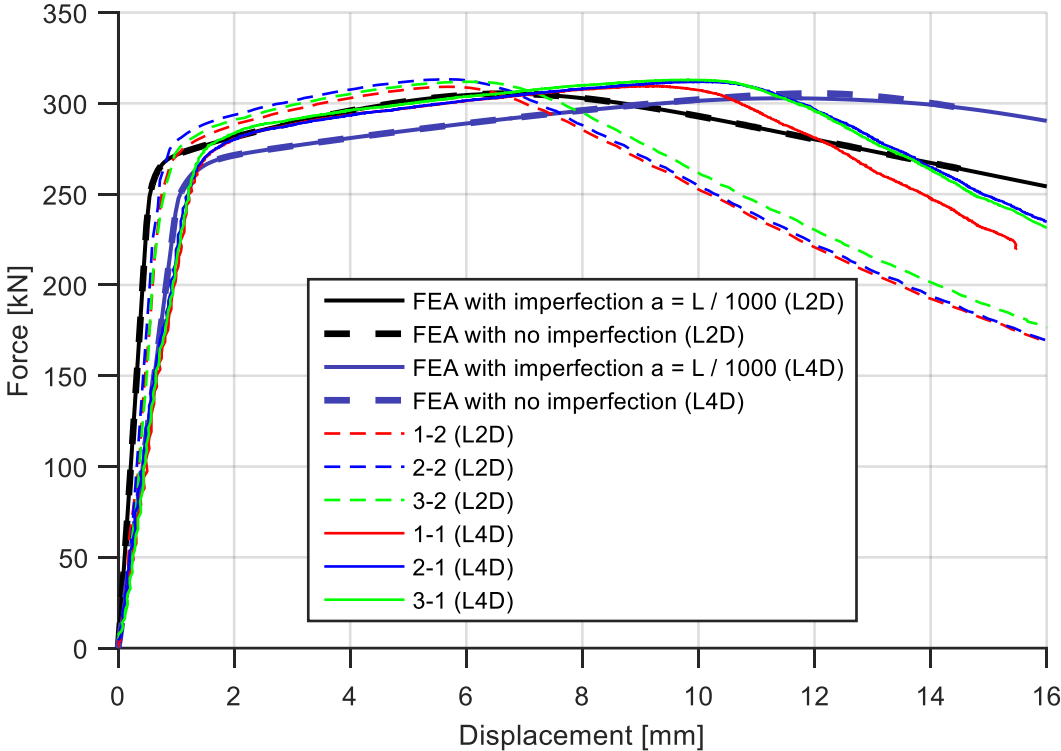


Figure h1 Force - displacement from laboratory and FEA analyses for A6060D100L2D and A6060D100L4D

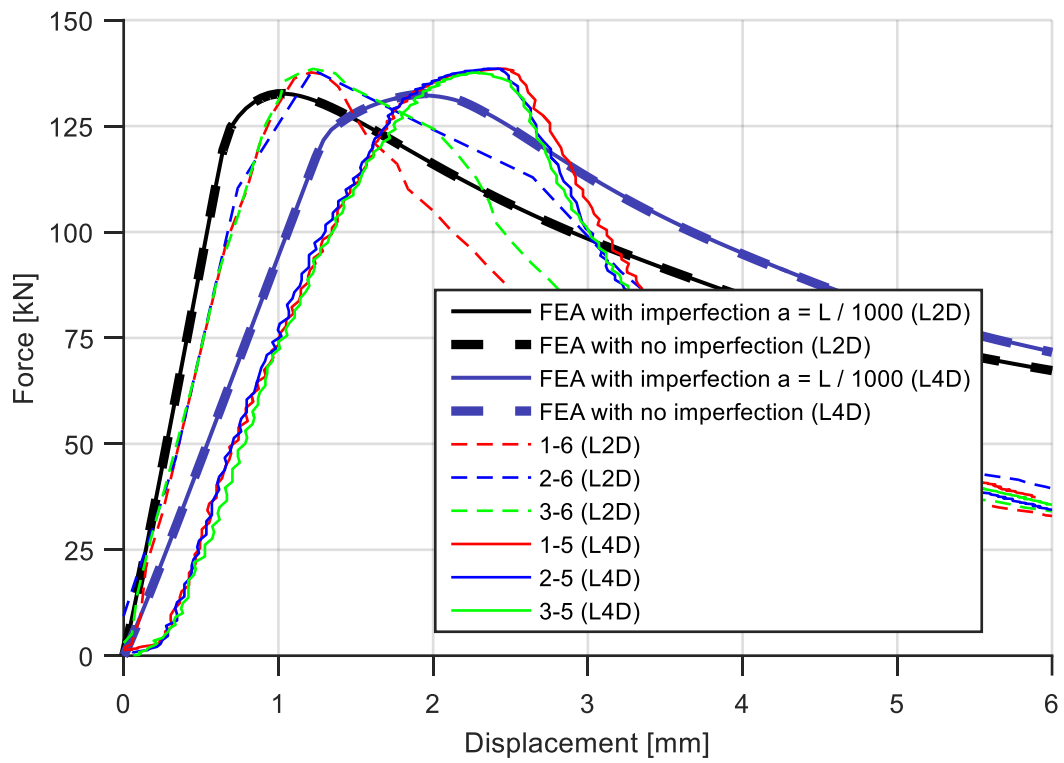


Figure h2 Force - displacement from laboratory and FEA analyses for A6060D127L2D and A6060D127L4D

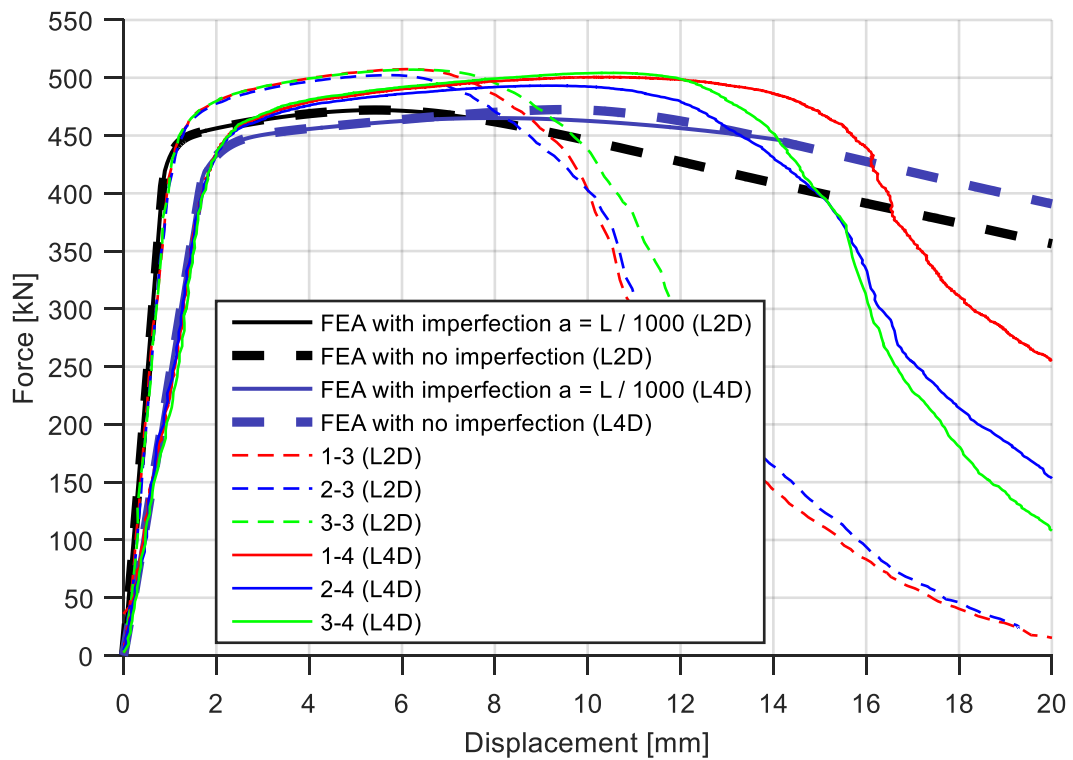


Figure h3 Force - displacement from laboratory and FEA analyses for A6082D100L2D and A6082D100L4D

Table h1 Axial capacity [kN] from FEA on lengths L0.5D to L30D

Length/Diameter	A6060D100			A6060D127			A6082D100		
	a [mm]			a [mm]			a [mm]		
	L/1000	L/2000	0	L/1000	L/2000	0	L/1000	L/2000	0
0.5	-	-	-	133.5	133.5	133.5	-	-	-
1	307.3	307.3	307.3	132.6	132.6	132.6	477.7	477.7	477.7
1.5	305.8	305.8	305.8	-	-	-	472.9	472.9	472.9
2	305.3	305.3	305.3	132.7	132.7	132.7	472.0	472.1	472.1
2.5	-	-	-	132.5	132.6	132.7	-	-	-
3	305.3	305.4	305.5	132.5	132.7	132.7	472.0	472.3	472.5
3.5	304.7	305.2	305.5	132.4	132.6	132.7	470.3	471.7	472.5
4	302.8	304.3	305.5	132.3	132.5	132.7	465.1	467.8	472.5
5	292.1	295.0	305.5	131.9	132.4	132.7	456.4	458.2	472.5
6	283.5	284.9	305.5	131.5	132.1	132.7	449.7	451.5	472.5
8	270.8	272.0	305.5	130.6	131.5	132.7	441.0	443.6	472.5
10	264.3	266.0	305.5	129.6	130.9	132.7	434.2	437.6	472.5
12	260.4	262.7	305.5	128.6	130.1	132.7	428.1	431.2	472.5
14	257.1	259.4	305.5	127.5	129.1	132.7	422.1	425.7	472.5
15.75	-	-	-	126.6	128.1	132.8	-	-	-
20	247.6	250.7	305.5	124.0	125.6	132.7	404.5	411.1	472.6
30	230.8	238.4	305.5	116.2	119.6	132.8	354.3	376.3	472.6